DOCTORATE PROGRAMME IN SUSTAINABLE AND ENERGY ENGINEERING

PLANTAS ELÉCTRICAS HÍBRIDAS OFFSHORE CON ENERGÍA EÓLICA, FOTOVOLTAICA Y ALMACENAMIENTO DE ENERGÍA

OFFSHORE HYBRID POWER PLANTS WITH WIND ENERGY, PHOTOVOLTAIC AND ENERGY STORAGE

University of Cádiz

ESCUELA TÉCNICA SUPERIOR DE INGENIERÍA DE ALGECIRAS

AUTOR/AUTHOR: EMANUEL PHILIPE P. SOARES RAMOS

DIRECTORES/SUPERVISORS: LUIS M. FERNÁNDEZ RAMÍREZ
RAÚL SARRIAS MENA

December 2021

Examining Committee

Resumen

Las grandes centrales eléctricas convencionales centralizadas, aunque son robustas y fiables, tienen numerosas desventajas. El uso de generación distribuida se ha incrementado para satisfacer la creciente demanda de energía y reducir la distancia entre generación y consumo. En consecuencia, los sistemas de energía híbridos que combinan varias fuentes de energía renovable están aumentando, principalmente en configuraciones conectadas a red.

La presencia de esta generación distribuida en la red eléctrica cambia significativamente su control y operación. Por ello, se debe prestar especial atención al estudio de sistemas híbridos compuestos por aerogeneradores y paneles solares fotovoltaicos, debido a sus características de intermitencia y fluctuación. Actualmente, una forma de mejorar la conexión de dichos sistemas a la red eléctrica es combinar diferentes fuentes de energía con sistemas de almacenamiento de energía. Debido al desarrollo de las tecnologías de almacenamiento, estas se pueden utilizar en numerosas aplicaciones, como regulación de frecuencia, estabilización de sistemas, reducción de pérdidas de transmisión, aumento de la fiabilidad, regulación de carga o soporte a servicios de red, entre otras.

Los sistemas híbridos de generación de energía utilizados hasta la fecha son en su mayoría de pequeña escala, con una potencia nominal de decenas o pocos cientos de kW. Otro aspecto relevante es que la mayoría de los sistemas eléctricos híbridos están ubicados en tierra. No obstante, en la actualidad existe en Europa un crecimiento considerable de los grandes parques eólicos marinos, principalmente debido a los avances en los aerogeneradores y las estructuras de cimentación, que han mejorado sus condiciones económicas y contribuido a la implantación de plantas marinas. Se espera que la capacidad instalada siga aumentando, ya que la Unión Europea tiene como objetivo alcanzar los 100 GW de capacidad eólica marina en 2030. En esta tesis, se ha realizado un estudio detallado que evidencia este crecimiento. Se han estudiado en detalle las características más significativas de 57 plantas instaladas en Europa con una potencia nominal superior a 150 MW y puestas en servicio a fecha de 2019, así como 11 plantas autorizadas o en construcción, extrayendo conclusiones relevantes de los datos recogidos. Los resultados muestran las tendencias en el tamaño y la capacidad

de los aerogeneradores, el modelo de aerogenerador, la distancia a la costa, la profundidad del agua, el coste de inversión, el tipo de cimentación, la tecnología de transmisión y los niveles de tensión, entre otros. Esta tesis recoge información actualizada sobre el tema, deduciendo las tendencias futuras a partir de la evaluación de parques eólicos marinos totalmente construidos, autorizados o en construcción.

Además, esta tesis evalúa el rendimiento de una planta eléctrica híbrida formada por un aerogenerador, una central solar fotovoltaica y un sistema de almacenamiento de energía que comparten el mismo punto de conexión a red. Esta central híbrida tiene una potencia nominal de 2.44 MW. Normalmente, los aerogeneradores basados en generadores síncronos de imanes permanentes presentan una topología de convertidor de potencia de dos etapas basada en un convertidor elevador CC/CC y un inversor en fuente de tensión. En la tesis, esta configuración se sustituye por un inversor en fuente de cuasi-impedancia ('*quasi-impedance source inverter*', qZSI), que es una solución atractiva para aumentar y convertir la tensión de CC en CA en una sola etapa. No se recomienda un modelo dinámico detallado del qZSI (incluyendo el modelado de todos los interruptores y sus pulsos de disparo) para estudios de estabilidad, simulaciones a largo plazo o grandes sistemas de energía eléctrica. Para tales estudios, en esta tesis se proponen dos modelos dinámicos promediados. Ambos modelos presentan el mismo sistema de control que el modelo dinámico detallado, a excepción de la generación de los pulsos de disparo, que no es necesaria en los modelos promediados.

Los dos modelos propuestos se evalúan y comparan con el modelo dinámico detallado. Los dos modelos promediados propuestos pueden sustituir al modelo dinámico detallado con una precisión satisfactoria en términos de respuesta en el dominio del tiempo en estudios de estabilidad. Además, se añadieron dos fuentes de tensión que emulan los terminales de C_1 y C_2 para mejorar la configuración propuesta y permitir la integración de la planta solar fotovoltaica y la batería, respectivamente. La planta eléctrica híbrida conectada a red en estudio consta de un aerogenerador de 1.5 MW, un generador solar fotovoltaico de 402 kW conectado al condensador C_2 y una batería de iones de litio de 532 kW conectada al condensador C_1, lo que hace un total de 2.44 MW para la potencia nominal de la planta híbrida. Además, una carga de 1.2 MVA comparte el punto de conexión a red con la planta híbrida.

Después de elegir la configuración más adecuada para la conexión del aerogenerador, la planta fotovoltaica y el sistema de almacenamiento de energía, un

segundo objetivo de la tesis es el desarrollo de estrategias de control de las fuentes de energía y sus convertidores. Se implementan y evalúan diferentes estrategias de control para regular la potencia activa, reactiva y los niveles de tensión.

Finalmente, un tercer objetivo es el diseño de un sistema de control supervisor para la planta híbrida. Este sistema debe poder gestionar y coordinar el flujo de energía entre los dispositivos del sistema híbrido. Algunas de las variables consideradas por el control supervisor son la referencia de generación establecida por el operador de la red, la producción instantánea de los aerogeneradores y los paneles fotovoltaicos, y el estado de carga de la batería. Se han desarrollado diferentes estrategias de control para una adecuada gestión energética, y una correcta regulación de los parámetros eléctricos de la planta híbrida, tanto internamente como en el punto de conexión a red. Utilizando modelos ampliamente reconocidos para los componentes de la planta híbrida, se ha representado el comportamiento del sistema, y se han evaluado los diseños originales de esta tesis mediante simulación en diferentes condiciones de funcionamiento (cambios en la velocidad del viento, radiación solar o generación de la red, etc.) Los resultados han mostrado el adecuado funcionamiento de la planta híbrida a través de las estrategias de control implementadas, que coordinan las fuentes de energía renovable, la batería y la carga mediante convertidores en fuente de impedancia.

Abstract

Large centralized conventional power plants, although robust and reliable, have numerous disadvantages. The use of distributed generation has increased to fulfill the growing energy demand, and to reduce the distance between generation and consumption. Consequently, hybrid energy systems that combine several renewable energy sources are flowering, mainly in grid-connected configurations.

The presence of this distributed generation in the electric grid changes its control and operation significantly. Therefore, special attention should be paid to the study of hybrid systems composed of wind turbines (WTs) and photovoltaic solar panels, due to their intermittent and fluctuation characteristics. Currently, a means of improving the connection of such systems to the electricity grid is to combine different energy sources with energy storage systems. Due to the development of storage technologies, they can be used in numerous applications, such as frequency regulation, system stabilization, reduction of transmission losses, increased reliability, load regulation or support for grid services, among others.

The hybrid power generation systems used to date are mostly small-scale, with a rated power of tens or hundreds of kW. Another relevant aspect is that most hybrid power systems are located onshore. Nevertheless, a considerable growth of large-scale offshore wind farms is noticeable currently in Europe, mainly due to advances in WTs and foundation structures, which have improved their economic conditions and contributed to the implementation of offshore plants. It is expected that the installed capacity will continue to increase, since the European Union aims at reaching about 100 GW of offshore wind capacity by 2030. In this thesis, a detailed study evidencing this growth has been carried out. The most significant characteristics of 57 plants installed in Europe with a rated power above 150 MW and fully commissioned until 2019, as well as 11 plants authorized or under construction, are studied in detail, drawing relevant conclusions from the data collected. The results show the trends on WT size and capacity, turbine model, distance to shore, water depth, investment cost, type of foundation, transmission technology, and voltage array systems among others. This thesis gathers the latest information about the topic, deducing future trends from

the evaluation of offshore wind farms fully commissioned, authorized or under construction.

Furthermore, this thesis evaluates the performance of a hybrid power plant consisting of a WT, a solar photovoltaic (PV) power plant, and an energy storage system that share the same grid connection point. This hybrid power plant has a rated power in the range of several MW. Typically, permanent magnet synchronous generator-based WTs present a two-stage power converter topology based on a DC/DC boost converter and voltage source inverter. In the thesis, this configuration is substituted by a quasi-Z-source inverter, which is an attractive solution for boosting and converting the voltage from DC to AC in a single stage. A switched dynamic model of the quasi-Z-source inverter (including the modelling of all switches and firing pulses) is not recommended for steady-state stability studies, long-term simulations, or large electric power systems. For such studies, two averaged dynamic models are proposed in this thesis. Both models present the same control system as the switched dynamic model, except for the generation of the firing pulses, which is not necessary in the averaged models.

The two models proposed are evaluated and compared with the switched dynamic model. Both proposed averaged models can substitute the switched dynamic model with satisfactory accuracy in terms of time-domain response in steady-state stability studies. In addition, two voltage sources emulating the terminals of C_1 and C_2 are added to enable the integration of PV and BES, respectively. The grid-connected hybrid power plant under study consists of a 1.5 MW WT, a 402 kW PV generator connected to the capacitor C_2, and a 532 kW lithium-ion battery connected to capacitor C_1, making a total 2.44 MW for the rated power of the hybrid plant. Moreover, a load of 1.2 MVA shares a common connection point with the hybrid power plant.

After choosing the most suitable configuration for the connection of the WT, the photovoltaic power plant, and the energy storage system; a second objective of the thesis is the development of control strategies for the energy sources and their converters. Different control strategies are implemented and evaluated to regulate active and reactive power, and voltage levels.

Finally, a third objective is the design of a supervisory control system for the hybrid power plant. This system must be able to manage and coordinate the energy flow between the devices in the hybrid system. For this purpose, some of the variables

considered by the supervisory control system are the generation set point established by the grid operator, the instantaneous production of WTs and the photovoltaic panels, and the state of charge of the battery. Different control strategies have been developed for a proper energy management, and an adequate regulation of the electric parameters of the hybrid plant internally and at the point of connection to grid. Using widely recognized models for the components of the hybrid power plant, it has been possible to represent the behaviour of the system and to evaluate the original designs of this thesis through simulation under different operating conditions (changes in wind speed, solar radiation, or electricity generation of the grid, etc.). The simulation results have shown the adequate performance of the hybrid power plant through the control strategies implemented, which coordinate the renewable energy sources, the battery and the load using impedance source converters.

Table of Contents

List of Figures

List of Tables

List of Abbreviations[1]

IGBT - Insulated-gate bipolar transistor

IRENA - International Renewable Energy Agency

SOC - State-of-charge

EMS - Energy management system

SVM - Space vector modulation

MVDC - Medium-voltage direct current

MVAC Medium-voltage alternate current

HVDC High-voltage direct current

PCC - Point of common coupling

FRT - Fault ride through

IEA - International Energy Agency

CSP - Concentrating solar power

USA - United States of America

REDII - Renewable energy directive

MENA - Middle East and North Africa

UAE - United Arab Emirates

UK - United Kingdom

MMC - Modular multilevel converter

EIA - Environmental impact assessment

SPA - Special protection areas

SAC - Special areas of conservation

MSDF - Marine Strategy Framework Directive

PWM - Pulse width modulation

SC - Super-capacitor

UC - Ultra-capacitor

MPC - Model predictive control

PEM - Proton exchange membrane

FC - Fuel cell

DOD - Depth of discharge

P&O - Perturb and observe

STS - shoot-through state

NSTS - Non-shoot-through state

ADM - Averaged dynamic models

SBC - Simple boost control

MBC - Maximum boost control

MCBC - Maximum constant boost control

ZSVM - Z-space-vector modulation

SO - System operator

---

[1] The use of an 's' after any of these abbreviations refers to the plural

Acknowledgements

Primeiramente agradeço a Deus pela vida, alegria e disposição.

Agradeço a minha esposa Laís, pelo amor, paciência, carinho, dedicação, incentivo, simplicidade, respeito, convívio....

Devo um carinho muito especial aos meus orientadores, Luis M. Fernández Ramírez e Raúl Sarrias Mena, pois além da admiração que tenho por eles, me fizeram parte suas famílias, suavizando toda a minha jornada em "terras espanholas". Agradeço pelas nossas conversas, principalmente aquelas de incentivo e amizade, a cada orientação e paciência ao longo do doutorado. Obrigado pelo respeito e carinho.

Agradeço aos amigos do grupo de pesquisa "Tesyr-023", Enrique, Paco e Carlos e todos os demais que de alguma forma contribuíram. Agradeço em especial a Professor Pablo, a quem confiei as minhas angústias, este "tío" me ajudou muito em toda caminhada.

Agradeço aos colegas do CEFET-MG, Curvelo, pelo carinho. Isso tudo contribui para resultados positivos.

Agradeço a meus pais, Sidney e Claudia pelos ensinamentos que ao longo dos anos me tornam cada vez mais maduro. A minha tia Gabriela e aos meus avôs Laércio e Tereza, a quem sempre terei dívidas sagradas. Ao meu irmão Caíke e a Tânia Colina pelo carinho.

Agradeço a Celeste, Hebert, Tia Nessa toda família da Laís, hoje são parte de minha família.

Aos meus amigos Sérgio e Alexandre (Xula), simplesmente pela grande amizade.

Emanuel Philipe P. S. Ramos

"É preciso que eu suporte duas ou três larvas se quiser conhecer as borboletas."

"O essencial é invisível para os olhos."

Antoine de Saint-Exupéry

Chapter 1: Introduction

The energy consumption keeps scaling over the years, and it is expected to increase 35% on 2005 levels, by 2030 [1]. Among energy sources, fossil fuels are the most commonly used, although they present certain disadvantages, such as the release of carbon dioxide (CO_2) and the dependency of some countries on this fossil resource. According to [2], CO_2, methane and nitrous oxide are the main generators of greenhouse gas emissions with 76%, 16% and 6% respectively, and the reduction of these gases was one of the issues discussed at the 26th Conference of the Parties (COP26). Furthermore, from 76% contribution of CO_2, 65% are from fossil origin. A feasible solution to contribute to the reduction of these gases is to give more space to renewables in the energy mix.

In this scenario, wind and solar energy are the fastest growing renewable energies in the world. Several factors contribute to favour the growth of wind energy, highlighting the fact that it has a lower environmental impact when compared to the use of fossil fuels, it also has social acceptance and improved efficiency due to advances in modern turbine projects. Figure 1.1 shows the evolution of the total wind installations in the world between 2001 to 2020, while Figure 1.2 shows the expectations for new wind installations (GW) in the world until 2030.
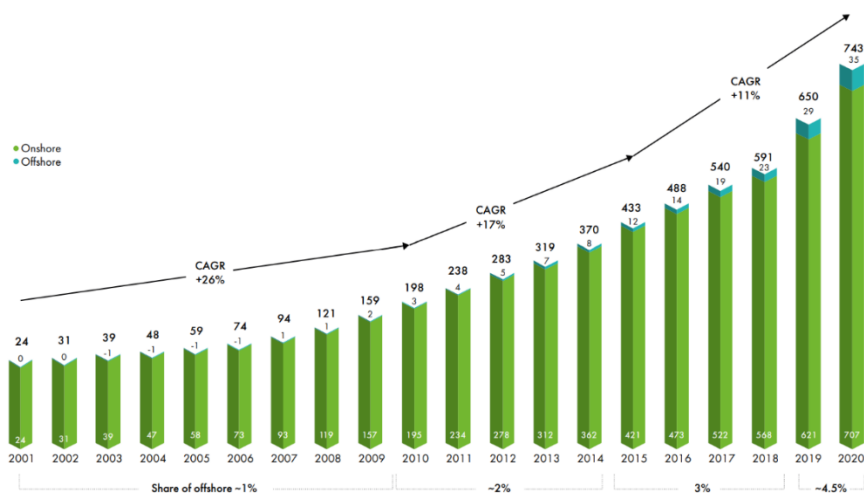
Figure 1.1. Growth of total wind installations in the world (GW)[3]
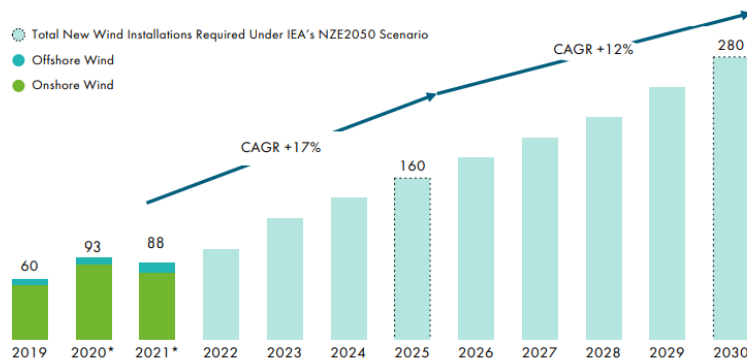
Figure 1.2. Expectations for new wind installations (GW) in the world [3].

Analyzing Figure 1.1 and Figure 1.2, it is possible to observe that before 2025, the wind industry will exceed 1TW in accumulated global wind energy installations onshore and offshore. Furthermore, it is possible to notice an increase in the relevance of offshore installations compared to onshore, in which the offshore reached a percentage of 4.5% of the share in 2019/2020. One of the factors that can influence the increase of offshore wind farms (OWF) is the decrease in the average levelized cost of electricity (LCOE). The average LCOE of onshore wind energy is expected to decrease 25% by 2030 when compared to 2018 levels. Concerning offshore wind, the expectation is that the LCOE will decrease by 55% from 2018 levels [3]. Moreover, offshore wind energy showed better indicators in almost every environmental impact index investigated according to [4], which is aligned with the sustainability trends pursued all over the world. In this context, OWF are an interesting option to contribute to renewable energy.

Regarding the photovoltaic (PV) generation systems, although they have some challenges such as cost reduction, increase efficiency and improve energy storage technologies, they have been showing great growth and are very promising systems. As well as wind, PV technology presents significant advances and the electrical energy generated stands out for being silent, non-polluting, low maintenance and inexhaustible. Moreover, like WTs, PV systems use maximum power point trackings (MPPT) algorithms and intelligent algorithms to improve their efficiency, and are usually combined with storage systems, obtaining interesting advantages [5,6].

Figure 1.3 shows the evolution of the grid-connected PV installations between 2011 to 2019. PV generation systems were increased almost 10 times in the decade,

achieving in 2019, the capacity of 623,2 GW of cumulative PV installations. The European Union (EU) targets generating 20% of its energy through renewable sources and improving 20% of its efficiency [7].
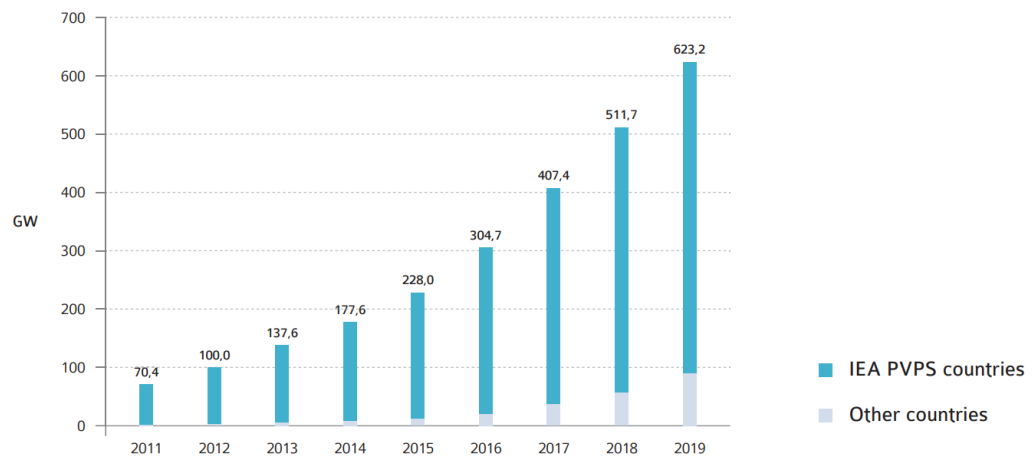
Figure 1.3. Growth of global PV installed capacity [8].

WTs share all the benefits of PV power plants, such as no carbon emission, an inexhaustible source and contribution to sustainable development, but they also have other advantages. For instance, smaller areas are available for larger plants in terms of installed capacity, and greater efficiency. On other hand, they cause a considerable visual and sound impact.

Although these systems are implemented separately, the combination of several generation sources, integrated into a single power plant (hybrid system), presents significant advantages, the reason why they are increasingly used today. Non-renewable hybrid power plants, although relevant, have disadvantages when compared to renewables, For this reason, a configuration frequently used today is hybrid wind/PV plants, since these systems represent a very interesting technological solution due to their complementary characteristics [9].

However, the insertion of large amounts of hybrid systems based on renewable sources in energy systems must be correlated in all aspects, as there are social, environmental, economic, and technical challenges. From a social point of view, these energies demand large areas, reducing, for example, areas of family cultivation and have other disadvantages already mentioned, such as visual impacts and noise, for wind power plants. As social benefits, we can highlight the generation of regional jobs, increased living standards in remote areas and also better health due to less pollution.

Concerning the environment, renewable energy belongs in the green industry context, and, in this sense, the intention is to maintain the green label associated with them by not causing and/or reducing the damage to the environment when manufacturing or installing these plants [10]. However, as in any human activity, a certain impact on the surrounding ecosystem is inevitable. There are positive and negative issues associated with renewable energy. The main positive effects are the replacement of fossil fuels with wind energy and solar, and the offshore structures, acting as artificial reefs, can increase the diversity of marine species. In contrast, the risks of collision for birds, the displacement of marine mammals and birds, and habitat loss or degradation can be mentioned as negative. Furthermore, the production of electricity from renewable energies, although they do not emit CO_2 at the time of generation, involves emissions associated with other phases of the life-cycle, for example, during manufacturing, transport, installation, maintenance and their de-installation and waste management.

From an economic point of view, the challenges of transitioning to the new matrix composed of renewable sources, including solar and wind, are immense. Although the average costs should decrease, they are still high when compared to other energy sources, such as hydroelectric power and biomass.

From a technical point of view, as a natural resource, wind speed is highly stochastic, uncertain, and therefore, challenging to predict with perfect accuracy [11]. An alternative to solve the problem of the intermittency of these wind and solar power plants is to insert some energy storage solution into the generation system, thereby providing a significant improvement in the stability and quality of energy generated [12,13]. Hybrid systems with energy storage help in the management and uncertainty of this type of generation, ensuring greater coupling between generated and consumed energy, contributing to the work of the system operator, who is responsible for ensuring accurate dispatch power. With this, it is eminent that the use of hybrid plants combining wind energy, solar PV and energy storage will contribute to this goal. The challenge is to achieve efficient, reliable and technically and economically viable hybrid power plants.

For these hybrid systems with energy storage, the use of batteries, supercapacitors (SC), flywheels, hydro-pumped and hydrogen stands out, depending on the time the energy is intended to be stored and the method of system management.

In general, it is interesting to combine a short time storage system with a long time, for example, the use of batteries (short time) with hydrogen (long time), and even with hydrogen production, which can be an interesting alternative [14].

The large-scale renewable systems connected to the grid, in general, must maintain high levels of reliability. As systems based on wind and solar energy present intermittent generation, they are susceptible to disconnect from the grid in the event of disturbances, to avoid damage to the equipment. However, to achieve smarter and more reliable electrical grids these systems are required to stay connected during the period of disturbance of the network to try to favour the recovery of the failure in the grid, being disconnected only in the last instance depending on the magnitude and duration of the failure. The authors propose in [15] to improve the reliability of these hybrid systems in case of failure, using a superconducting magnetic energy storage system (SMES). The hybrid system studied features a 24 MW PV power plant and two 27 MW wind power plants, one onshore and the other offshore, and a 10 MW SMES unit connected to the common connection point.

Another important parameter to improve the performance of the hybrid systems is the study and evaluation of the most suitable configuration according to technical criteria, to guarantee the best design, control and operation of the hybrid power plants. Among the different variable speed WT technologies available, squirrel cage induction generator (SCIG) with a full converter can be operated at variable speed. However, double-fed inductor generator (DFIG), and permanent magnet synchronous generator (PMSG) are usually employed, due to their higher energy efficiency [16–18]. PMSG has several advantages as high performance, low maintenance compared to DFIG, and they do not need the gearbox. Sufficient information regarding the models of these turbines can be found in [19]. Regarding PV plants, four topologies for large-scale power plants are analyzed in [20], the central, the string, the multi-string and the fourth topology, module integrated. With regards to the converters, different converter models can be implemented. For example, the topology used in [21] is connected to the grid through two conversion stages, consisting of two parallel-connected triple-port dual active bridge (DAB) combined into a two-level inverter.

WTs can be connected in several ways. In [22] different topologies to connect the converter at the machine side (machine side converter, MSC) for PMSG WTs are suggested. In [23], different topologies are proposed to be connected to the grid. For

instance, PMSG can be connected by two-level pulse width modulation voltage source converter (2L-PWM-VSCs), which are usually configured as a back-to-back structure (2L-B2B). The 2L-B2B solution is relatively simple, robust, and reliable. The drawbacks of this configuration are the larger switching losses and lower efficiency at megawatts (MW) and MV power levels, and furthermore it has high indices of THD [23]. On other hand, for the rectifier stage, a simple diode rectifier can be applied to the generator side converter (GSC). However, when the turbine is at low speed, due to the low incidence of wind, the rectifier may be insufficient to reach the levels of voltage required by the input of VSI. In these cases, a boost converter DC/DC is employed to increase the voltage level to values sufficiently high for attending GSC. This solution is simple, cost-efficient and allows to extract maximum power from the WT. However, it has the disadvantages of high harmonic current distortions in the windings of the generator, heating and oscillations in the torque.

An alternative for WTs connected to the grid are impedance source converters (ZSCs). In [24,25], this solution was proposed as a possible improvement compared to the traditional voltage source inverter (VSI). After this promising initial research, several topologies of ZSCs were proposed [26,27]. Among these topologies ZSC, the quasi Z source inverter (qZSI) [28] was attractive due to several improvements compared to traditional impedance source inverters (ZSIs). In this thesis, a WT based on PMSG is connected to the grid through a qZSI with battery energy storage (BES) and the PV system is connected through a DC/DC impedance source converter (DC/DC ZSC).

A qZSI can be modelled by a detailed or switched dynamic model (SDM), which includes the modelling of all switches and their firing pulses. However, this model is not recommended for steady-state stability studies, long-term simulations, or large electric power systems because of its large computational requirements. Therefore, a simplified model that can accurately represent the system response while significantly reducing the computational time is an interesting option for such studies. To the best of our knowledge, only the small-signal model described in [29] has been presented as an alternative to the SDM of the qZSI with lower computational efforts. However, it is based on the circuit analysis of the qZSI, rather than on the use of averaged voltage and current sources that can be easily implemented in an electric circuit representation of the qZSI. Thus, averaged dynamic models of the qZSI were developed in this study.

These models are implemented using controlled voltage and current sources, reproducing a response similar to the SDM.

After determining the proper configuration for the hybrid power plant, special attention should be given to the control and operation of these systems, Active and reactive power flows must be ensured, as well as appropriate voltage levels for their correct functioning. Different energy management and control strategies are used in these hybrid power plants. In general, the control strategies coincide in prioritizing the use of the most appropriate generation, based on weather conditions, generation availability and available storage resources, while trying to guarantee the electricity supply to the load or the grid. In [30], the battery-based storage system included in the hybrid system was used to smooth fluctuations in the generation. The control strategy regulated the power levels and the state of charge (SOC) of the battery, employing a new control strategy based on the battery SOC. A strategy control can prioritize the use of the renewable energy system to satisfy the load demand taking into account the climatic conditions, and efficiently managing the system energy by using batteries as support [9]. On other hand, a supervisory system based on fuzzy logic can be implemented to manage the operation of each of the components of the hybrid system [31].

In conclusion, the topic investigated in this thesis is current, of interest and requires more research, as has been demonstrated in this section. In particular, the existence of few published works that address the study of large hybrid power plants combining wind energy, PV and energy storage with ZSCs has been detected. Topics such as the possible topologies for the internal connection of energy sources within the hybrid plant, the efficient management and the integration of these plants in aspects of the electrical grid are discussed in this thesis. The results obtained from the simulations are also analysed and these outcomes provided crucial information on the performance and adequacy of the configuration of the hybrid system under study. The energy management systems proposed are suited to manage power flows between the various components of the hybrid system, including the storage system. The control strategy is demonstrated to be adequate, for the operational conditions considered in the simulations.

1.1 CONTEXT

Due to the increase in world energy demand, the concern with the preservation of the environment and the modernization of energy systems, new solutions are needed for the electrical system. Therefore, the migration from the current model to a more efficient, safe, reliable, with higher quality and adapted to distributed renewable generation technologies is inevitable.

In this context, research on energy sources that benefit the environment is particularly relevant, highlighting research focused on the use of renewable resources, in different configurations of distributed and smart grid technologies. In addition, the great interest in research on renewable hybrid systems is known, fundamentally applied to the optimization of the configuration of the hybrid system, the design of the converters, their controllers and the supervisory system, and the improvement of the efficiency of each of the elements involved in the system.

Wind and solar generation are clean and renewable energy sources (RES), which have an inexhaustible primary source, wind and sun, respectively. In this context, the research of this thesis focuses on hybrid power plants, combining wind energy, PV and energy storage systems, to provide new knowledge and solutions to improve the efficiency of these systems and their integration into the electricity grid. In addition, special attention is given to converters that use a single-stage voltage buck-boost with a high DC-voltage gain, based on ZSCs, being an efficient converter for connection between source and load.

It is also worth mentioning that until the present date, most of the hybrid power plants are small-scale, or isolated plants that present a nominal power of the order of tens of kW [32]. Typically, small power systems have a nominal power of less than 5 kW, and medium power systems are those with power between 5kW and 100kW, in both cases in isolated or grid-connected applications. Higher power systems have a power greater than 100kW and are generally connected to the grid. This thesis proposes the study of new topology of hybrid power plants connected to the grid with a rated power in the range of MW, combining qZSI and BES to provide enhanced solutions. In addition, active and reactive power are controlled based on the Space Vector Modulation technique adapted for ZSC and an energy management system (EMS) is proposed to test the correct performance of the control implemented. The thesis presents a complete control of the DC and AC side using a new configuration

based on qZSI integrating a BES (qZSI-BES) and evaluates the performance of a qZSI in a large-scale grid-connected renewable energy system. Moreover, averaged dynamic models of the qZSI are developed. These models are implemented using controlled voltage and current sources. The derivation of these models and their control strategies is presented in this thesis. The proposed models can replace the switched dynamic model of the qZSI in several scenarios to reduce the simulation time and computational efforts, such as long-term simulations, or large, complex systems with many power sources and/or conversion devices, such as the case of this thesis, reproducing a response similar to the SDM.

This thesis is part of the research project "Research Challenges 2018" from the Spanish Ministry of Science, Innovation and Universities, entitled "MVDC grids integrating renewable energy technologies, energy storage systems and DC/AC impedance-source converters" (Ref. RTI2018-095720-B-C32), whose objective is to study the DC/AC ZSC and their applications in medium voltage DC grids with renewable energy technologies and ESS.

1.2 HYPOTHESES OF THE THESIS

The participation of renewable generation sources in the electrical energy mix is increasing, and studies regards to the configuration, control and management of these systems, needs to be further performed. In this sense, this thesis addresses the following hypotheses:

- The use of hybrid power plants combining wind, PV and energy storage based on single-stage converters, such as a qZSI, will contribute to achieving more efficient, reliable and viable power plants from a technical and economical point of view, favouring its development and implementation.

Although hybrid systems need constant research to be developed, the configurations evaluated in this work based on single-stage converters, such as qZSI and with DC/DC ZSC are efficient, reliable and viable from a point of view technical, showing satisfactory operating results.

- Choosing the most suitable configuration for a hybrid power plant, the appropriate control and operation of the energy sources integrated into the hybrid plant and its energy converters, will contribute to improving the grid

integration and obtaining more reliability from a technical point of view, favoring their development and implementation.

The hypothesis described above are evidenced with the thesis, as the proper configuration of the hybrid power plant and the control systems implemented have contributed to improving the integration of the hybrid plant with the electric power system.

- It is possible to implement hybrid systems based on qZSI, which is able to achieve medium-voltage DC voltage combined with a storage system, without the need for an additional converter, according to the characteristics of devices commercially available nowadays.

In the configurations evaluated in this thesis, a hybrid system based on qZSI and integrating a BES was implemented from the devices commercially available nowadays, which was able to achieve medium-voltage DC voltage and a right performance under different operating conditions.

- The incorporation of an ESS in the hybrid plant will improve the plant response to variations in weather conditions (wind and solar radiation), reducing its intermittency.

The incorporation of the BES integrated into the qZSI provided an improvement in the efficiency of the system, being less sensitive to climatic variations. Due to the incorporation of the BES, the plant is more predictable from an energy dispatch point of view, as it is capable of managing the energy stored in the BES, reducing the intermittency from these generation sources.

- The hybrid system can withstand disturbances in the electrical grid without disconnecting the plant.

As required by grid codes in many countries, hybrid systems integrating BES have to remain connected during disturbances in the electrical grid, such as voltage sags at the point of common coupling (PCC). Hence, the fault-ride-through (FRT) capability of some of the configurations proposed has been evaluated in this work.

- The control of the converters together with the EMS considered, will allow managing the exchange of active and reactive power with the grid and coordinate the performance of all energy sources (WT, PV and BES) allowing a reliable and controlled system.

The control and EMS of the system implemented in this thesis allowed a satisfactory operation at the AC and DC sides. Several operating conditions were considered, such as above and below rated wind speeds, with and without disturbances on the grid, to verify the control and the EMS strategy. Furthermore, it was possible to ensure the management of the system through the EMS.

1.3 OBJECTIVES OF THE THESIS

Given the importance of ESS in the field of renewable energies, it is necessary to deeply understand how these hybrid systems work. Dynamic modelling and simulation are important tools in this context, as they can bring relevant knowledge about the operation, control and design. Thus, the main objective of this thesis is to study the design, control, operation and integration of hybrid plants based on renewable energies (wind and PV energy) and ESSs, generating new knowledge on the topic, and proposing innovative solutions that favour its viability and contribute to its development. Taking this into account, the specific objectives of this thesis are:

- Determination of the hybrid power plant under study, including the selection and sizing of the WT, PV system and energy storage devices applicable to the hybrid configurations proposed.

There are several possibilities for the configuration of hybrid power plants based on these three elements. Therefore, a necessary first stage is to select the appropriate WT, PV panel and BES to be used in each hybrid configuration. Additionally, BESs have various operating principles and characteristics, depending on their model, so careful choice of the BES is necessary.

- Modelling of each of the elements of the hybrid plant, and evaluation of its operation.

Due to the complexity of the different devices and components of the hybrid power plant, it is interesting to model each of its elements separately and evaluate their functioning through the implementation of models supported by simulation software.

- Developing and analyzing several hybrid configurations, regarding the placement and interconnection of the PV system and BES which was integrated into the converter.

The connection point of the PV system and BES can significantly interfere with the performance of the hybrid system. The internal topology of the qZSI converter

offers the possibility to connect the BES to capacitor C_1 or C_2 of its impedance network. In the same sense, PV can be coupled to both capacitors. However, an additional DC/DC converter should be considered for the control of the PV system. These topologies can be modelled and their responses analysed to assess the benefits and drawbacks of each of these configurations.

- Design of the control systems for the energy sources and associated power converters, and evaluation of their correct operation.

Parameters such as active and reactive power, as well as voltage at the DC link and the grid are of particular interest. These variables determine how the hybrid system interacts with the power system where it is connected. To achieve a satisfactory integration of these hybrid arrangements in larger networks, it is crucial to develop adequate control strategies for the previously stated magnitudes.

- Design of the supervisory control system of the hybrid plant, in charge of achieving adequate management of the energy, of the internal electrical variables of the hybrid plant and at the point of connection to the grid. Evaluation of the operation of the plant under real operating conditions (change in wind conditions or solar radiation, in the electricity grid generation set point, etc.).

Besides a stable and controlled operation of each element individually, all components of the hybrid systems have to work coordinated to comply with global commands, such as fulfilling the active and reactive power grid demand or monitoring the SOC of the BES when required. This task is performed by the EMS, which is responsible for setting the references for the individual controllers. To prove the success of the EMS, the system was exposed to several operating conditions.

- Evaluation and comparative analysis of the different solutions proposed to establish the conclusions of the thesis.

After the modelling and simulation stages, it is essential to undertake a thorough and critical observation of the results obtained. A correct interpretation allows concluding the strengths and weaknesses of the newly implemented hybrid system topology, controls and EMS. The study of the responses of the system connected to the power grid, under different simulation conditions, allows for a better understanding of hybrid systems with storage systems.

1.4 METHODOLOGY

To evaluate these hypotheses and reach the objectives of this thesis, the research methodology followed during this thesis consists of the logic steps presented in this section. Initially, a complete bibliographical review on the subject was carried out, where onshore and offshore hybrid systems based on PV, wind and storage energy were reviewed. For this task, a large investigation was carried out to identify the configurations of these hybrid systems, the main energy storage devices used and the types of converters typically applied to the generation and transmission systems of these hybrid configurations, the control methods and resource management. An article based on this review was published.

In this task, several topologies of hybrid power plants were also analysed, to define the internal configuration of the studied plant, evaluating the best connection point for the ESS and PV system. At this stage, it was decided to work with ZSCs and the feasibility of connecting an ESS and a PV plant in parallel to the capacitors of the qZSI converter was analysed. Nevertheless, for the connection of the PV power plant to one of these capacitors, the requirement of a DC/DC ZSC to control the power flow coming from the panels was verified. The internal configuration, aspects such as voltage levels, control and operation strategies in this study phase were considered.

Then, it was crucial to define the power of all the hybrid plant components and carefully choose their main elements, including the WT, the PV panels and the ESS. A three-bladed horizontal axis WT with a PMSG was used, which allows operation at variable speed, and active regulation of the blade angles. The model of this WT consists of four large blocks: WT, power train, electric generator and control systems. The PV panels were chosen with technical and economic criteria from real manufactured models and a lithium-ion battery was considered as ESS.

To contrast the above hypotheses, and achieve the defined objectives, the dynamic models that define the behaviour of the main components of hybrid systems were modelled in Simulink/MATLAB. The latest versions of Simulink/MATLAB incorporate detailed models of WTs, PV and batteries, which are used to implement more complex models that make up hybrid systems as a whole. The WT model was designed according to physical models sufficiently validated in the technical literature specialized. Models accepted and validated in the literature for the BES were implemented. Whenever possible, the design and dimensioning processes used the

technical characteristics provided by the manufacturers of devices and components available on the market.

Regarding the design of control strategies for the power converters, simulations and experimental tests were performed for their validation under different operating conditions and changes in the references for the control variables. The designs were implemented, assessed and validated by simulations. The application of this detailed methodology allowed the simulation of the complex hybrid plant developed in the Simulink software. The results obtained with the different control systems implemented were compared to observe the improvements achieved.

Subsequently, the study and design of supervisory control systems were carried out. The objective was to carry out a coordinated operation of the generation, BES and grid systems, improving the generation capacity and energy management of the hybrid plant. Within the control strategy, variables such as the active power of the PV and WT, the reactive power exchanged with the grid, the internal voltage of the plant or the electrical grid, the power of BES or its SOC were taken into account. The control strategy implemented in the controllers and the EMS coordinates the exchange of active and/or reactive power with the grid, the energy stored in BES or its SOC, among others. To evaluate the control, simulations and experimental tests were carried out under different operating conditions of the hybrid plant, and the results obtained were analysed to choose the best control, management and operation in the hybrid plant.

Finally, the developed models were simulated in different operational situations, using Simulink-MATLAB simulation software. The simulations supported the expected results. The results obtained from the simulations completed have been discussed in the corresponding sections. The analysis of the results obtained over different simulations allowed us to clarify the main differences between the different cases studied, thus being able to highlight the most favourable aspects of each alternative simulated.

1.5   THESIS OUTLINE

The rest of this document is organised as follows. After this introduction, the context, objectives, hypotheses, and methodology of the thesis are presented. In Chapter 2, a thorough review of the backgrounds is carried out. The configurations under study are described in Chapter 3. The control systems are detailed in Chapter 4.

Chapter 5 describes the energy management systems. The simulation results are shown and discussed in Chapter 6. Finally, Chapter 7 presents the main conclusions of the thesis, its main contributions and proposes future research works.

Chapter 2: Literature Review

Energy sources based on fossil fuels have been replaced gradually by alternative energy sources. Among the several clean energy sources, wind energy and PV stands out due to the abundance of wind and sun availability. Therefore, the number of large-scale wind and PV power plants has grown significantly. At the last COP 26 meeting, climate targets were set to encourage renewable energy to reach new levels [33]. In this chapter, a review focusing on large-scale renewable energies is provided. Concerning wind energy, an extensive analysis of offshore wind energy was included, due to the fact of the exponential increase in installed capacity of these plants.

2.1   RENEWABLE ENERGY IN THE WORLD

The energy sources used in the world is constantly changing, as can be seen in Figure 2.1. These changes are based on climate and energy crises and are supported by international agreements, seeking to promote greater energy efficiency. The world's first energy transition occurred around 1910, from the massive use of coal, due to the first industrial revolution, passing to oil. In a second phase, although there was an increase in the use of oil between the 1960s and the present, natural gas became relevant from the 1970s onwards, and in the same period, there was an increase in energies based on nuclear and water sources. The current scenario is pronounced by the energy transition to renewable energies, as can be seen in Figure 2.1 [34].

Among the advantages of using renewable energy is possible to highlight that they are nondepletable, ubiquitous (found everywhere across the world, in contrast to fossil fuels and minerals), and essentially non-polluting. On other hand, the drawbacks are higher initial cost, intermittence and low density. Other perceived problems are visual pollution, odour from biomass, avian and bat mortality with WTs, and brine from geothermal energy [35].

Therefore, it is important to understand the current status of renewable energies and which sources are part of this segment. RES are considered, derived from theoretically inexhaustible resources or that are naturally replenished. It can be cited as an example the biomass, ethanol, wood and wood waste, landfill gas and biogas, hydropower, biodiesel, geothermal, wind and solar [35].
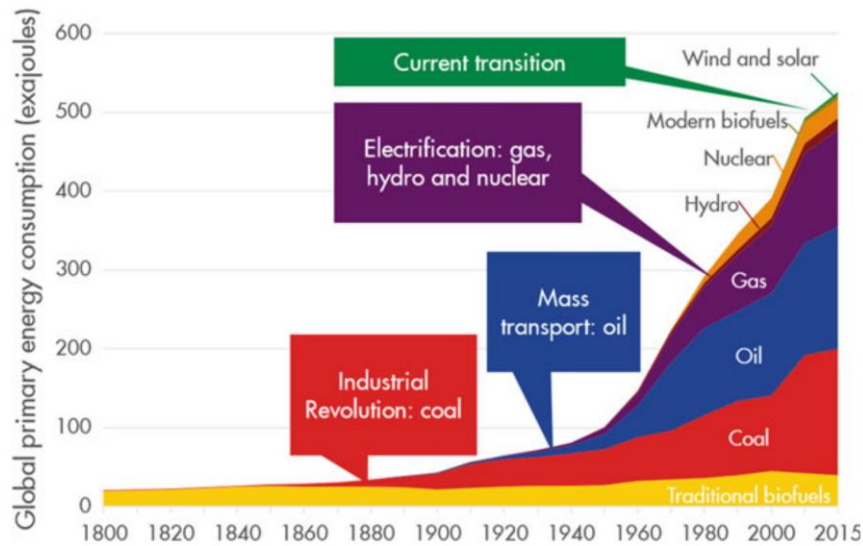
Figure 2.1. World energy transition.

Therefore, it is important to understand the current status of renewable energies and which sources are part of this segment. RES are considered, derived from theoretically inexhaustible resources or that are naturally replenished. It can be cited as an example the biomass, ethanol, wood and wood waste, landfill gas and biogas, hydropower, biodiesel, geothermal, wind and solar [35].

An overview of main RES can be seen in Figure 2.2a, whereas that Figure 2.2b shows the increase of the main RES, separated by technology, between 1990 and 2020, including a forecast for the year 2026. These predictions are based on [33], an important report from International Energy Agency's (IEA's), which provides information about current policies and market developments. Between 1990 and 2002, renewable energy came mainly from hydropower, however, this scenario transformed from 2008 onwards, providing opportunities for greater diversification of the renewable electricity generation matrix. It is possible to notice an even greater diversification planned for the 2026 scenario and among the highlights in terms of growth are wind and solar energy, as can be seen in Figure 2.2c.
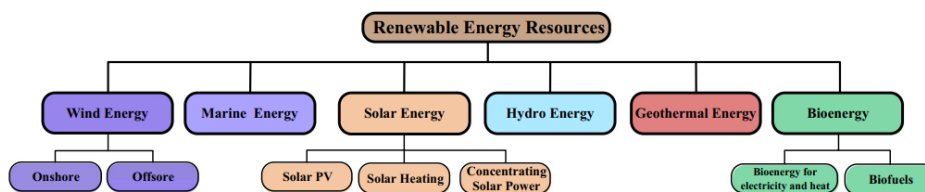
(a)
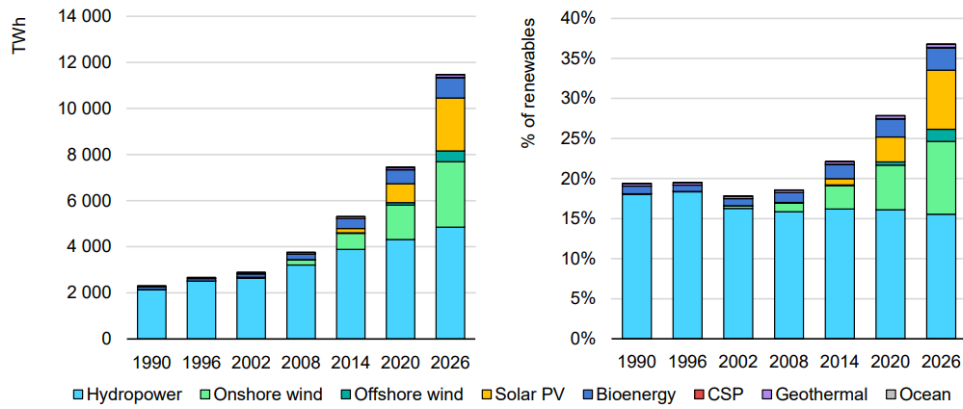
(b)
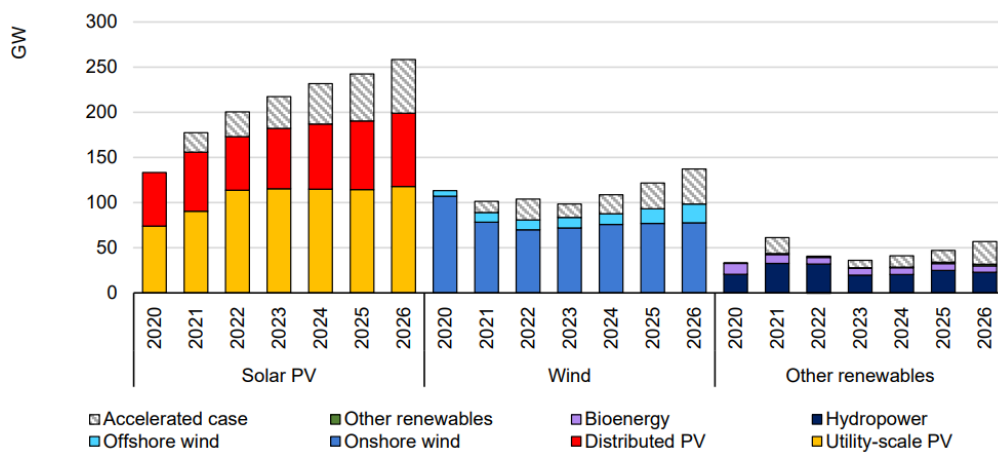
(c)

Figure 2.2. (a) Overview of main renewable energy [36], (b) current status and forecast renewable energy capacity worldwide [33], (c) trends additions wind and solar energy [33]

According to [37], to achieve the zero CO_2 scenarios until 2050, the world must accelerate the pace in meeting the targets established concerning renewable energy, because, although growing, it is significantly below ideal levels for the "Net Zero Scenario" target to be achieved. The report [33] predicts that to reach this target the average addition of wind and solar will have to more than double in the next five years. Among the problems highlighted in the report regards to solar energy, it should have more political and regulatory support to be further increased, while wind faces problems of environmental permits and social acceptance. Hydropower plants are sources that, due to their characteristics, integrate properly with solar and wind, nevertheless, also face challenges concerning environmental permissions and social

acceptance. The great problem of renewable energies, such as geothermal, CSP (concentrating solar power) and bioenergy, is from an economic point of view, as they still do not have the necessary economic cost to grow exponentially.

Figure 2.3 presents a summary of the current status of renewable energy in China, including the generation technology. The evolution of renewable energy installed capacity yearly (from 2011 to 2020) in China is also illustrated. On the left side of Figure 2.3b, it can be observed the China renewable capacity additions between 2009-2026, including a historical, main case and accelerated case (Acc. case), being the last two, projections.

China has added approximately 500 GW of the capacity renewable energy installed in the last five years, with its main renewable sources being led by wind power followed by PV-utility, PV-commercial, PV-residential, hydropower and bioenergy, respectively. In the main case, China has expected to increase 800 GW, and in an optimistic scenario can reach 900 GW. Figure 2.3b (right) shows an ambitious growth of the non-hydro renewable for 2026, almost 15% concerning 2020. Wind and solar can reach 1.2 TW until 2030.

Analyzing Figure 2.3a along with Figure 2.3b, the plans for expansion of renewable energy in China become even more evident, considering that currently has an installed capacity of 900 GW and could double this capacity until 2026. This event has occurred before since in 2015, China had just over 450 GW of installed potential and in just five years, it practically doubled its capacity, reaching 900 GW in 2020.
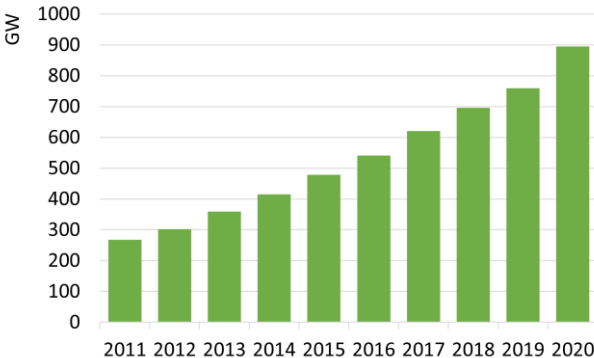
(a)
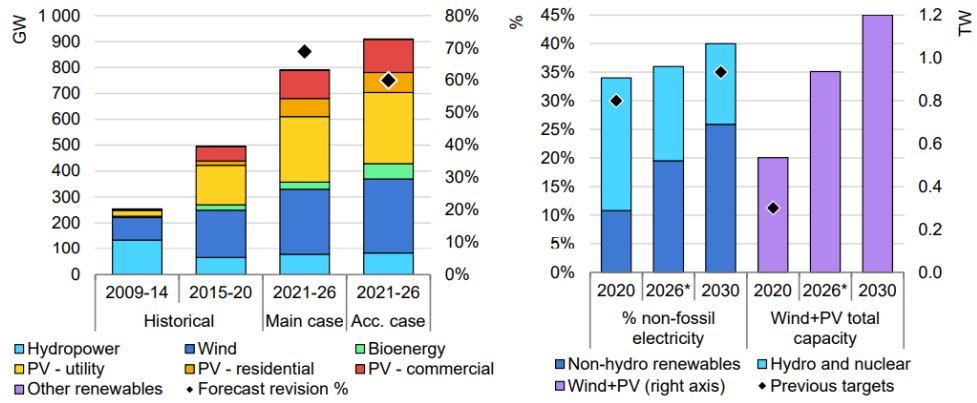
(b)

Figure 2.3. China (a) Current status renewable energy, (b) renewable capacity additions between 2009-2026 [33].

Figure 2.4a depicts the evolution of renewable energy capacity installed by years in the United States of America (USA), which also has audacious targets for renewables. The USA has been increasing its renewable targets over the years. The capacity of renewable practically doubled in the last decade, in 2011 it had an installed capacity of almost 150 GW, while in 2020 its installed capacity is close to 300 GW.

Figure 2.4b illustrates that the USA added nearly 140 GW of the capacity in the last five years, with the focus on wind and PV-utility. However, the USA plans to increase in a normal scenario almost 210 GW between 2021 and 2026, while for an optimistic scenario almost 275 GW could be reached. As can be seen, the average price decrease significantly for solar, justifying the increase of solar energy in the last years, while the average price remains stable for wind power, with a slight decrease compared to 2014.
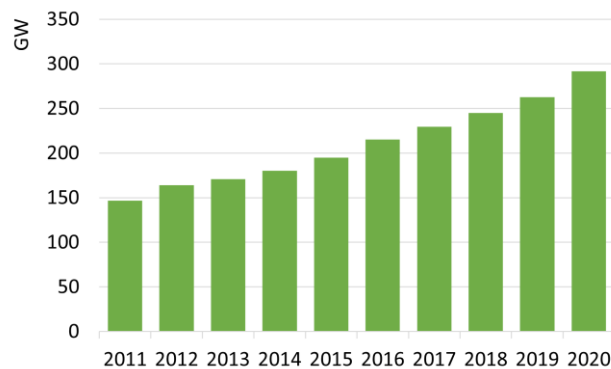
(a)
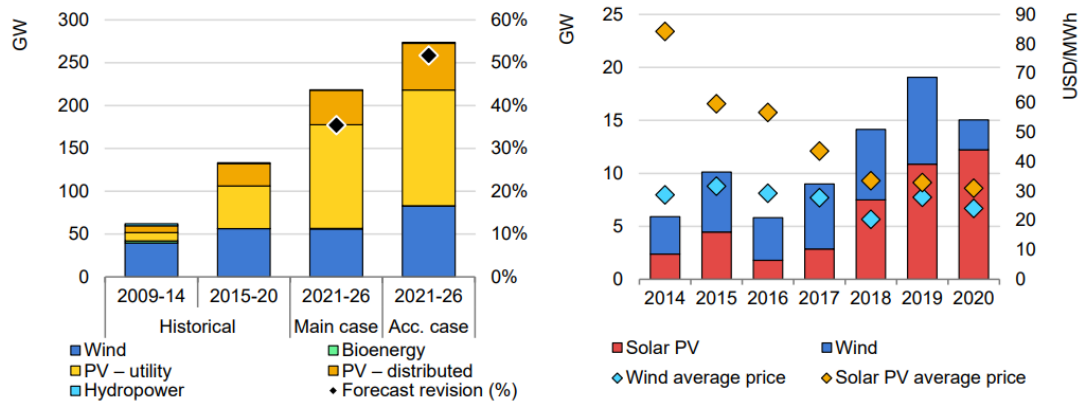
(b)

Figure 2.4. USA (a) Current status renewable energy, (b) renewable capacity additions between 2009-2026 [33].

Figure 2.5 shows the additional trends for renewable energy in the Asia Pacific. Concerning countries in this region, the growth of renewable energy in India can be seen in Figure 2.6. Although the growth in this region is lower when compared to the USA and China, it is noteworthy that in an optimistic scenario these countries together can reach an increase of about 100 GW of installed capacity only 2026, being predominantly distributed in solar.
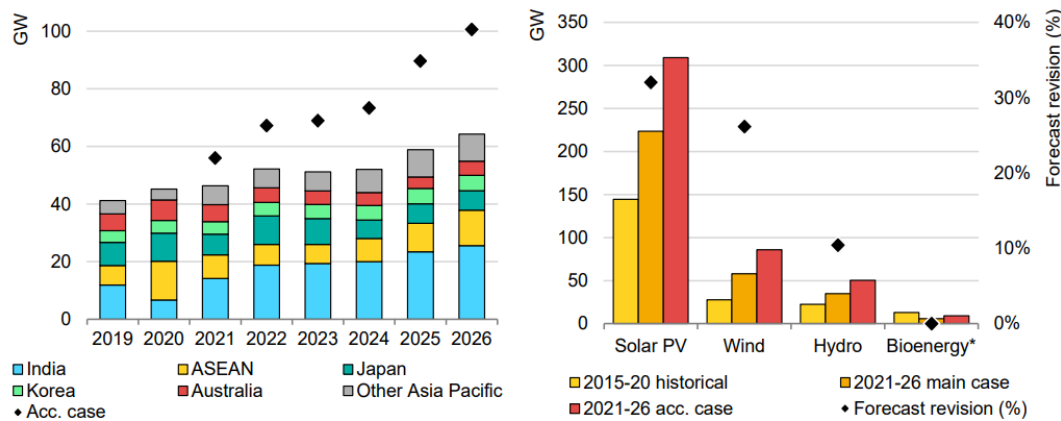
Figure 2.5. The Asia Pacific, Renewable capacity additions between 2009-2026 [33].

India intends to invest in the main case scenario for an increase of 120 GW and can reach 180 GW in the case of the optimistic scenario (Figure 2.6b), totalizing 500 GW until 2030 (Figure 2.6a). The main focus of investment is in PV-utility followed the PV-distributed and wind. Unlike China, which is going to reduce investments in

hydropower between 2009 and 2026, India intends to subtly enhance this type of generation.
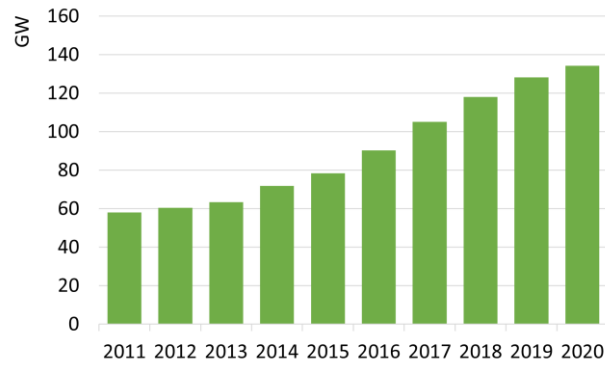
(a)
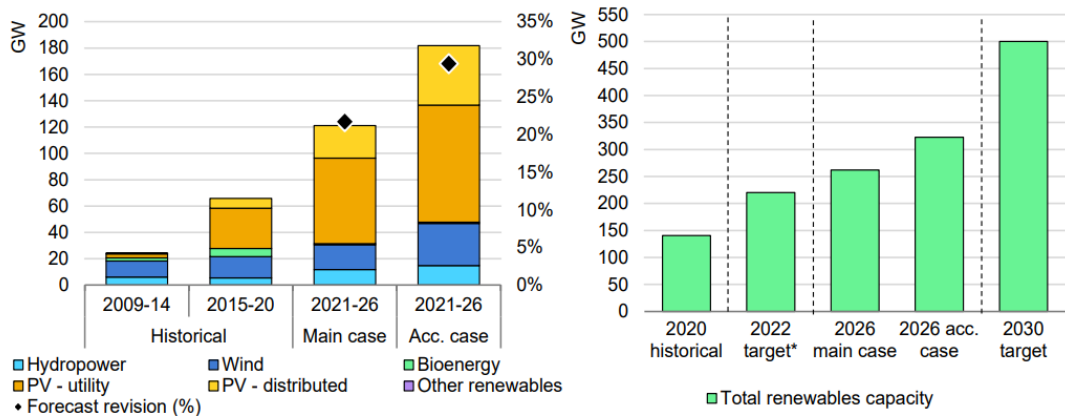
(b)

Figure 2.6. India (a) Current status renewable energy, (b) Renewable capacity additions between 2009-2026 [33].

In the case of Europe, investment targets remained at high levels in the last 10 years, where almost 400 GW of renewable energy were added in Europe, as can be seen in Figure 2.7b, which shows renewable capacity additions between 2009-2026. Over the next five years, the main installed energy source will be solar energy, followed by onshore and offshore wind energy (Figure 2.7b). Currently, Europe has more than 600 GW of renewable installed and comes from a growth trend since 2011.

Moreover, The European Commission is committed to reducing emissions by 55% by 2030, compared to 1990 [38]. Although under discussion, a positive revision of the renewable energy targets under the Renewable Energy Directive (REDII) is foreseen through a policy package called Fit-for-55. The package aims to encourage the use of renewable energy in buildings, industries, heating, and cooling.

Regarding trends, Germany leads the additional installations planned for the next five years, followed by Spain and France. Figure 2.7b shows in detail the growth trends in Europe, in a normal scenario the addition of 300 GW is expected and almost 400 GW in an accelerated scenario.

(a)

(b)
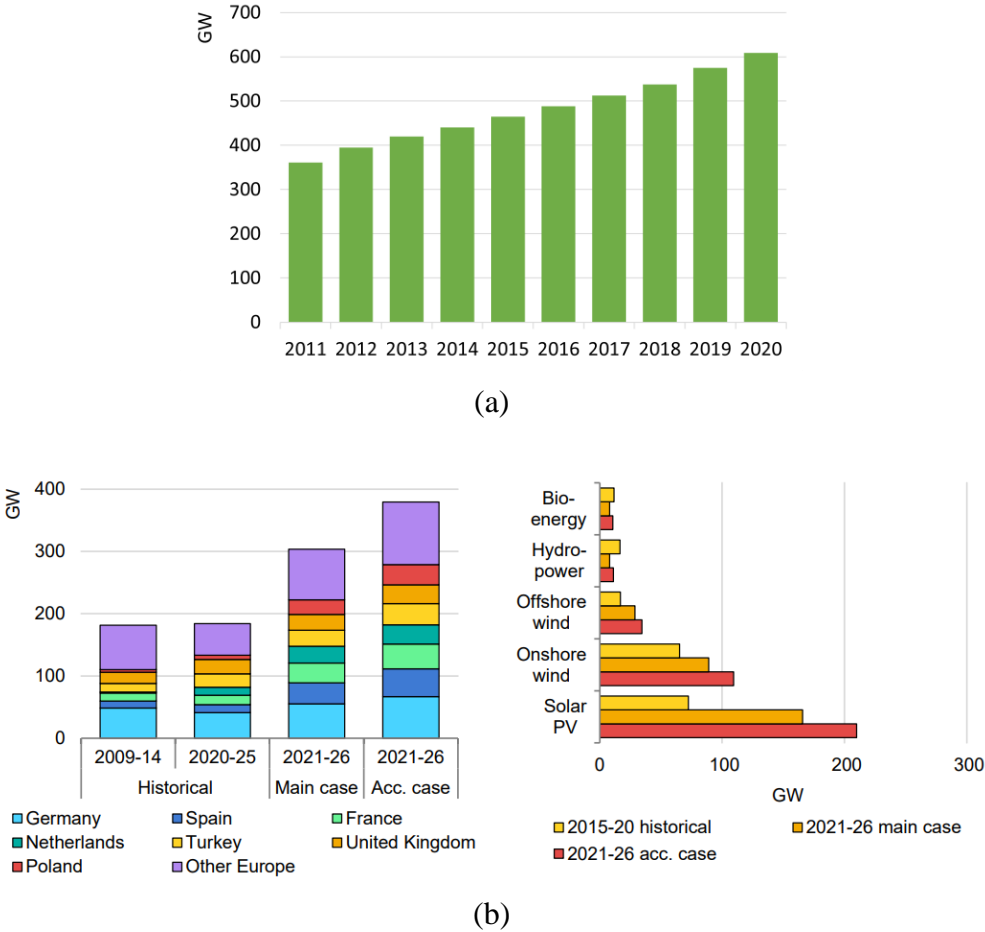
Figure 2.7. Europe, (a) Current status renewable energy, (b) Renewable capacity additions between 2009-2026 [33].

Figure 2.8b shows the growth trends in Germany. It is possible to observe an increment of almost 55 GW in renewable energy for the years between 2021 and 2026. If the optimistic scenario occurs, almost 70 GW of installed capacity could be reached. Germany has supported policies to meet long-term climate goals, in addition to a new regulation, namely the new Renewable Energy Sources Act (EEG 2021), that aims to facilitate onshore wind energy. This act encourages self-consumption, since removing a surcharge that was previously charged in the case of self-consumed electricity, this

removal is valid for systems between 10 and 30 kW. The current situation is shown in Figure 2.8a where a great increase over the years can be observed.

(a)

(b)
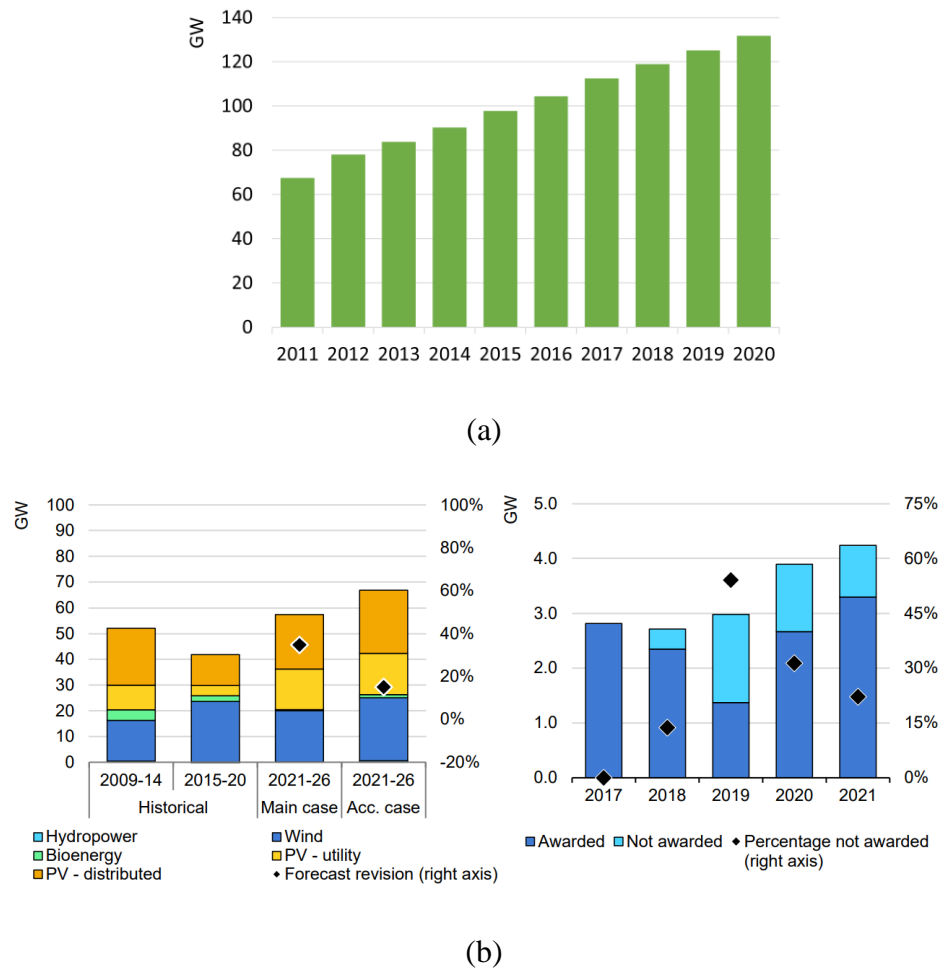
Figure 2.8. Germany, (a) Current status renewable energy, (b) Renewable capacity additions between 2009-2026 [33].

Latin America can increase its matrix by almost 100 GW between 2021 and 2026. Brazil leads the additional installations planned for five years, followed by Chile. These countries together could contribute more than 10 GW in 2022 alone. Brazil currently has approximately 150 GW of installed renewable capacity (Figure 2.9b). The potential is divided into 60% of hydropower, 8.5% in wind, 8.2% in biomass, 3.1% PV [39]. Currently, a significant portion of this capacity, mainly from solar and wind, is being acquired through the deregulated market through PPAs. In addition, a considerable increase in residential installations through PV-distributed is observed. Only in the last five years, there was an increase of almost 5 GW. In a normal scenario, renewable capacity additions between 2009-2026 in Brazil could reach close

to 40 GW, however, in an accelerated scenario, this value can reach 50 GW (Figure 2.9c). Unlike reported in the USA, prices for renewables (wind and solar) in 2021 were slightly increased when compared to 2018.

(a)

(b)

(c)

Figure 2.9. Latin America, (a) renewable capacity additions between 2009-2026 in Latin America [33] (b) Current status renewable energy in South America and Brazil and (c) renewable capacity additions between 2009-2026 in Brazil [33].

With regards to Sub-Saharan Africa and the Middle East and North Africa (MENA), the analysis was divided into Figure 2.10a and Figure 2.10b, respectively. In the case of Sub-Saharan Africa, a significant difference in the analysis concerning all the previous ones is a relevant increase of its renewable matrix based on hydropower between the years 2015 and 2021. For the following years, this segment surpasses the others, being foreseen 14 GW of hydropower compared to 13 GW of solar, as can be seen in Figure 2.10a.

Figure 2.10b illustrates the case of MENA. In a normal scenario, investments in renewable energy for the next five years will be almost double when compared to the last 5 years. The growth expectation between 2021 and 2026 is expected close to 30 GW, being the United Arab Emirates (UAE) the leader. Opposed to Sub-Saharan Africa, the focus of investments is on PV-utility and CSP. If an optimistic scenario occurs this target of 30 GW could increase to 60 GW.

(a)

(b)
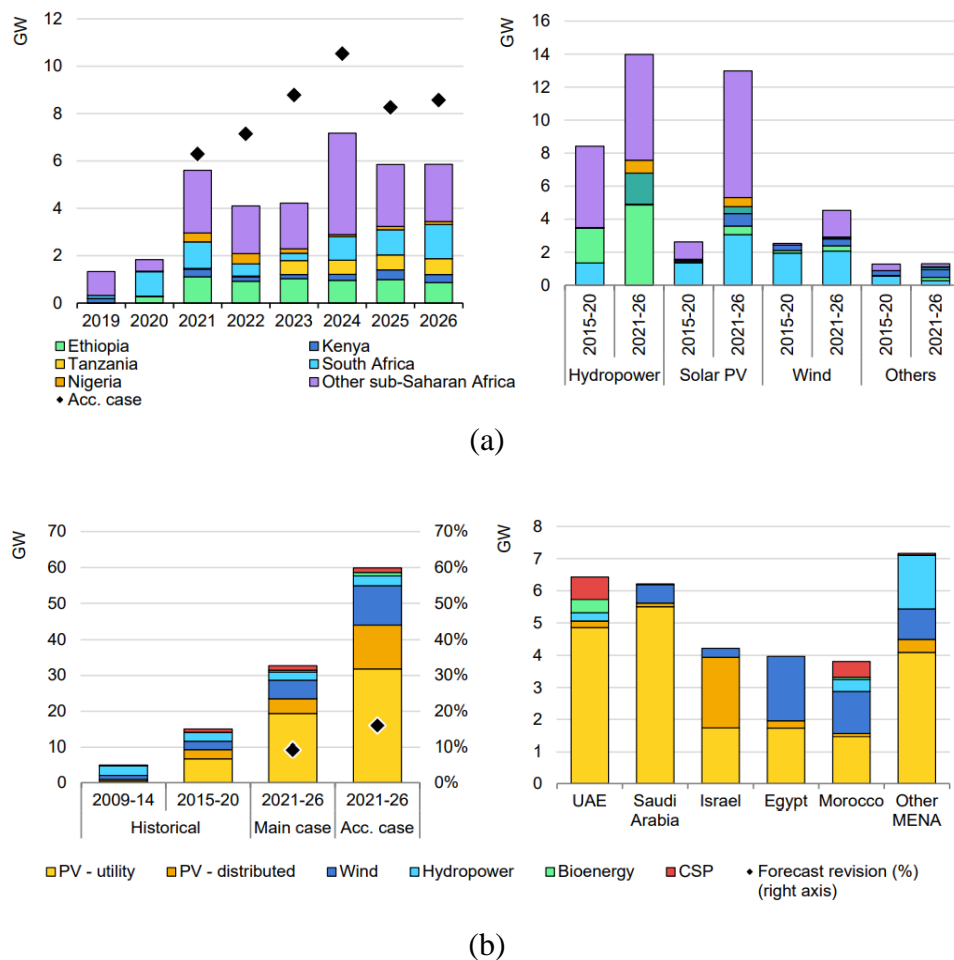
Figure 2.10. Africa and the Middle East, (a) Sub-Saharan Africa, (b) the Middle East and North Africa [33].

In summary, the growth of renewable energy is evident and proven. However, several challenges will have to be solved for this energy transition to renewable sources to occur. Many of these challenges were discussed in the aforementioned reports [33,37], which address several issues related to the current energy situation in the world and how to solve these challenges. There is much debate about the importance of governmental policies [40], the actions of the state agencies, and the reduction of prices of renewable energies [41,42]. Another topic addressed is concerning the use of transitional sources such as natural gas to support this new model [43,44], the role of nuclear energy in decarbonisation, to reach Net-zero [45–47] and finally, what are the impacts and availability of some commodities to meet this new model [33].

2.2 LARGE WIND FARMS

This part of the thesis analyses the current status and the trends of large-scale OWFs with an installed capacity above 150 MW in Europe and the world. The review shows the trends on WT size and capacity, turbine model, distance to shore, water depth, investment cost, type of foundation, transmission technology, and voltage array systems among others.

OWFs show favourable indicators in almost every environmental impact index investigated, which is aligned with the search for sustainability in electric power generation [4]. OWFs share all the benefits of onshore power plants and present further advantages. For instance, larger areas are available for bigger plants, greater plants in terms of installed capacity, steadier wind speeds with less turbulence, and lower visual and acoustic impacts [48].

However, these systems also present certain drawbacks, such as limited access to the sea, costly marine foundations, and connection to the grid through marine electric lines. Those disadvantages are attenuated by the possibility to have a higher capacity factor in OWF [48–50]. Moreover, to offset the higher costs associated with OWF, the developers are focusing on increasing the installed capacity [51].

In this sense, an increasing trend towards large-scale based systems has been reported in the literature [49,52], although the fast growth experienced after 2013 was not fully addressed. The perspective and challenges in the development of offshore wind power were highlighted in [49], mainly dealing with the potential interests of this

sector, although the authors did not differentiate by country in their analysis as in [52], where the authors also explored some technical, economic and environmental issues.

The rearrangement in OWF has been significant since 2013 in terms of types and models of turbines, transmission systems, increase of the installed capacity and distance to shore. Rodrigues et al. brought out information of interest related to the topic, although not emphasizing large-scale power plants [53]. The commitment towards the reduction of greenhouse emissions from electricity generation is reinforced by the importance of wind in the energy mix [54]. Some reviews about OWF have been performed separately by the country. For instance, an inquiry into offshore in the United Kingdom (UK) highlighted an increase and accelerated development of offshore wind energy in this country [55], whereas [56] presented an overview of the status and future development in Spain in 2016.

To understand the development of OWF, it is very important to identify the trends that are driving the sector in certain vital aspects. In this topic, the latest information demonstrating the status and trends of existing OWF above 150 MW in Europe is gathered and analyzed. The trends are derived and justified with actual data obtained from official reports and literature, not only based on the impressions of the authors or other experts. The primary aim of this study is to establish the future trends in OWF and demonstrate the wide growth of this technology, especially in large-scale OWF, where the sector is very economically competitive. With this purpose, the most significant characteristics of 57 plants installed in Europe with rated power above 150 MW and fully commissioned until 2019, as well as 11 plants authorized or under construction, are studied in detail, drawing relevant conclusions from the data collected. To date, significant evidences of large-scale OWF in operation were not found in other locations except for China, which is a market in constant development.

2.2.1 Trends Offshore wind farms in Europe

In Europe, OWF will continue to grow and increase their contribution to the energy mix. This trend is favoured by the support that renewable energies receive from regulatory policies, fiscal incentives and public funding, which increases their competitiveness [57].

Eleven European countries contributed to the installed capacity of OWF until 2019, where the UK and Germany stand out with the largest capacity. Offshore

technologies are growing in Europe, as seen in Table 2.1, which shows the evolution of offshore energy over the years, as well as the expected trends for 2025 and 2030. The data presented in Table 2.1 were obtained from [58–67].

Table 2.1. Growth of OWF in Europe over the years.

Years	Current average										Trends	
	2010	2011	2012	2013	2014	2015	2016	2017	2018	2019	2025	2030
Number of OWF	45	53	55	69	74	80	81	92	105	110	139	172
Number of Turbines	1136	1371	1662	2080	2488	3230	3589	4149	4543	5047	11126	16850
Installed Capacity (GW)	2.95	3.81	4.99	6.56	8.05	11.03	12.63	15.78	18.5	22.07	47.4	76
Average Power (MW)	155.3	200	285.6	485	386	337.9	379.5	493	561	621	849	1080

The trends for 2025 and 2030 were estimated from the number and average power of OWF in the period between 2008 and 2019 using linear regression. For these estimations, a neutral scenario was considered, in which the investments on OWF will remain the same when compared to the current scenario. Thus, the number of OWF (N_{WF}) can be deduced from Equation (2.1), whereas the average power of wind farms (A_{PF}) is given by Equation (2.2), obtained from Figure 2.11, where x indicates the year of the projection. These trends are presented in Table 2.1.

$$N_{WF} = 6.73 \cdot x - 13489.13 \tag{2.1}$$

$$A_{PF} = 46.1 \cdot x - 92483.86 \tag{2.2}$$
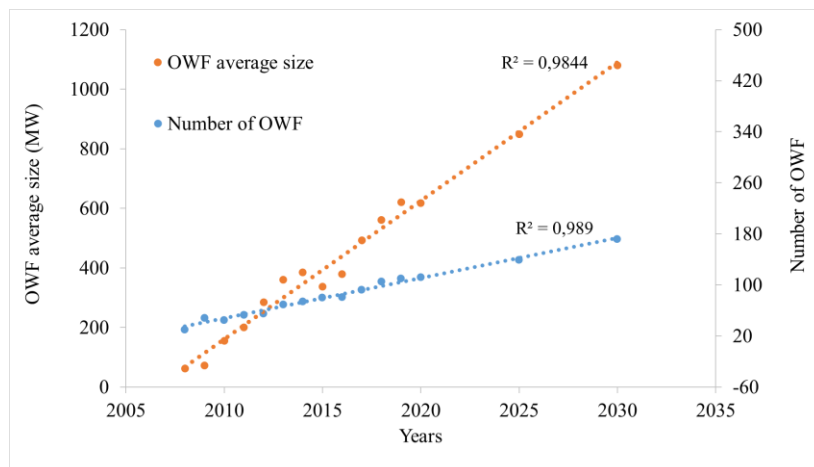
Figure 2.11. Average power and number of OWF in Europe.

The values of 47.4 and 76 GW included in Table 2.1 correspond to a neutral scenario for 2025 and 2030, i.e.: considering the same growth rate as in the previous

years. These values were found through the polynomial regression presented in Equation (2.3), deduced from Figure 2.12.14, where IC indicates the installed capacity. Finally, the number of wind turbines (N_{WT}) was estimated using the polynomial regression in Equation (2.4), obtained from Figure 2.12.14.

$$IC = 140.74 \cdot x^2 - 564911.49 \cdot x + 566878201 \tag{2.3}$$

$$N_{WT} = 24.97 \cdot x^2 - 100092.35 \cdot x + 100321939.49 \tag{2.4}$$
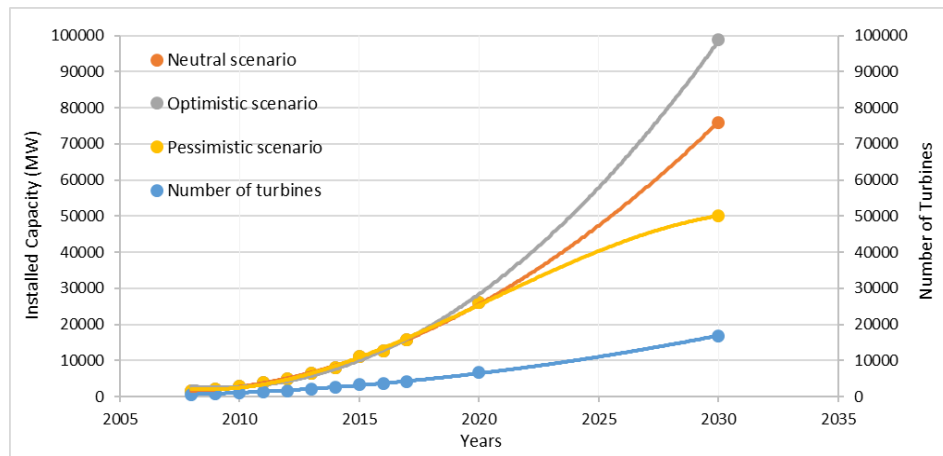
Figure 2.12. Trends in installed capacity and number of offshore wind turbines in Europe.

From Table 2.1, it can be observed that, under the scenarios considered, the generation capacity increases more sharply than the number of generators installed, indicating that the rated power of the WTs installed in OWF shows a tendency to grow.

The results estimated through linear and polynomial regression were close to the values found in [68] and [69], which describe possible scenarios for 2030. In [68] and [69], three scenarios for the installed capacity in 2030 were evaluated. In the first report, a neutral scenario of 66 GW, an optimistic projection with values that reach 98 GW, and a pessimistic projection of 44.6 GW were considered. While the second report indicates a neutral scenario of 70 GW, an optimistic projection of 99 GW, and a pessimistic projection of 49 GW. This trend towards a growing rated power of the WTs in European OWF is also highlighted in [64,65,70].

2.2.2 Europe's large-scale OWF

Until 2019, about 89% of the total installed capacity in European OWF corresponds to plants with rated power above 150 MW. For this reason, this section focuses on large-scale OWF.

The parameters evaluated for large-scale OWF are depicted in Figure 2.13. When applicable, the data is differentiated by the colour, size and line style of the circle to appreciate the variation taking 2013 as a reference, when OWF experienced fast growth in many segments. The same applies to the cluster diagrams in the subsequent sections. Nevertheless, some parameters do not have a red circle in Figure 2.13. This is justified because some of them can be further sub-divided and they are dealt with in the corresponding sub-sections; or simply because they cannot be quantified, as is the case of the array systems. Additionally, the cluster diagrams of some sub-sections also indicate numerically the installed power belonging to the cluster, the percentage of the cluster installed power compared to the total installed power, and the average power of the WTs included in the cluster.
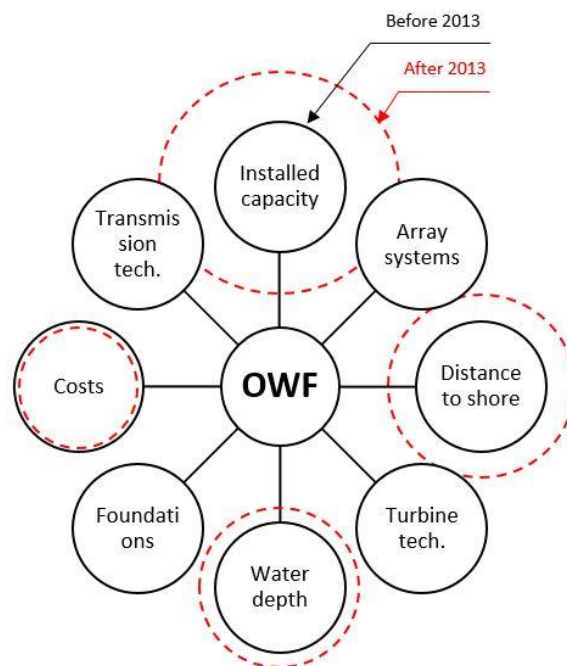
Figure 2.13. Cluster diagram of the main parameters of OWF.

Installed capacity and size

Only in 2019, an increase of nearly 3412 MW new installed capacity was seen, with around 504 new turbines connected in Europe [65]. The trends indicate that these figures will continue to increase in the coming years.

Currently, Europe is the leader in offshore wind power generation and experiences fast growth. The total installed capacity in the years 2008 and 2019 was approximately 1.5 and 22 GW respectively [61,65]. Regarding exclusively plants over 150 MW, they contribute 89% of the total. Figure 2.14 illustrates the increase in the installed capacity of OWF above 150 MW between 2002 and 2019. From 2013 onwards, about 76% of the new plants installed are above 150 MW.

	2002	2003	2009	2010	2011	2012	2013	2014	2015	2016	2017	2018	2019
■ MW Installed	160	165,6	465,7	992,4	293,6	1867,3	1171,9	1029,8	3241,4	1326	3213,7	2246,4	3412,7
■ Accumulated	160	325,6	791,3	1783,7	2077,3	3944,6	5116,5	6146,3	9387,7	10713,7	13927,4	16173,8	19587
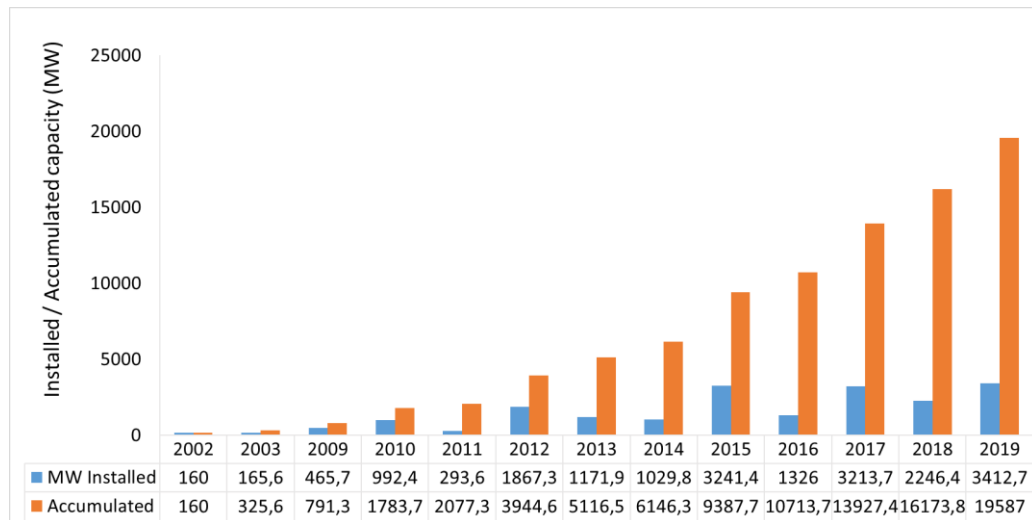
Figure 2.14. Yearly installed and accumulated capacity of large-scale European OWF.

Another aspect worth noting is that about 98% of OWF installed capacity in Europe is concentrated in only five countries. Considering plants above 150 MW, the UK and Germany sum 80% of the installed capacity, and the 20% remaining is divided among Belgium, Denmark and the Netherlands, with 8%, 8% and 4% of the installed capacity respectively.

The UK represents 44% of the offshore WTs installed and in operation, therefore being the country with the largest installed capacity. For more details, a thorough review of the offshore generation in the UK is presented in [55].

Distance to shore and water depth

Most of the area available for OWF is located far from the coast (above 50 km). In this sense, Figure 2.15 summarizes the status of OWF in terms of distance to shore and water depth. The black circles contain the total installed power until 2013, its percentage compared to the total, and the average rated power of the offshore WTs included in each range. The red dashed circles contain the same parameters as the black

circles from 2013 to 2019. For instance, in Figure 2.15 (a), the amount of offshore wind power installed for a distance to the shore below 20 km was 4.28 GW, corresponding to 1.89 GW before 2013, and 2.39 GW after (and including) 2013. Regarding the percentage of the total installed power, these values correspond to 9.65% and 12.22%, before and after 2013 respectively, for a total installed capacity of 19.58 GW. Before 2013, no OWF with a distance to shore above 50 km had been reported, and for this reason, only the red circle is represented.
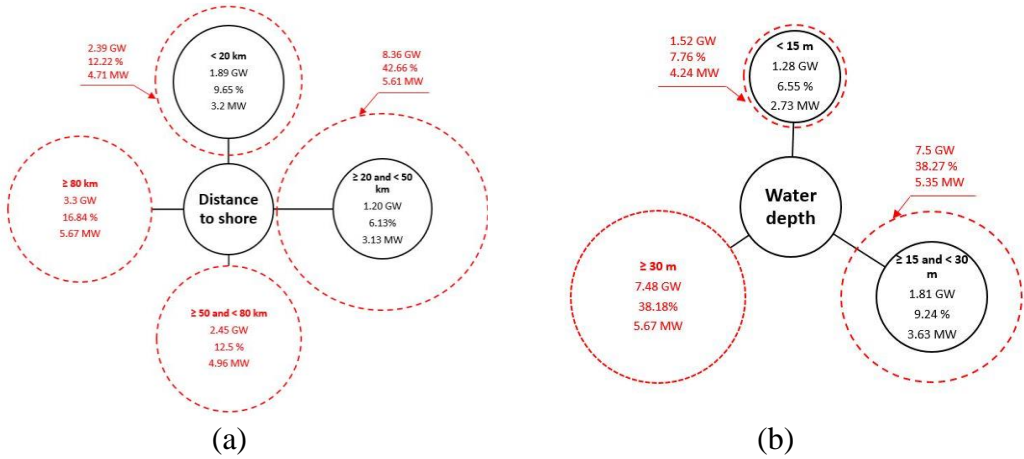
Figure 2.15. (a) Distance to shore cluster diagram; and (b) Water depth cluster diagram.

The distance to the shore is increasing over the years, and consequently, the WTs have to be installed in deeper waters. This trend can be observed in Figure 2.16, which represents in a separate coordinate axis the average depth and distance to shore of OWF from 2008 to 2019. Additionally, the average rated power of the turbines and OWF is indicated by the size of the blue and orange circles, respectively, together with the corresponding numerical values.

Figure 2.16 shows a 193% increase between the deepest and shallowest OWF. Furthermore, the average distance in 2019 is approximately 4.5 times higher than in 2008, and the average power of the WTs is about 3.25 times larger for the same period. The average distance to shore and depth of OWF have increased by 132% and 60% respectively, since 2013. Regarding the deepest offshore wind generator, it is installed at about 56 m, and the furthest is less than 120 km away from the coast.
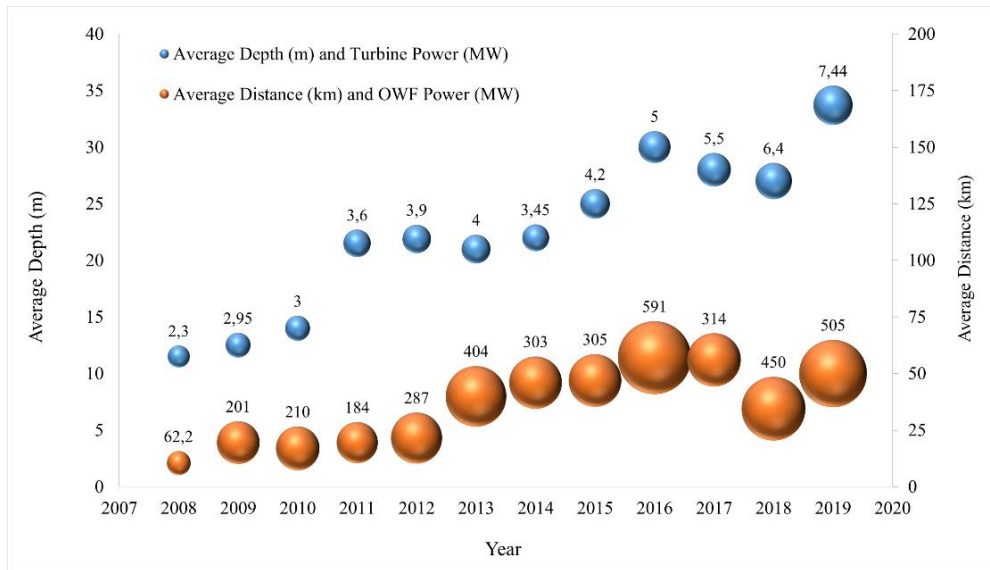
Figure 2.16. Average depth and turbine power (blue) and average distance to shore and OWF power (orange).

Figure 2.17 shows the trends for the distance and depth for the years 2025 and 2030. A polynomial regression shows that the predicted depth for OWF above 150 MW for 2025 and 2030 is 44 and 53 m, respectively. When considering all OWF, these values decrease to 42 and 50 m, respectively. The distance predictions only for OWF above 150 MW are 80 and 100 km for 2025 and 2030, respectively. However, the average values for all the OWF decrease to 70 and 87 km, respectively.
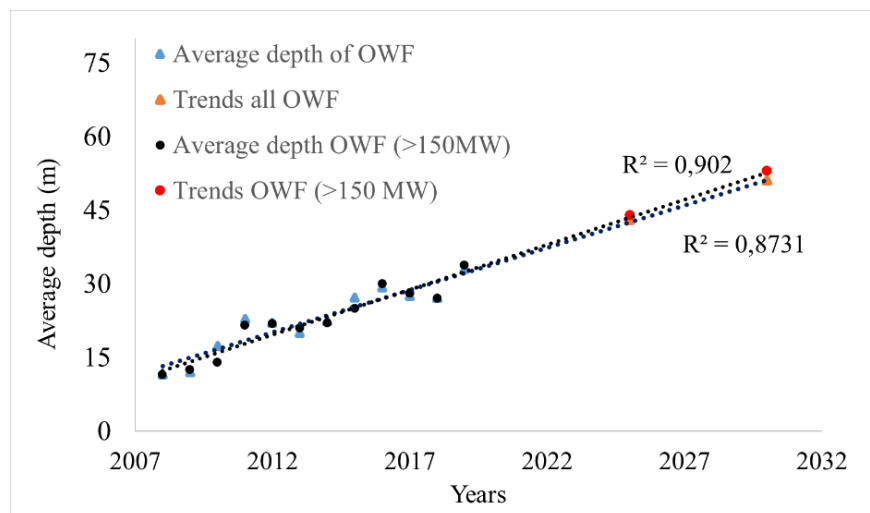
(a)
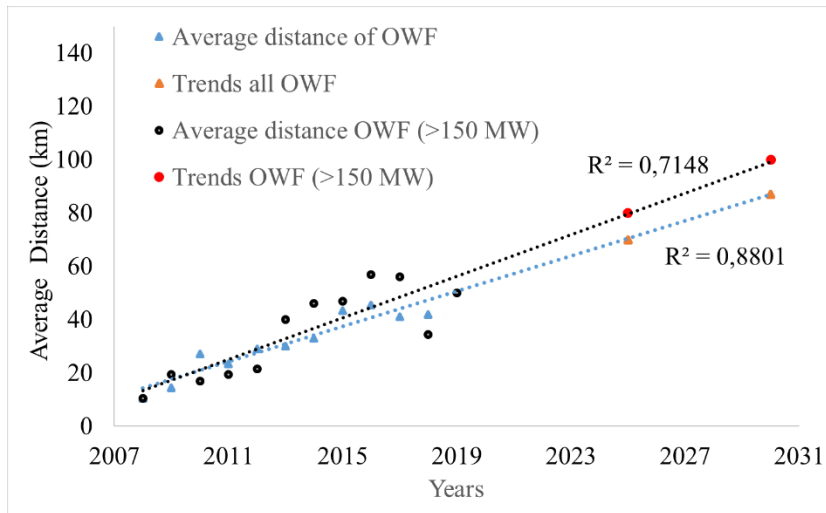
(b)

Figure 2.17. Average trends for: (a) depth; and (b) distance.

Turbine technologies

Regarding WTs, among the different variable-speed technologies available, DFIG and PMSG are usually employed due to their high energy efficiency [16–18,23]. PMSG has several advantages, such as high performance, low maintenance compared to DFIG, and the possibility of direct-drive operation. Detailed information about commercial models of these WTs can be found in [19].

Offshore wind turbines present certain differences compared to onshore WTs. They are designed to withstand severe corrosion and stress conditions. Furthermore, offshore WTs can have larger rotor and blade sizes, as well as more powerful generators. Another important point is that the installation, operation, maintenance and electrical infrastructure costs decrease as the size of the offshore turbine increases. Therefore, the increase in the rated power of offshore wind turbines has become a trend [52,71].

Among the different WT technologies available, the DFIG, SCIG with full-scale converter and PMSG are usually employed in OWF, due to their higher energy efficiency [16]. Several generators used in OWF were presented in [19]. The relevance of each of these technologies is illustrated in Figure 2.18. The offshore wind turbines are clustered into the aforementioned technologies.

The total installed capacity until 2013, percentage, and the average rated power of the turbines in each category are also indicated. The red dashed circles represent the variation in the percentage of installed capacity from 2013 to 2019. It is possible to observe a modest increase in DFIG driven WT in OWF commissioned after 2013, whereas the increase for SCIG is slightly higher. On the other hand, the PMSG technology started to be employed after 2013, and its installed capacity has increased significantly since then.
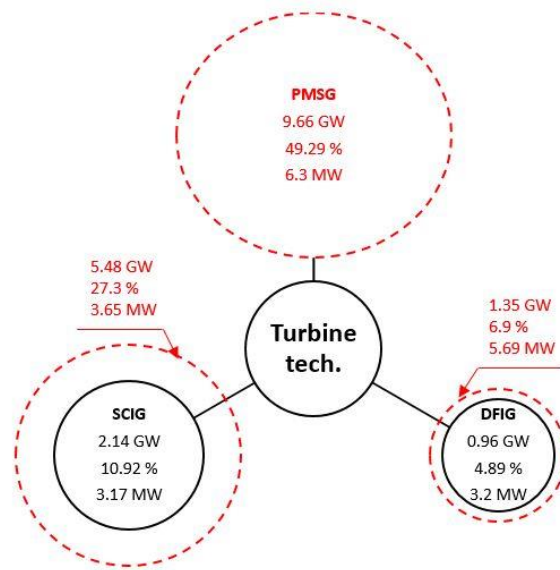
Figure 2.18. Cluster diagram of turbine technologies.

The generator models installed in Europe in large OWF between 2002 and 2019 can be found in Table 2.2. In total, 4307 WTs above 150 MW were installed and fully commissioned in European OWF during this period. SCIG with the full converter is currently the most used technology with 2180 turbines (51%), mainly due to its lower initial cost. DFIG shares correspond to 562 turbines (13%), and they were widely used between 2009 and 2013. PMSG reaches 1565 turbines (33%). However, it can be noticed that the trend for offshore turbines targets this technology, since 1265 PMSG were installed between 2016 and 2019, against only 54 DFIG and 388 SCIG. Moreover, no DFIGs were installed in large wind farms in 2018 and 2019.

Another important trend for offshore turbines is the increasing concern of manufacturers with the reliability, durability and cost of these elements. In this sense, the industry leaders are developing modular offshore wind turbines. This concept

consists in dividing the traditional single-pieced blades of the turbine into smaller pieces [71].

The natural path of WT manufacturers is the development of larger turbines in the next years. In general, when the power and size of the turbine increase, the costs of the foundations also increase. However, this increase in the rated power and size of the WTs reduces the number of units needed. Therefore, the total cost per MW tends to decrease with the growth of the rated power of turbines and plants.

Table 2.2. Generator models installed in large OWF in Europe.

Country	Turbine Model	Technology	Number of Turbines	Total	%
GE	Bard VM 5 MW – Bard [72]		80		
UK	Senvion 5 MW – Repower [73]		36		
BE, GE	Senvion 6.15 MW – Senvion [74]	DFIG	150	562	13%
DK	V80-2.0 MW – Vestas [75]		80		
UK, BE	V90-3.0 MW – Vestas [76]		216		
GE	AD5-135-5 MW – Adwen [77]		70		
DK, GE	M5000-116-5 MW – Areva [78]		120		
GE	Haliade-150-6.0 MW – GE Renewable Energy [79]		62		
GE, NL, BE	V164-8.4 MW – Vestas [80]		180		
NL	SWT108-3.0 MW – Siemens [81]	PMSG	48	1565	36,3%
UK, GE	SWT154-6.0 MW – Siemens [82]		473		
BE, UK	V112-3.0 MW – Vestas [83]		145		
UK	V164-8.0 MW – Vestas [84]		72		
BE,UK,GE	SWT154-7.0 MW – Siemens [85]		395		
UK	SWT107-3.6 MW – Siemens [86]		667		
UK, GE	SWT120-3.6 MW – Siemens [87]		794		
GE, NL	SWT120-4.0 MW – Siemens [88]	SCI	300	2180	50,7%
DK	SWT82-2.3 MW – Siemens [89]		253		
BE	V112-3.3 MW – Vestas [90]		50		
UK	V112-3.45 MW – Vestas [90]		116		

Currently, offshore wind turbines have diameters ranging from 80 to 164 m and a rated power between 2 and 8.4 MW, with the largest turbines being manufactured by MHI Vestas [91] and Siemens Gamesa [92]. Hence, there is a growing tendency regarding the rated power and rotor diameter of turbines in OWF. The average size of the turbines in 2019 was 3.72 times bigger than in 2002. In [93,94], the feasibility of a 20 MW turbine was investigated, concluding that the project would be feasible and could significantly improve the final cost of wind power plants, further revolutionizing this market.

Based on the information gathered, it can be indicated that, by 2025, generators ranging between 6 and 12.5 MW will be common in OWF, raising to 20 MW by 2030 [94–96]. Similar values are obtained from the polynomial regression of Figure 2.19. However, linear regression with the values registered up to 2019 yields lower figures: 8.6 MW for 2025 and 10.7 MW for 2030. In [97], an average value of 8 MW for 2020 and 10 MW for 2030 is envisaged.
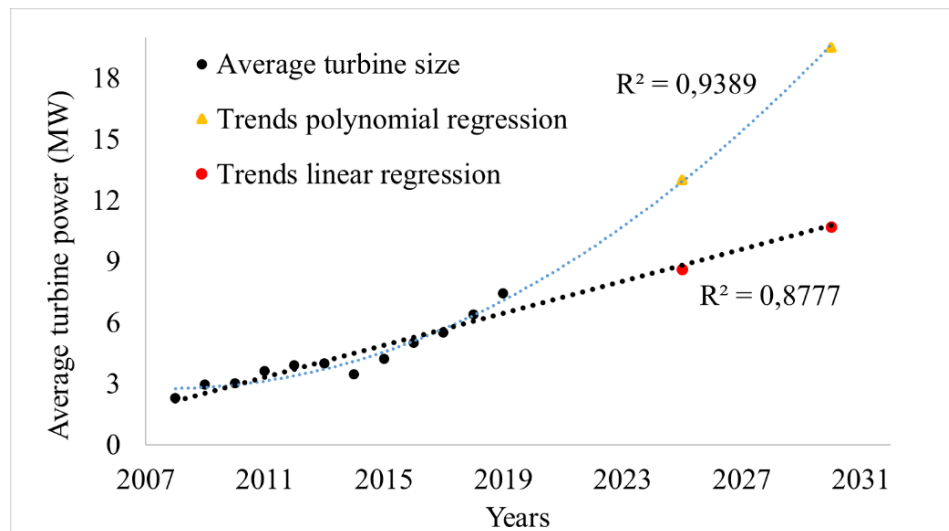
Figure 2.19. Trends for average offshore wind turbine power.

Transmission technologies

The trends for offshore transmission systems are presented in this section. Detailed studies of offshore transmission technologies can be found in [98–103].

In OWF, the transmission stage usually occurs at medium or high voltage AC (MVAC or HVAC), or high voltage DC (HVDC). Currently, MVAC transmission is

an option only for plants near the coast (20 km maximum) and with an installed capacity of up to 100 MW. This alternative is not profitable under conditions others than the mentioned according to [104]. Since 2002, HVAC has become the most used technology. This technology is consolidated, simple and more suitable for OWF with distances between 15 and 50 km from the shore. However, with an increase in the transmission distances, some drawbacks of the AC technology become more visible, such as a large amount of reactive current due to the high capacitance of the transmission lines, the unfeasible direct connection of two AC networks with different frequencies, and the failures in the HVAC cables. Based on these drawbacks, HVDC has become a technically viable and economical solution in cases of large distances and power [53,102].

In HVDC systems, power converters are used to adapt and control the DC voltage. The VSC-HVDC projects built up to 2010 used a two-level converter technology, which uses PWM due to its higher performance. The other alternative is the modular multilevel converter (MMC), which presents lower switching losses and a higher output voltage with low harmonic distortion [105,106].

Among the OWF observed, MVAC transmission (33 kV) was used only in the Lynn e Inner Dowsing and Westermeerwind projects. These projects have an installed capacity of 209 and 144 MW respectively. However, they are very close to the coast (6 and 1 km). As shown in Table 2.3, 70% of the transmission systems in OWF above 150 MW correspond to HVAC. However, a significant increase in HVDC transmission occurred in 2013.

Currently, several plants employ HVDC transmission, and this trend increases as the distance to the coast of the OWF rises. In 2015, eight OWF were connected through an HVDC link, and many more will be connected after 2018. Nowadays, Germany is the leader in OWF connected through HVDC links. Germany has twelve offshore HVDC links, while the UK has one wind farm (Global Tech 1 of 400 MW), and the next country to connect an HVDC to the coast will be Belgium.

Figure 2.20 summarizes all the information in terms of transmission technologies. The HVDC transmission was first used after 2013, and it has a total installed capacity of approximately 6 GW and average rated power of the turbines of 5.4 MW. Despite the huge increase of HVDC, HVAC transmission still dominates the scene.

Table 2.3. Transmission voltage level used for plants above 150 MW.

Transmission technologies	Number of Offshores	Voltage levels
		2	33 kV
		14	132 kV
HVAC	40	8	150 kV
		1	155 kV
		14	220 kV
		1	245 kV
		1	150 kV
HVDC	17	2	250 kV
		3	300 kV
		11	320 kV
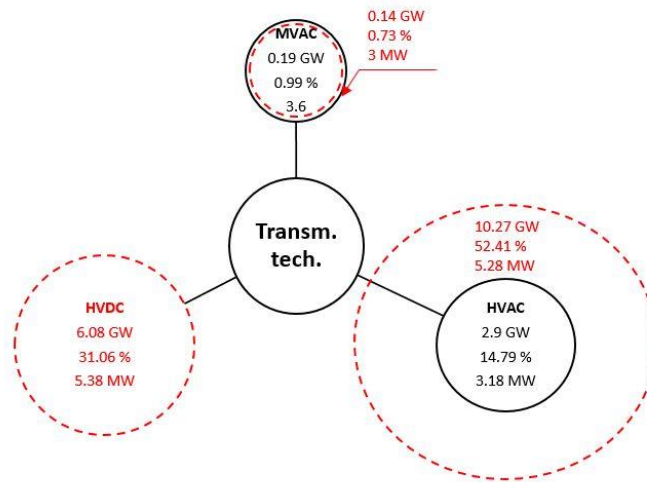
Figure 2.20. Cluster diagram of transmission technologies.

Array systems

Currently, there are several options for the internal topology of OWF regarding their design. The main topologies are reviewed here, and they can be divided into two groups: AC collection and DC collection [107,108].

AC topologies are consolidated and used in most cases. Radial parallel AC topology is the most common, which is used in various onshore and offshore plants. However, although this topology is the cheapest and commonly applied, it is not the most adequate option for OWF. Due to this inconvenience, "Single-Sided Ring Topology", "Double-Sided Ring", and "Star Topology" are better options for AC

collection in OWF. DC collection, or even the mix of two or more topologies, are relatively new, and currently under research. As the array collector system can be developed from different possibilities, the best topology is sought concerning investment vs. reliability. In this context, the aforementioned topologies are beginning to become viable options [109].

The selection between AC and DC has impacts in many aspects of the project, including the WT technology. A voltage of 33 kV is the most frequently used in internal array systems of OWF. However, with the increase of the rated power of the turbines in OWF, the trend is to increase the voltage rating as well. Hence, a rated voltage of 66 kV has been proposed in several works, and, although it has not been implemented yet, it might be the future trend for the internal array [110–113]. Moreover, some plants authorized in Europe will use this 66 kV voltage in their internal array.

Costs

The costs of OWF are divided into capital, variable and decommissioning costs [114]. Figure 2.21 shows the composition of costs in OWF in more detail. In general, due to their greater complexity, an OWF is more expensive than an onshore with the same rated power [115]. Nevertheless, offshore energy generation begins to turn competitive with other renewable energies, and the maturity of the technology can be highlighted. Many papers present cost reductions for offshore wind generation [116–118]. On the other hand, the necessity to be realistic is emphasized in [119], because there are still uncertainties regarding costs.

At a global level, offshore wind power witnessed a price drop between 2010 and 2018. The global weighted average levelized cost of energy (LCOE) of offshore wind projects commissioned in 2018 was 0.11 €/kWh, which represented a decrease of 20% in relation to 2010 (0.14 €/kWh). Moreover, offshore wind projects that will be commissioned after 2020 expect to reach between 0.053 and 0.088 €/kWh [120]. The LCOE represents the average income per unit of electricity generated that would be needed to recover the costs of building and operating a generating plant during a defined financial life and duty cycle [121].

In Europe, the LCOE dropped from 0.14 to 0.12 €/kWh between 2010 and 2018, representing a decrease of 14%. Belgium reduced by 28%, Germany 24% and the UK

14% falling to 0.125, 0.11, and 0.123 €/kWh respectively. Another important observation is that the capacity factor of OWF, that is the average power generated divided by the rated peak power, increased from 38% in 2010 to 43% in 2018 [120]. In the last decade, the highest average cost of offshore power occurred in 2014, reaching 4.77 M€/MW. This is justified by the fact that, between 2012 and 2015, OWF reached deeper waters, and the challenges faced were enormous. Moreover, in 2018, offshore average costs reached 3.87 M€/MW, showing a reduction of approximately 20% compared to 2014.
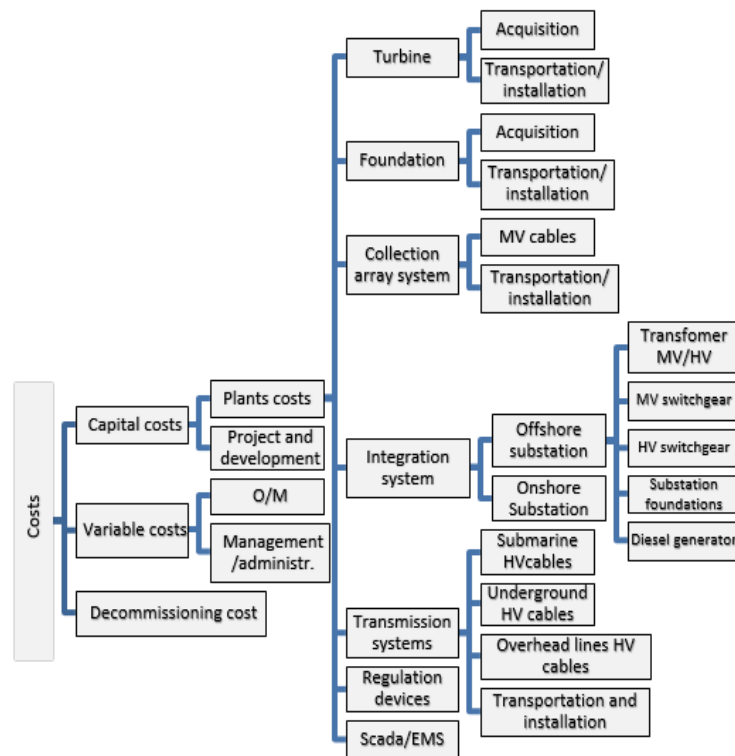
Figure 2.21. Distribution of costs for OWF.

Figure 2.22 presents the global weighted average of LCOE and capacity factors for different renewable energy systems. It can be observed that, although OWF have a slightly higher price per kWh when compared to onshore and PV solar, their LCOE has been decreasing over the last years. Moreover, the capacity factor of OWF is increasing with a higher rated power of the turbines.

Due to the tendency of OWF to move away from the coast, projects with HVDC are becoming more common. When analyzing the costs of the OWF above 150 MW, it is verified that the HVDC technology is currently more expensive than the HVAC, which has matured the most in recent years. However, from the first plant in HVDC

(Bard Offshore 1), their cost has been decreasing gradually. Other illustrative examples are the first phases of Trianel Borkum 1 and Borkum Riffgrund 1, which are 20% and 38% higher than their second phases respectively, even though they present the same characteristics.

For AC technology, there is a slight increase in costs per MW. Hence, when the first phases of Belwind 1 and Horns Rev 1 are analyzed, their costs are approximately 10% and 20% lower than their second phases respectively.
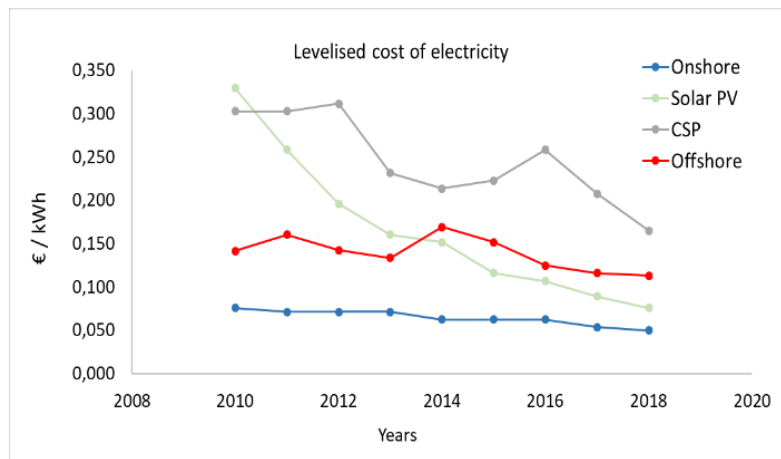
(a)
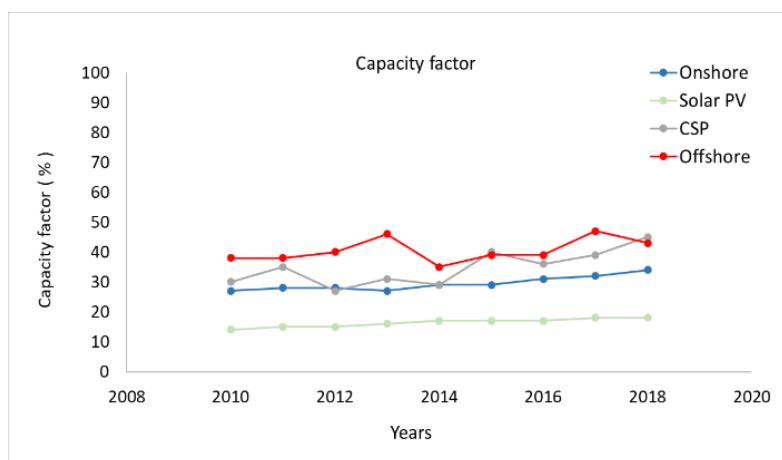
(b)

Figure 2.22. (a) A global weighted average of LCOE; and (b) capacity factors for Renewable systems.

2.2.3 Offshore wind farms outside Europe

Although Europe is the main contributor when it comes to OWF, it is possible to find some power plants above 150 MW operating in China. China is the third producer of offshore wind energy in the world with an installed capacity of 4.3 GW, and another 4 GW of OWF under construction [122], whereas the target is to reach 5 GW by 2020

[123]. When analyzing only plants above 150 MW, Figure 2.23 shows the installed and accumulated capacity, where significant growth can be noticed. The construction of OWF began with a single plant in 2010, and it started growing in 2016. Other upcoming markets that have shown interest in OWF are Japan, Korea, Taiwan, USA, India and Vietnam, but in these countries, the OWF are not in operation, nor classified as large-scale plants. Figure 2.24 shows the cumulative capacity of OWF in MW and the projections for 2031 according to [122]. It can be observed that the estimation in installed capacity for China is approximately 39 GW for 2031, which is below the 49 GW estimated for Europe.

	2010	2011	2012	2013	2014	2015	2016	2017	2018	2019
MW Installed	201	0	0	0	0	0	400	300	2254,4	552
Accumulated	201	201	201	201	201	201	601	901	3155,4	3707,4
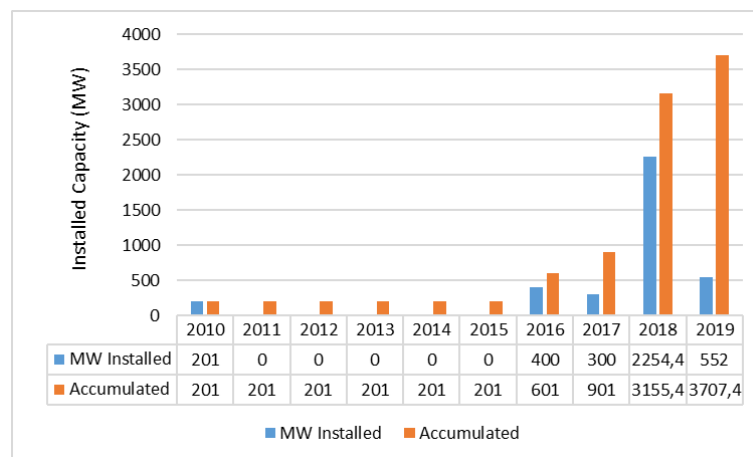
Figure 2.23. Installed capacity of the largest OWF installed in China [124].
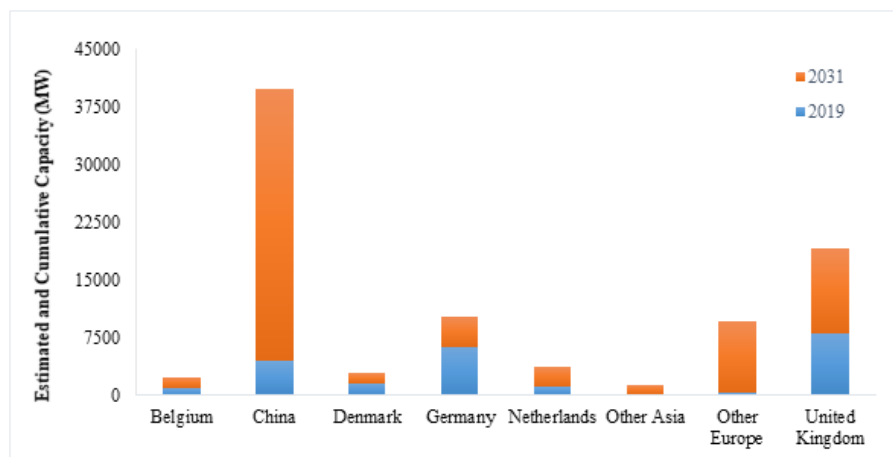
Figure 2.24. Estimated 2031 cumulative offshore wind capacity by country by country [122].

In terms of water depth, the early commissioned projects in China came from nearshore plants, which includes depths ranging from 10 to 15 meters. Previously, the water depth was mainly less than 10 meters [122,125]. When compared to Europe, it

can be noticed that the Chinese OWF are located in shallow waters, while the European plants are in deeper waters, being an average depth of 33 m. Regarding the distance to shore, the European OWF are furthest from the coast (50 km average) than the Chinese plants (25 km average) [122,124].

In China there are approximately 1100 WTs installed offshore, as can be observed in Table 2.4, while in Europe there are about 4307 WTs for plants above 150 MW (see Table 2.2). The average rated power of the WTs used in the European OWF nowadays is approximately 7.5 MW, whereas it decreases to 4.1 MW in the Chinese OWF [124]. The European OWF already use the HVDC technology as a transmission system (see Table 2.3), while only HVAC technology, mainly with a rated voltage of 220 kV, is used in the Chinese OWF [124]. For the internal array system, the voltage of 33 kV is the most frequently used in the OWF in Europe, while China typically uses a standard of 35 kV.

Table 2.4. Average parameters of OWF in China above 150 MW [124].

Total Nº WTs	Avg. Rating (MW)	Avg. Capacity (MW)	Avg. Depth	Avg. Dist. to shore (km)	Avg. Array (kV)	Avg. Transm.
1082	4	265	10	26	35	220kV (HVAC)

2.2.4 Environmental issues and constrained potential

The OWF belong in the green industry context, and, in this sense, the intention is to maintain the green label associated with that by not causing and/or reducing the damage to the environment when manufacturing or installing these plants [10]. However, as in any human activity, a certain impact on the surrounding ecosystem is inevitable. According to [126], there are positive and negative issues associated with OWF. The main positive effects are the replacement of fossil fuels with wind energy, and the offshore structures acting as artificial reefs, increasing the diversity of marine species. In contrast, the risks of collision for birds, the displacement of marine mammals and birds, and habitat loss or degradation can be mentioned as negative impacts. Some measures during the planning process can reduce the negative impacts associated with OWF. For instance, the authors in [127] mention that the proper election of an OWF location includes choosing a place outside protected areas and scheduling the construction operations outside the breeding season.

Regarding the legal framework, proper regulation is required given the remarkable expansion of the offshore plants and to avoid harmful impacts. To deal with the legal aspects of OWF, the Environmental Impact Assessment (EIA) is essential. Through the EIA, the impacts of the project are identified, and measures are adopted to mitigate these adverse effects. Any OWF with the potential to cause adverse impact must be able to produce an appropriate EIA, and if significant disturbances to the surrounding environment are verified, the power plant construction can only continue with compensatory measures [128].

Following the same reasoning towards sustainable development, there is an important legislative structure at the European level, such as The Birds and Habitats Directives (79/409/EEC and 92/43/EEC, respectively), which provide a structure for preserving species and habitats of interest, including the designation of Special Protection Areas (SPAs) and Special Areas of Conservation (SACs) under the Natura 2000 network [126]. Natura 2000 is a network of protected areas on land and sea across the 28 countries of the European Union (EU) for rare and threatened species and habitats [129]. If a certain location is identified as sensitive, this place should not be used for the construction of OWF, especially under the presence of endangered species. The Convention on the Conservation of Migratory Species of Wild Animals (Bonn Convention) on wildlife protection also grants responsibilities to signatory parties. This convention provides a platform for the conservation of migratory birds, aquatic or not, and their habitats. A Marine Strategy Framework Directive (MSFD) is working on marine management strategies to achieve a beneficial environmental status by 2021. This directive is part of the EU legislation specifically targeted at the protection of the marine environment and natural resources for sustainable use of these waters [97]. More detailed information regarding legal framework and obligations in Europe can be found in [128].

The offshore plants have to coexist in harmony with shipping routes, military use, oil and gas extraction, natural protected areas and tourist zones, due to the varied economic exploitation of the seas. For this reason, the potential for OWF development is limited. Currently, only 4% of the area with a distance to shore between 0 and 10 km can be used for OWF applications. This figure increases to 10% for distances between 30 and 50 km, and 25% for distances above 50 km [97]. Another important issue open to debate is the visual impact caused by OWF. This impact is considerable for OWF less than 10 km away from the coast. For this reason, the Netherlands and the UK have

prohibited building OWF less than 22 km away from the coast [97,126]. Figure 2.25 illustrates the total and the available unrestricted technical potential in TWh in the European sea. According to [97], if there were no restrictions, the amount of electricity generated by OWF would be enough to supply about 60% of the energy demand in Europe by 2030.
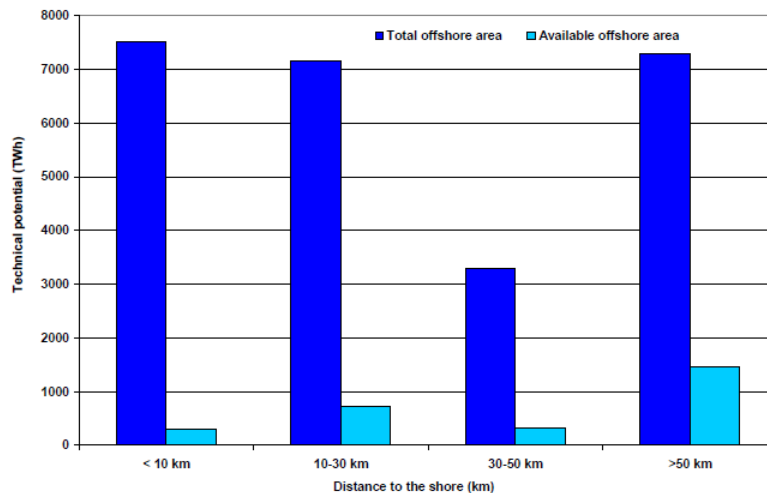
Figure 2.25. Available potential for OWF [97].

The aforementioned points highlight the difficulty to find the balance between positive and negative impacts. Therefore, it becomes necessary to reach a trade-off between sustainable development and ever-growing electricity demand.

2.3 PV POWER SYSTEMS

This chapter presents some of the current trends for PV power plants with energy storage in terms of topologies used, storage system and control. It is a solution little used to date, with a great future, which requires more research for its development and implementation.

2.3.1 Current status PV solar in the world

Figure 2.26a has presented a summary of the current status of solar and solar PV in the world, showing the evolution of installed capacity yearly (from 2011 to 2020). Figure 2.26b shows the current status of solar PV separated by country. Asia leads the installed capacity due to the great contribution of China, which has been investing massively in PV-utility. China has approximately 250 GW of solar PV installed. Evaluating Figure 2.26c it is possible to observe that it increased its matrix by approximately 125 GW in the last three years, the USA added nearly 40 GW, while

that Europe and UK together added nearly 42 GW in the same period. USA has approximately 75 GW of installed solar PV capacity and Europe has just over 150 GW.
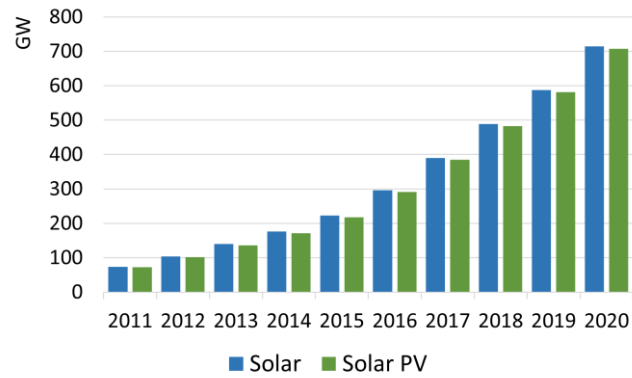
(a)
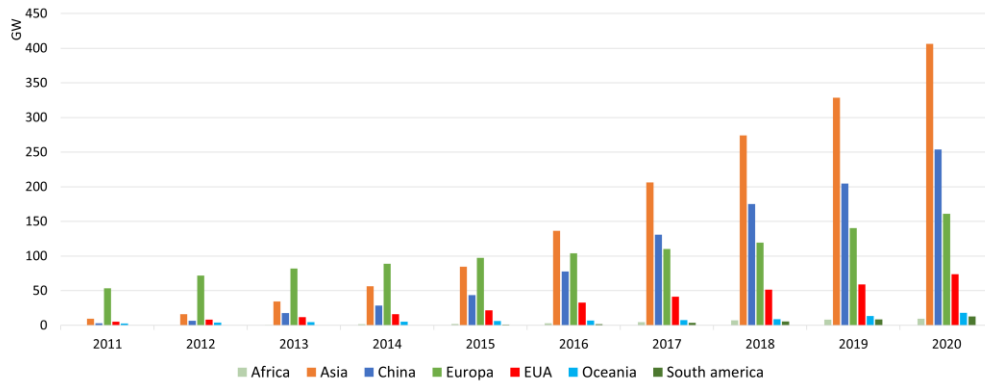
(b)
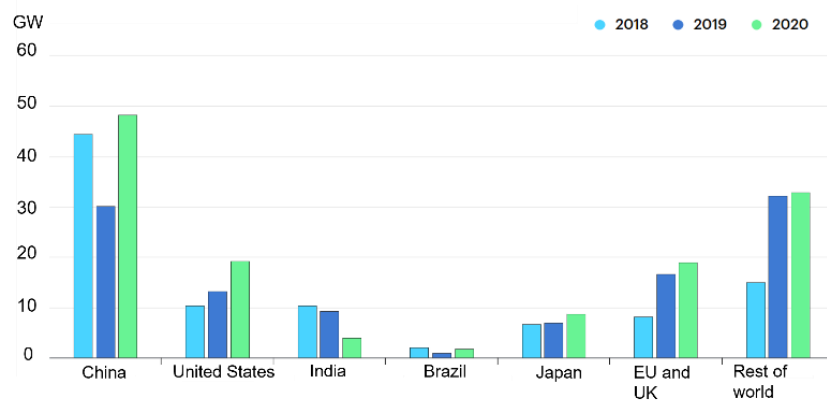
(c)

Figure 2.26. PV installed capacity in the world: (a) Solar and solar PV in the world, (b) Solar PV by continents and main countries, (c) Increment in the last three years of solar PV by countries

2.3.2 Small-scale PV power plants

Briefly, before discussing high-power PV plants, the current situation of small-power PV plants, less than 100 kW, with energy storage, which corresponds to the vast majority of published applications and works, is discussed. In this sense, some significant references have been chosen to show the current state of the use of energy storage in small PV power plants.

The first article to be analyzed is a review of distributed PV generation systems with energy storage [32]. Although right now, for isolated or grid-connected small power installations, the most widely used options are lead and lithium-ion batteries [130], for the authors in [32], NaS batteries in small power PV systems represent an efficient option as a storage system as it is a technology that is already well developed, has a long useful life and high efficiency, requiring little space. This last factor is convenient, especially in areas of high population density. It is also noted that the use of NaS batteries is interesting to control energy peaks, increase the reliability of the system and increasingly include renewables in the grid.

In [131] an optimization of PV plants with grid-connected BES in commercial buildings in the UK is presented. The developed linear programming model finds the most cost-effective configuration of PV and BES while providing information on how such systems should operate at half-hour intervals at different times of the year. The technology selection and operation model has been tested using a case study in a food distribution centre in London, UK. The results indicate that the most attractive technology configuration is a combination of lithium-ion batteries and mono-crystalline silicon PV panels and that financial payback is completed in eight years. However, this does not mean that this is always the best option, as each building is different and no one solution fits all the applications. The result found in general terms indicates that, without incentives or reductions in the cost of the technology, PV and BES constitute a questionable investment for most of the organizations that establish short periods of recovery of the investment (less than 3 years). This finding implies that, if there were not the incentives set by the UK government, much of the installed capacity so far would not have taken place.

Other examples, considering PV systems with qZSI/ZSI for small-scale applications can be found in the literature [132–137]. An optimization based on a novel perturbation and observation algorithm was proposed in [132] to achieve the MPPT of a 4.5 kW PV system connected to the grid through a qZSI. In [133–135], different

modulation techniques were applied to ZSI/qZSI in small-scale PV system applications. A control strategy based on model predictive control was implemented for a three-phase qZSI in [136], while control loops with conventional PI controllers were used in [137].

Some of the first applications of qZSI connected to small-scale PV systems and integrating ESS can be seen in [138,139]. After these first applications, other research works with the same elements were also published, connecting the inverters in the cascaded multilevel topology [140], managing the battery SOC [141] or the power flow [142].

2.3.3 Large-scale PV power plants

Concerning large scale PV plants, until 2016 seven of the ten largest PV systems in terms of installed capacity were located in the USA. Among these top ten, the installed capacity has been increasing since the last decade, as the capacity went from 250 MW in 2011 to 580 MW by the end of 2015. There is a tendency to increase the global installed capacity until 2050, especially in China and USA, reaching 1800 GW and 500 GW respectively [143] [144], as shown in Figure 2.27. In this figure, two situations are considered for China, one with an optimistic forecast (indicated by "x" in yellow) considering a high PV penetration through government incentives, and another in case of continuing to follow the current patterns (red triangles). The mentioned data justify the importance of developing studies on large scale PV plants to improve their quality and spread their use.
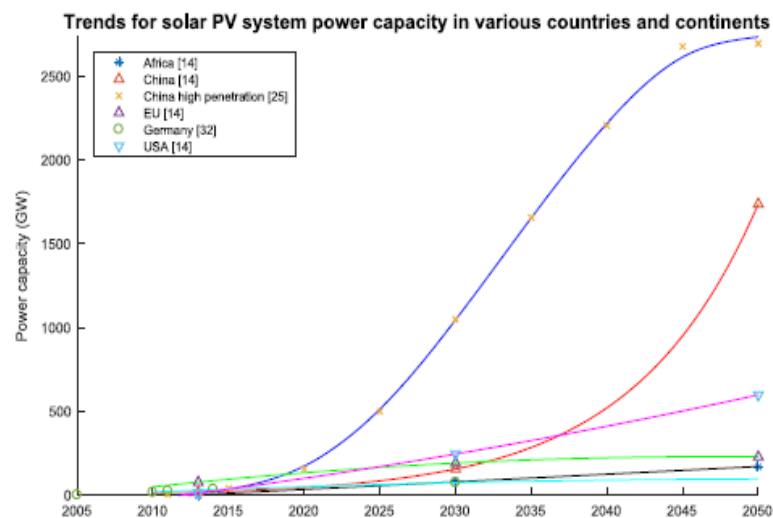
Figure 2.27. Trends for installed PV power systems by countries/continents [144].

One important parameter to consider to improve large-scale power plants is the study and evaluation of the most suitable configuration according to technical criteria. To guarantee the best design, control and operation of the PV power plants, the PV generation components are being investigated, as well as the internal design of the plants. Hence, the topologies used in PV plants are investigated next.

Four topologies for large-scale power plants are analyzed in [20]. In the central topology, all PV panels are interconnected to an inverter. In the string topology, a PV string is connected to an inverter. The multi-string topology presents a PV string connected to a DC/DC converter, with 4 or 5 DC/DC converters connected to a DC/AC inverter. The fourth topology, module integrated, has one inverter for each PV module, but until the present date, it has not been used in large-scale plants.

It can be stated that the central topology has the following advantages: robustness, low AC energy losses, low variation of AC voltage and reasonable installation and maintenance costs in contrast with the other topologies. The general characteristics of the string and multi-string topologies are very attractive, but their main drawback is the installation and maintenance costs as the number of inverters increases. The string topology has characteristics similar to the multi-string topology, but its use is recommended when each PV string has different orientation angles. The multi-string topology has better efficiency because it has a dedicated MPPT control per string. However, the complexity of the installation and the large number of inverters needed make this topology less attractive to investors.

Four different configurations for PV plants were evaluated in [145]. The contribution of ESS was also considered in this paper. Furthermore, the connection to the grid of the configurations was analyzed. The configurations evaluated were: independent, AC-Coupled, DC-Coupled and DC tightly coupled.

The independent configuration represents the way that most of the large-scale storage and PV systems are currently implemented. In this configuration, the PV generators and the ESS can be located in completely different locations and do not share common components or control strategies. The ESS can be charged with any source in the network that provides low-cost power, and it can discharge during periods of high demand.

In the AC-Coupled configuration, the PV and ESS are located together and share a point of common coupling to the AC network. Because the plant does not share any

component, the ESS can still act independently of the PV system, that is, it can store energy from the PV plant or the network.

The systems in which the PV plant and the ESS are coupled on the DC side of a shared inverter are the DC-Coupled and the DC tightly coupled configuration. The DC-Coupled system includes a bidirectional inverter that allows the energy storage to be charged from the network, in addition to being charged from the PV. The DC tightly coupled system assumes that the ESS can only store energy from the PV panels, not from the grid.

For large scale PV plants, different converter models have been implemented. For example, the topology used in [21] is connected to the grid through two conversion stages, consisting of two parallel-connected triple-port dual active bridge (DAB) combined into a two-level inverter. Each triple-port DAB integrates a PV and a battery-based ESS through a multi-winding transformer. The high-power density, galvanic isolation, seamless switching between the different operating modes, and modular nature, are notable features of the triple-port DAB-based DC/DC converter modules. All these features make this PV-ESS integrated triple-port DAB converter interfaced to an inverter an attractive solution for large scale plants integration to the grid.

Other works found in the literature suggest the use of ZSI and qZSI with ESS. A large voltage boost in a single-stage can be achieved by ZSI, which includes an impedance network before the VSI. Different topologies for ZSI can be found in [146,147]. A modified topology with a bi-directional power flow was proposed in [146]. An improved boost capability and low voltage stress in the impedance source of a ZSI were analyzed in [147]. A derivation of ZSI is the qZSI, which presents differences in configuration while maintaining the same operating principle. The benefits of the qZSI, when compared to the ZSI, are a lower component rating, no need for extra filtering capacitors, reduced switching ripples and constant DC input current from the PV panel [139].

2.4 CONVERTER TECHNOLOGIES

Converters are elements capable of altering the characteristics of the voltage and current inputs, transforming them in an optimized way for the desired specific output [148]. The converters are responsible for adapting the energy generated by PV panels,

WTs, BESs or any other source to the necessary characteristics so that it can be injected into the electrical network or used by an isolated installation.

The desirable characteristics for a converter can be summarized in high efficiency, low no-load consumption, high reliability, protection against short circuits, safety, good regulation of the output voltage and frequency [149]. A common classification is through the relationship between the input and the output of the converter [150], being those the: DC/DC, AC/DC (also called rectifiers), AC/AC, DC/AC (also called inverters). When connected to the grid, the inverter should provide an alternating current that presents the same characteristics of the electrical network to which it is being connected, concerning the frequency, form, and effective value. Variations are practically not allowed to avoid disturbances on the electrical distribution network.

The energy generated by the sources needs to be converted before being delivered to the load or the grid. This conversion occurs typically in two stages. The first one is performed through a DC/DC converter, and in the second one, usually, a voltage source inverter (VSI) allows the connection to the grid [151]. When dealing with PV plants, typically, the DC/DC conversion stage boosts the voltage of the PV panels and implements the maximum power point tracking (MPPT) strategy of the PV generator, while the VSI is controlled to keep the voltage at the DC link constant and regulate the reactive power exchange with the grid [152–154].

Nowadays, WT can have different topologies regarding their power converters. Some alternatives for the machine-side converter (MSC) of PMSG WT were suggested in [22], whereas several options for the grid-side converter (GSC) were presented in [23]. For instance, a three-phase diode bridge can be used as a rectifier for the MSC. However, when the WT rotates at a low speed, the uncontrolled rectifier may not provide the DC voltage level required at the input of the GSC. In these cases, a DC/DC boost converter can be employed to increase the voltage to adequate values for the GSC. This solution is simple, cost-efficient and allows extracting the maximum power from the WT. Nevertheless, it presents high harmonic current distortions in the generator windings, overheating and oscillations in the torque.

On the other hand, PMSG can be connected to the grid through two two-level voltage source converters (VSC) in a B2B configuration and controlled by pulse-width modulation (PWM). Additionally, a voltage transformer is usually inserted between

the GSC and the grid. This solution is relatively simple, robust and reliable. The drawbacks of this configuration are larger switching losses and lower efficiency at high powers, in addition to high THD [23].

Converters based on voltage or current source have the drawbacks of being a buck or boost converter and they cannot be a buck-boost converter. It means that the obtainable output voltage range is limited to higher or lower than the input voltage and their main circuits cannot be interchangeable [29,155].

To overcome these problems, ZSC is a power converter that has buck and boost capabilities in a single conversion state. A single-stage conversion is an attractive option due to its reduced losses, low device count and lower costs [24]. This type of device incorporates an impedance network between the voltage source and the converter so that the converter can overcome the technological barriers of traditional VSI [156]. The structure of a ZSC is presented in Figure 2.27.
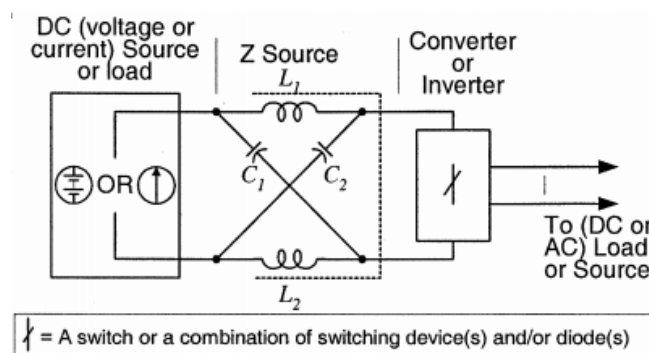
Figure 2.28. Estructura general de un convertidor Z [156].

Another important advantage of the ZSC is that they can work in a shoot-through state without damaging the devices. The operating principle of this shoot-through state is based on taking advantage of the overlapping states, not allowed in the other converters, to increase or decrease the voltage on the DC bus, thanks to the impedance network.

Several advantages of this type of converter were highlighted in [155], where the configuration based on DC/DC boost converter and VSI was compared to a configuration based on ZSC. ZSC achieved better performance due to their shoot-through capability. However, their main drawbacks are a discontinuous input current in the boost mode and high voltage stress in the capacitors of the impedance network [28].

Several ZSC topologies were analyzed in [26,27]. Among them, the qZSI is particularly attractive due to several improvements compared to the ZSC [28]. For instance, the qZSI presents continuous input current and reduced current and voltage in the inductor L_2 and the capacitor C_2, respectively. Furthermore, it can also work as a bidirectional converter replacing the diode with a bidirectional controlled switch. The DC/DC converter proposed in [157] is a variation of the traditional qZSI that can be coupled to the VSI. This converter improves the voltage gain in the DC/DC stage, on the other hand, it reduces the duty-cycle range. In [158] is proposed a converter based on an impedance source that, in addition to a good duty-cycle range, has a high voltage gain capacity, maintaining an acceptable degree of stress in the components. The converter proposed in [159], that is used in this work, in addition to a high degree of boost/buck capacity, reasonable efficiency and stress on the components, its gain concerning the duty-cycle is linear, making control much easier.

Regarding the use of qZSI with renewable energies, several works on small-scale PV solar energy (with rated power below 10 kW) can be found in the literature. The qZSI was used in [137] and [160] for PV distributed generation with rated powers of 1 kW and 1.3 kW, respectively. In both papers, the closed-loop control of the output voltage/current was applied through the voltage on the capacitor C_1 of the impedance network. A model predictive control (MPC) technique was applied to a 550 W qZSI and PV array system in [161].

Some applications based on small-scale wind power generation were also discussed in the literature. A control strategy for a grid-connected ZSI was presented and compared with a conventional VSI in [162], highlighting the main benefits of the former. A solution using double-input ZSI was proposed in [163] for a WT with dual-star PMSG. The authors emphasized the increased generator reliability against short circuits, the need for less passive components, and the desired output voltage waveform as the main advantages.

A dynamic model of the qZSI equipped with an ESS was presented in [164,165]. This converter was used on a PMSG WT in a stand-alone application. Additionally, a closed-loop control scheme for the DC and AC sides was presented, validating the adequate performance of the control system through simulation. The authors highlighted the need for further studies in this area.

In Sections 3.1.2 and 3.1.4, the modelling and control of the ZSC-DC/DC and qZSI with battery used in this thesis are described in detail.

2.5 BATTERY ENERGY STORAGE SYSTEM

On the other hand, due to the intermittency and fluctuation of the hybrid sources, it is important to pay attention to the integration of these systems in the electric grid. If this integration is not dealt with properly, excessive RES connected to the grid may lead to voltage instability, power fluctuation, malfunctioning of the voltage regulation equipment, among other issues. Thus, it is necessary to find solutions by developing advanced control and operation techniques to maximize renewable power utilization while keeping the system reliable and stable [166].

Many solutions in the literature are proposed. To reduce the intermittent characteristic of RES, the authors in [167–170] proposed the use of ESS. Among the different ESS, BESs are nowadays considered as the main technology applied to PV and wind power plants. Other technologies such as flywheels, SC and fuel cells, for example, need to be further studied. According [167], the high uncertainty and fluctuation of the PV power cause poor power quality and control issues. The energy storage and dispatch strategies could play an important role in the stability of future power systems with high PV penetration. Reference [168] studies the use of batteries with large renewable generation as one of the effective technologies to deal with power fluctuation and intermittency, while that in [169], an ESS composed of a combination of battery and SC is used to complement each other in terms of power and energy. The use of hydrogen as an ESS for a PV power plant, with simulations based on real data from a 1.62 MWp plant located in central Italy, was analyzed in [170]. In the same way, the authors of [13,171] investigated a hybrid system consisting of WT, PV panels, a fuel cell with a proton exchange membrane (PEMFC), a hydrogen tank, electrolyzer and BES. The excess power produced by the WTs or by the PV system is used to charge the BES and to generate hydrogen through the electrolyzer, which is stored in a tank and later used as input fuel in the fuel cell, to generate energy again electrical.

ESS integrated into PV plants allow the excess energy generated to be stored for later use when necessary. ESS can help power grids withstand peak demand, allowing transmission and distribution grids to function efficiently. In shorter periods, energy storage can be effective in smoothing short peaks and distortions in voltage [172].

Energy storage technologies can be classified as electrical, electrochemical, chemical, thermal and mechanical, as presented in Figure 2.29.
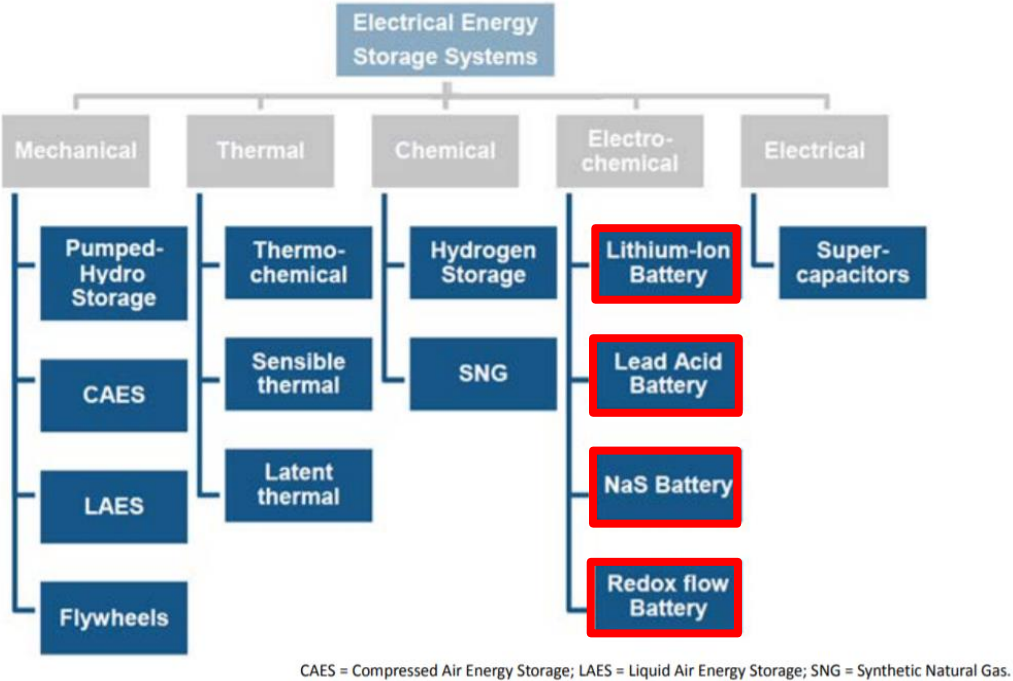
Figure 2.29. Examples of energy storage systems [173]

In this section, the technologies that are highlighted in red will be addressed in the following subsections, and the others that are not marked were not studied due to their little use or relevance to the proposed objective.

2.5.1 Battery

Batteries are based on the chemical storage system and have the double function of storing and releasing electricity, alternating the charging and discharging phases, without noise and emissions [174].

There is a wide range of technologies used in the manufacture of accumulators, such as lead-acid, nickel-cadmium, nickel-metal hydride, nickel-iron, zinc-air, iron-air, sodium-sulfur, lithium-ion, lithium-polymer, etc. and its main strengths are its energy densities and technological maturity. However, its main drawback is its relatively low durability for high amplitude cycles [174].

According to DTI Report [175], large-scale storage was rare until recently, due to its low energy density, small power capacity, high cost of ownership, low life cycle,

and limited discharge capacity. Furthermore, most batteries contain toxic material, and therefore the environmental impact of discarding these batteries must be considered.

For Karpinski A P, Makovetski B, Russell S J, et al. [176], BES that are in use and/or potentially suitable for storage use are lead-acid, nickel-cadmium, sodium-sulfur, sodium nickel chloride and lithium-ion.

Currently, the conventional BES that are widely applied today are lead-acid batteries, nickel-based batteries, and lithium-based batteries. In addition to the three main types of BES described above, there are some additional types, albeit with low market penetration. These are the sodium-sulfur (NaS), the redox flow storage system, and the metal-air battery [175][176].

Lead-acid

Lead-acid batteries are the oldest of the rechargeable type and are based on chemical reactions involving lead dioxide (cathode), lead (anode) and sulfuric acid that acts as an electrolyte [177]. Lead-acid batteries are highly energy efficient (between 85 and 90%), are easy to install and require a relatively low level of maintenance and a low investment cost [172]. Moreover, provides competitive cost but have a relatively limited lifetime, low energy density, and can cause a large environmental impact [176].

Nickel Cadmium

As for the positive electrode, nickel hydroxide is applied, for the negative electrode, cadmium hydroxide and in the electrolyte an aqueous solution of potassium hydroxide with some lithium hydroxide. NiCd batteries have a high energy density (50-75 Wh / kg), robust reliability and very low maintenance requirements, but a relatively short cycle life (2000-2500) [178]. The main disadvantages of these batteries are a relatively high cost due to the expensive manufacturing process and cadmium is a toxic heavy metal and therefore poses problems associated with the disposal of NiCd batteries [32].

Lithium-ion (Li-ion)

In these batteries, the cathode is a lithiated metal oxide and the anode is made of graphitic carbon with a layered structure. The electrolyte is composed of lithium salts dissolved in organic carbonates [175]. The self-discharge rate is very low, with a maximum of 5% per month and the battery life can reach more than 1500 cycles [179].

However, the life of a lithium-ion battery is temperature dependent and can be severely shortened by deep discharges. Also, lithium-ion batteries are fragile and require a protection circuit to maintain safe operation. Built into each battery pack, the protection circuit limits the maximum voltage of each cell charge and prevents the cell voltage from dropping too low on discharge [172].

Sodium sulphur (NaS)

Sodium sulfur batteries consist of a positive molten sulfur electrode and a negative molten sodium electrode separated by a sodium beta-alumina ceramic electrolyte [32]. NaS batteries have an expected operational duration of 15 years considering 2500 cycles (charge and discharge) for a depth of discharge of 100% (DOD); they have a high energy density, three to five times more than a lead-acid battery; it is not affected by the ambient temperature (it works from 290 to 360 ° C); allows remote operation and monitoring with minimal maintenance; no emissions or vibrations, low noise level compared to other energy conversion systems; 98% of the material used in NaS batteries can be recycled, only sodium cannot be reused [167].

Vanadium redox flow

Redox technology offers significant advantages, such as the absence of self-discharge and the absence of degradation for deep discharge [172]. The cell efficiency can be as high as 85%. This type of battery is suitable for a wide range of energy storage applications for electric utilities and industrial end-users. Most development work has focused on stationary applications due to the relatively low energy density [175].

Metal-air

Metal-air batteries are the most compact and potentially the least expensive [175]. It offers a high energy density (compared to lead-acid batteries) and long life. However, tests have shown that metal-air batteries have a limited operating temperature range [172]. Among the various metal-air batteries, the lithium-air battery is an attractive option. However, the high reactivity of lithium with air and humidity can cause a fire, which is a high safety risk. Currently, only a zinc-air battery is technically feasible [180].

2.5.2 Battery energy storage comparison

To compare the performance of the different types of storage systems, some criteria were taken into consideration such as cost, energy density, recyclability, durability and efficiency.

Another perspective to analyze the most suitable storage system for a determined application is comparing the rated power of the system and the discharge time, as shown in Figure 2.30. Large-scale permanent energy storage applications can be classified into three main operational categories:

• Power quality: the energy stored in these applications is only used for a few seconds or less to guarantee the quality of the energy delivered.

• Buffer and emergency storage: the energy stored in these applications is used from seconds to minutes to guarantee continuity of service when changing from one source of electricity to another.

• Grid management: storage systems, in these applications, are used to decouple the timing between power generation and consumption. A typical application is load levelling, which involves storing energy during off-peak hours (low energy cost) and using stored energy during peak hours (high energy cost).

Figure 2.30 compares which of the storage options are more suitable according to the application and the intended power.
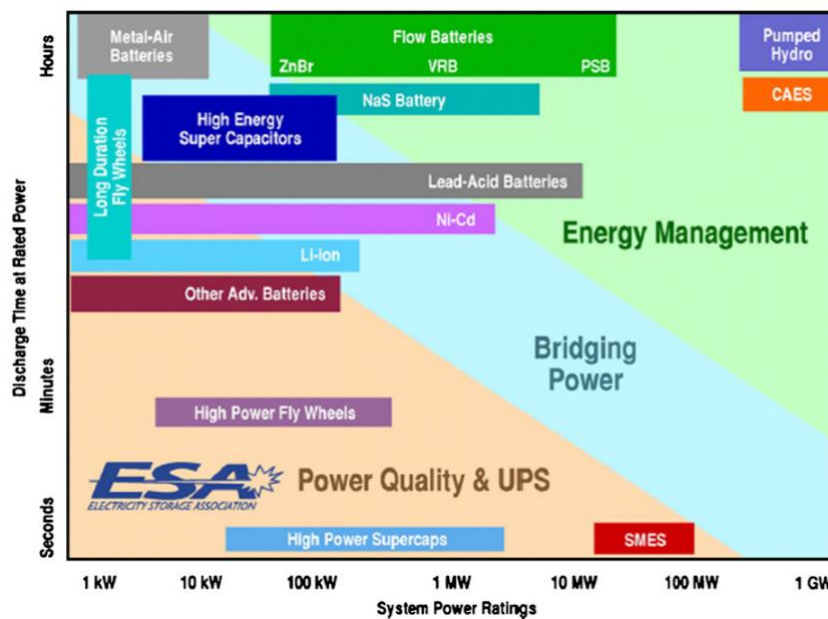
Figure 2.30. Distribution of storage techniques according to the application [174].

The characteristics of the different storage techniques concerning efficiency and life cycle are illustrated in Figure 2.31. The two technologies with the longest lifespan and efficiency are the UC and the flywheel, and among the batteries, the Li-ion technology presents higher efficiency.
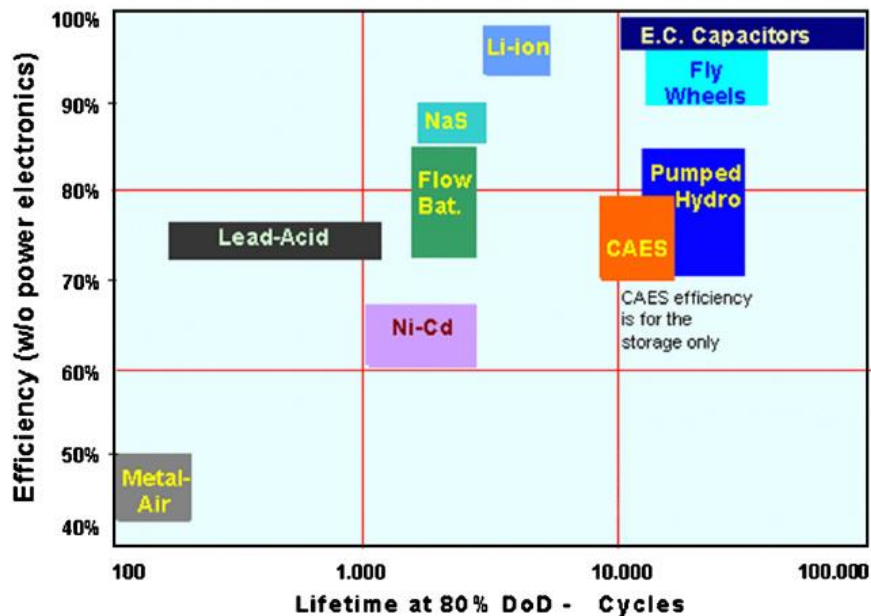
Figure 2.31. Distribution of storage techniques based on energy efficiency and lifetime [174].

Energy efficiency and lifespan (maximum number of cycles) are two important parameters to consider, among others, before choosing a storage technology, as they affect overall storage costs. Low efficiency increases effective energy costs as only a fraction of the stored energy can be used. A short service life also increases long-term costs, as the storage unit must be replaced more frequently.

With regards to costs, the investment associated with a type of storage is an important economic parameter and affects the total price of energy production. Therefore, some types of storage systems can only be profitable if a certain minimum of energy is supplied. Then, the overall cost of the system (including durability of the equipment and cost of investigation) must be considered to achieve a complete analysis. For example, even though lead-acid batteries are relatively inexpensive, they are not necessarily the least expensive option for power management, due to their relatively low durability.

The cost of batteries per unit of power and energy is as shown in Figure 2.32.
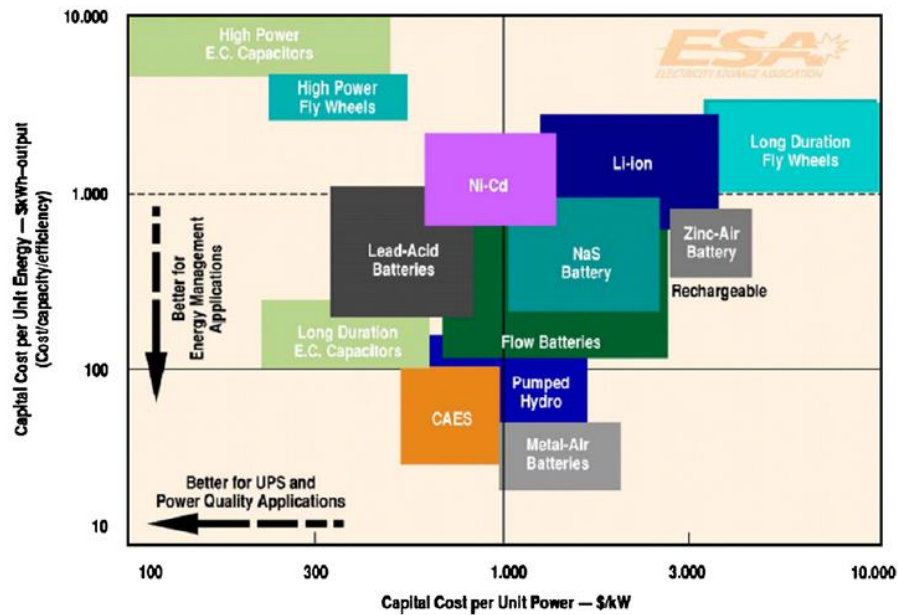
Figure 2.32. Distribution of storage technologies as a function of investment costs per unit of power [174]

To conclude from the data presented, it is possible to note that there is a great variety of storage technologies, each one intended for different applications. The choice of the best option is conditioned by the amount of energy to be stored, the time during which it is required to retain or release this stored energy, the available space and environmental restrictions, the cost and the exact location of the network in that storage is required.

It is clear from the review above those BES are the dominant technology to be used when the continuous power supply is primordial, while technologies such as flywheel and UC are most suitable for energy storage applications where a shorter power supply is demanded. Li-ion batteries are becoming increasingly important and have several advantages over traditional lead-acid batteries. Finally, fuel cell performance is constantly improving in terms of reliability and investment cost, yet the future penetration of fuel cells remains linked to costly hydrogen production and storage processes.

Chapter 3: Description of the configurations evaluated

In this thesis, several hybrid configurations using renewable systems have been analysed. These configurations although are varying in terms of elements that integrate the power plant were based on PMSG, PV, and BES. The systems under study were modelled using MATLAB/Simulink and simulated in various scenarios to evaluate their performance. In this chapter, all components involved in the configurations under study are described and presented.

3.1   HYBRID POWER PLANTS

The grid-connected hybrid power plant under study (Figure 3.1) is composed of a PMSG-based WT of 1.5 MW, a PV plant of 402 kW and a lithium-ion BES of 532 kW, totalling a 2.44 MW hybrid power plant. Moreover, a load of 1.2 MVA shares the same connection point with the hybrid power plant.

The PMSG-based WT has a rated power of 1.5 MW, and it is connected to the grid through a qZSI with BES. The PMSG has an AC output voltage of 0.69 kV connected to a non-controlled rectifier in the first stage. Then, the impedance network of the qZSI boosts this DC voltage for achieving an AC output voltage controlled of 0.69 kV, which is connected to a transformer to adapt the voltage and connect the hybrid power plant to the grid and the load. The capacitor C_1 of the impedance network works as a controlled DC bus and the PV system is connected to this capacitor C_1 through a DC/DC ZSC, which ensures the control of the PV plant.

Furthermore, the qZSI has an integrated BES connected to capacitor C_2 without an additional converter. Several battery cells are connected in series/parallel to reach the adequate capacity and output voltage for the connection to the capacitor C_2. This BES has the main objective of supplying an extra power demand required by the grid.

An LCL filter is considered at the qZSI output because it provides high harmonic attenuation and it is suitable for large-scale renewable energy applications [181]. Residential and industrial load were considered in the microgrid under study. The residential and industrial load are connected to the microgrid through a transformer of

0.75MVA, 25 kV/240V and 0.75MVA, 25 kV/2.3 kV, respectively, and both are connected in Y/Y.
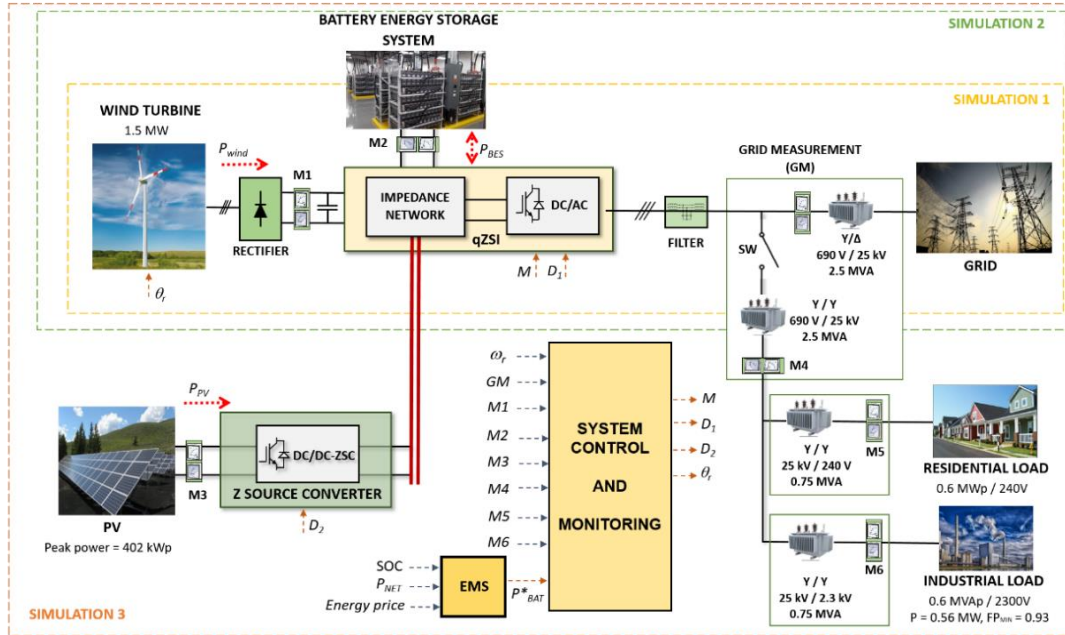
Figure 3.1. Configuration of the grid-connected microgrid with the hybrid power plant (PV, WT and BES), and residential and industrial load.

The components of the system implemented were detailed and modelled in this chapter. Figure 3.2 shows all voltage levels of the microgrid. The values in the graphs correspond to the peak values of the phase voltage. Moreover, Table 3.1 shows the main parameters of the system simulated.

Table 3.1. Specifications of the system under study

Parameter	Value
PV generator	
Optimal PV power (P_{PVopt})	335.2 W
Optimal PV voltage (V_{PVopt})	57.3 V
Optimal PV current (V_{PVopt})	5.85 A
Open-circuit voltage (V_{oc})	67.9 V
Short circuit current (I_{sc})	6.23 A
Wind turbine	
Rated wind power	1.5 MW
RMS voltage	690 V
Power coefficient (Cp)	0.48
Blade radius (R)	60 m
Number of pair of poles	60

Stator resistance	5.5 mΩ
Stator inductance	0.8 mH
Rated wind speed	11.5 m/s
Battery	
Battery nominal voltage	48 V
Battery rated capacity	74 Ah
Filter	
Inductor L_{1f}	0.15 mH
Capacitor C_f	230 µF
Inductor L_{2f}	6.6 µH
qZSI	
Inductor $L_1 = L_2$	100µH
Capacitor $C_1 = C_2$	360 µF
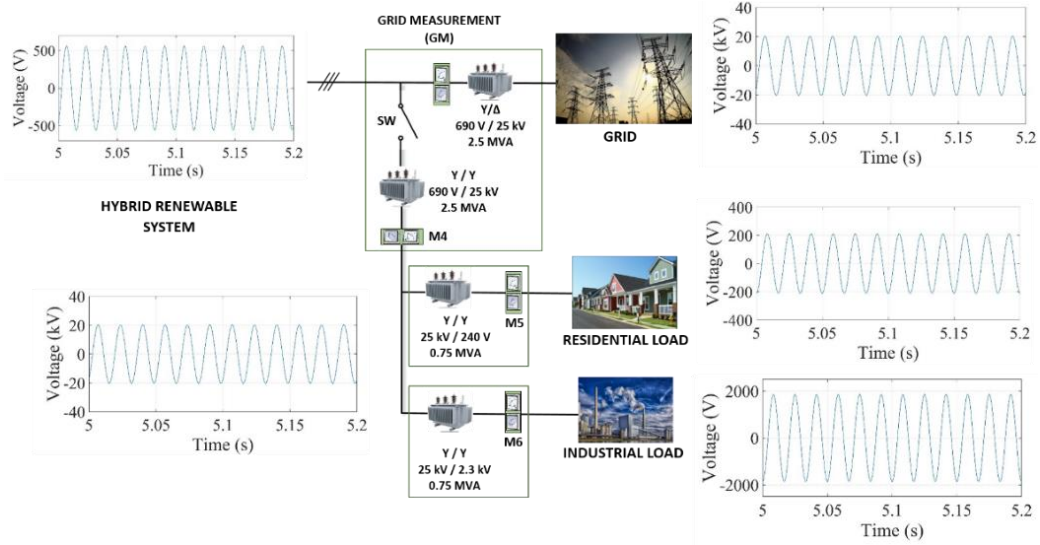
Figure 3.2. Voltage levels in the microgrid

3.1.1 PV power plant

The SPR-X21-335-BLK PV modules [182] are used and grouped in a 120x10 structure to reach a PV peak power of 402 kWp, with an output voltage of 573 V. The model presented in [183] is used to implement the PV system. This model receives the irradiance and temperature as inputs, while the I-V characteristics are outputted. The model consists of a diode, a controlled current source, a series and a shunt resistor. Moreover, irradiance and temperature are the input parameters, whereas the output parameters are the voltage and current. According to [184,185], this model is accurate and simple to implement. The equations to find the output current is supplied in Equation (3.1) – (3.3).

$$I_{pv} = I_L - I_{sat}\left(e^{q\frac{(Vpv+IpvRs)}{NkTpv}}\right) - \frac{\left(V_{pv} + I_{pv}R_s\right)}{R_{sh}}$$ (3.1)

$$I_L = I_{L0}\left(1 + K_0\left(T - 300\right)\right) \cdot \frac{G}{G_n}$$ (3.2)

$$I_{sat} = I_{sat,n}\left(\frac{T_n}{T}\right)^3 e\left[\frac{qE_g}{ak}\left(\frac{1}{T_n} - \frac{1}{T}\right)\right]$$ (3.3)

where I_{L0}, I_L are solar-induced current at 300 K and the solar-induced current (A), respectively; $I_{sat,n}$, I_{sat} is the nominal saturation current of the diode and the saturation current (A); Boltzmann constant (J·K^{-1}) is represented by k; the elementary charge of an electron (C) is represented by q; K_O is a constant depending on the PV characteristic; T and T_N are the operating and the nominal temperature (K) of the PV; E_g is the bandgap energy of the semiconductor (eV); a is the diode ideal constant; R_{sh} and R_s are the shunt resistance and series resistance (Ω), respectively; and G and G_n are the irradiation and the nominal irradiation (W / m2) on the device surface, respectively.
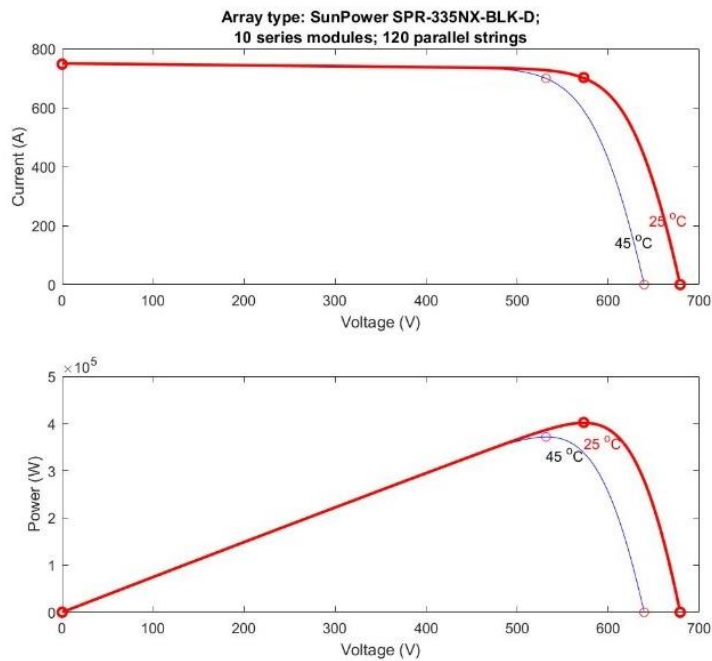
Figure 3.3. P-V and I-V curve of the PV power plant

An MPPT strategy is necessary to benefit from the maximum solar radiance received by the PV modules. In the proposed configuration, the perturb and observe

(P&O) algorithm was used, where the value of the maximum voltage is continuously tracked [186]. The MPPT algorithm provides the reference voltage at the output of the PV panels ($V_{in\_pv}*$), which is then compared with the voltage measured at the panels in the active power control loop. Figure 3.3 illustrates the P-V and I-V curves of the PV power plant simulated.

3.1.2 DC/DC ZSC

For the control of the PV plant, the DC/DC ZSC proposed in [159] was used. This converter is based on a ZSC, which consists of inserting a set of components, such as capacitors, inductors and switching, between the source and the load. In the application of this thesis, this converter is used as a boost to raise the voltage level between the PV power plant to connect it to capacitor C_1 of the impedance network of the qZSI. Figure 3.4 illustrates this converter as well as the working mode. It consists of 5 steps (S_{1U}, S_{2U}, S_{3U}, S_{4U} and S_{5U}).
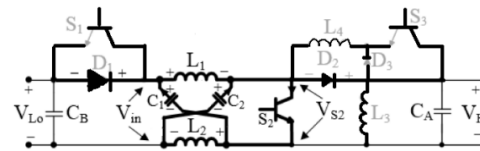
(a)
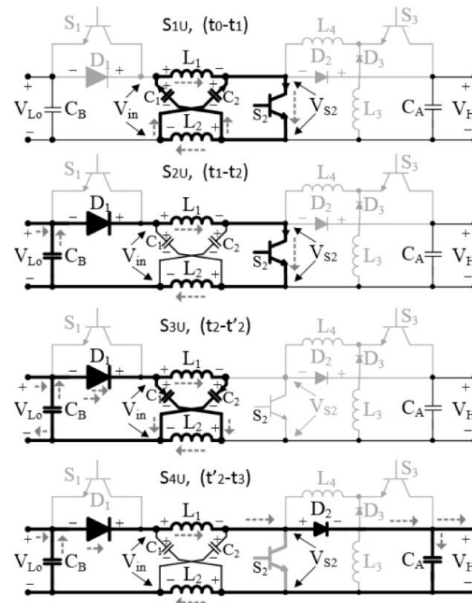
(b)

Figure 3.4. (a) DC/DC ZSC, (b) Steps of operation and current-flow paths of DC/DC ZSC [159].

The inductances and capacitances, respectively, meet $L_1 = L_2 = L$, $C_1 = C_2 = C$. The values can be calculated according to [159]. The switching technique of this circuit is very simple and only has a switching device S_2. In this thesis, the averaged model of this converter was used, which will be detailed in Section 4.1.9.

3.1.3 Wind Turbine

Figure 3.1 illustrates the overall configuration of the PMSG-based WT with qZSI under study. It uses a full-scale power converter, which is composed of a 3-phase uncontrolled bridge rectifier and qZSI. The use of an uncontrolled rectifier is an economical solution, but it has the main drawback of a great dependence of the DC bus voltage on the wind speed [22]. Hence, the uncontrolled rectifier usually requires a two-stage power converter based on DC/DC boost converter and B2B-VSI to control, not only the power flow between the WT and the grid but also the DC bus voltage. In this work, this two-stage power converter is replaced by a qZSI, which is composed of an impedance network and a 3-phase VSI. The switching control of the VSI allows regulating the active power generated by the WT, the reactive power exchanged with the grid and the DC bus voltage. A 1.5 MW PMSG WT is considered in this work. Table 1 shows the main parameters of the WT.

The WT rotor is modelled by the quasi-static model defined through the actuator disk theory, and the drive train is represented by the two-mass model, as usual in fundamental frequency simulations [187]. Equations (3.4) – (3.10) refers to the WT and PMSG model. The rotor model defines the mechanical power by Equation (3.4). The tip speed ratio is the ratio between blade tip linear speed and the wind speed is defined in Equation (3.5). The power coefficient C_p is given in Equation (3.6) and λ_i is given by Equation (3.7).

The generator of PMSG is modelled, assuming that the flux distribution in the stator is sinusoidal, by its third-order model, which is defined by the following equations in the synchronous dq reference frame [188].

$$Pm = c_p(\lambda, \beta) \frac{\rho \pi r^2}{2} v^3_{wind} \tag{3.4}$$

$$\lambda = \frac{\omega_t \cdot r}{v_{wind}} \tag{3.5}$$

$$C_p(\lambda, \beta) = 0.5176 \cdot (\frac{116}{\lambda_i} - 0.4 \cdot \beta - 5) \cdot e^{-\frac{21}{\lambda_i}} + 0.0068 \cdot \lambda \tag{3.6}$$

$$\frac{1}{\lambda_i} = \frac{1}{\lambda + 0.08 \cdot \beta} - \frac{0.035}{\beta^3 - 1} \tag{3.7}$$

$$u_{ds} = R_s i_{ds} + L_{ds} \frac{di_{ds}}{d_t} - \omega_e L_{qs} i_{qs} \tag{3.8}$$

$$u_{qs} = R_s i_{qs} + L_{qs} \frac{di_{qs}}{d_t} + \omega_e \left(L_{ds} i_{ds} + \psi_{pm} \right) \tag{3.9}$$

$$T_e = \frac{3}{2} p \left(L_{ds} - L_{qs} \right) i_{ds} i_{qs} + \psi_{pm} i_{qs} \tag{3.10}$$

where u and i denote voltage and current, respectively; indexes d and q are the direct and quadrature components, respectively; index s refers to the stator; R_s and L_s are the stator resistance and inductance, respectively; ω_e is the electrical speed; ψ_{pm} refers to permanent magnetic flux; T_e is the electromagnetic torque; and p is the number of pole pairs of the generator. Each element of the rectifier is modelled by an ideal diode with an RC snubber circuit connected in parallel, and a small resistance in series.

3.1.4 Energy-stored qZSI (qZSI integrating a BES)

The typical qZSI configuration is presented in Figure 3.5a. It consists of a three-level VSI and an impedance network composed of two capacitors (C_1, C_2) and two inductors (L_1, L_2). These components are sized to limit the switching frequency of current and voltage [189]. For the proposed system under study, a qZSI with BES connected in parallel to the capacitor C_2 was considered, as can be seen in Figure 3.6. The output of the qZSI with BES, as well as qZSI without a BES can be connected to a traditional VSI. In general, for this type of DC/AC conversion stage, a boost stage is needed to achieve an adequate DC voltage level before connecting to a VSI, being that the shoot-through state is a characteristic of the qZSI and not allowed in the VSI. During a switching cycle T, the qZSI works at one of the two possible operating states, namely shoot-through-state (STS) and non-shoot-through states (NSTS), as shown in Figure 3.5b and Figure 3.5c, respectively. In the NSTS, the qZSI operates like a traditional VSI, having six active states and two zero states. Hence, from the DC side,

the VSI is seen as a current source. On the other hand, in STS, the VSI is a short-circuit, with both switches of a leg closed simultaneously.

(a)

(b)   (c)
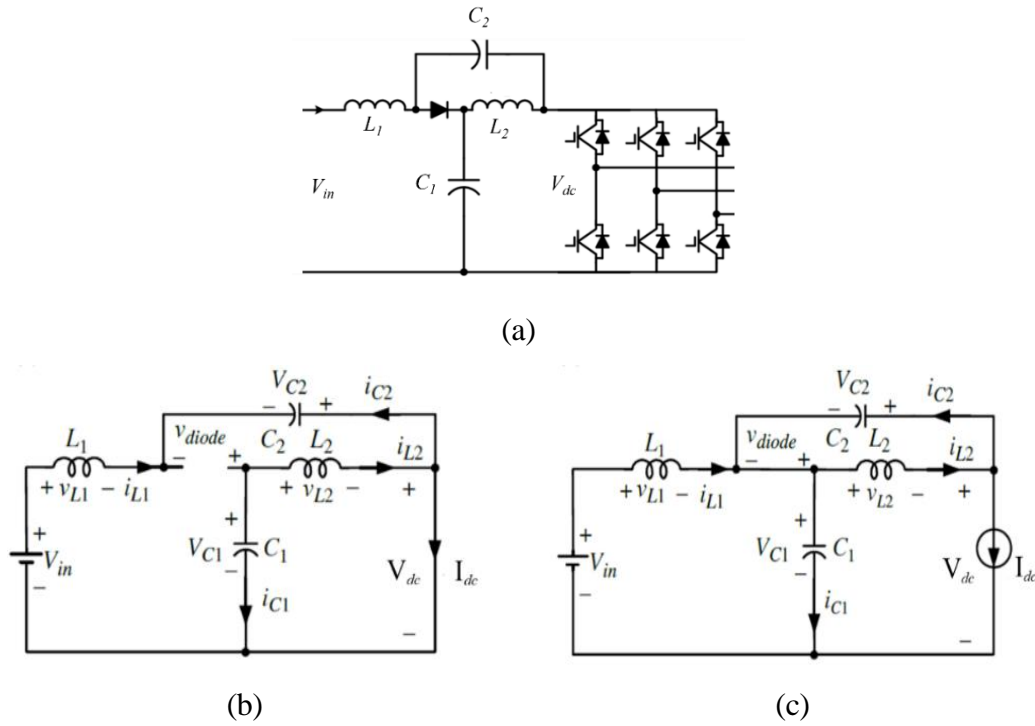
Figure 3.5. (a) General structure of a qZSI converter, (b) shoot-through state (STS); and (c) non-shoot-through state (NSTS) of the qZSI

Figure 3.6a and Figure 3.6b illustrate the aforementioned topology of the qZSI with the BES in the STS and non-shoot through states, respectively. During a switching cycle T, the qZSI works in one of the two possible operating states, namely STS (Figure 3.6a) and NSTS (Figure 3.6b). Considering the shoot-through interval as T_{sh}, and the non-shoot-through T_{nsh}, then $T = T_{nsh} + T_{sh}$, being the shoot-through duty ratio $D = T_{sh}/T$.

(a)   (b)
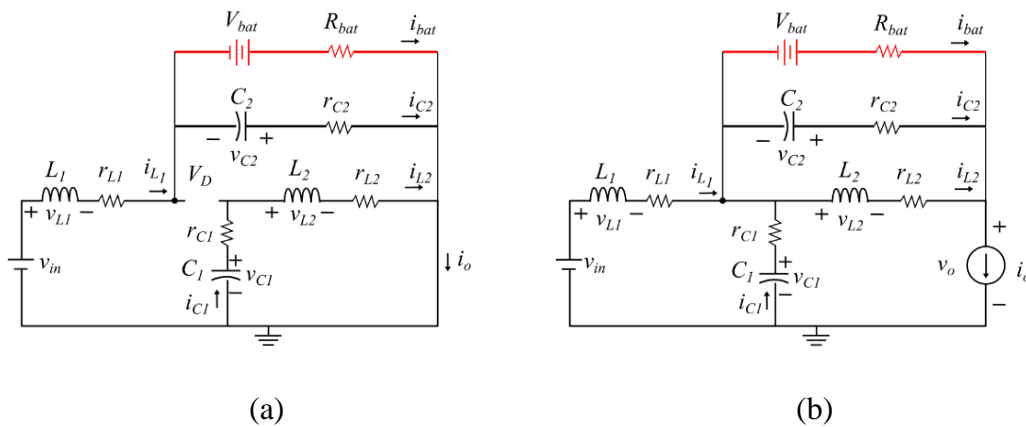
Figure 3.6. qZSI with BES in the STS (a) and NSTS (b)

Average steady‑state model

Average steady-state and dynamic small-signal models can be applied for the study of converters. The average steady-state model can be obtained from the evaluation of the STS and NSTS illustrated in Figure 3.6.

The relation between the currents in STS shown in Figure 3.6a is given by:

$$i_{C1} = -i_{L2}; \; i_{C2} = i_{bat} - i_{L1} \tag{3.11}$$

while that the voltage in the components can be solved following the equations below:

$$V_{L1} = v_{in} - i_{L1}r_{L1} - i_{L1}r_{C2} + v_{C2} \tag{3.12}$$

$$V_{L2} = -i_{L2}r_{C1} + v_{C1} - i_{L2}r_{L2} \tag{3.13}$$

Assuming that $L_1 = L_2 = L$, $C_1 = C_2 = C$, $r_{L1} = r_{L2} = r_L$ and $r_{C1} = r_{C2} = r_C$, and that the voltage across the capacitor is clamped by the BES terminal voltage, it can be obtained:

$$v_{C2} = V_{bat} - R_{bat}i_{bat} \tag{3.14}$$

$$\dot{v}_{C2} = -R_{bat}i_{bat} \tag{3.15}$$

where V_{bat} is the battery voltage, i_{bat} is the battery current and R_{bat} is the battery resistance. The state equations for STS are given by:

$$\frac{di_{L1}(t)}{dt} = -\frac{r_L}{L}i_{L1} - \frac{1}{L}i_{bat}R_{bat} + \frac{1}{L}v_{in} + \frac{1}{L}V_{bat} \tag{3.16}$$

$$\frac{di_{L2}(t)}{dt} = -\frac{r_L}{L}i_{L2} + \frac{1}{L}v_{C1} \tag{3.17}$$

$$\frac{dv_{C1}(t)}{dt} = -\frac{1}{C}i_{L2} \tag{3.18}$$

$$\frac{di_{bat}(t)}{dt} = \frac{1}{R_{bat}C}i_{L1} - \frac{1}{R_{bat}C}i_{bat} \tag{3.19}$$

The relation between the currents in the NSTS shown in Figure 3.6b is given as follows:

$$i_{C1} = i_{L1} - i_o; \; i_{C2}(t) = i_{L2} - i_o + i_{bat} \tag{3.20}$$

The voltage across the inductors can be calculated as:

$$V_{L1} = v_{in} - i_{L1}r_L - i_{L1}r_C + i_o r_C - v_{C1} \tag{3.21}$$

$$V_{L2} = -i_{C1}r_C - i_{L2}r_L - v_{C2} \tag{3.22}$$

The state equations for NSTS are given by:

$$\frac{di_{L1}(t)}{dt} = -\frac{r_L}{L}i_{L1} - \frac{1}{L}v_{C1} + \frac{1}{L}v_{in} \tag{3.23}$$

$$\frac{di_{L2}(t)}{dt} = -\frac{r_L}{L}i_{L2} + \frac{1}{L}i_{bat}R_{bat} - \frac{1}{L}V_{bat} \tag{3.24}$$

$$\frac{dv_{C1}(t)}{dt} = \frac{1}{C}i_{L1} - \frac{1}{C}i_o \tag{3.25}$$

$$\frac{di_{bat}(t)}{dt} = -\frac{1}{R_{bat}C}i_{L2} + \frac{1}{R_{bat}C}i_o - \frac{1}{R_{bat}C}i_{bat} \tag{3.26}$$

Reorganizing in space-state $\dot{x} = Ax + Bu$ and assuming $A = A_1D + A_2(1-D)$ and $B = B_1D + B_2(1-D)$, the following space-state model for STS is obtained:

$$
\begin{bmatrix} \dot{i}_{L1} \\ \dot{i}_{L2} \\ \dot{v}_{C1} \\ \dot{i}_{bat} \end{bmatrix} =
\begin{bmatrix} -\dfrac{r_L D}{L} & 0 & 0 & -\dfrac{DR_{bat}}{L} \\ 0 & -\dfrac{r_L D}{L} & \dfrac{D}{L} & 0 \\ 0 & -\dfrac{D}{C} & 0 & 0 \\ \dfrac{D}{R_{bat}C} & 0 & 0 & -\dfrac{D}{R_{bat}C} \end{bmatrix}
\begin{bmatrix} i_{L1} \\ i_{L2} \\ v_{C1} \\ i_{bat} \end{bmatrix} +
\begin{bmatrix} \dfrac{D}{L} & 0 & \dfrac{D}{L} \\ 0 & 0 & 0 \\ 0 & 0 & 0 \\ 0 & 0 & \dfrac{D}{C} \end{bmatrix}
\begin{bmatrix} v_{in} \\ i_o \\ V_{bat} \end{bmatrix} \tag{3.27}
$$

The space-state model for NSTS is expressed as follows:

$$
\begin{bmatrix} \dot{i}_{L1} \\ \dot{i}_{L2} \\ \dot{v}_{C1} \\ \dot{i}_{bat} \end{bmatrix} =
\begin{bmatrix} -\dfrac{r_L(1-D)}{L} & 0 & -\dfrac{(1-D)}{L} & 0 \\ 0 & -\dfrac{r_L(1-D)}{L} & 0 & \dfrac{(1-D)R_{bat}}{L} \\ \dfrac{(1-D)}{C} & 0 & 0 & 0 \\ 0 & -\dfrac{(1-D)}{R_{bat}C} & 0 & -\dfrac{(1-D)}{R_{bat}C} \end{bmatrix}
\begin{bmatrix} i_{L1} \\ i_{L2} \\ v_{C1} \\ i_{bat} \end{bmatrix} +
\begin{bmatrix} \dfrac{(1-D)}{L} & 0 & 0 \\ 0 & 0 & -\dfrac{(1-D)}{L} \\ 0 & -\dfrac{(1-D)}{C} & 0 \\ 0 & \dfrac{(1-D)}{R_{bat}C} & 0 \end{bmatrix}
\begin{bmatrix} v_{in} \\ i_o \\ V_{bat} \end{bmatrix} \tag{3.28}
$$

Finally, the steady-state model for NSTS is represented as follows:

$$0 = \begin{bmatrix} -\dfrac{r_L}{L} & 0 & \dfrac{(D-1)}{L} & -\dfrac{DR_{bat}}{L} \\[2mm] 0 & -\dfrac{r_L}{L} & 0 & \dfrac{(1-D)R_{bat}}{L} \\[2mm] \dfrac{(1-D)}{C} & -\dfrac{D}{C} & 0 & 0 \\[2mm] \dfrac{D}{R_{bat}C} & \dfrac{(D-1)}{R_{bat}C} & 0 & -\dfrac{1}{R_{bat}C} \end{bmatrix} \begin{bmatrix} I_{L1} \\ I_{L2} \\ V_{C1} \\ I_{bat} \end{bmatrix} + \begin{bmatrix} \dfrac{1}{L} & 0 & \dfrac{D}{L} \\[2mm] 0 & 0 & \dfrac{1-D}{L} \\[2mm] 0 & \dfrac{(D-1)}{C} & 0 \\[2mm] 0 & \dfrac{(1-D)}{R_{bat}C} & 0 \end{bmatrix} \begin{bmatrix} V_{in} \\ I_o \\ V_{bat} \end{bmatrix} \qquad (3.29)$$

Thus,

$$\begin{cases} 0 = -r_L I_{L1} + (D-1)V_{C1} - DR_{bat}I_{bat} + V_{in} + V_{bat} \\ 0 = -r_L I_{L2} + (1-D)R_{bat}I_{bat} + (1-D)V_{bat} \\ 0 = (1-D)I_{L1} - DI_{L2} + (D-1)I_o \\ 0 = DI_{L1} + (D-1)I_{L2} - I_{bat} \end{cases} \qquad (3.30)$$

Through Equations (3.30) can be obtained:

$$\begin{cases} V_{C1} = \dfrac{(1-D)}{(1-2D)}V_{in} + \dfrac{-r_L(1-D)I_o + r_L DI_{bat}}{(1-2D)} \\[4mm] V_b = V_{C2} = \dfrac{D}{(1-2D)}V_{in} + \dfrac{-r_L(1-D)I_o + r_L DI_{bat}}{(1-2D)} \end{cases} \qquad (3.31)$$

$$\begin{cases} I_{bat} = I_{L1} - I_{L2} \\[2mm] I_o = \dfrac{(1-2D)I_{L1} + DI_{bat}}{1-D} \\[3mm] I_{bat} = \dfrac{V_b + V_{bat}}{R_{bat}} \end{cases} \qquad (3.32)$$

where V_b, V_{C1}, V_{C2} are the steady-state average voltage across the BES, and capacitors C_1 and C_2 respectively; V_{in} is the voltage input to the Qzsi; I_{bat}, I_{L1} and I_{L2} are the average currents of the BES and the inductors L_1 and L_2, respectively.

Finally, the output voltage of the impedance network V_{dc} can be expressed as follows:

$$V_{dc} = \frac{1}{1-2D} V_{in} \tag{3.33}$$

Small signals model

For the study of small signals, a small disturbance is inserted around an operating point. For the state variables, for input variables $\hat{u} = \begin{bmatrix} \hat{v}_{in} & \hat{i}_o & \hat{V}_{bat} \end{bmatrix}^T$ and the control term $\hat{d}$ [29], replacing:

$$(\dot{X} + \dot{\hat{x}}) = \left[A_1 d + A_2 (1-d) \right] (X + \hat{x}) + \left[B_1 d + B_2 (1-d) \right] (U + \hat{u}) \tag{3.34}$$

$$\dot{X} + \dot{\hat{x}} = \left[A_1 \left(D + \hat{d} \right) + A_2 \left(1 - D + \hat{d} \right) \right] (X + \hat{x}) + \left[B_1 \left(D + \hat{d} \right) + B_2 \left(1 - D + \hat{d} \right) \right] (U + \hat{u}) \tag{3.35}$$

$$\dot{\hat{x}} = A\hat{x} + B\hat{u} + \left[\left(A_1 - A_2 \right) X + \left(B_1 - B_2 \right) U \right] \hat{d} \tag{3.36}$$

$$\dot{\hat{x}} = \begin{bmatrix} -\dfrac{r_L}{L} & 0 & \dfrac{(D-1)}{L} & -\dfrac{DR_{bat}}{L} \\ 0 & -\dfrac{r_L}{L} & 0 & \dfrac{(1-D)R_{bat}}{L} \\ \dfrac{(1-D)}{C} & -\dfrac{D}{C} & 0 & 0 \\ \dfrac{D}{R_{bat}C} & \dfrac{(D-1)}{R_{bat}C} & 0 & -\dfrac{1}{R_{bat}C} \end{bmatrix} \begin{bmatrix} \hat{i}_{L1} \\ \hat{i}_{L2} \\ \hat{v}_{C1} \\ \hat{i}_{bat} \end{bmatrix} + \begin{bmatrix} \dfrac{1}{L} & 0 & \dfrac{D}{L} \\ 0 & 0 & \dfrac{1-D}{L} \\ 0 & \dfrac{(D-1)}{C} & 0 \\ 0 & \dfrac{(1-D)}{R_{bat}C} & 0 \end{bmatrix} \begin{bmatrix} \hat{v}_{in} \\ \hat{i}_o \\ \hat{V}_{bat} \end{bmatrix} + \begin{bmatrix} V_{C1} - R_{bat}I_{bat} + V_{bat} \\ V_{C1} - R_{bat}I_{bat} + V_{bat} \\ I_o - 2I_{L1} + I_{bat} \\ I_o - 2I_{L1} + I_{bat} \end{bmatrix} \hat{d} \tag{3.37}$$

$$\begin{cases} (sL + r_L)\hat{i}_{L1} = (D-1)\hat{v}_{C1}(s) - DR_{bat}\hat{i}_{bat}(s) + \hat{v}_{in}(s) + D\hat{v}_{bat}(s) + (V_{C1} - R_{bat}I_{bat} + V_{bat})\hat{d}(s) \\ Cs\hat{v}_{C1} = (1-2D)\hat{i}_{L1}(s) + D\hat{i}_{bat}(s) + (1-D)\hat{i}_o(s) + (I_o - 2I_{L1} + I_{bat})\hat{d}(s) \\ (R_{bat}Cs + D)\hat{i}_{bat} = (2D-1)\hat{i}_{L1}(s) + (1-D)\hat{i}_o(s) + (I_o - 2I_{L1} + I_{bat})\hat{d}(s) \end{cases} \tag{3.38}$$

The minimum values of the components of the impedance network (L_1, L_2, C_1 and C_2) are calculated according to [29]. Thus, the value of the inductors is obtained as follows:

$$L = L_1 = L_2 = \frac{1}{2} \cdot T_{0max} \cdot \frac{M_{min}v_{in}}{r_i I_{in}} \tag{3.39}$$

where r_i is the current ripple (20%); T_{omax} represents the maximum value of the shoot-through period; M_{min} is the minimum value of the modulation index (M); and V_{in} and I_{in} are the input voltage and current to the impedance network of the qZSI, respectively. The capacitors are calculated by the following expression:

$$C = C_1 = C_2 = \frac{2T_{0\max}I_{in}(1-2D_{\max})}{r_v v_{in}} \qquad (3.40)$$

where r_v is the voltage ripple (1%); D_{max} is the maximum value of the shoot-through duty ratio (D); and V_{in} is the DC voltage at the input of the impedance network.

3.1.5 Battery

The application of energy storage on systems that have intermittent sources reduces their disadvantages. Several ESS are discussed in [190]. The BES considered in this thesis is a Lithium-ion BES. The Lithium-ion BES has a good life-cycle, high efficiency, deep discharge depth and fast charging [191], and due to these advantages, it was applied in this work. The BES model is composed of a variable voltage source and a resistance connected in series according to the model available in Simulink [192]. This model has been adapted to properly represent the V-I and V-SOC curves and dynamic response of the device, according to the information provided in the datasheets. The BES output voltage can be obtained through Equation (3.41).

$$U_{bat} = E_b - I_b \cdot R_{int} \qquad (3.41)$$

where E_b is the open-circuit voltage of the battery (V), which depends on if the battery is charging or discharging; R_{int} is the internal resistance (Ω); and I_b is the battery current (A). The SOC is an important parameter of the BES, which has to be controlled to avoid a great discharge and an overcharge. It is calculated as follows.

$$SOC = SOC_o + \frac{1}{C_{nom}} + \int I_{bat} dt \qquad (3.42)$$

where SOC_o is the initial state of charge; C_{nom} is the battery nominal capacity (Ah) given by the manufacturer; and I_b is the battery current (A).

A lithium-ion BES with a capacity of 78 Ah and a nominal voltage of 48 Vdc was. The battery cells were associated in series to reach the adequate output voltage of 240 V for the connection to the capacitor C_2 and connected in parallel to provide a nominal capacity of 2220 Ah. The discharge curves characteristics of the BES can be seen in Figure 3.7.
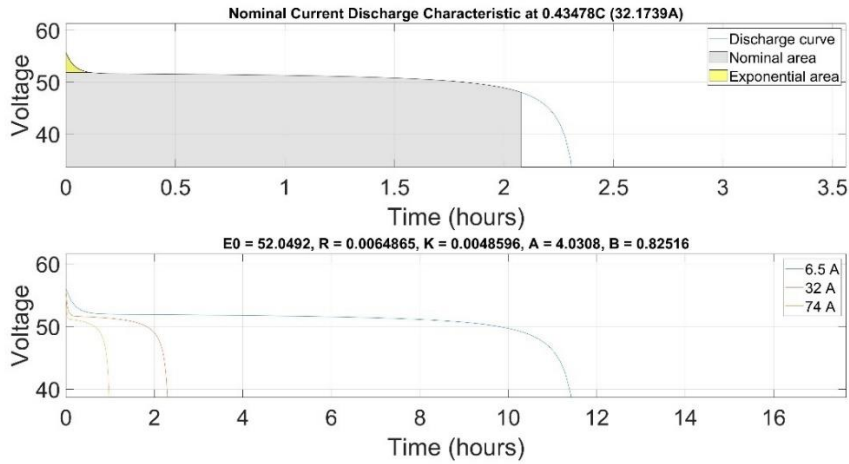
Figure 3.7 - The discharge curves characteristics

3.1.6 LCL Filter

An LCL filter is considered at the qZSI output because it provides high harmonic attenuation and it is suitable for large-scale renewable energy applications [181]. Proper sizing of the inductors and capacitors of the filter requires to consider the following criteria: 1) the inductor reactance X_{L1} must be lower than 10% of the base impedance to limit the voltage drop; 2) the capacitance C_f is limited to absorb less than 5% of the rated reactive power converter; and 3) to avoid resonance problems, the resonant frequency must remain between ten times the grid frequency and half of the switching frequency [181]. To size the LCL filter, the base impedance Z_b and capacitance C_b are determined first.

$$Z_b = \frac{V_0^2}{P_0} \tag{3.43}$$

$$C_b = \frac{1}{Z_b \omega_n} \tag{3.44}$$

where ω_n is the grid angular frequency. To calculate the inductor on the converter side L_{1f}, a maximum percentage of the allowable current ripple ΔI_{L1} (%) must be defined. With the inverter power (P_0) and the nominal line voltage (V_0), the maximum tolerable current ripple ΔI_{L1} (I_{max} - I_{min}.) is given by Equation (3.45)

$$\Delta I_{L1f} = \Delta I_{L1f}(\%) \cdot \sqrt{2} \cdot \left(\frac{P_0}{3 \cdot \frac{V_0}{\sqrt{3}}} \right) \tag{3.45}$$

The minimum value of the inductor L_{1f} can be obtained through Equation (3.46) [193].

$$L_{1f} = \frac{V_0}{2 \cdot \sqrt{6} \cdot f_s \cdot \Delta I_{L1f}}$$ (3.46)

where f_s is the frequency of the first harmonic of the converter output voltage and I_{L1f} is the maximum tolerable current ripple. The percentage of the impedance X_{L1f} in relation to Z_b and the resonant frequency can be obtained through Equation (3.47) and Equation (3.48), respectively:

$$\% X_{L1f} = \frac{2 \cdot \pi \cdot f_r \cdot L_{1f}}{Z_b}$$ (3.47)

$$f_{res} = \frac{1}{2\pi} \sqrt{\frac{L_{1f} + L_{2f}}{L_{1f} L_{2f} C_f}}$$ (3.48)

The minimum value of the filter capacitor (C_f) is calculated considering the reactive power absorbed by the filter in rated conditions [181].

$$C_f = X_f \cdot C_b$$ (3.49)

where X_f is a percentage of the absorbed reactive power (5%); and C_b is the base capacitance.The minimum value of the inductor L_{2f} can be determined as a function of L_{1f} [181].

$$L_{2f} = r \cdot L_{1f}$$ (3.50)

where r represents the ratio between both inductances. The parameter r is obtained through Equation (3.51).

$$\frac{I_{2(h)}}{I_{1(h)}} = \frac{1}{|1 + r(1 - C_b L_{1f} \omega_s^2 X_f)|}$$ (3.51)

If the resonant frequency is not satisfied, a damping resistance R_d can be added [194]. The value of this resistance can be calculated through Equation (3.52):

$$R_d = \frac{1}{6\pi f_{res} C_f}$$ (3.52)

Chapter 4: Control systems

The control system uses a Z-Space-Vector Modulation (ZSVM) as a modulation method to generate the gating signals for the inverter bridge switches to control the active and reactive power delivered by the qZSI with battery (qZSI+BES) to the grid. Moreover, the MPPT of the PV panels and WT (MPPT of the WT, pitch angle control and active and reactive power control) are also included in the global control strategy. The control of the duty cycle D_1 of the qZSI varies with the presence or not of BES on capacitor C_2. Furthermore, the control of D_1 is slightly modified in the case of using the averaged dynamic model for the qZSI. The charge and discharge of BES on capacitor C_2, when inserted at this point, is controlled by using D_1 of the qZSI. The PV control is performed by the duty-cycle D_2 of the DC/DC ZSC. Before the complete system was implemented using average dynamic converters, simulations were performed with the switched dynamic model (SDM) of the converter to validate the results and controls obtained from the averaged dynamic models (ADM) of the converters used in this thesis. All these controls are described in this section.

4.1 CONTROL STRATEGY

The control strategy aims to optimize the energy extracted from the hybrid power plant, coordinating all power flows, from the hybrid plant to the grid and loads or from the grid to the hybrid plant, in the case the BES is charged from the grid. The control system uses a ZSVM modulation technique applied to qZSI, described previously. The qZSI control is performed by controlling the shoot-through time (T_{sh}) through D_1, and by the modulation signals m_a, m_b and m_c. These last three terms represent a balanced three-phase signal. The module of these signals represented in the dq reference frame (m_d and m_q) corresponds to the modulation index M.

As observed in Figure 4.3, M is controlled to regulate the active power generated by the hybrid system, and the reactive power injected into the grid. M used in the modulation method is obtained through two control loops based on PI controllers, which are responsible for generating the reference current $I_d{}^*$ and $I_q{}^*$ for the adjacent control loop, called current control loops (control I_d and I_q). This control system allows the decoupled control of the active and reactive powers through I_d and I_q. Thus, the

active and reactive power delivered by the WT with BES and PV to the grid through the qZSI is controlled. Moreover, the MPPT of the WT and the pitch angle control for above-rated wind speeds are considered in the control scheme depicted in Figure 4.9.

The charge and discharge of the BES are controlled through the shoot-through duty-cycle (D_1) of the qZSI. The control of D_1 is performed through a PI controller and applied to the ZSVM6 modulation method so that T_{sh} is calculated, and thus, the modulation method can calculate all the necessary times to switch the converter. The control of the duty-cycle (D_2) used to control the PV power plant is performed through a PI controller and applied to the DC/DC ZSC.

4.1.1 Z-Space-Vector Modulation

The main objective of the modulation techniques is to generate the switching pulses for the converter, providing a minimum harmonic distortion and maximum fundamental component in the output. Several control strategies based on pulse width modulation (PWM) have been used for the control of the duty cycle of converters. Typical modulation techniques applied to the qZSI are the simple boost control (SBC) [156], maximum boost control (MBC) [195], maximum constant boost control (MCBC) [196] and ZSVM. According to the switching pattern, several options appear for the latter, such as ZSVM6, ZSVM4, ZSVM2 and ZSVM1. These ZSVM techniques are described in [134].

The ZSVM technique applied in this thesis is based on ZSVM6 [134]. It has the relevant advantages of low voltage stress in the switches and high voltage gain when compared with other modulation methods. To implement the ZSVM algorithm, an *abc* to *αβ* reference frame transformation is necessary. Thus, eight space vectors are obtained, named U_0 to U_7. U_0 and U_7 are the zero vectors, while U_1 to U_6 are the active vectors.

The ZSVM, compared with the traditional SVM, allows one extra state called shoot-through and zero states. The ZSVM technique has a ratio of Vdc/√3 concerning V_{ref}, thus achieving a higher modulation index of 90.7%. The conventional sinusoidal PWM (SPWM), which includes the SBC, MBC and MCBC algorithms, allows a voltage output maximum magnitude of Vdc/2, achieved with a maximum modulation index of 78.55% [197].

Figure 4.1 shows the six possible sectors generated by the eight space vectors. Considering the $\alpha\beta$ bi-dimensional reference frame, a voltage vector reference V_{ref} is generated resulting from the weighted average application of non-zero vectors, shoot-through and zero states in relation to the switching period T_s. V_{ref} can be calculated by:

$$V_{ref} = V_1 \frac{T_1}{T_s} + V_2 \frac{T_2}{T_s} + V_0 \frac{T_0}{T_s} + V_{sh} \frac{T_{sh}}{T_s} \tag{4.1}$$

where T_1 and T_2 represent the application time of the vector V_1 and V_2 respectively; T_s is the sample time of the ZSVM; and T_{sh} is the shoot-through time ($T_{sh} = D \cdot T_s$). These times can be obtained as follows:

$$T_1 = T_s M \sin\left[\frac{\pi}{3} - \theta + \frac{\pi}{3}(i-1)\right]$$
$$T_2 = T_s M \sin\left[\theta - \frac{\pi}{3}(i-1)\right] \tag{4.2}$$
$$T_s = T_0 + T_1 + T_2 + T_{sh}$$
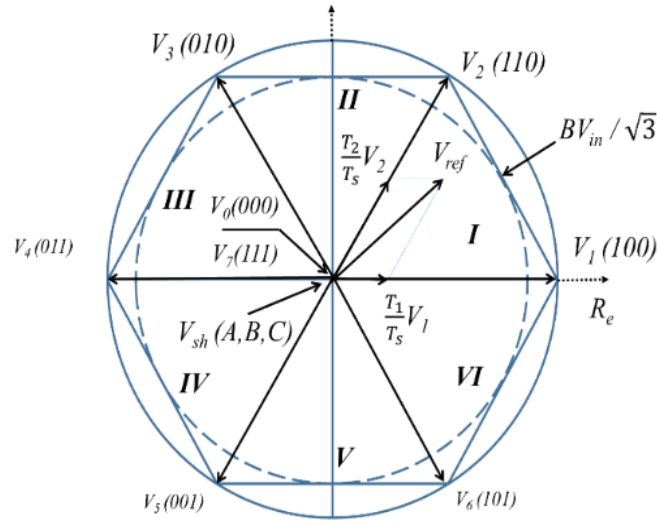
Figure 4.1. Voltage space vectors modulation adapted to ZSVM.

where $M = \sqrt{3} V_{ref} / V_{dc}$, θ is the angle between V_{ref} and V_1, and i represents the sector.
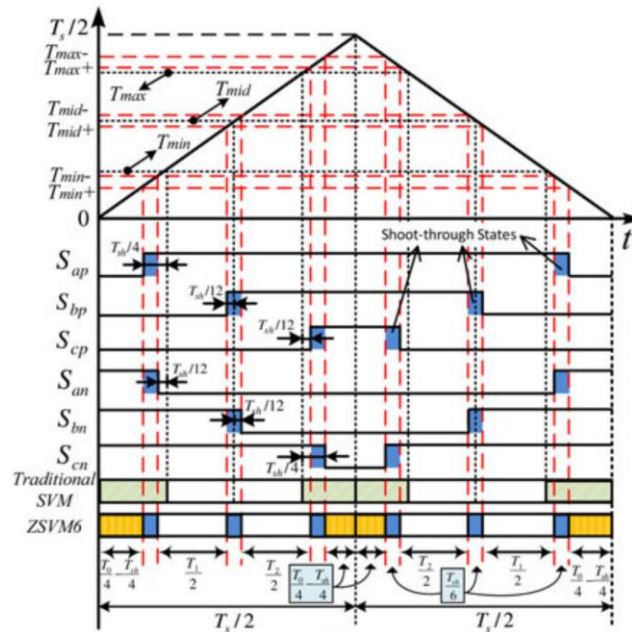
Figure 4.2a shows all switching time sequences, referring to sector 1 modified from traditional SVM for ZSVM6. The switching times for the three bridge legs, T_{max}, T_{mid}, and T_{min} are the maximum, medium, and minimum are described in Equation (4.3).

$$\begin{cases} T_{\min} = \dfrac{T_0}{4} \\[2mm] T_{mid} = \dfrac{T_0}{4} + \dfrac{T_1}{2} \\[2mm] T_{\min} = \dfrac{T_S}{2} - \dfrac{T_0}{4} \end{cases} \qquad (4.3)$$

In the ZSVM, in addition to T_1 and T_2, it is necessary to calculate the intermediate times. These times occur during the shoot-through periods, and, for the ZSVM6 technique implemented herein, the switching times are calculated by [134]:

$$\begin{cases} T_{\max+} = T_{\max} + \dfrac{T_{sh}}{12} \quad \begin{cases} T_{mid+} = T_{mid} - \dfrac{T_{sh}}{12} \\[2mm] T_{\max-} = T_{\max} + \dfrac{T_{sh}}{4} \quad \begin{cases} T_{mid-} = T_{mid} + \dfrac{T_{sh}}{12} \end{cases} \\[2mm] T_{\min+} = T_{\min} - \dfrac{T_{sh}}{4} \\[2mm] T_{\min-} = T_{\min} - \dfrac{T_{sh}}{12} \end{cases} \qquad (4.4)$$

To summarize, the algorithm implemented initially identifies the sectors through the theta angle, all times are calculated, and then the triggers for all sectors with the switching states described in Figure 4.2b are generated. A complete state of the switches applied for switching the converter with STS states for ZSVM6 can be seen in Figure 4.2b.

(a)

= STS

Sector 1

S_1,S_3,S_5	0 0 0	1 0 0	1 0 0	1 1 0	1 1 0	1 1 1	1 1 1
S_2,S_4,S_6	1 1 1	1 1 1	0 1 1	0 1 1	0 0 1	0 0 1	0 0 0
0	T_{min+}	T_{min-}	T_{mid+}	T_{mid-}	T_{max+}	T_{max-}	$T_s/2$

Sector 2

S_1,S_3,S_5	0 0 0	0 1 0	0 1 0	1 1 0	1 1 0	1 1 1	1 1 1
S_2,S_4,S_6	1 1 1	1 1 1	1 0 1	1 0 1	0 0 1	0 0 1	0 0 0
0	T_{min+}	T_{min-}	T_{mid+}	T_{mid-}	T_{max+}	T_{max-}	$T_s/2$

Sector 3

S_1,S_3,S_5	0 0 0	0 1 0	0 1 0	0 1 1	0 1 1	1 1 1	1 1 1
S_2,S_4,S_6	1 1 1	1 1 1	1 0 1	1 0 1	1 0 0	1 0 0	0 0 0
0	T_{min+}	T_{min-}	T_{mid+}	T_{mid-}	T_{max+}	T_{max-}	$T_s/2$

Sector 4

S_1,S_3,S_5	0 0 0	0 0 1	0 0 1	0 1 1	0 1 1	1 1 1	1 1 1
S_2,S_4,S_6	1 1 1	1 1 1	1 1 0	1 1 0	1 0 0	1 0 0	0 0 0
0	T_{min+}	T_{min-}	T_{mid+}	T_{mid-}	T_{max+}	T_{max-}	$T_s/2$

Sector 5

S_1,S_3,S_5	0 0 0	0 0 1	0 0 1	1 0 1	1 0 1	1 1 1	1 1 1
S_2,S_4,S_6	1 1 1	1 1 1	1 1 0	1 1 0	0 1 0	0 1 0	0 0 0
0	T_{min+}	T_{min-}	T_{mid+}	T_{mid-}	T_{max+}	T_{max-}	$T_s/2$

Sector 6

S_1,S_3,S_5	0 0 0	1 0 0	1 0 0	1 0 1	1 0 1	1 1 1	1 1 1
S_2,S_4,S_6	1 1 1	1 1 1	0 1 1	0 1 1	0 1 0	0 1 0	0 0 0
0	T_{min+}	T_{min-}	T_{mid+}	T_{mid-}	T_{max+}	T_{max-}	$T_s/2$

(b)

Figure 4.2. (a) Switching time sequences applied ZSVM6, (b) Complete switch states in the six sectors for ZSVM6.

4.1.2 Switched dynamic model (SDM): Active and reactive power control

As in a VSI, in the proposed control scheme, the qZSI is responsible for controlling the active and reactive power through *M*. For this reason, a *dq* reference frame oriented along the grid voltage is used to decouple active and reactive power control. Two cascaded control loops are used to control these powers [198], as shown in Figure 4.3.

The outer control loops are dedicated to active and reactive power regulation, which can be calculated using Equation (4.5) in the *dq* reference frame. It can be seen

that controlling the d and q components of the grid current ($i_{d,grid}$ and $i_{q,grid}$) is equivalent to controlling P_{grid} and Q_{grid}, respectively, because $u_{d,grid}$ is constant at a stiff grid [29].

$$P_{grid} = \frac{3}{2} u_{d,grid} i_{d,grid}$$

$$Q_{grid} = \frac{3}{2} u_{d,grid} i_{q,grid}$$

(4.5)

The reference values for these currents ($i_{d,grid}$ and $i_{q,grid}$) are generated by the outer control loops through PI controllers, one controlling active power indirectly through V_{in_wind}, and the other one controlling reactive power. The reactive power reference is imposed externally, whereas the active power depends on the power extracted from the system. In this sense, an MPPT controller based on the *perturb & observe* (P&O) algorithm is implemented to define the optimum DC input voltage for the qZSI ($V_{in\_wind}{}^{ref}$) that achieves maximum power generation in the WT.

The inner loops are the current control loops, where two PI controllers regulate $i_{d,grid}$ and $i_{q,grid}$ to follow the reference values provided by the outer control loops. These PI controllers generate the compensation terms (u_d and u_q). With the contribution of the decoupling terms shown in Equation (4.6), independent control of $i_{d,grid}$ and $i_{q,grid}$, and thus, active and reactive power, can be achieved through the d and q components of the modulating signal (namely m_d and m_q) [198].

$$m_d = \frac{\sqrt{3}}{V_{DC}} (u_d - L_f \omega i_{q,grid} + u_{d,grid})$$

$$m_q = \frac{\sqrt{3}}{V_{DC}} (u_q + L_f \omega i_{d,grid} + u_{q,grid})$$

(4.6)

where u_d and u_q are the dq components of the qZSI output voltage; L_f is the inductance from the qZSI output to the grid connection ($L_f = L_{1f} + L_{2f}$); and ω_0 is the electric angular frequency.

Once m_d and m_q are determined, they are transformed into m_a, m_b and m_c (*abc/dq* transformation) to generate the switching pulses of the qZSI according to the ZSVM6

technique. A phase-locked loop (PLL) ensures the tracking of the grid voltage frequency [199]. The magnitude of M can be obtained by m_d and m_q.
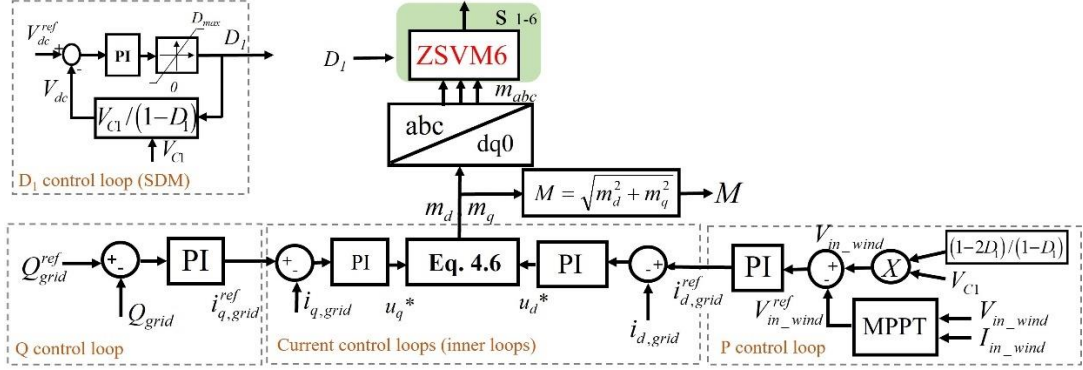

Figure 4.3. Control schemes implemented for the qZSI (active and reactive power)

4.1.3 Shoot-Through Control (D_1)

If there is no BES present in the capacitor C_1 of the impedance network of the qZSI, the shoot-through state control aims to maintain the voltage (V_{dc}) at the output of the impedance network controlled. Figure 4.3 shows the control scheme implemented to control D_1, which is used to maintain V_{dc} around the desired value (1.35 kV). Since measuring V_{dc} is quite difficult and inaccurate in the qZSI, its value is approximated employing the voltage across the C_1 (V_{C1}) as in Equation (4.7). A PI controller is used to obtain D_1 from the error between the reference voltage (V_{dc}^{ref}) and V_{dc}.

$$V_{dc} = \frac{1}{1-D_1} V_{C1} \tag{4.7}$$

The output of the PI controller is limited by the maximum value of D_1 (D_{max}), which is a function of M [200]. Finally, the pitch angle controller of the WT adjusts the blade pitch angle to reduce the power extracted from the wind, and thus limiting the power generated by the WT for above-rated wind speeds.

4.1.4 Averaged dynamic model 1 (ADM1) qZSI: Description and control

In this model, the dynamic response of a qZSI is obtained through the equivalent modelling of two power converters connected in series, one for the impedance network and the other for the VSI, as shown in Figure 4.4a. This ADM adapts the variable DC

input voltage (WT output) to a constant 3-phase AC output voltage. Thus, the voltage boost provided by the impedance network and its behaviour is modelled as a conventional DC converter using a switching-function model directly controlled by D [201]. Figure 4.4b shows the control schemes implemented to control D_1 in ADM1.
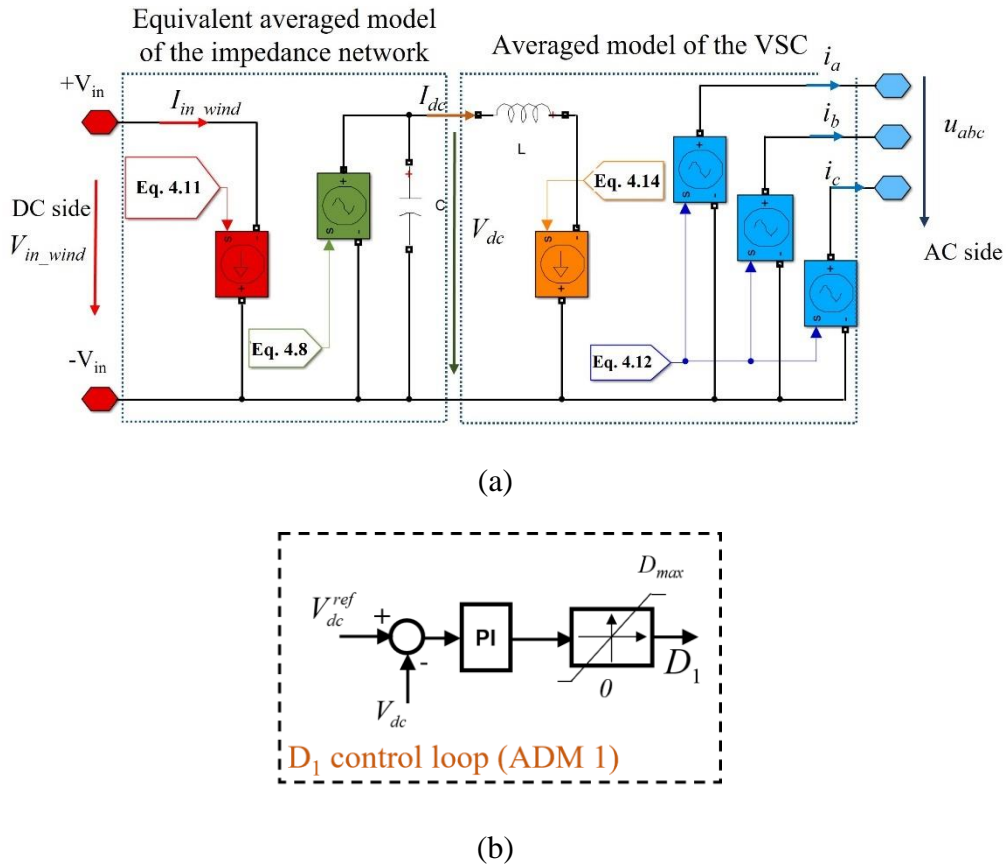

(a)

(b)

Figure 4.4. Proposed averaged dynamic model a) ADM1 and (b) V_{dc} control

On the other hand, the VSI is modelled by the averaged equivalent circuit of a three-level VSI, which is composed of a controlled current source at the DC side and three controlled voltage sources at the AC side. In this case, the value of these sources is governed by M, which is output by the control system.

For the equivalent model of the impedance network, the relation between the input (V_{in_wind}) and output (V_{dc}) voltages, assuming a lossless converter, is given by [202]

$$V_{dc} = \frac{1}{1-2D_1} V_{in\_wind}$$

(4.8)

The boost factor of the qZSI (B), which represents the voltage gain of the equivalent model, is expressed as follows:

$$B = \frac{1}{1 - 2D_1} \tag{4.9}$$

Therefore, V_{dc} can be calculated from:

$$V_{dc} = BV_{in\_wind} \tag{4.10}$$

It can be derived from a power balance in which the input current (I_{in_wind}) is also related to the output current of the impedance network (I_{dc}) through D_1.

$$I_{in\_wind} = \frac{1}{1 - 2D_1} I_{dc} \tag{4.11}$$

In this model, the output voltage of the VSI u_{abc} is calculated through the modulating signal m_{abc}, which is a balanced 3-phase signal.

$$u_a = \frac{1}{\sqrt{3}} \left(V_{dc} m_a \right)$$

$$u_b = \frac{1}{\sqrt{3}} \left(V_{dc} m_b \right) \tag{4.12}$$

$$u_c = \frac{1}{\sqrt{3}} \left(V_{dc} m_c \right)$$

Assuming a lossless VSI, it implies that the input power on the DC side equals the output power on the AC side.

$$V_{dc} I_{dc} = u_a i_a + u_b i_b + u_c i_c \tag{4.13}$$

Merging Equations (4.12) and (4.13), the DC current injected into the VSI can be obtained.

$$I_{dc} = \frac{1}{\sqrt{3}} \left(i_a m_a + i_b m_b + i_c m_c \right) \tag{4.14}$$

The control scheme implemented to generate m_{abc} was the same as that used in the SDM, without the modulation method.

4.1.5 Averaged dynamic model 2 (ADM 2) qZSI: Description and control

In ADM2, the dynamic performance of the qZSI is modelled using the averaged model of a VSI. The scheme is composed of a controlled current source at the DC side and three controlled voltage sources at the AC side, as illustrated in Figure 4.5a.

V_{dc} was not measured, and it was calculated from V_{in_wind} and B (Equation (4.8)). Thus, by substituting V_{dc} into Equation (4.10), a direct relationship between V_{in_wind} and the AC output voltage can be obtained.

$$u_a = \frac{B}{\sqrt{3}}\left(V_{in\_wind}m_a\right)$$

$$u_b = \frac{B}{\sqrt{3}}\left(V_{in\_wind}m_b\right) \tag{4.15}$$

$$u_c = \frac{B}{\sqrt{3}}\left(V_{in\_wind}m_c\right)$$

Moreover, the following equation can be obtained applying the power balance:

$$V_{in\_wind}I_{in\_wind} = u_a i_a + u_b i_b + u_c i_c \tag{4.16}$$

Finally, by substituting Equation (4.15) into Equation (4.16), the value of I_{in_wind} was calculated.

$$I_{in\_wind} = \frac{B}{\sqrt{3}}\left(i_a m_a + i_b m_b + i_c m_c\right) \tag{4.17}$$

Equations (4.15) and (4.17) show that the input controlled current source and the output controlled voltage source depend on B and m_{abc}, respectively.

In this model, the control schemes for m_{abc} and D_1 are the same as those used in ADM1. A PI controller is used to obtain D_1 from the error between V_{dc}^{ref} and V_{dc}, calculated from Equation (4.8). D_1 is also limited by D_{max}. Figure 4.5b illustrates this control scheme for ADM2.
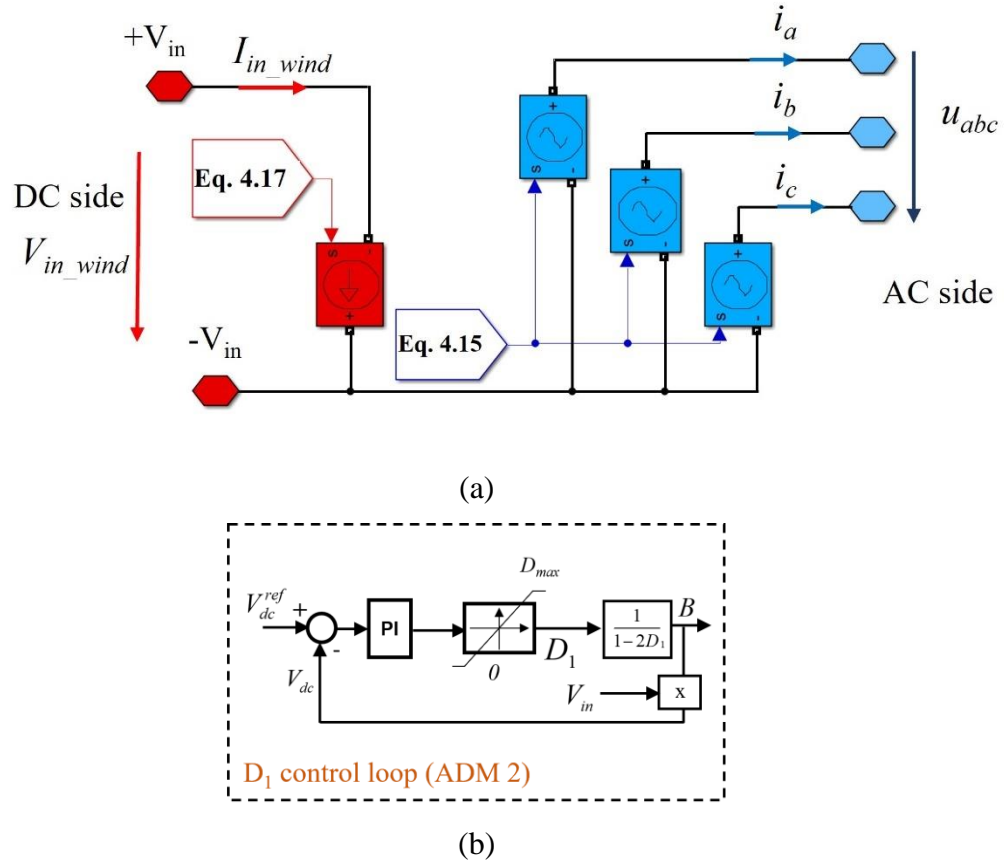
(a)

(b)

Figure 4.5. Proposed averaged dynamic model a) ADM2 and (b) V_{dc} control

4.1.6 STABILITY ANALYSIS OF THE PROPOSED MODELS

The following stability analysis focuses on the DC side of the converter, provided that the AC dynamics rely on the characteristics of the grid connection filter, which is the same for the three models presented. It is well known that the qZSI is an open-loop unstable system with regard to its DC side dynamics [160,203]. Therefore, a feedback control loop is required to regulate V_{dc}.

In this study, a PI controller was implemented in the V_{dc} control loop, as shown in Figure 4.4b and Figure 4.5b. The Bode plot shown in Figure 4.6 illustrates that both SDM and ADM1 are closed-loop stable systems with such configurations, thus proving the stability of the proposed ADM1. Regarding ADM2, the DC side dynamics are modelled simply as a static gain that provides the voltage gain of the impedance network in the SDM of the qZSI. Therefore, no stability analysis is required for ADM2.
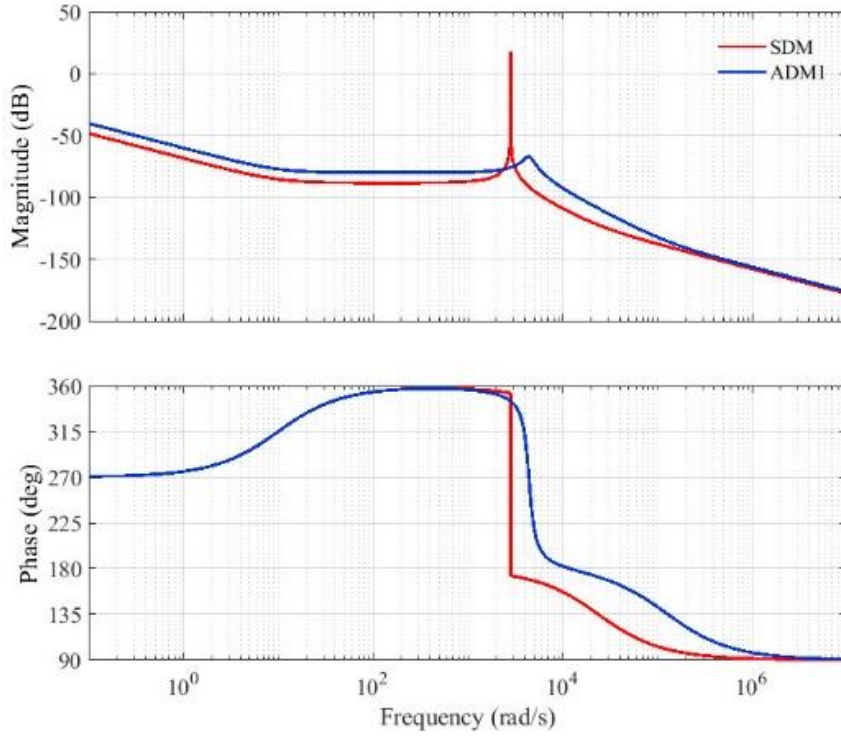
Figure 4.6. Open-loop Bode plot of SDM and ADM1 with the controller.

4.1.7 Averaged dynamic model 2 (ADM2B) qZSI with Battery: Description and control

The proposed ADM2 with battery (ADM2B) is composed of a controlled current source on the DC side, three controlled voltage sources on the grid side and a controlled voltage source that simulates the terminals of the capacitor C_2, where the BES is connected.

Figure 4.7a illustrates a scheme of the ADM2B proposed for the BES-qZSI. As well as the previous model, the ADM 2B of the qZSI replaces the impedance network and the VSI switches with controlled sources governed by the boost factor (B) and the modulation signals $m_a(t)$, $m_b(t)$ and $m_c(t)$. Because the firing pulses of the switches are not considered, the data processing needs are reduced notably (the sample time can be increased), while obtaining a performance similar to the SDM. Thus, the proposed model does not show the current and voltage harmonics but the dynamic performance of the SDM, which results important when it comes to managing the power flow.

Considering ZSVM6 in the qZSI, the following two expressions relate to the different voltages in the qZSI (i.e., V_{in_wind}, V_{dc}, and V_{ac}).

$$V_{dc} = V_{in\_wind} \frac{1}{1-2D} \qquad (4.18)$$

$$u_a = \frac{1}{\sqrt{3}}\left(V_{dc} \cdot m_a\right)$$

$$u_b = \frac{1}{\sqrt{3}}\left(V_{dc} \cdot m_b\right) \qquad (4.19)$$

$$u_c = \frac{1}{\sqrt{3}}\left(V_{dc} \cdot m_c\right)$$

If V_{dc} is replaced in Equation (4.18) using Eq. (4.19), a direct relationship between the AC output voltage of the converter and the input voltage V_{in} appears in Equation (4.20).

$$u_a = \frac{B}{\sqrt{3}}V_{in\_wind} \cdot m_a$$

$$u_b = \frac{B}{\sqrt{3}}V_{in\_wind} \cdot m_b \qquad (4.20)$$

$$u_c = \frac{B}{\sqrt{3}}V_{in\_wind} \cdot m_c$$

Since m_a, m_b and m_c constitute a balanced three-phase signal, so is the aggregation of u_a, u_b and u_c. This can be achieved using the same control loops as in the SDM.

In the DC side of the qZSI (Wind system terminals), the value of the controlled current source is calculated based on the power balance principle derived from the DC system side terminals (V_{in}).

$$P_{grid} = i_a \cdot u_a + i_b \cdot u_b + i_c \cdot u_c$$

$$P_{in} = V_{in\_wind} \cdot I_{in\_wind} \qquad (4.21)$$

$$P_{BES} = V_{C2} \cdot I_{BES} = V_{BES} \cdot I_{BES}$$

Equation (4.21) taken to the wind system side becomes Equation (4.22). Note that V_{ESS} is equivalent to $V_{in\_wind} \cdot B \cdot D$.

$$P_{grid} = \frac{V_{in\_wind}}{\sqrt{3}} \cdot B \cdot \left(i_a \cdot m_a + i_b \cdot m_b + i_c \cdot m_c \right)$$

$$P_{in} = V_{in\_wind} \cdot I_{in}$$

$$P_{BES} = V_{in\_wind} \cdot B \cdot D \cdot I_{BES}$$

(4.22)

Finally, the input current can be calculated through the power balance.

$$I_{in\_wind} = \frac{1}{\sqrt{3}} \cdot B \cdot \left(i_a(t) \cdot m_a(t) + i_b(t) \cdot m_b(t) + i_c(t) \cdot m_c(t) \right) - B \cdot D \cdot I_{BES}$$

$$i_a(t) \cdot m_a(t) + i_b(t) \cdot m_b(t) + i_c(t) \cdot m_c(t) \rightarrow m_{abc}(t) \cdot i_{abc}(t)$$

(4.23)

$$I_{in\_wind} = \frac{1}{\sqrt{3}} \cdot B \cdot m_{abc}(t) \cdot i_{abc}(t) - B \cdot D \cdot I_{BES}$$

(4.24)

where, $i_{abc}(t)$ is the current at the AC side, I_{BES} is the BES current and I_{in_wind} is the current generated by the PV system.

Finally, as commented above, the energy storage is connected to a controlled voltage source that simulates the terminals of the capacitor C_2.

$$V_{BES}^{out} = V_{in\_wind} \cdot D \cdot B$$

(4.25)

The BES power exchange is regulated through D_1 in the BES current (I_{BES}) control loop. To achieve a fast response, D_1 is calculated as the sum of two terms ($D_1 = \Delta D_1 + D_0$). ΔD is the output of the battery current control loop, and D_0 is defined through Equation (4.26), where V_{BES}^{nom} is the nominal voltage of the energy storage system and $V_{in\_wind}^{std}$ is the input voltage of the qZSI at standard conditions of the DC system. Note that D_0 is constant. Therefore, ΔD_1 varies D_1 around D_o to control the power in the energy storage device.
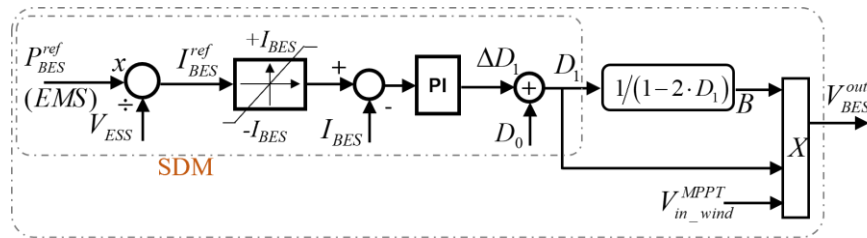
$$D_0 = V_{BES}^{nom} / \left(2 \cdot V_{BES}^{nom} + V_{in\_wind}^{std} \right)$$

(4.26)

The current reference, I_{BES}^{ref}, is limited to the maximum and minimum recommended values. Then, a PI controller generates ΔD_1 to make the BES current track its reference value. This control scheme is depicted in Figure 4.7b.
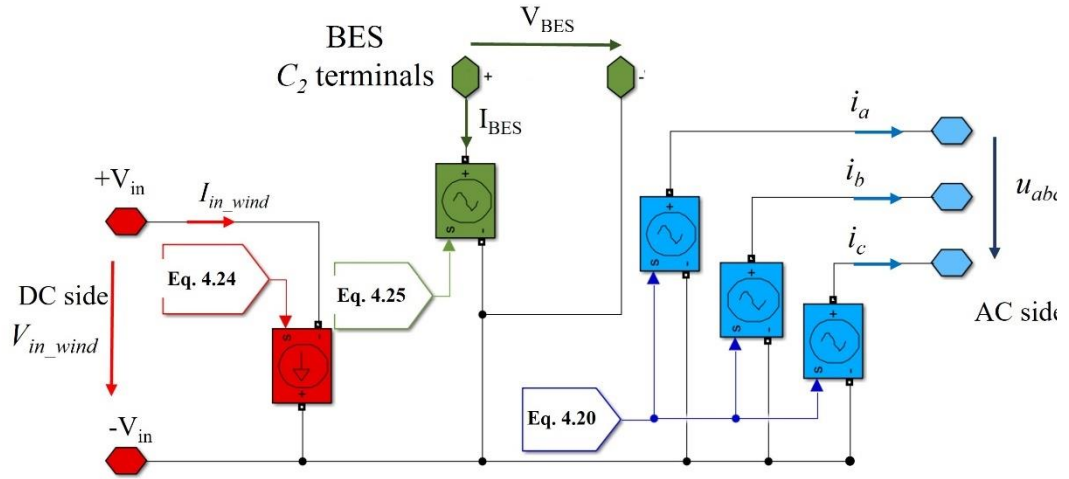
(a)

Averaged dynamic model 2 battery (ADM 2B)

(b)

Figure 4.7. Proposed averaged dynamic model a) ADM2B and (b) V_{dc} control

In this thesis, a controlled voltage source that simulates the terminals of the capacitor C_1 was added to the proposed ADM2B. In this terminal, the PV systems was connected. In a lossless qZSI, the input voltage (V_{in_wind}) and the voltage across the capacitor C_1 (V_{C1}) is related through Equation (4.27), considering the voltage in the capacitor C_1 (V_{C1}) as V_{DC} bus voltage (V_{DC_C1}). Figure 4.8 illustrates a scheme of the ADM2B proposed for the qZSI with the terminals of the capacitor C_1.

$$V_{C1} = V_{DC\_C1} = \frac{1-D_1}{1-2D_1} V_{in\_wind} \tag{4.27}$$

Considering the connection of the PV power plant in parallel to the capacitor C_1, Equation (4.28) must be added to the power balance described in Equation (4.21), because the value of the controlled current source is obtained based on the power balance principle ($P_{grid} = P_{wind} + P_{BES} + P_{DC\_C1}$) calculated in the wind side terminals (V_{in_wind}).

$$P_{DC\_C1} = V_{DC\_C1} I_{DC\_C1}$$

$$P_{DC\_C1} = B \cdot (1 - D_1) V_{in\_wind} \cdot I_{DC\_C1}$$

(4.28)

Finally, if the power balance is carried out, the input current can be calculated.

$$I_{in} = \frac{1}{\sqrt{3}} \cdot B \cdot m_{abc}(t) \cdot i_{abc}(t) - B \cdot D_1 \cdot I_{BES} - B \cdot (1 - D_1) \cdot I_{DC\_C1}$$

(4.29)

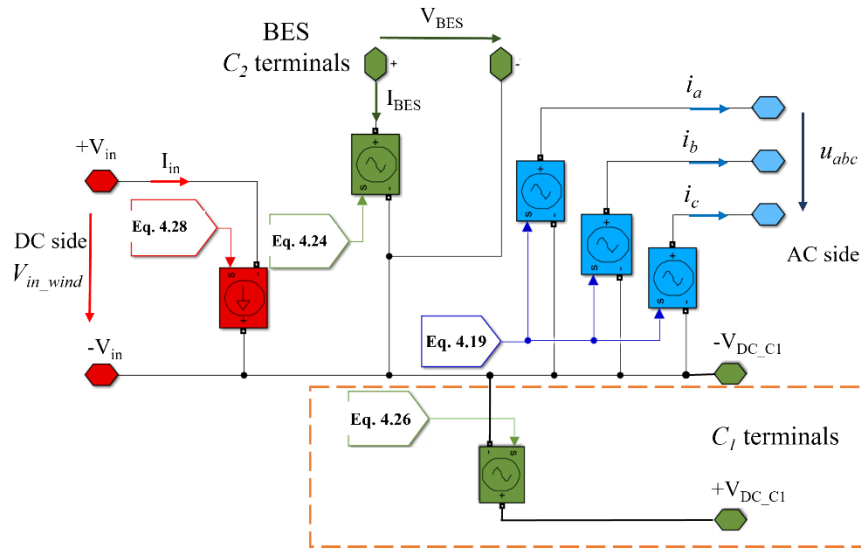Figure 4.8. Complete averaged model of the qZSI

Considering the connection of the PV power plant in parallel to the capacitor C_1, Equation (4.28) must be added to the power balance described in Equation (4.21), because the value of the controlled current source is obtained based on the power balance principle ($P_{grid} = P_{wind} + P_{BES} + P_{DC\_C1}$) calculated in the wind side terminals (V_{in_wind}).

$$P_{DC\_C1} = V_{DC\_C1} I_{DC\_C1}$$

$$P_{DC\_C1} = B \cdot (1 - D_1) V_{in\_wind} \cdot I_{DC\_C1}$$

(4.28)

Finally, if the power balance is carried out, the input current can be calculated.

$$I_{in} = \frac{1}{\sqrt{3}} \cdot B \cdot m_{abc}(t) \cdot i_{abc}(t) - B \cdot D_1 \cdot I_{BES} - B \cdot (1 - D_1) \cdot I_{DC\_C1}$$

(4.29)

4.1.8 Pitch angle control

For below-rated wind speeds, the blade pitch angle of the WT remains at zero to extract the maximum power from the wind. For above-rated wind speeds, the controller adjusts the pitch angle to reduce the power extracted from the wind, ensuring a safe operation of the system. Figure 4.9 shows the PI controller used in the pitch angle control system.
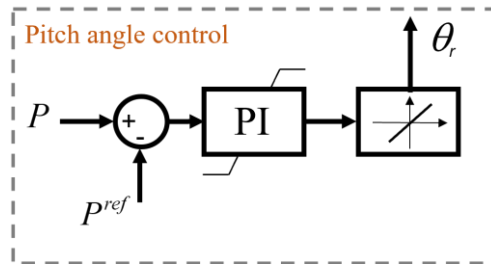

Figure 4.9. Pitch angle control

4.1.9 Averaged model of the DC/DC ZSC

Figure 4.10a illustrates the averaged model of the DC/DC ZSC used to connect the PV power plant to the capacitor C_1. This model consists of a controlled current source in the input and a controlled voltage source at the output, and it is based on the converter designed in [159]. The converter reaches a high boost gain regulated with a duty cycle, making it more suitable and providing good control for power regulation. The voltage gain of this converter is given by Equation (4.30).

$$G = \frac{V_{out,ZSC}}{V_{in,ZSC}} = \frac{24.8 \cdot D_2 - 0.8569 \cdot D_2}{0.0146 \cdot D_2 + 0.3919} \tag{4.30}$$

where $V_{out,ZSC}$ corresponds to V_{DC_C1}; and $V_{in,ZSC}$ is related to the voltage of the PV plant. Finally, considering the power balance in the converter, the relation between the input and output current is obtained as follows.

$$G = \frac{I_{in\_pv^{ZSC}}}{I_{DC\_C1^{ZSC}}} = \frac{V_{DC\_C1^{ZSC}}}{V_{in\_pv^{ZSC}}} \tag{4.31}$$

Considering Equation (4.31), which relates the gain of the converter with the relation between the input and output current and voltage, Equations (4.32) and (4.33) can be obtained. Figure 4.10b shows the PI controller used for the DC/DC ZSC.

$$I_{in\_pv^{ZSC}} = I_{DC\_C1^{ZSC}} G \tag{4.32}$$

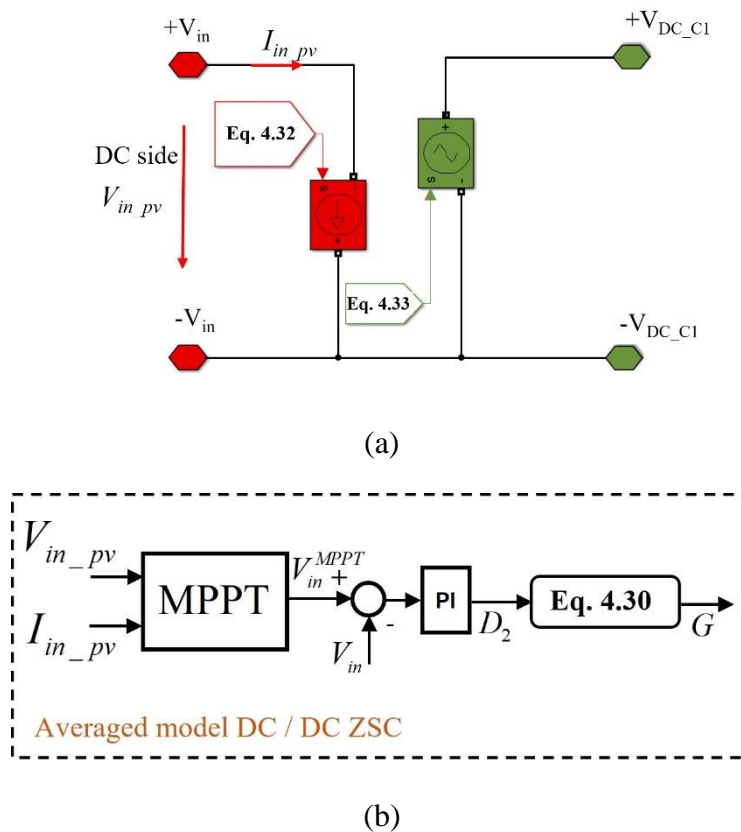$$V_{DC\_C1^{ZSC}} = V_{in\_pv^{ZSC}} G \tag{4.33}$$

(a)

(b)

Figure 4.10. (a) Averaged model of the DC/DC ZSC, (b) Control schemes implemented for the DC/DC ZSC.

Chapter 5: Energy management system

The hybrid power plant requires an energy management system (EMS) that coordinates the performance of all energy sources (WT, PV, and BES) and allows a reliable and controlled response. The main aim and novelty of this section is to describe two different EMSs, denoted as EMS 1 and EMS 2, which will be applied to the hybrid power plant under study.

5.1 ENERGY MANAGEMENT SYSTEM 1

The EMS 1 sets the power reference for the BES, depending on its SOC and the power demanded by the grid through of the system operator (SO), charging or discharging according to the several operating modes described. The BES connected in parallel to the C_2 has a capacity of 74 Ah and a nominal voltage of 48 V. Several battery cells were connected in series/parallel to reach the adequate output voltage of 240 V and a capacity of 2220 Ah.

Three cases of BES discharge were considered. The first one, namely discharge 1 (dis 1), is at a constant current of 40% of the BES capacity (Equation (5.1)). In this situation, the BES can inject a surplus of 215 kW into the grid until achieving a minimum final SOC of 5%, and the SOC is calculated according to Equation (5.2).

$$P_{max}^{dis,1} = \frac{E_{nom}^{bat}}{t}\left(\frac{40}{100}\right)\bigg|_{t=1h} \tag{5.1}$$

$$SOC(\%) = 100\left(1 - \frac{1}{E_{bat}^{nom}}\right)\sum P_{bat}t\bigg|_{t=1h} \tag{5.2}$$

where E_{bat}^{nom} represents the battery nominal capacity in energy terms

The second operational situation (dis 2) depends on the PMSG WT and BES SOC. In this case, the higher the BES SOC and the power generated by the WT, more power will be injected into the grid (Equation (5.3)).

$$P_{\max}^{dis,2} = \left(\frac{SOC - SOC_{\min}}{100} \right) \left(P_{wind} \right) \Big|_{t=1h} \tag{5.3}$$

The third one (dis 3) depends on the BES SOC. In this case, over time as much as the BES discharges, less current will be available to the grid, which means more time will be necessary to discharge the BES completely (Equation (5.4)).

$$P_{\max}^{dis,3} = \frac{E_{nom}^{bat}}{t} \left(\frac{SOC - SOC_{\min}}{100} \right) \left(\frac{50}{100} \right) \Big|_{t=1h} \tag{5.4}$$

The maximum available power of the system is calculated as the sum of the power generated through the PMSG and the maximum instantaneous power available in the battery (Equations (5.5), (5.6) and (5.7)).

$$P_{\max}^{Av,1} = P_{wind} + P_{\max}^{dis,1} \tag{5.5}$$

$$P_{\max}^{Av,2} = P_{wind} + P_{\max}^{dis,2} \tag{5.6}$$

$$P_{\max}^{Av,3} = P_{wind} + P_{\max}^{dis,3} \tag{5.7}$$

where $P_{\max}^{dis,1}$, $P_{\max}^{dis,2}$ and $P_{\max}^{dis,3}$ represent the maximum instantaneous power discharge for modes 1, 2 and 3; $P_{\max}^{Av,1}$ and $P_{\max}^{Av,2}$, $P_{\max}^{Av,3}$ represents the maximum instantaneous power available for three-mode operation.

As an operating restriction, the power required by the SO must be equal to or less than the maximum power available and the minimum power must be the power generated by the PMSG WT minus the maximum BES charge capacity at the requested time. To preserve the lifecycle, the instantaneous power charge of the BES was limited to a maximum of 40 % of BES capacity.

The SOC or the Depth of Discharge (DOD) is an important BES parameter to be controlled by the EMS. Discharging the battery fully, reaching a DOD of 100% is not recommended, as it reduces its useful life. For this reason, the EMS was based on the references defined by the SO, energy generated by the PMSG WT and BES SOC.

Two cases for EMS were defined:

Case 1: The SO has priority if authorized by the operator of the wind farm and since it meets the aforementioned restrictions of maximum and minimum available power. If the SO requests more power than is available, the hybrid power plant will inject the maximum available into the network. If it requests less than what is desirable, the minimum will be injected.

Case 2: If the SO does not request a specific demand, the hybrid power plant operates according to the BES charge status, following the steps below.

If 5% < SOC < 9%, the BES priority is to charge. Therefore, if the power generated by PMSG WT is greater than 60% of its nominal power (0.9 MW), it will charge the BES with 40% of the total energy of the BES (dis 1, mode 1). Otherwise, all the energy generated by the PMSG WT will be injected into the grid (mode 2).

If 9% < SOC < 90%, the BES will be discharged depending on the energy generated by the PMSG WT. If the PMSG WT generates a power greater than 60% of its nominal power, the EMS will discharge the BES using dis 1, mode 3. Otherwise, the BES will be discharged by dis 3, which means more time will be necessary to discharge the BES completely (mode 4).

If SOC > 90%, the BES will be discharged. Therefore, if the power generated by PMSG WT is greater than 60% of its nominal power, the EMS will discharge the BES with 40% of the BES nominal capacity (dis 1, mode 5). If the power generated by the PMSG WT is below 0.9 MW, the EMS will discharge the BES depending on the power generated by the WT and SOC (dis 2, mode 6).
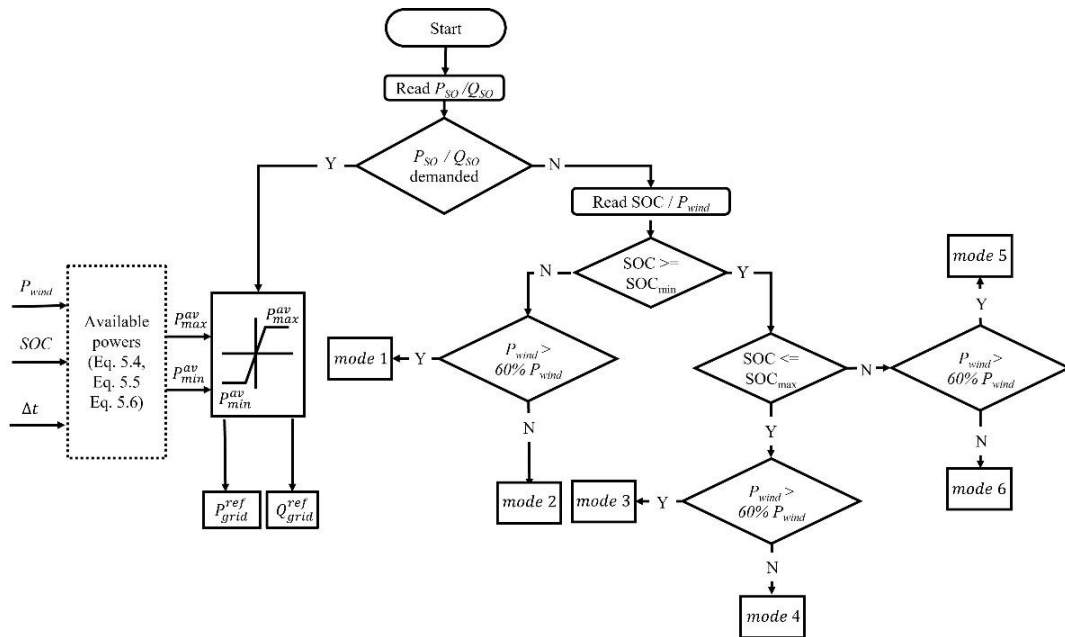

Figure 5.1. EMS 1 flowchart.

5.2   ENERGY MANAGEMENT SYSTEM 2

This section describes the EMS 2 implemented to control the power flow between the energy sources, i.e. the WT, PV system, battery, load and the grid (namely P_{wind}, P_{pv}, P_{bes}, P_L, P_{grid}, respectively).

The main priority of this EMS is to meet the active and reactive power of the load demand, reducing the dependence of the grid and optimizing the use of energy. In a second stage, the EMS waits for instructions of the SO, being the second priority comply with the active and reactive power requirements of the SO (P_{so} and Q_{so}), which must be within the minimum and maximum limits established according to the availability, informed by the operator of the hybrid power plant. If the SO does not set any operating instructions, then the system is operated to make an economic profit, buying energy from the grid and storing it in the BES (if possible), or selling the previously stored energy.

The difference between the power generated by the renewable system (P_{RW}) and the power consumed by the load is named net power (P_{net}), described by Equation (5.8). This P_{net} always must be attended, as it guarantees the priority in meeting the power demanded by the load. If the P_{net} is positive, the renewable system generates more than the load consumes, and then there is extra energy that can be generated by renewable energies. On other hand, if P_{net} is negative, the P_{RW} generates less than the load consumes, and therefore, there is an energy deficit in the hybrid power plant. The maximum available power (P_{so}^{max}) that can be delivered to the SO is the result of the sum P_{net} and the power associated to the energy stored in the BES. The minimum power allowed to the SO (P_{so}^{min}) is the difference between the P_{net} and the power that can be stored in the BES. Equations (5.9) and (5.10) show the maximum and minimum available power, respectively.

$$P_{net} = P_{RW} - P_L \tag{5.8}$$

$$P_{so}^{max} = P_{net} + P_{bes}^{dis,max} \tag{5.9}$$

$$P_{so}^{min} = P_{net} - P_{bes}^{char,max} \tag{5.10}$$

where P_{RW} is the sum of the power supplied by the WT and the PV.

The maximum charge and discharge power of the battery ($P_{bes}^{char,\max}$ and $P_{bes}^{dis,\max}$ respectively) are given by Equations (5.11) and (5.12), which consider the BES SOC, thus preserving its life cycle [204].

$$P_{bes}^{char,\max} = \min\left(P_{bes}^{m\max}, \frac{E_{bat}^{nom}}{\Delta t}\left(\frac{100 - SOC}{100} \right) \right) \tag{5.11}$$

$$P_{bes}^{dis,\max} = \min\left(P_{bes}^{m\max}, \frac{E_{bat}^{nom}}{\Delta t}\left(\frac{SOC - SOC_{\min}}{100} \right) \right) \tag{5.12}$$

A flowchart of the proposed EMS is illustrated in Figure 5.2. Initially, the algorithm will read all the necessary grid requirements, including the energy demand requested by SO (P_{net}), the price of the use of the grid and the BES SOC. Then, the available power for the SO is calculated considering that the priority is to attend the load.

If there is a power required by the SO, seven possibilities (*mode(1,7)*) can occur depending on the net power and the BES SOC. If the net power is positive, the SO can be served with this extra power generated or/and even with a surplus power available in the BES.

In *mode 1*, the P_{net} is greater than that required by the SO, and the BES is still capable of being charged, as it is below the maximum SOC level. In this mode, the SO complies with your demand and the BES is charged. If the BES is not being able to receive the excess of the P_{net} because it has already reached the maximum SOC. The power available to the SO is updated and the energy is dispatched to the grid according to *mode 2*. In this case, the BES cannot be charged. If the P_{net} is lower than that required by the SO, the BES is discharged to meet the SO (*mode 4)*, as long as it does not exceed the minimum SOC level. If the minimum SOC level is reached (*mode 3*), the power available to the SO is updated and the BES cannot be discharged.

When the P_{net} is negative, there is an energy deficit to meet the load, so it will be evaluated whether the power stored in the BES will be able to meet the deficit P_{net} required by the load and the power required by the operator (P_{so}). If possible, the system works in *mode 5*. In this mode, the energy stored in the BES is capable of meeting both demands, from the operator, and the power deficit in the load. If the BES reaches the critical SOC minimum (*mode 6*), the BES can no longer be discharged to be preserved

and the net power must be attended by the grid. If the SO requests more power than is available in the BES, it will be discharged with the maximum available power (*mode 7*).
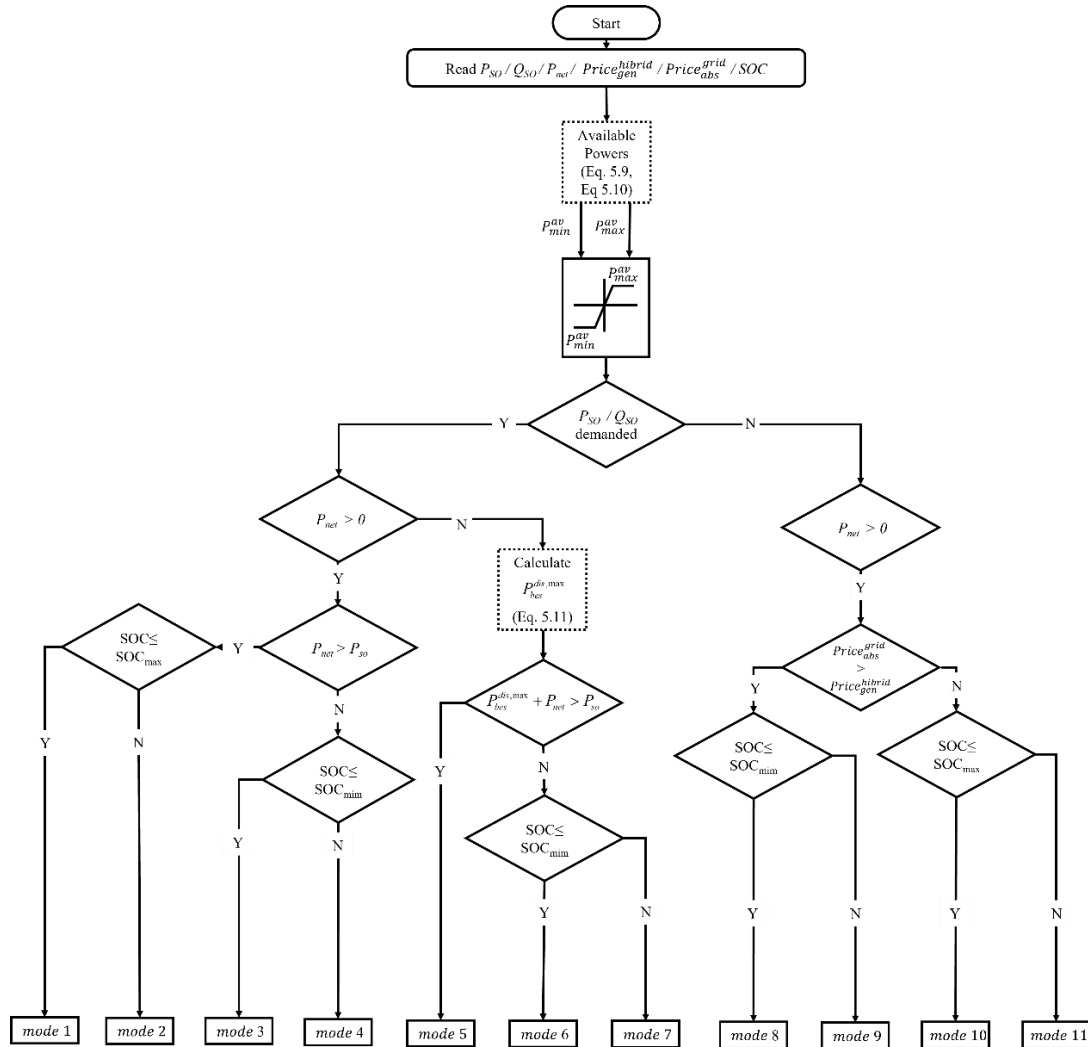

Figure 5.2. EMS 2 flowchart

If the SO does not request a specific demand, the hybrid power plant operates to make an economic profit, buying or selling energy, according to the BES SOC, changing from *mode 8* to *mode 11*. Because this thesis does not focus on the detailed regulation of power generation in a complex electricity market, the EMS considers a fixed cost of operation of the hybrid plant (called $Price_{gen}^{hybrid}$), while the price of absorbing energy from the grid ($Price_{abs}^{grid}$) varies during the simulation. Thus, a binary

variable is determined to discriminate between high and low prices in the electricity market.

If SOC is low (9%), the priority is to charge the battery. Therefore, if the price of energy is high, it means the price of absorbing from the grid is bigger than the renewable energy plant. Thus, all the energy generated by the hybrid power plant will be injected into the grid, choosing not to charge the battery (*mode 8*). Otherwise, in case the SOC is bigger than the minimum SOC, the BES will be discharged until it reaches the critical value of the SOC (*mode 9*). If the price of energy is low, that is, the cost of generation is greater than the cost of absorption from the grid, the grid works as a storage system. Then it is possible to buy energy from the grid (*mode 10*) and to charge the BES until it reaches the SOC maximum. When the BES reaches this state, it will no longer be able to charge to preserve its lifetime (*mode 11*).

Chapter 6: Results

Chapter 6 details all the results of the thesis, which were divided into three parts to facilitate understanding. The first simulation (relative to the systems shown in Figure 3.1, highlighted in yellow and denoted as simulation 1) was used to validate the averaged dynamic models (ADM 1 and ADM 2) proposed in chapter 4. Both models present the same control system as the switched dynamic model (SDM), except for the generation of firing pulses, which is not necessary for the averaged models. The two proposed models were evaluated and compared with the SDM. The application and control of qZSI for large wind energy grid-connected systems with BES, relative to the systems shown in Figure 3.1a and highlighted in green (simulation 2), was evaluated in the second simulation. Moreover, the EMS 1 was implemented to control the SOC, charge and discharge of the battery. Finally, in the third simulation (relative to the configuration shown in Figure 3.1a, highlighted in orange and denoted as simulation 3), the system under study is composed of a WT, PV and BES. In addition, the EMS 2 was used to control and management of all energy of the system.

## 6.1   SIMULATION 1 – VALIDATION OF AVERAGED MODELS

To validate the average model described in chapter 4, the system presented in Figure 3.1 (highlighted in yellow and denoted as simulation 1) was implemented in MATLAB/Simulink® using the SDM, ADM1, and ADM2. However, for this simulation, the PV power plant and the BES were not considered. Only the WT was used to validate the averaged model so that it was possible to analyze a significant improvement in the simulation time when using the averaged models.

The main parameters of the PMSG-driven WT modelled are given in Table 3.1. The time-domain response and control performance of the proposed models are evaluated under different operating conditions: fluctuating wind speed (below and above rated values), variable reactive power reference, and grid disturbances (voltage sag and presence of harmonics in the grid). Three simulation cases are used to test the proposed models, in which the responses of the averaged models (ADM1 and ADM2) are compared with those obtained from the SDM.

6.1.1 CASE 1: OPERATION WITH VARIABLE WIND SPEED AND CHANGES IN REACTIVE POWER

Case 1 includes a 90-second simulation with variable wind speed (Figure 6.1a) between 8.8 (below-rated wind speed) and 12.6 m/s (above-rated wind speed) and changes in the reactive power reference between -0.15 and 0.15 MVAr (Figure 6.2b).

As shown in Figure 6.2a, the active power delivered to the grid is maintained at its rated value for above-rated wind speeds, mainly because of the performance of the pitch angle controller (Figure 6.1b). For below-rated wind speeds, the pitch angle is kept at 0°, and the WT operates at variable speed to inject the maximum power into the grid according to the incoming wind speed. Both ADM1 and ADM2 show similar results to those provided by SDM, with very small differences in pitch angle for above-rated wind speeds and active power for below-rated wind speeds.
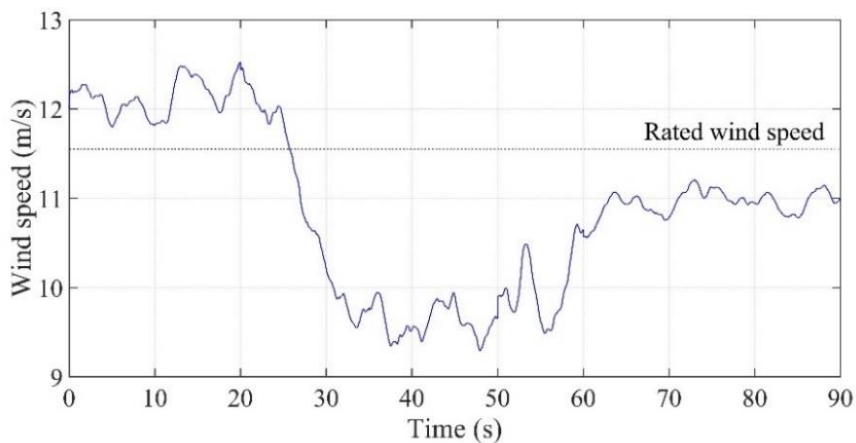

(a)
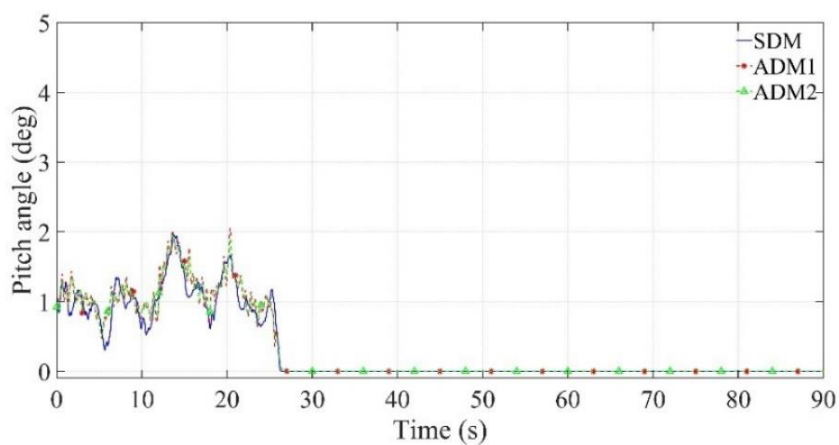
(b)

Figure 6.1. Simulation 1: Case 1. (a) Wind speed; (b) pitch angle

Figure 6.2b shows the reactive power exchanged with the grid. It can be observed that the WT provides the desired reactive power, which varies between 0.15 and -0.15 MVAr, remaining at zero (unity power factor) for some periods. Regarding the reactive power, the results obtained by ADM1 and ADM2 matched perfectly with those achieved by SDM.
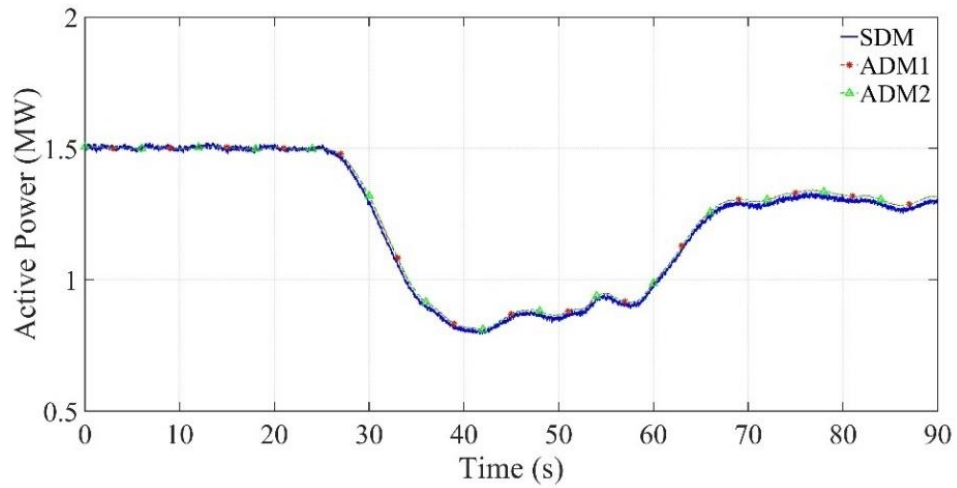

(a)
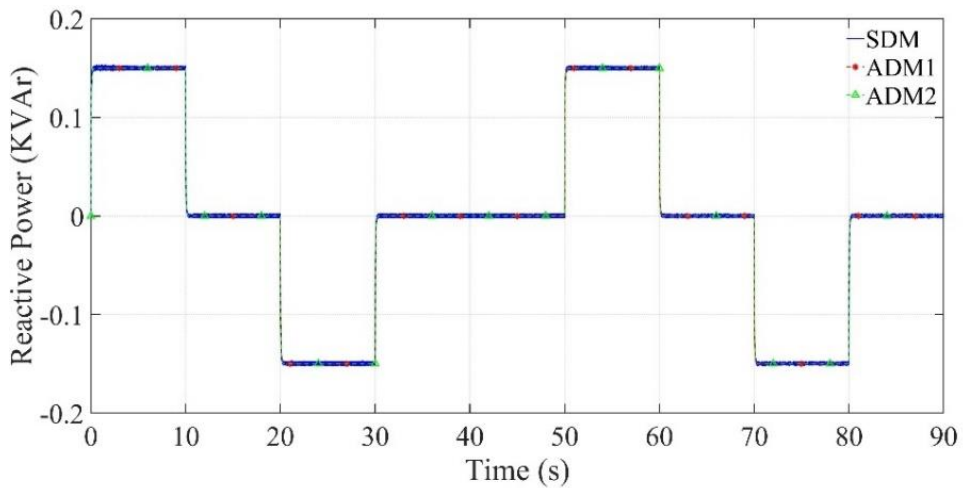
(b)

Figure 6.2. Simulation 1: Case 1. (a) grid active power, and (b) grid reactive power.

M and *D* are shown in Figure 6.3a. *M* was used to control the active and reactive powers. It varies significantly with the changes in the reactive power and slightly with the changes in the active power at below-rated wind speeds (variable speed operation).

In this case, ADM1 and ADM2 show differences with SDM, although the results obtained for the active and reactive powers are very similar, as illustrated in Figure 6.2a and Figure 6.2b. *Vdc* is perfectly controlled at 1.35 kV (Figure 6.3b). As shown in Figure 6.3a, the three models present identical results to control *Vdc* through *D*.
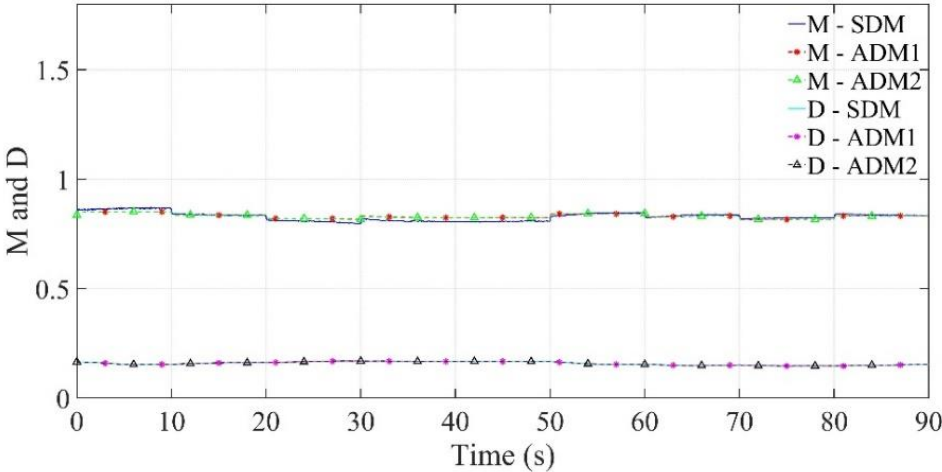
(a)
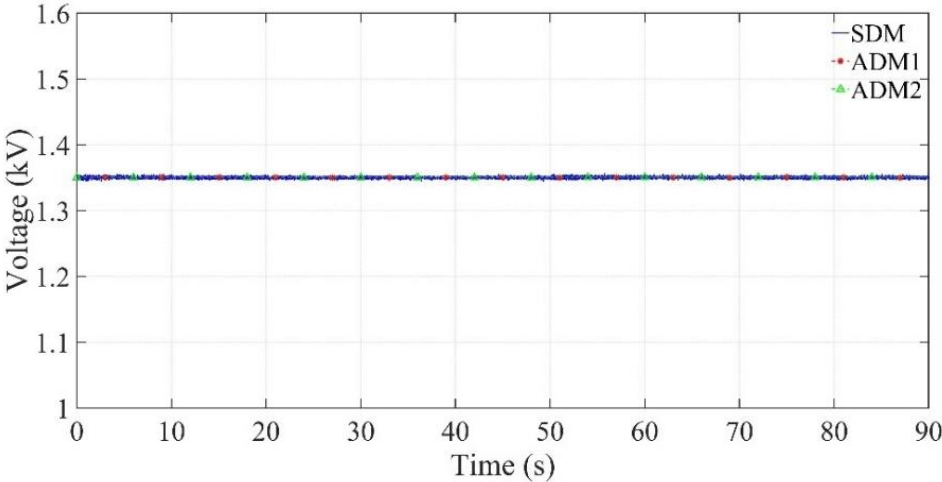
(b)

Figure 6.3. Simulation 1: Case 1. a) Modulation index (*M*) and Duty cycle (*D*), and b) *V$_{dc}$*

6.1.2 CASE 2: OPERATION WITH GRID DISTURBANCES

The WT and the proposed models are evaluated in Case 2 under two grid disturbances: grid voltage sag and grid voltage with 3rd and 5th harmonics. A 3-second

simulation with a constant wind speed of 11.5 m/s (rated wind speed) was performed for both grid disturbances.

Figure 6.4 and Figure 6.5 show the grid voltage and current. Disturbances occur at the second 1. Figure 6.4 shows the simulation with the voltage sag, where the grid voltage decreases from 1 to 0.3 p.u. during 60 ms, whereas Figure 6.5 shows the simulation with harmonics in the voltage. Were considered the 3rd and 5th harmonics with an amplitude of 0.08 p.u. each, during 60 ms. As can be observed, ADM1 and ADM2 can accurately reproduce the grid voltage and current before and after the disturbances.
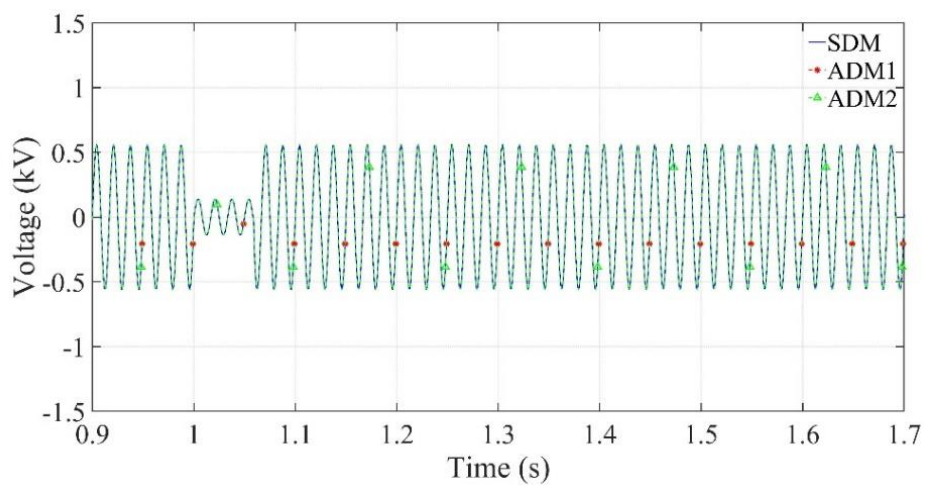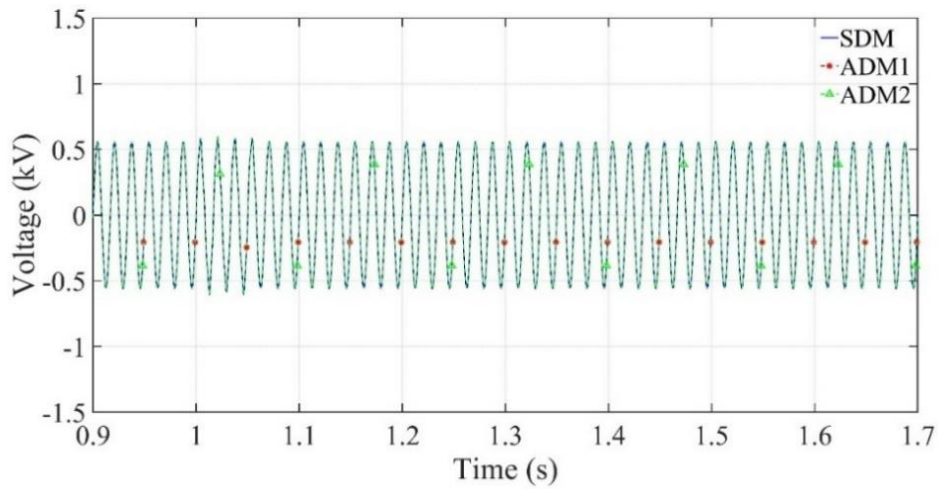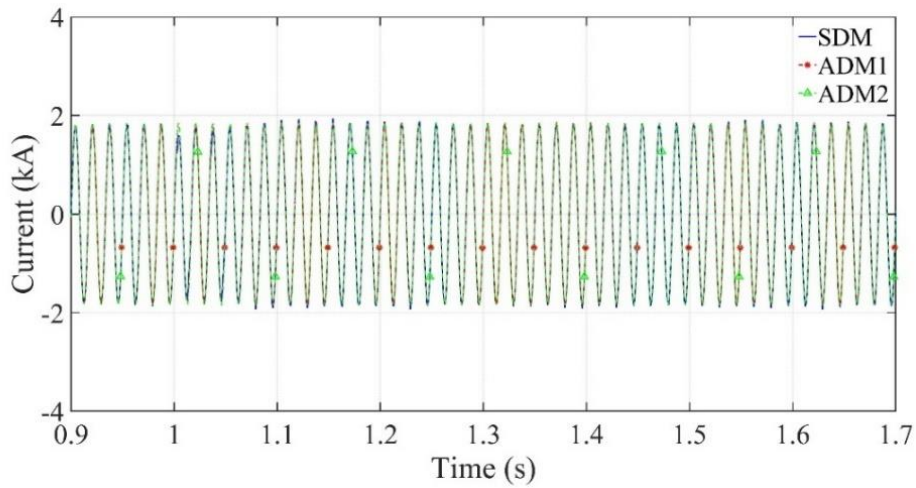

(a)
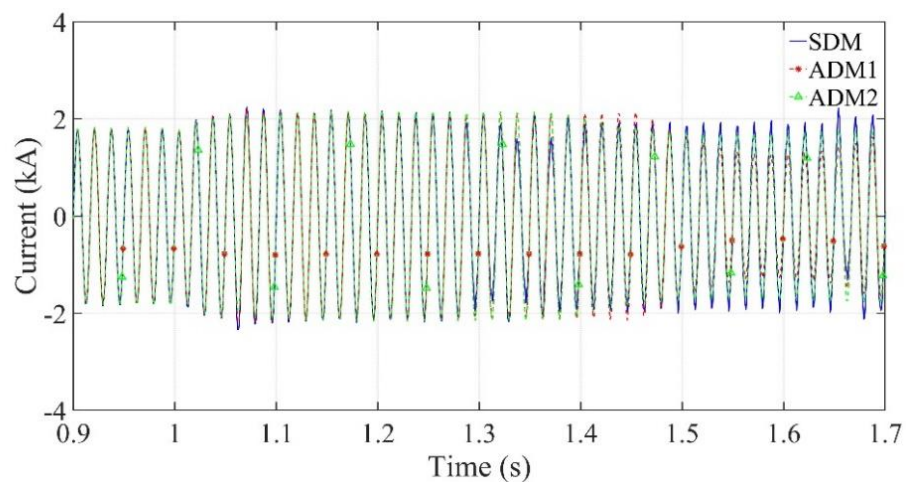
(b)

Figure 6.4. Simulation 1: Case 2. a) Grid voltage sag: Phase-A voltage; (b) Grid voltage with 3rd and 5th harmonics: Phase-A voltage

(a)

(b)

Figure 6.5. Simulation 1: Case 2. a) Grid voltage harmonics: Phase-A current; (b) Grid voltage with 3rd and 5th harmonics: Phase-A current.

The active and reactive powers delivered to the grid are shown in Figure 6.6. As shown, the WT operates at the rated active power and unity power factor before the grid disturbances. During the voltage sag, the active power falls equally in all three models owing to the voltage drop. When the disturbance disappears and the grid voltage is recovered, the active power increases above the rated value transitorily, reaching the same maximum value in all three models. Then, owing to the action of the controllers (active power, V_{dc}, and pitch angle controllers), a transient occurs until the steady-state value of the active power (rated active power) is recovered. Some differences between the models were observed in this transient. ADM1 and ADM2 present less variability in the transient and reach pre-fault conditions earlier than SDM.
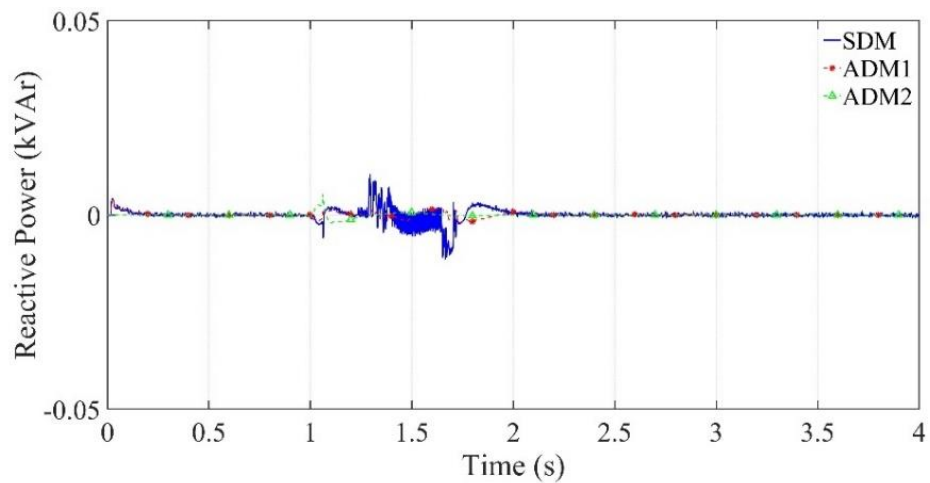
On the other hand, a small variation in the active power can be seen when the other disturbance (grid voltage with 3rd and 5th harmonics) occurs. In both disturbances, the reactive power hardly deviates from zero.
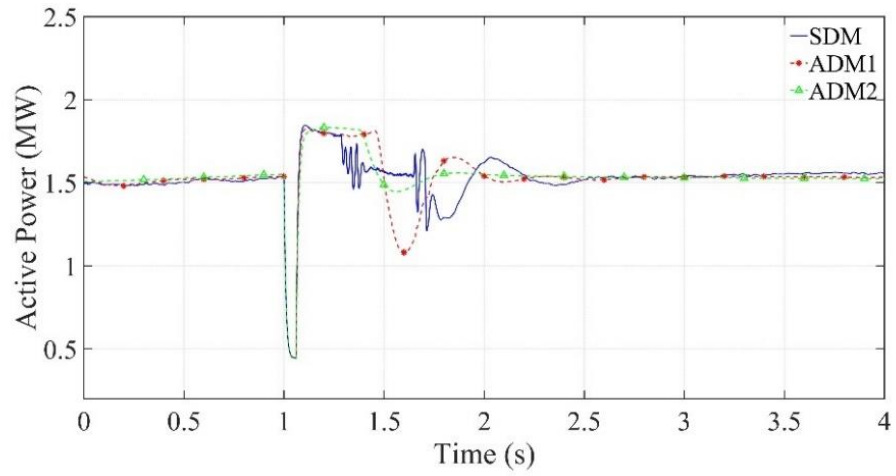
(a)
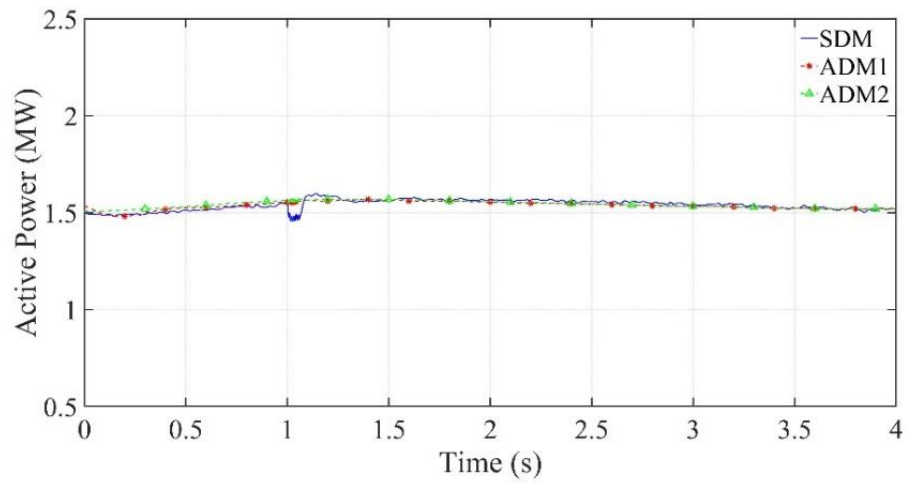
(b)

(c)
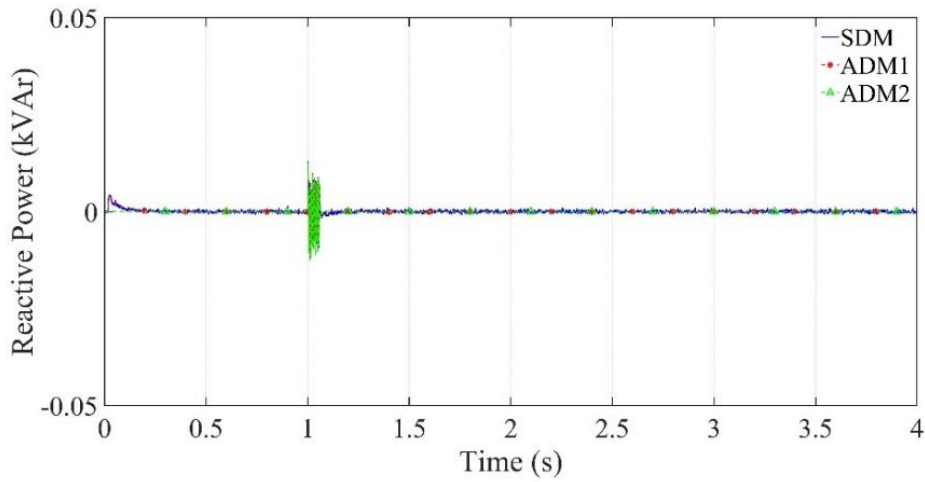
(d)

Figure 6.6. Simulation 1: Case 2. a) Grid voltage sag: Active power; b) Grid voltage with harmonics: Active power; c) Grid voltage sag: Reactive power; d) Grid voltage with harmonics: Reactive power.

In the case of the voltage sag, ADM1 and ADM2 present less variability in the control variables M and D (Figure 6.7) than SDM, which explains the differences observed mainly in the active power (Figure 6.6a) and V_{dc} (Figure 6.8a). On the contrary, M and D are very little affected by the other grid perturbations, as seen in Figure 6.7a, Figure 6.7b, and Figure 6.7c, Figure 6.7d.
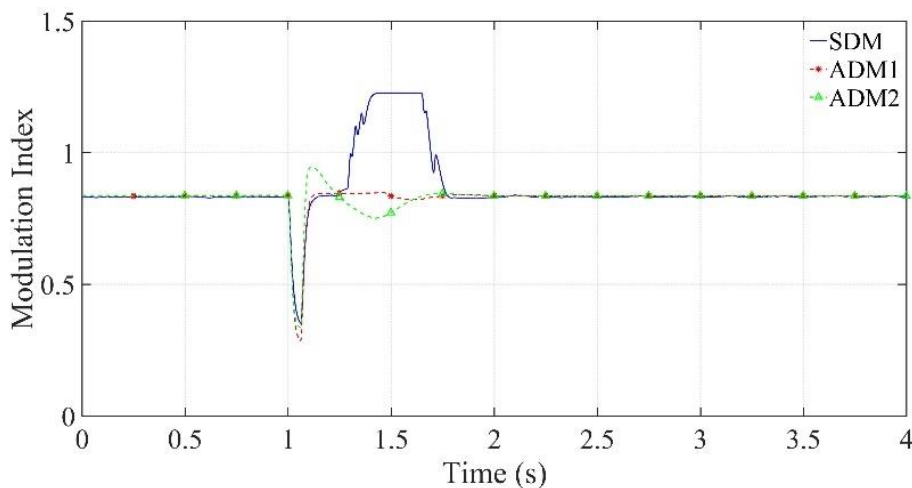
(a)
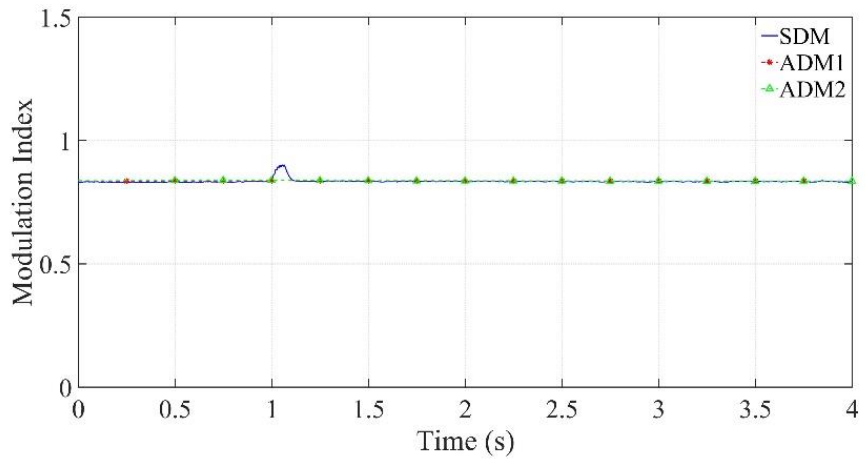
(b)
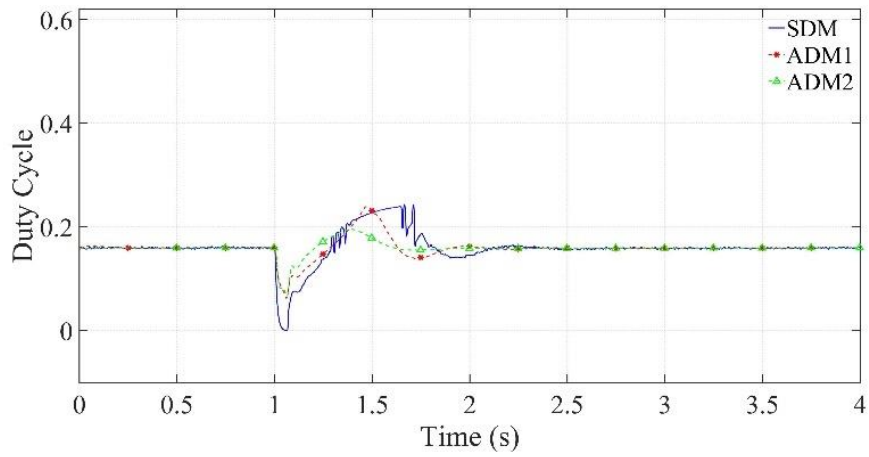
(c)
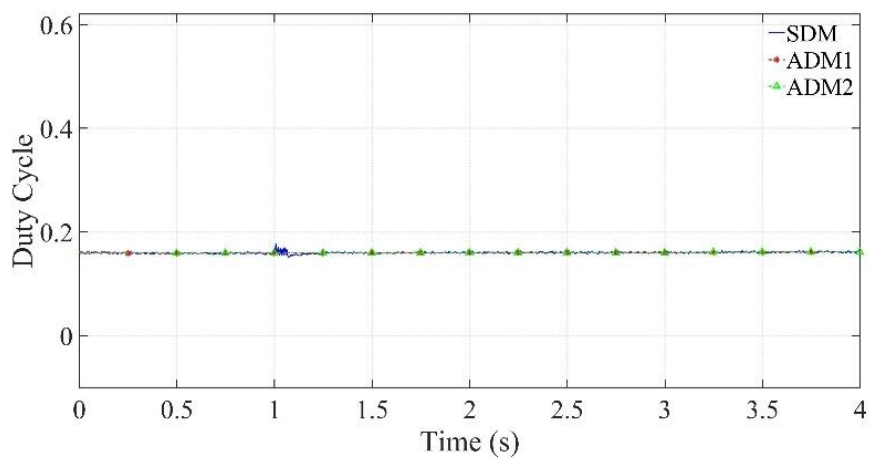
(d)

Figure 6.7. Simulation 1: Case 2. a) Grid voltage sag: Modulation index (*M*); b) Grid voltage with 3rd and 5th harmonics: Modulation index (*M*); c) Grid voltage sag: Duty-cycle; d) Grid voltage with 3rd and 5th harmonics: Duty-cycle.

Figure 6.8 illustrates the control of V_{dc}. In the transient after the voltage sag, significant differences appear for ADM1 and ADM2 compared to SDM because of the simplifications made in the averaged models, although an adequate regulation of V_{dc} can be observed. Finally, as expected, the harmonics in the grid voltage do not affect the control of V_{dc}.
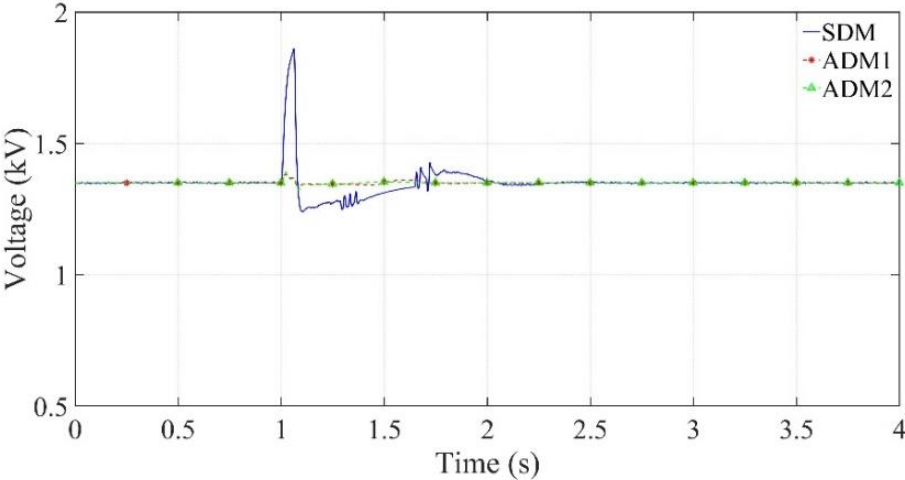
(a)
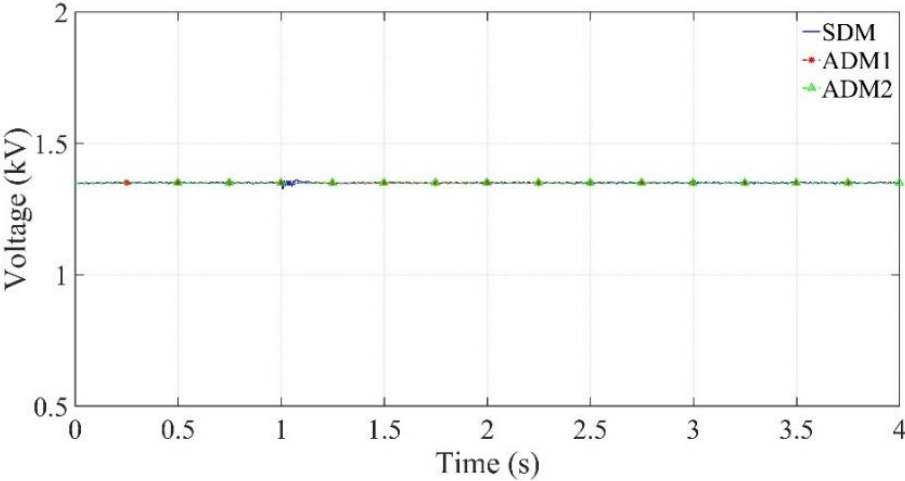
(b)

Figure 6.8. Simulation 1: Case 2. V_{dc}: a) Grid voltage sag; b) Grid voltage with 3rd and 5th harmonics.

The results obtained show the satisfactory response of the averaged models proposed in this work to represent the steady-state response and control performance

of the system under study, although some differences can be observed during the transient response, as expected.

6.1.3 COMPUTATIONAL EFFORT

Finally, the models described in Chapter 4 are simulated for different time intervals to compare the reduction in the computational effort for ADM1 and ADM2 against SDM. The models were simulated on a computer with an Intel Core i7-4510U processor at 2.60 GHz and 8 GB RAM. As the purpose was to analyze the simulation time and computational effort, the WT was simulated using the rated wind speed and unity power factor.

Table 6.1 presents the reduction in the simulation time achieved by ADM1 and ADM2 over SDM for several simulation horizons (from 2.5 s to 80 s). Very significant reductions in the simulation time registered for the proposed models compared with the SDM can be observed. ADM1 achieved an average time reduction of 91%, whereas the average reduction was 94% for ADM2. Therefore, ADM2 is the fastest among the models used to represent the time-domain response of the system under study. Furthermore, the average reduction in ADM2 was 27% compared to ADM1.

Table 6.1. Comparison of the Computational Effort of the Models

	TIME REDUCTION (%)		
Simulation horizon (s)	ADM1 vs SDM	ADM2 vs SDM	ADM2 vs ADM1
2.5	83	88	30
5	87	92	37
10	89	94	37
20	92	94	27
30	92	94	24
40	93	95	24
50	94	95	21
60	93	95	25
70	93	95	23
80	94	95	23
Average time reduction	91	94	27

6.2 SIMULATION 2 – WIND TURBINE WITH BATTERY

The system described in chapter 3 and the control described in chapter 4 was simulated in MATLAB / Simulink® to evaluate the efficiency of the control and EMS 1 described in Section 5.1. The WT was simulated for below and above rated wind speeds, the BES allows reducing the intermittence of the generation and improving the operability of the WT. Two case studies were studied: one case considering the performance of the SO and the other case where the SO is disabled.

Figure 6.9 shows the wind speed considered in the simulation. The EMS 1 performance can be seen Figure 6.10 (with initial SOC below 9%), Figure 6.11 (with initial SOC 50%) and Figure 6.12 (with initial SOC 95%). If the system operates according to Case 1, the SO can require a specific power reference, according to the maximum and minimum values informed by the wind farm operator. If the SO does not request a specific power reference, the system will operate according to the battery SOC.
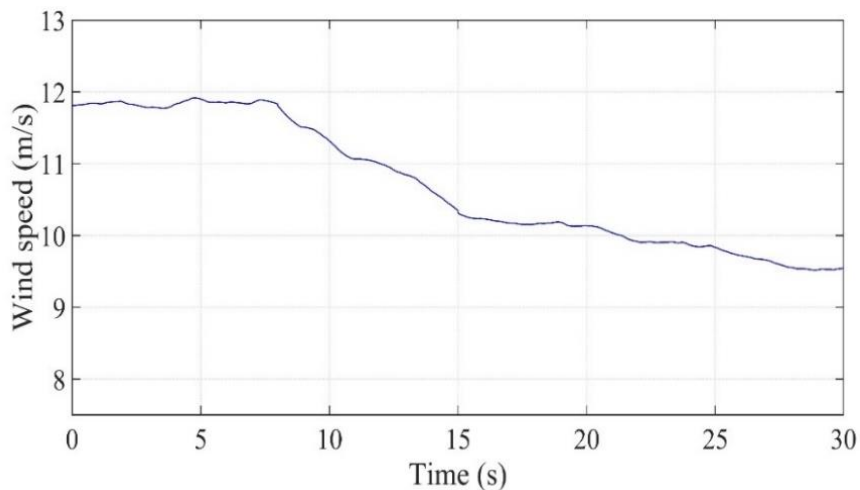
Figure 6.9. Simulation 2: Wind speed.

Figure 6.10a shows the active power provided by the WT, the power injected into the grid and the BES charge/discharge according to the EMS 1, with initial SOC below 9%. Since the BES SOC is below 9%, while the WT is generating above 60% of its rated power, the BES is charged. However, when the power generated by the WT is below 60% of its rated power, all the wind power generation is injected into the grid.

From 0 to 5 s the SO does not require any power reference and while the power generated is above 60% of the WT rated power, the BES is charged with 40% of the

total energy of the BES (mode 1). At 5 s, as the SO requires more power than the maximum available, the system injects into the grid the WT generation, as the BES cannot be discharged further. At 7.5 s and after 20 s, the SO does not require any power reference and the behaviour is the same as in the first seconds of simulation. At 10 s, the power required by the SO is greater than the maximum power, and thus the power injected into the grid is the maximum power allowed (WT). From 12.5 to 15 s the SO requirements are smaller than the minimum power, and thus the power injected into the grid is the minimum power available to the wind farm operator. From 15 to 20 s the SO requirements are satisfied. Figure 6.10b shows the SOC variation, the BES only charges in this case because the SOC is below the lower critical limit of 9%. As seen in Figure 6.10c, which shows the BES current control for this simulation, the BES current is satisfactorily controlled to its reference by the control proposed in chapter 4.
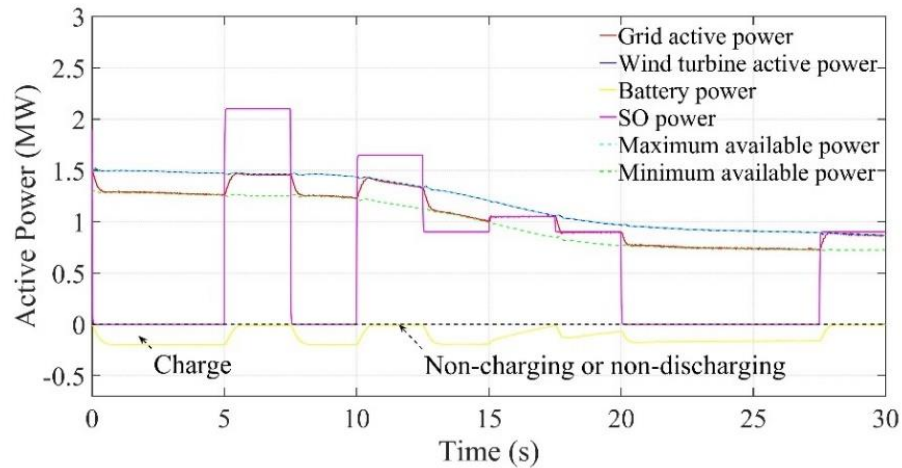
(a)
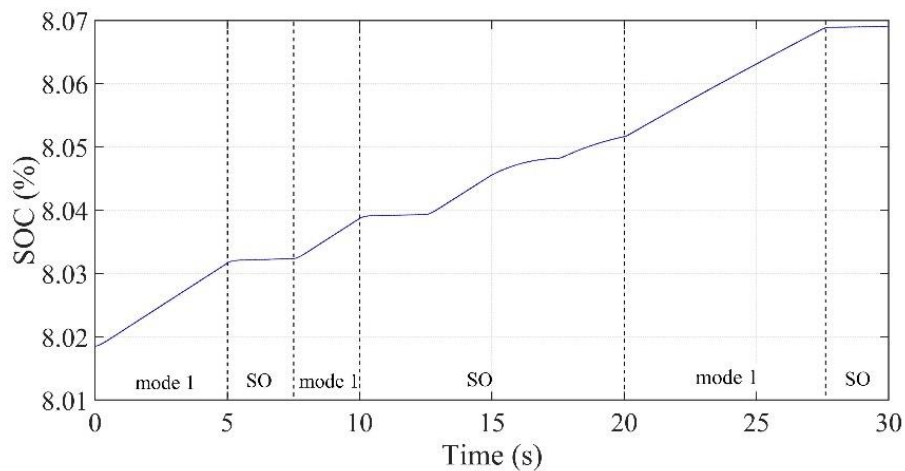
(b)
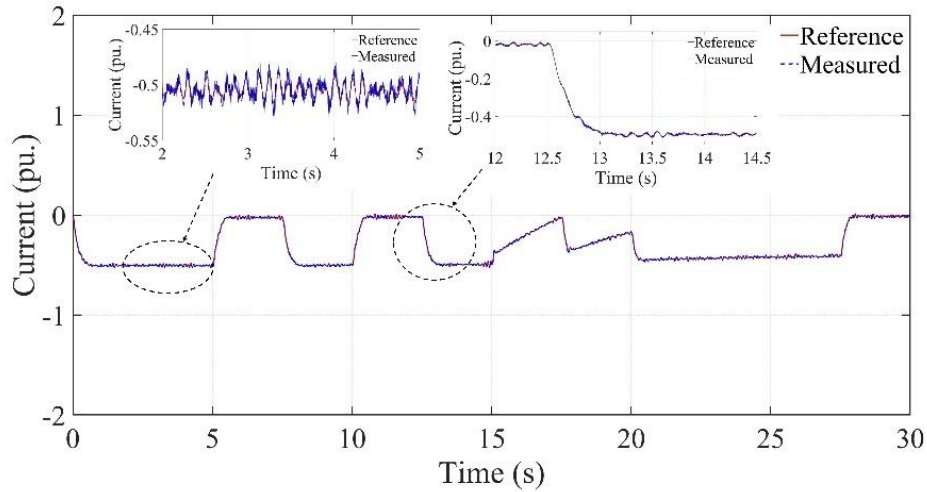
(c)

Figure 6.10. Simulation 2: (a) Grid active power, WT active power, BES power, SO power, and limits available power, (b) SOC close to lower limit 9%, (c) BES current control.

Figure 6.11a shows several operating situations of charge and discharge of the BES, with the required power by SO and without SO. From 0 to 5 s, the SO does not impose any power reference, and therefore, the system works according to Case 2. In this case, because of an initial SOC of 50%, the BES can be charged, or discharged depending on the power generated by PMSG WT. At 5 s, the SO requires more power than the maximum available power. Therefore, the system injects into the grid the maximum available power (WT plus BES power).

At 7 s and from 20 to 27.5 s, the working principle is similar to the first situation, in which the SO does not impose any power reference, however, the discharge of the BES is different, varying between mode 3 and 4, as seen in Figure 6.11b. At 10 s, the working principle is like the situation in 5 s, where the power required by SO is above the maximum available. From 12.5 to 17.5 s and from 27.5 to 30 s, the power required by the SO is within available power limits, and the BES is charged or discharged to comply with the requirements of the SO.
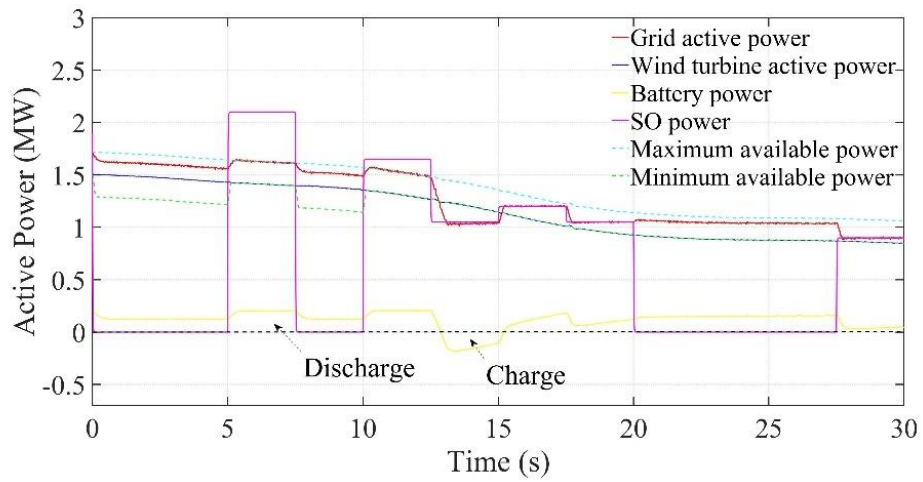
(a)

(b)
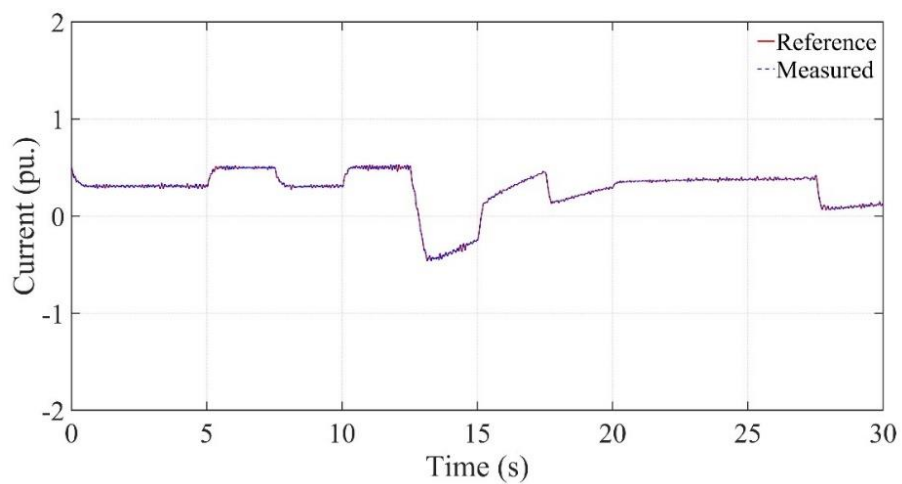
(c)

Figure 6.11. Simulation 2: (a) Grid active power, WT active power, BES power, SO power, and limits available power, (b) SOC close to 50%, (c) BES current control.

Figure 6.12a shows operating situations described in mode 5, which occur when the SOC is above the upper limit of 90%. From 0 to 5 s, the SO does not impose any power reference, and therefore, the system works according to Case 2. In this case, because of a high initial SOC, the BES provides constant power, and all the power generated by the system (WT and BES) is injected into the grid. At 5 s, the SO requires more power than the maximum available power. Therefore, the system injects into the grid the maximum available power. At 7 s, the working principle is similar to the first situation, in which the SO does not impose any power reference. From 10 to 15 s the wind farm operator injects the maximum and minimum available power according to the demand of SO. From 15 to 30 s, the power required by the SO is below the maximum available power, and the BES is discharged to comply with the requirements of the SO. The SOC variation can be seen in Figure 6.12b.
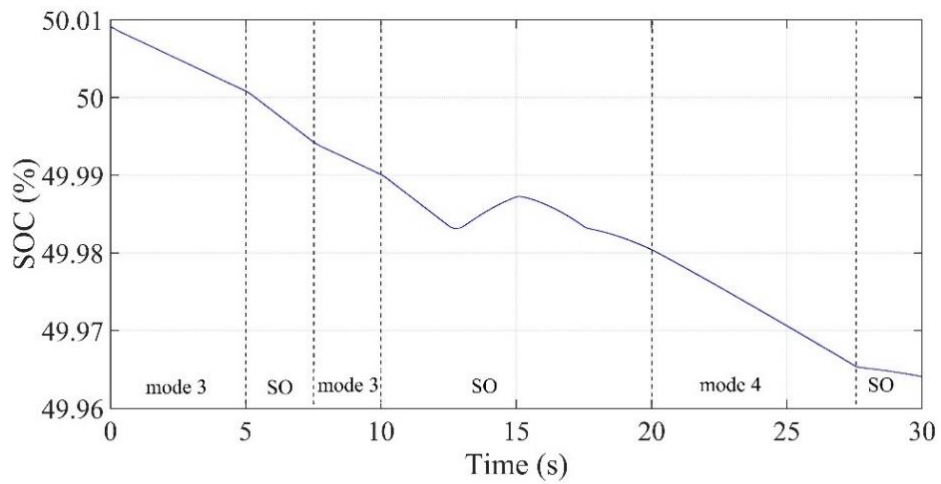

(a)

(b)

Figure 6.12. Simulation 2: (a) Grid active power, WT active power, BES power, SO power, and limits available power, (b) SOC above to upper limit 90%.

6.3 SIMULATION 3 – PV, WIND TURBINE AND BATTERY SYSTEM

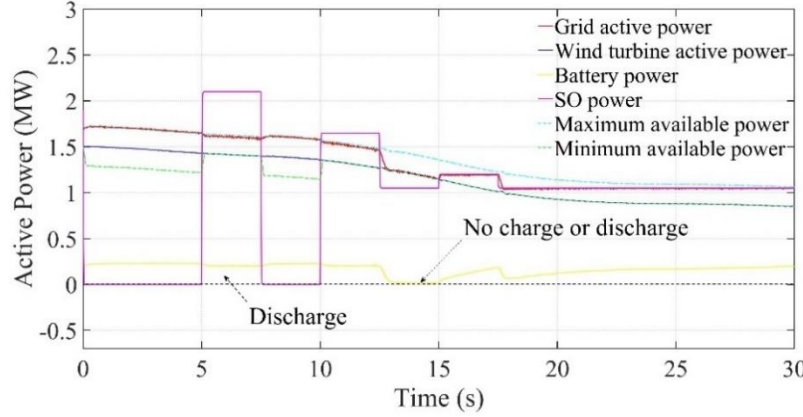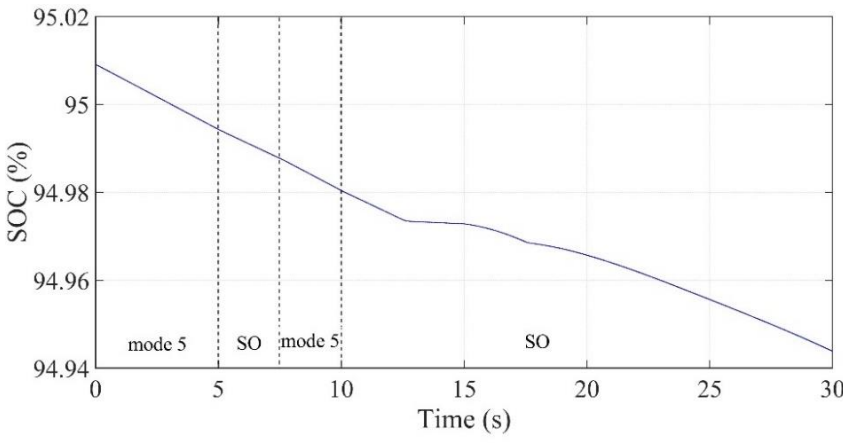The system described in chapter 4 was simulated in MATLAB/Simulink® to evaluate the efficiency of the control and EMS 2, which is more complex than the EMS 1 described previous. In addition to the WT and BES existing in the previous case (EMS 1), the EMS 2 should manage the power flow of a PV power plant and a load that must be primarily served by the hybrid power plant. The EMS 2 must maintain the correct power flow between the renewable generation system composed of wind and PV energy, BES, load, and grid.

The WT was simulated for below and above rated wind speeds, while that the radiance was variable in the PV power plant. In this way, the simulation is even closer to real situations that can occur during the functioning of the hybrid power plant. Furthermore, the charging and discharging of the BES depend on the energy price, and the EMS 2 is responsible for managing the charging and discharging situations. The EMS2 developed in this thesis does not focus on the detail of the regulation of power generation in a complex electricity market, but rather on the possibility of being carried out with the suggested EMS. Cases with the performance of the SO and without the SO were considered to evaluate the EMS 2 with several modes of operation.

The wind speed profile used in this case study is shown in Figure 6.13a, while Figure 6.13b shows the irradiance considered in the PV power plant. The wind speed remains mostly above the rated value of the WT during the first 10 s, while it fluctuates below and near the rated speed for the rest of the simulation. The irradiance varies from 50 to close to 1000 W/m^2 during the simulation, and some shading moments can be seen in Figure 6.13b. The residential and industrial loads varies equally for the three considered cases (SOC low, SOC medium and SOC high), as can be seen in Figure 6.13c, where P_{net} is the net power, P_{RW} is the renewable power, and P_L is the load power. From 0 to close 18s, the P_{net} is positive, representing an extra energy generated by renewable power. From 18 to close 77s, the P_{net} is negative, representing an deficit energy generated by renewable power. In this case, the EMS will manage the energy available in the BES, discharging to meet the load or will take the decision to meet the load with the external grid. At 77 s, as well as the situation between 0 to 18 s, the P_{net} returns to positive.
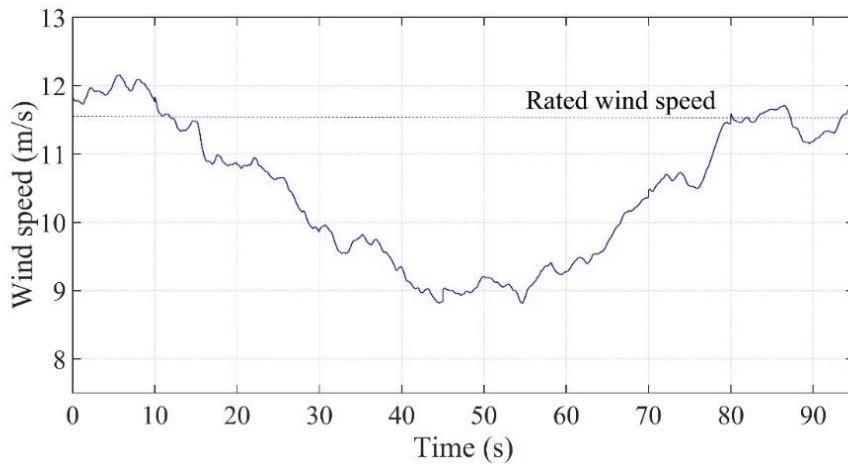
(a)
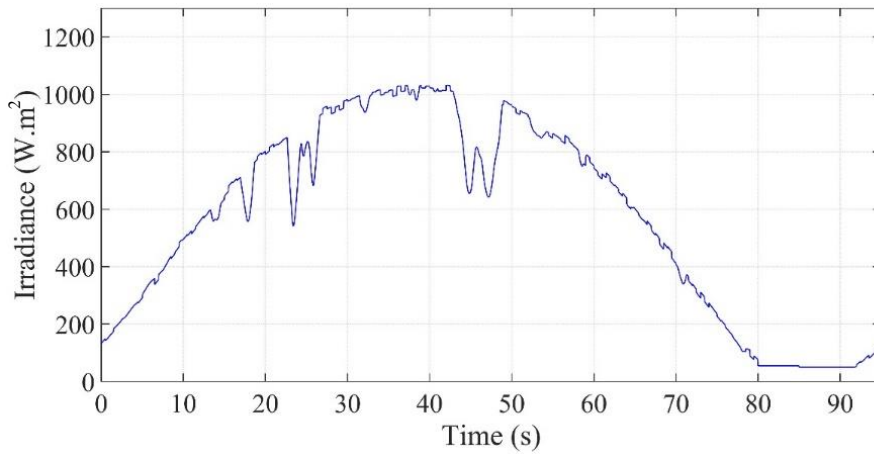
(b)
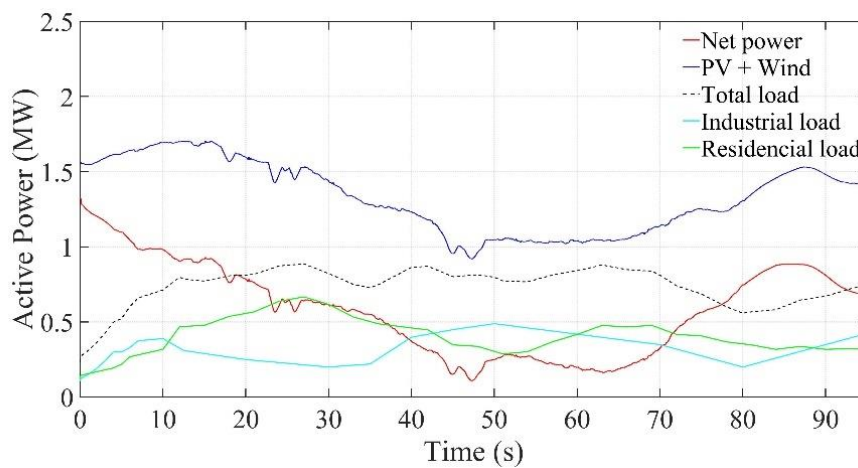
(c)

Figure 6.13. Simulation 3: (a) Wind speed, (b) Irradiance and (c) Net active power, PV and WT active power, total load active power, residential and industrial load active power.

As can be noticed in Figure 6.14a, the WT speed remains close to 1 p.u. even for winds above the rated value, and for below-rated wind speeds, the WT speed varies accordingly, achieving a variable speed operation. Figure 6.14b shows the performance of the pitch angle for above-rated wind speeds. From 0 to 10 s the wind speed remains above the rated value of the WT, thus the pitch angle acts to maintain the speed and power controlled. At 10 s, the wind fluctuates below and near the rated speed, thus the pitch angle remains at zero to the WT to provide the maximum available power.
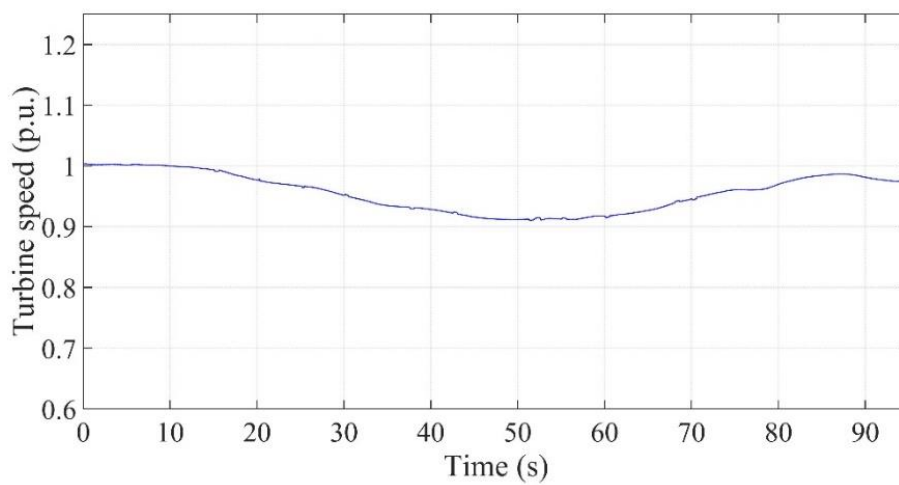
(a)
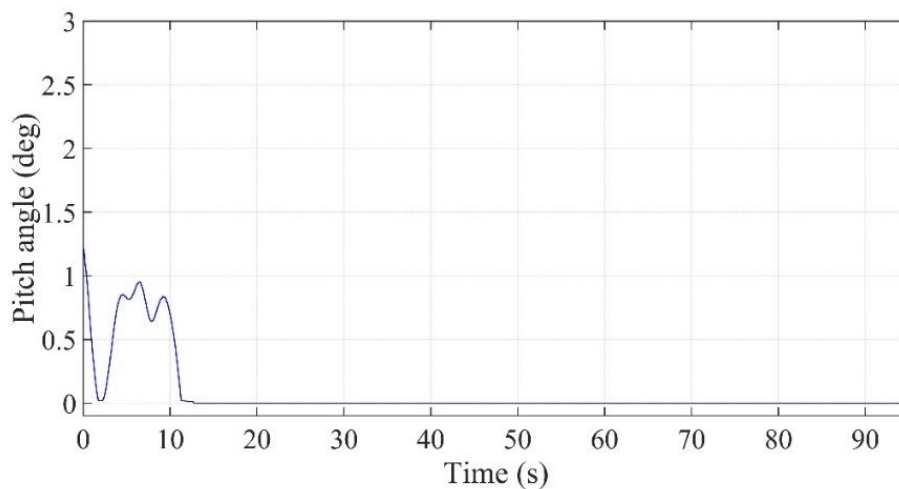
(b)

Figure 6.14. Simulation 3: (a) Turbine speed, (b) Pitch angle control.

The EMS 2 was evaluated with three initial SOC (below 9%, 50% and above 90%) to prove the correct functioning of the operation modes. In the first case, a BES with initial SOC below 9% was considered. Figure 6.15a shows the grid active power, which represents the power injected in the grid, the power generated by renewable energies (sum of WT and PV plant power), BES power, the active power requested by SO, the available power limits for SO and total load power.

From 0 to 15s, the SO imposes the maximum available power as power reference , and therefore, the system works according to *mode 3*. In this mode, the power available is calculated considering SOC low, and thus the BES should not be discharged, and the power injected to the grid is the maximum power allowed according to net power available.

At 15s, the SO does not request a defined power and the energy price is favourable to buy, thus the BES is charging with a maximum power of charge according to Equation (5.11). At 20 s, the power required by the SO is between the minimum and maximum available power, as the load was already attended, the BES is charging and at the same time complying with the requirements of the SO.

From 30 to 55 s, the working principle is similar to the first situation, in which the SO does not impose any power reference, however, the energy generated by renewable sources is injected into the grid according to economic advantage, selling (*mode 8*) or buying (*mode 10*) according to the energy price. The EMS decision is executed being 0 favourable to buy energy from the grid and 1 favourable to sell energy to the grid according to Figure 6.15b.

At 55 s, the energy injected complies with the SO requirements. From 60 to 95 s, the working principle is similar to the situation between 30 to 55 s, selling or buying according to the energy price. The operation mode and energy price state during the simulation can be seen in Figure 6.15b. The SOC variation can be seen in Figure 6.15c, the BES is only charged in this case because the SOC is below the lower critical limit of 9%.
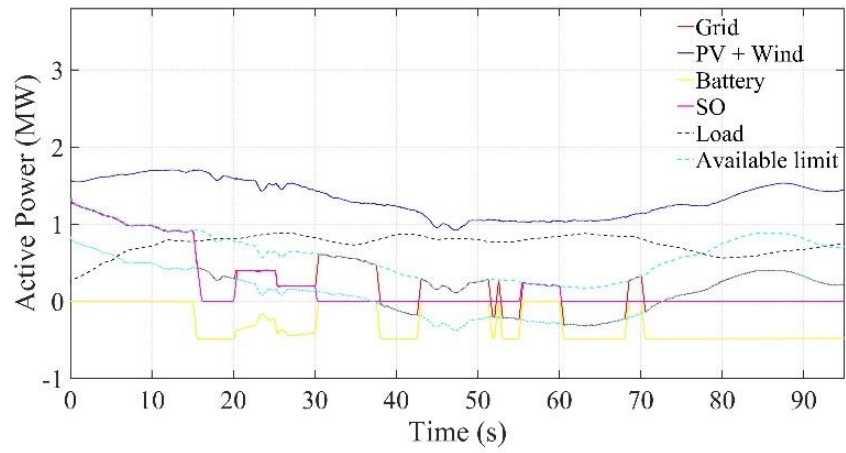
(a)
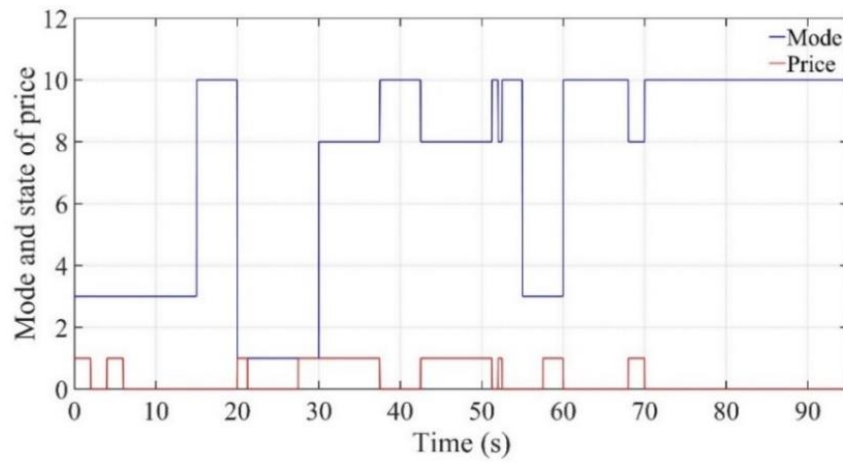
(b)

(c)

Figure 6.15. Simulation 3: (a) Grid active power, PV and WT active power, BES active power, SO active power, load active power and limits available power; (b) SOC close to lower limit 9%

The control performance for the i_d and i_b with initial SOC below 9% can be seen in Figure 6.16a and Figure 6.16b, respectively. The PI controller of the *P* control loop generates the reference for the *d*-current of the converter, which is inputted to the current control loop. As seen in Figure 6.16a, i_d is satisfactorily controlled to its reference by the current control loop. The results of charge/discharge of the BES controlled through the shoot-through state can be seen in Figure 6.16b, where the measured BES current i_b and its reference are highlighted between 20 and 30 s.

(a)

(b)
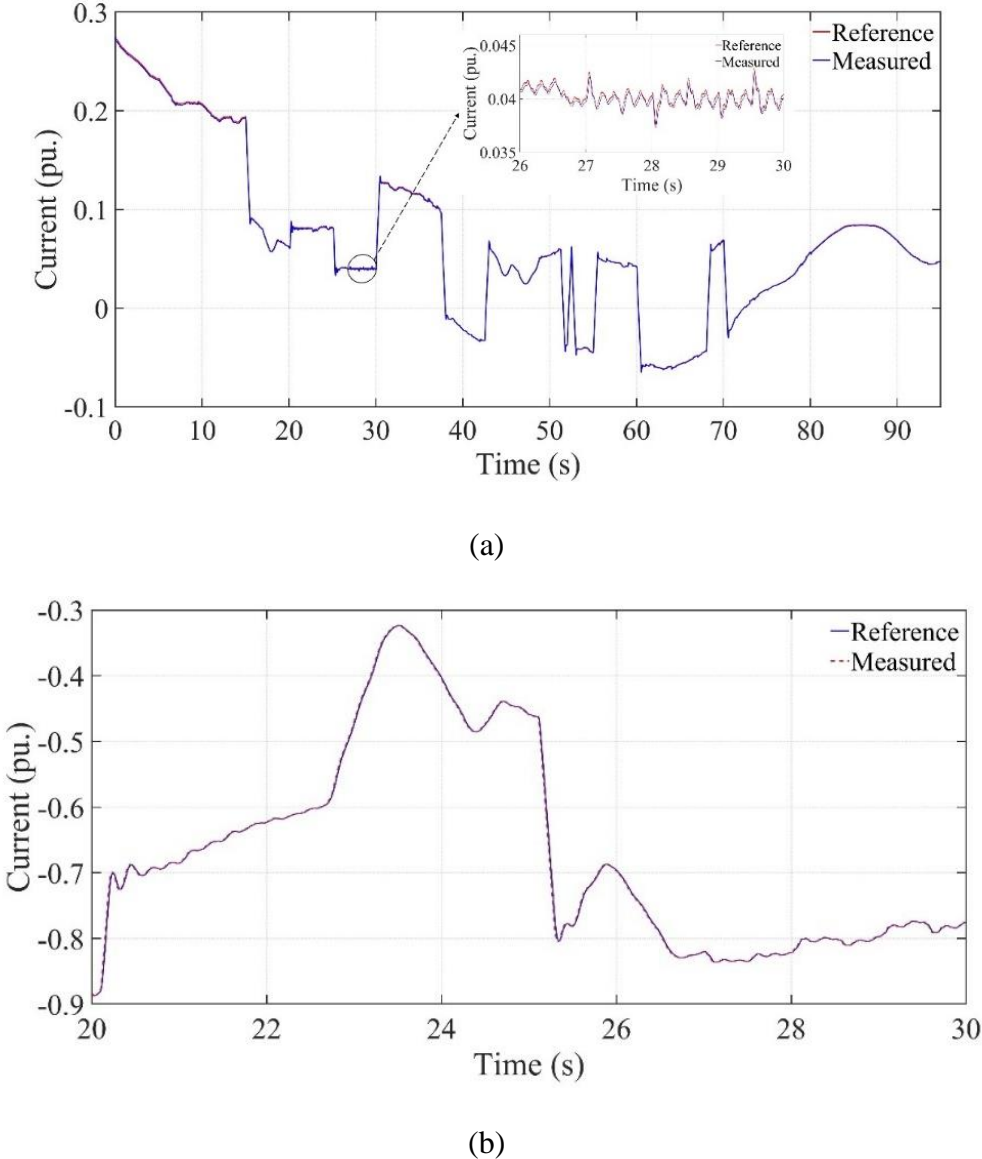
Figure 6.16. Simulation 3: (a) i_d current control, (b) BES current control

The WT voltage V_{in_wind} remains around 930 V (Figure 6.17a), but it varies slightly for below-rated wind speeds to achieve the MPPT. A similar situation occurs for V_{in_pv}

of the PV system, as can be seen in Figure 6.17b. The voltage remains around 573V varying slightly to achieve the MPPT. The MPPT algorithm generates a reference value for V_{in_pv} and V_{in_wind}, which are later controlled by a PI controller in the active power control loop to achieve the optimal generation of the PV and WT, respectively. These results show the appropriate control performance.
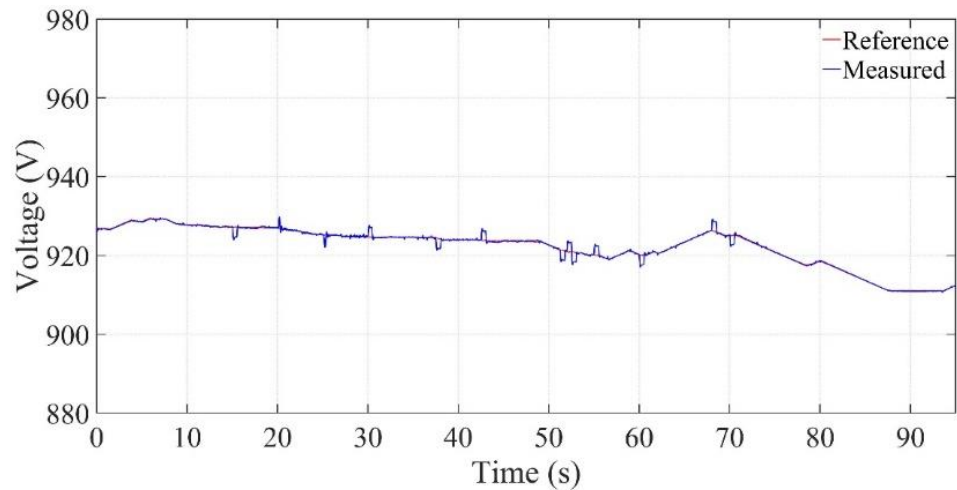
(a)
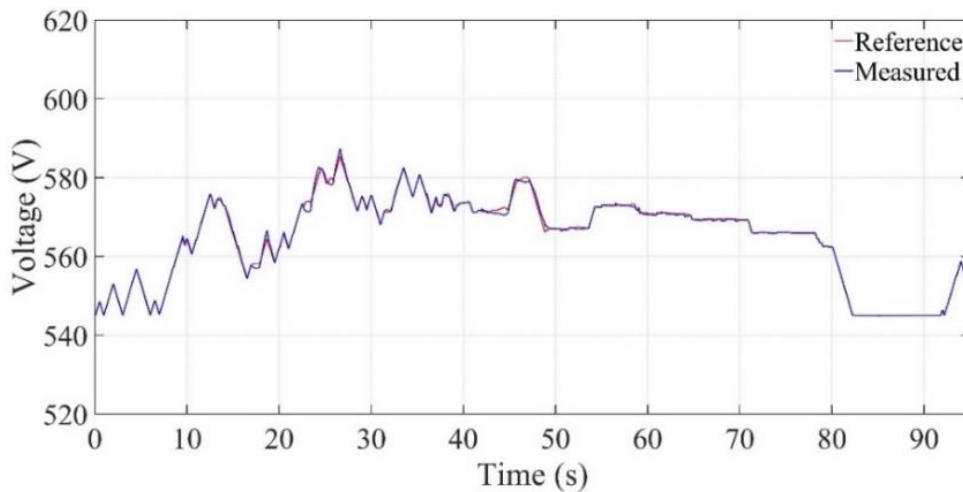
(b)

Figure 6.17. Simulation 3: Voltage V_{in} with initial SOC below 9% (a) V_{in_wind} voltage control, (b) V_{in_pv} voltage control

For the case of the BES with initial SOC of 50%, a variation of the reactive power was inserted to prove the correct functioning of the reactive power control and the impact of changing the reactive power reference on the other controls. The results are illustrated in Figure 6.18, Figure 6.19 and Figure 6.20.

Figure 6.18a shows the grid active power, the power generated through renewable energies, the BES power, the active power requested by SO, the available power limits for SO and total load power. Figure 6.18b shows the operation mode and energy price state, which can change between 0 and 1, representing low (favourable to buy energy) and high (favourable to sell energy) prices, respectively. The SOC variation can be seen in Figure 6.18c. When the SOC is medium, the BES can be charged or discharged until it reaches its lower or upper limits. In this case, for SOC 50%, the power available is calculated considering SOC medium, increasing the operating range of the system, as it is possible to charge and discharge the BES.

From 0 to 15s, the BES is discharging to comply with the requirements of the SO and the EMS 2 is functioning in *mode 4* (Figure 6.18b). At 15s, the SO does not request a defined power and the energy price is favorable to buy, and thus, the BES is charging with a maximum of charge, and the operation is being executed in *mode 10*. At 20 s, the power required by the SO is between the limits minimum (Equation (5.9)) and maximum (Equation (5.10)) authorized, as the load was already attended, the battery is charging to comply with the requirements of the SO. From 30 to 55 s, the EMS alternates between *mode 9* and *mode 10*, buying and selling energy, and thus the BES is charged and discharged according to the energy price. In the previous case (BES with an initial SOC below 9%), the BES could just be charged due to its low SOC. At 55 s, the energy injected again complies with the requirements of the SO. From 60 to 95 s, the working principle is similar to the situation between 30 to 55 s, buying and selling energy according to price.
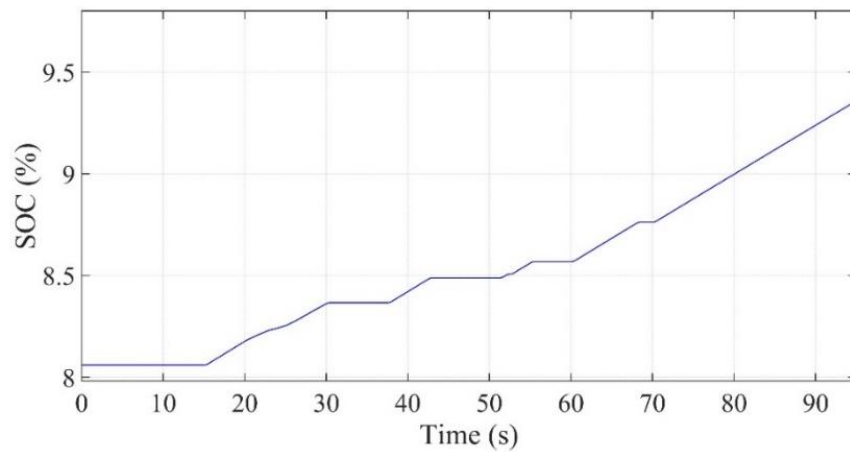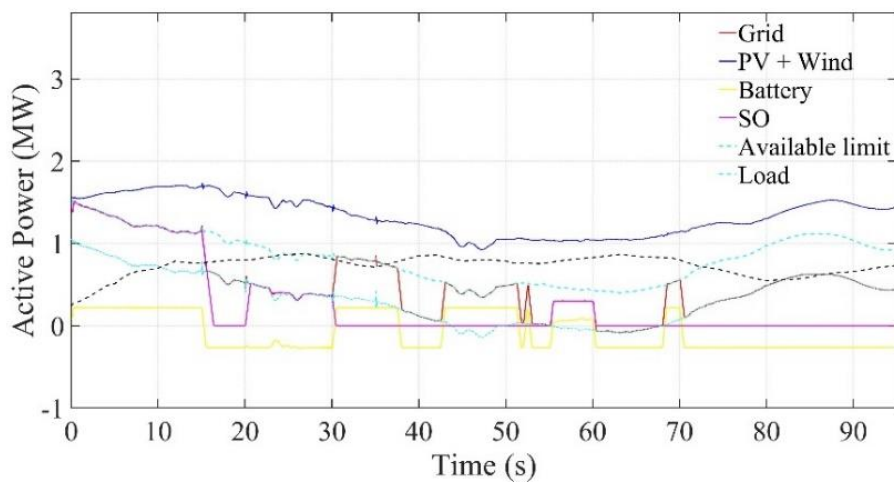

(a)
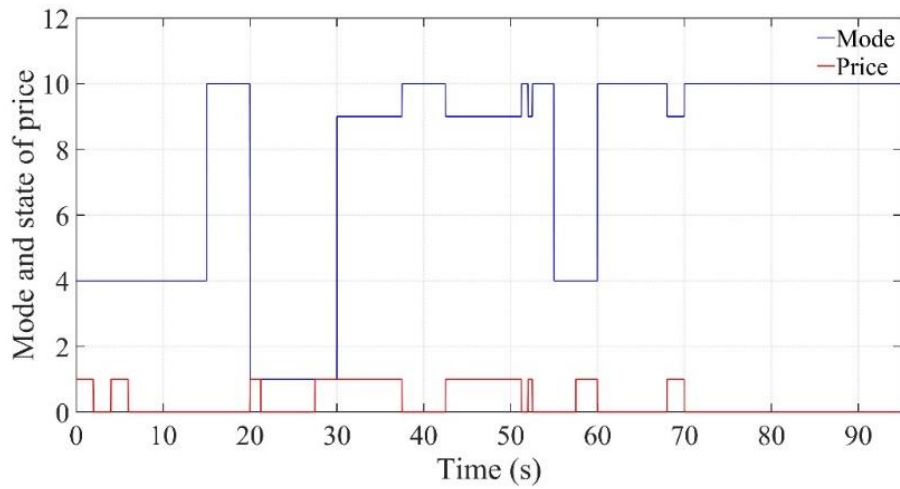
(b)
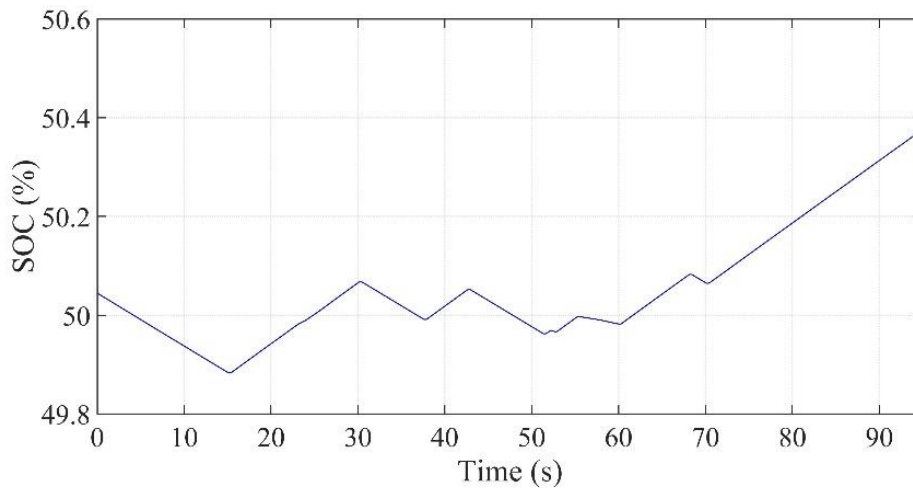
(c)

Figure 6.18. Simulation 3: (a) Grid active power, PV and WT active power, BES active power, SO active power, load active power and limits available power; (b) SOC close to 50%.

The control performance for the i_q can be seen in Figure 6.19a. The PI controller for the reactive power control generates the reference for the q-current of the converter, which is inputted to the current control loop. From 0 to 15 s, the reference is fixed at zero, and, in this case, it is not required reactive power in the grid. At 15 s, the reactive reference changes to 0.1 p.u. and returns to zero reference in 20 s. The same occurs at 30 s, where the reference changes to -0.1 p.u., returning to zero in 35 s. In all the cases, i_q is satisfactorily controlled to its reference by the current control loop. Figure 6.19b shows the reactive power exchanged with the grid. It can be observed that the system

provides the desired reactive power, which varies between 0.25 and -0.25 MVAr, remaining at zero (unity power factor) for some periods.
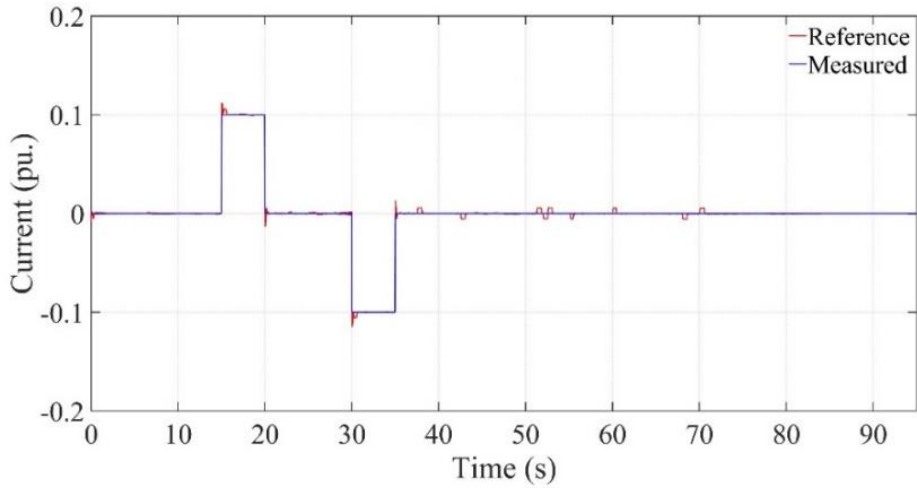
(a)
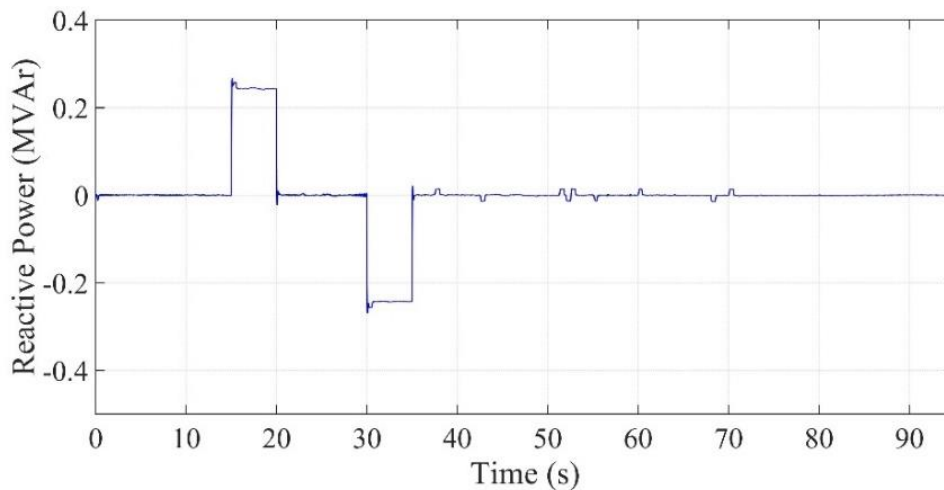
(b)

Figure 6.19. Simulation 3: Reactive power control with initial SOC 50% (a) i_q control and (b) reactive power

As in the previous case, the WT voltage V_{in_wind} and PV voltage V_{in_pv} remain around 930 V and 573 V, respectively, varying slightly to achieve the MPPT. Although the voltage V_{in_wind} was more sensitive to changes implemented in the reactive power, the system remains properly controlled, as can be seen in Figure 6.20a. The V_{in_pv} also remains properly controlled (Figure 6.20b).
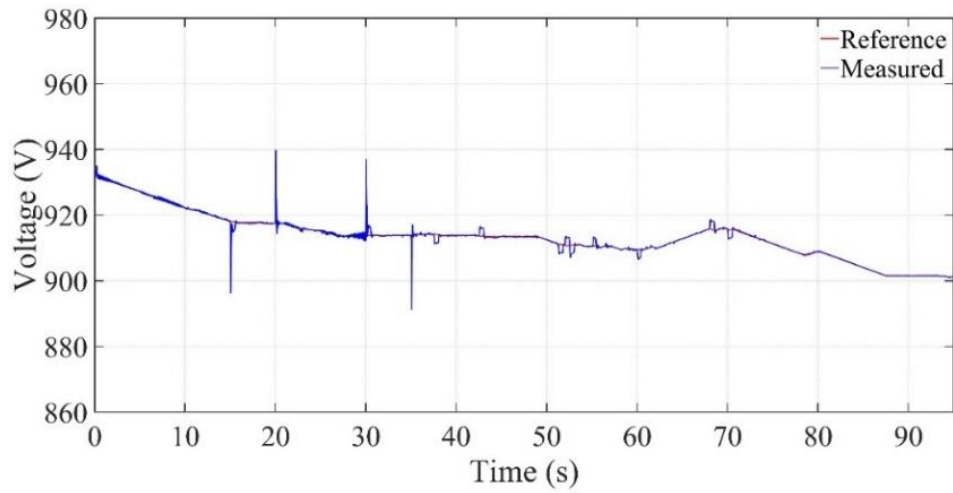
(a)
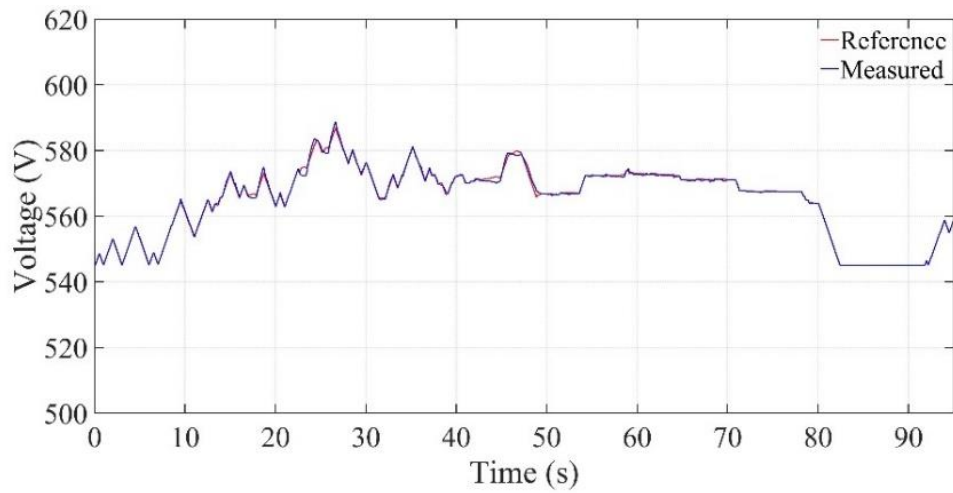

(b)

Figure 6.20. Simulation 3: Voltage V_{in} with initial SOC 50% (a) V_{in_wind} voltage control, (b) V_{in_pv} voltage control

For the case of a SOC close to the upper limit of 90%, the results can be seen in Figure 6.21, Figure 6.22 and Figure 6.23. In this simulation, the reactive power remains at zero (unity power factor) for all periods (Figure 6.21a and Figure 6.21b). Figure 6.21a shows that the i_q is controlled at the reference value (0), and Figure 6.21b shows the reactive power exchanged with the grid. The V_{in_wind} remains around 930 V and has less impact of abrupt variations (Figure 6.22), which occurs because Q remains at 0.
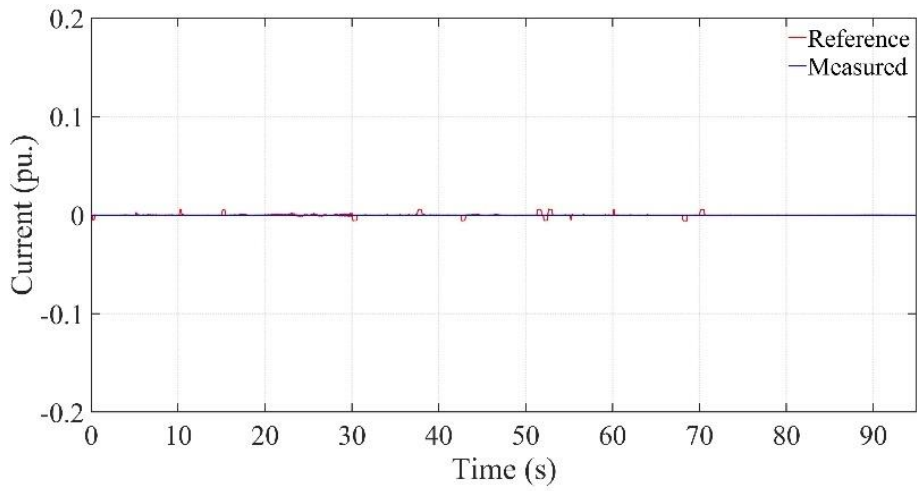
(a)
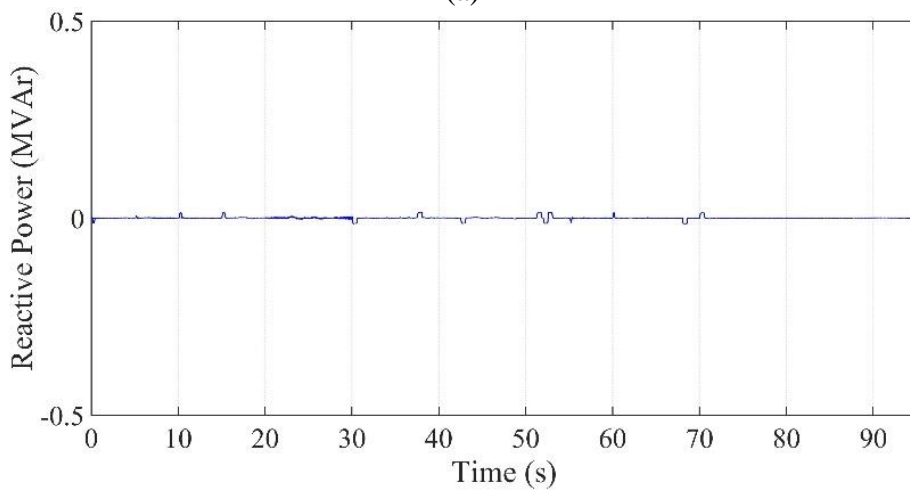
(b)

Figure 6.21. Simulation 3: Reactive power control with initial SOC 90% (a) i_q control and (b) reactive power
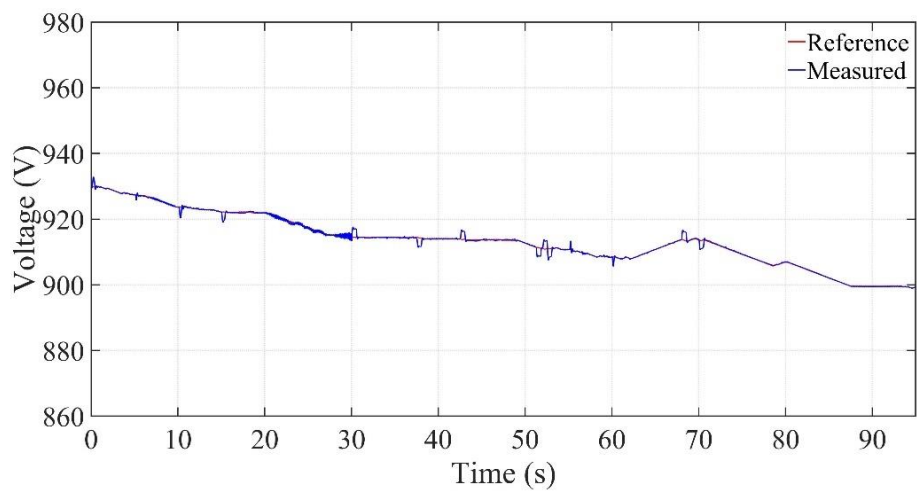
Figure 6.22. Simulation 3: Voltage V_{in_wind} voltage control

Regarding active power, Figure 6.23a shows the active power of the grid, renewable energies, BES, SO, load and the available power limits for the SO. From 0 to 15s, the BES is discharged to comply with the requirements of the SO (Figure 6.23c). From 15 to 30 s, the BES is charged softly since the BES is close to the upper limit of 90%. From 30 to 55 s, the SO does not request a defined power, and thus the BES is discharged with maximum power, when the price is favourable for it. However when the price is favourable to buy, the BES is charged softly to safeguard. At 55 s, the energy injected complies with the requirements of the SO. From 60 to 95 s, the working principle is similar to the situation between 30 to 55 s, selling or buying according to the energy price. The differences with the case of SOC 50% is the intensity of BES charge and discharge current, as can be noticed in Figure 6.23c.
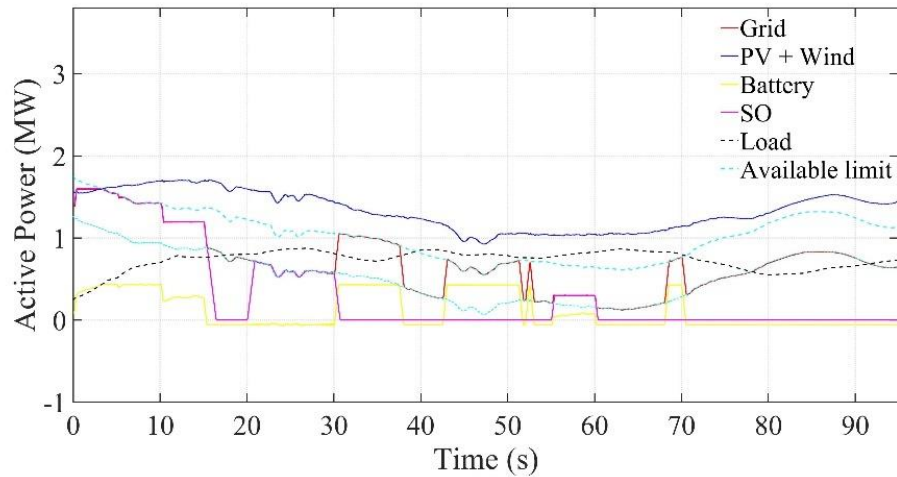

(a)
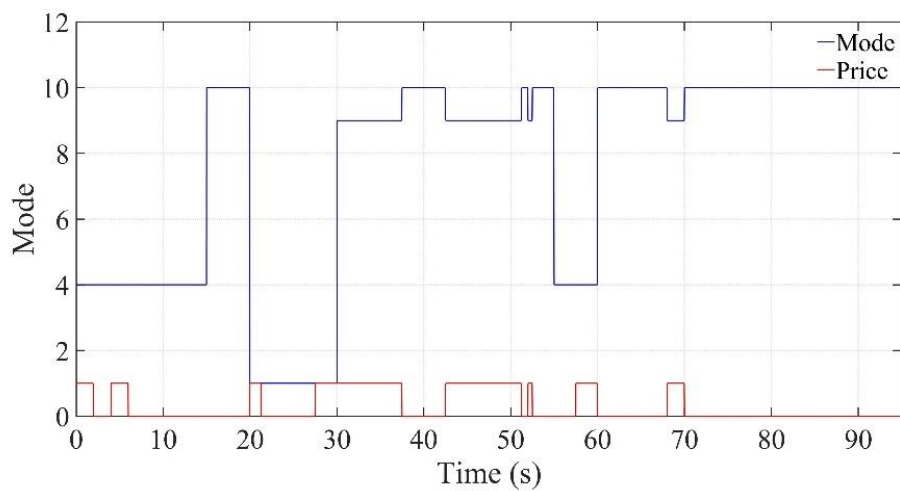
(b)
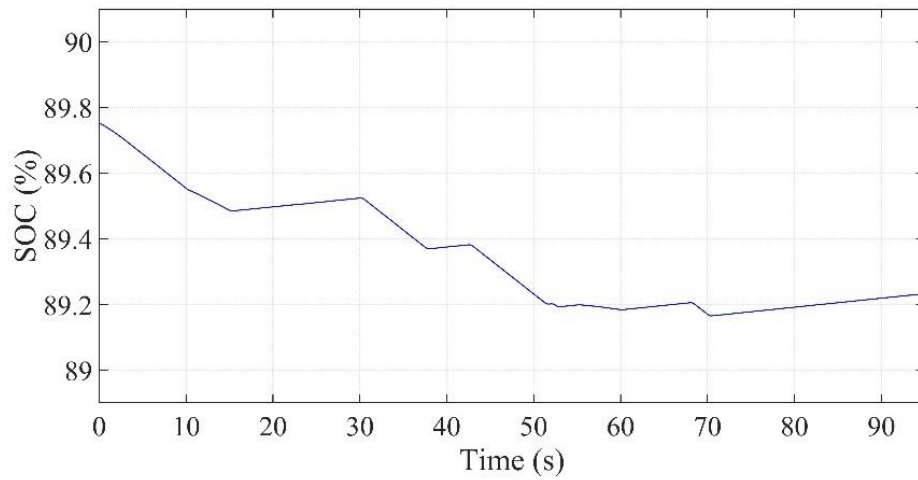
(c)

Figure 6.23. Simulation 3: (a) Grid active power, PV and WT active power, battery active power, SO active power, load active power and limits available power; (b) SOC close to upper limit 90%

Chapter 7: Conclusions

In this section, the main conclusions of the thesis are presented, based on the observation of the results obtained through the simulation of the developed hybrid configurations. In addition, the most relevant contributions are highlighted, and finally, future research is proposed.

7.1 CONCLUSIONS

The thesis conclusions can be divided into two stages. First, the thesis proposes a complete review of the current state of renewable energies, deepening the study of OWF, estimating future trends and their main implications. Then, this thesis proposes the study of a hybrid power plant consisting of a WT, a PV power plant, and a BES that share the same grid connection point and with a nominal power of MW.

To understand the development of renewable energies, it is very important to identify the trends that are driving the sector in certain vital aspects. In this thesis, the latest information demonstrating the status and trends of renewable energy mainly existing offshore wind farms above 150 MW in Europe is gathered and analyzed. The trends are derived and justified with actual data obtained from official reports and literature, not only based on the impressions of the authors or other experts. The primary aim of this part of the thesis is to establish the future trends in OWF and demonstrate the wide growth of this technology, especially in large-scale OWF, where the sector is very economically competitive. With this purpose, the most significant characteristics of 57 plants installed in Europe with rated power above 150 MW and fully commissioned until 2019, as well as 11 plants authorized or under construction, are studied in detail, drawing relevant conclusions from the data collected. The results show the trends in WTsize and capacity. The polynomial regression for the offshore WT average rated power estimates 12.7 and 18.8 MW for 2025 and 2030, whereas the linear regression indicates 8.6 MW and 10.7 MW, respectively. The installed power estimation for 2025 and 2030 is 47.4 and 76 GW, respectively, whereas the estimated number of OWF for 2025 and 2030 is 139 and 172.

Concerning the WT technology, the PMSG reaches 1565 turbines (33%) installed. However, it can be noticed a trend for offshore turbines targets at this

technology, since 1265 PMSG were installed between 2016 and 2019, against only 54 DFIG and 388 SCIG. Moreover, no DFIGs were installed in large wind farms in 2018 and 2019. Regarding distance to shore and water depth, the new OWF are moving away from the coast into deeper waters. For OWF above 150 MW, the average depth predicted for 2025 and 2030 is 44 and 53 m, and the distance estimations are 80 and 100 km, respectively. The main foundation technology is the monopile, used in 80% of the cases. However, there is a tendency towards the jacket due to the increase in the turbine power and depth. Another conclusion is referring to transmission technologies and the internal collection, there is an increase in the use of HVDC transmission lines justified by the larger distances to the coast and decreasing costs of the technology and a tendency towards 66 kV in the internal collection systems of the OWF as the rated power of the WTs grows. In addition, due to the increase in HVDC transmission, some new internal configuration topologies in DC are being proposed. The study gathers the most representative characteristics of large OWF in Europe. The figures given envisage a relevant growth of this type of power source for the following years. The development and increasing use of the OWF rely on a reduction in costs and a further maturation of the technology.

In a second stage of the thesis, a new configuration of a hybrid power plant consisting of a WT of 1.5 MW, a PV plant of 402 kW and a lithium-ion battery of 532 kW, totalling a 2.44 MW plant was implemented, and sharing the same connection point with a load of 1.2 MVA. The WT based on PMSG is connected to the grid through an uncontrolled rectifier qZSI with a BES, which is connected to the capacitor C_2 of the qZSI, eliminating the need for an additional converter. The capacitor C_1 of the impedance network works as a controlled DC bus and the PV system is connected to this capacitor C_1 through a DC/DC ZSC, which is responsible for ensuring the control of the PV power plant. Due to the complexity and long simulation time of the proposed hybrid system, two new averaged models for qZSI were presented in this thesis. In the ADM1, the voltage boost provided by the impedance network of the qZSI, as well as its dynamic behaviour, are modelled as a DC/DC converter using a switching-function model directly controlled through the shoot-through period. This DC equivalent-averaged model of the impedance network is connected to the averaged equivalent circuit of a three-phase VSI. On the other hand, the qZSI is modelled through the averaged model of a VSI with a static gain on the DC side in ADM2,

obtaining V_{dc} from V_{in} and boost factor B. Both proposed models are simple, easy to implement and to integrate into large power systems as an electric circuit based on controlled voltage and current sources.

To validate the averaged dynamic models (ADM 1 and ADM 2), a simulation, namely simulation 1, was carried out, where these models were used on a 1.5 MW PMSG-driven WT connected to a grid through an uncontrolled rectifier and a qZSI, and the active and reactive powers delivered to the grid were controlled by the qZSI. The time-domain response and control performances of the proposed models were evaluated under different operating conditions: fluctuating wind speed, variable reactive power reference, and grid disturbances. The results showed a suitable time-domain performance and a significant reduction in the simulation time for both averaged models compared to the SDM (ADM2 reached a 94% reduction in the simulation time). ADM1 showed a better response under grid disturbances than ADM2. Hence, ADM1 is recommended for studies in which such situations are relevant. ADM2 was 21 times faster than SDM and 1.6 times faster than ADM1 in the best scenario, due to the absence of dynamic states on the DC side. Therefore, ADM2 is preferred, where the speed of simulation and lower computational effort is more valuable than the response to grid disturbances. Notwithstanding the previous remarks, it can be concluded from the results obtained that both proposed averaged models can substitute the SDM with satisfactory accuracy in terms of time-domain response in steady-state stability studies, long-term simulations, or large electric power systems to reduce the computational effort and simulation time. Given the significant reduction in simulation time provided by the ADM2, two voltage sources emulating the terminals of C_1 and C_2 are added to enable the integration of PV and BES, respectively. This model was used on the studied hybrid power plant connected to the grid. The control of the system allowed a proper operation at the DC and AC sides of the system. The PMSG WT was simulated with above and below rated wind speeds to verify the pitch angle control, and the PV plant works with variable irradiance, proving the MPPT strategy for both sources. Furthermore, it was possible to ensure the stability of the system even under voltage disturbances and load variation. The simulation results showed an appropriate voltage regulation, active/reactive power generation and maximum power extraction from the WT and PV, thus verifying the effectiveness of the system.

Finally, an EMS was implemented to coordinate the performance of all energy sources (WT, PV, and BESS), load and the grid, allowing a reliable and controlled response. The main priority of the EMS is to meet the active and reactive power of the load demand, reducing the dependence of the grid and optimizing the use of energy, taking into account the power demanded by the SO, the renewable generation, the BES SOC and energy price. The second priority of EMS is to comply with the active and reactive power requirements of the SO, which must be within the minimum and maximum limits established according to the availability, informed by the operator of the hybrid power plant. If the SO does not set any operating instructions, then the system is operated to make an economic profit, buying energy from the grid and storing it in the BES (if possible), or selling the previously stored energy. The simulation results showed an adequate performance of the hybrid power plant. The control strategy implemented with EMS enabled the coordination of all renewable energy sources, load and grid, where the ZSCs played a key role.

7.2 MAIN CONTRIBUTIONS OF THE THESIS

Several contributions can be mentioned with the development of the thesis, and the main can be summarized here.

- An extensive bibliographical review of renewable energy sources in the world, with a detailed study of 57 plants installed in Europe with rated power above 150 MW and fully commissioned until 2019, as well as 11 plants authorized or under construction.

- Different topologies of hybrid power plants were studied to choose the most interesting from a technical point of view. At this point in the thesis, it has been possible to contribute to the determination of the proper connection point of the BES and PV in the qZSI. Contributing a new topology configuration for hybrid power plant, including WT, PV and battery.

- For the simulation of hybrid power systems, two new averaged models for qZSI were proposed. The models are simple, easy to implement and to integrate into large power systems as an electric circuit based on controlled voltage and current sources. Moreover, two voltage sources representing the terminals of C_1 and C_2 were added to enhance the proposed configuration and enable the integration of PV and BES, respectively.

- Different control strategies for hybrid power plants comprising WT, PV and BES were implemented and compared in different scenarios. These control systems were able to control satisfactorily the DC and AC side of the systems through the converters used in the WT and PV. The comparative studies included evaluation under wind fluctuation, irradiance variation and variable load demand. In addition, the system was exposed to grid failure conditions, attesting to its reliability.

- Two EMS were implemented to coordinate the performance of all energy sources. The EMS is responsible for determining when the BES should be charged, paying particular attention to allowable SOC levels. The proposed EMS guarantees the effective fulfilment of the determined energy service priorities. For the developed EMS, the load has priority concerning the grid and the EMS is able to sell or buy energy according to the financial interest of the plant.

7.3 FUTURE WORKS

In this chapter, future research areas are appointed in the field of the studied topic and as an extension of the work performed in this thesis:

- The use of other energy storage technologies can be added to the capacitor C_2, comparing which option is more interesting from the technical and economical point of view. The interest in the storage elements is increasingly and needed, considering the inherited characteristic regards fluctuating generation of renewable systems (PV, wind).

- Other devices, such as electric vehicles and hydrogen systems, ultra-capacitors, and batteries, could also be added to the same configuration presented in this thesis, substituting the PV system for one of the mentioned devices.

- Other ZSC could be studied to connect the PMSG WT to the grid, such as Transformer-Based Z-Source/Quasi-Z-Source Inverters. In addition, the possibility of adding storage systems to these converters can be studied.

- Other EMS strategies, adding optimized systems, can generate interesting results, because the optimization of the cost of using the grid can be profitable

for the plant, and real cases of the electricity market could be considered and compared with results obtained of the optimization.

- The application of model predictive control for the PV power plant and WT can bring anticipate information for the hybrid power plant operation, and with this, optimize the results obtained.

- Advanced control techniques and alternative control strategies can be interesting to regulate the power delivered to the grid, while ensuring a stable and satisfactory operation.

Bibliography

[1]   Expronews 2019. https://expronews.com/2019/05/18/the-world-needs-more-energy/ (accessed May 20, 2019).

[2]   IPCC. Climate Change 2021: The Physical Science Basis. Contribution of Working Group I to the Sixth Assessment Report of the Intergovernmental Panel on Climate Change [Masson-Delmotte, V., P. Zhai, A. Pirani, S. L. Connors, C. Péan, S. Berger, N. Caud, Y. Chen,. Cambridge Univ Press 2021:3949.

[3]   Lee J, Zhao F. Global Wind Report 2021. Glob Wind Energy Counc 2021:75.

[4]   Wagner H-J, Baack C, Eickelkamp T, Epe A, Lohmann J, Troy S. Life cycle assessment of the offshore wind farm alpha ventus. Energy 2011;36:2459–64. doi:10.1016/j.energy.2011.01.036.

[5]   Parida B, Iniyan S, Goic R. A review of solar photovoltaic technologies. Renew Sustain Energy Rev 2011;15:1625–36. doi:10.1016/j.rser.2010.11.032.

[6]   González JM, Domínguez JA, Ruiz JM, Alonso C. Ultracapacitors utilization to improve the efficiency of photovoltaic installations. Sol Energy 2016;134:484–93. doi:10.1016/j.solener.2016.04.051.

[7]   Klessmann C, Rathmann M, de Jager D, Gazzo A, Resch G, Busch S, et al. Policy options for reducing the costs of reaching the European renewables target. Renew Energy 2013;57:390–403. doi:10.1016/j.renene.2013.01.041.

[8]   G. Masson and I. Kaizuka. IEA PVPS report - Trends in Photovoltaic Applications 2020. 2020.

[9]   Roumila Z, Rekioua D, Rekioua T. Energy management based fuzzy logic controller of hybrid system wind/photovoltaic/diesel with storage battery. Int J Hydrogen Energy 2017;42:19525–35. doi:10.1016/j.ijhydene.2017.06.006.

[10]   Thomsen KE. Offshore wind: A Comprehensive Guide to Successful Offshore Wind Farm Installation. Second edi. 2014.

[11]   Chen K, Yu J. Short-term wind speed prediction using an unscented Kalman filter based state-space support vector regression approach. Appl Energy 2014;113:690–705. doi:10.1016/j.apenergy.2013.08.025.

[12]   Tamalouzt S, Benyahia N, Rekioua T, Rekioua D, Abdessemed R. Performances analysis of WT-DFIG with PV and fuel cell hybrid power sources system associated with hydrogen storage hybrid energy system. Int J Hydrogen Energy 2016;41:21006–21. doi:10.1016/j.ijhydene.2016.06.163.

[13]   Tamalouzt S, Benyahia N, Rekioua T, Rekioua D, Abdessemed R. Wind turbine-DFIG/photovoltaic/fuel cell hybrid power sources system associated with hydrogen storage energy for micro-grid applications. 2015 3rd Int. Renew. Sustain. Energy Conf., IEEE; 2015, p. 1–6. doi:10.1109/IRSEC.2015.7455060.

[14] Vivas FJ, De las Heras A, Segura F, Andújar JM. A review of energy management strategies for renewable hybrid energy systems with hydrogen backup. Renew Sustain Energy Rev 2018;82:126–55. doi:10.1016/j.rser.2017.09.014.

[15] Seung-Tak Kim, Byung-Kwan Kang, Sun-Ho Bae, Jung-Wook Park. Application of SMES and Grid Code Compliance to Wind/Photovoltaic Generation System. IEEE Trans Appl Supercond 2013;23:5000804–5000804. doi:10.1109/TASC.2012.2232962.

[16] Aly HH, El-Hawary ME. An overview of offshore wind electric energy resources. CCECE 2010, IEEE; 2010, p. 1–8. doi:10.1109/CCECE.2010.5575209.

[17] Zhang Z, Chen A, Matveev A, Nilssen R, Nysveen A. High-power Generators for Offshore Wind Turbines. Energy Procedia 2013;35:52–61. doi:10.1016/j.egypro.2013.07.158.

[18] Zhaoqiang Zhang, Matveev A, Ovrebo S, Nilssen R, Nysveen A. State of the art in generator technology for offshore wind energy conversion systems. 2011 IEEE Int. Electr. Mach. Drives Conf., IEEE; 2011, p. 1131–6. doi:10.1109/IEMDC.2011.5994760.

[19] Arrambide I, Zubia I, Madariaga A. Critical review of offshore wind turbine energy production and site potential assessment. Electr Power Syst Res 2019;167:39–47. doi:10.1016/j.epsr.2018.10.016.

[20] Cabrera-Tobar A, Bullich-Massagué E, Aragüés-Peñalba M, Gomis-Bellmunt O. Topologies for large scale photovoltaic power plants. Renew Sustain Energy Rev 2016;59:309–19. doi:10.1016/j.rser.2015.12.362.

[21] Viju Nair V, Gulur S, Chattopadhyay R, Beddingfield R, Mathur S, Bhattacharya S, et al. Large Scale Grid Integration of Photovoltaic and Energy Storage Systems Using Triple Port Dual Active Bridge Converter Modules. IEEE Power Energy Soc Gen Meet 2018;2018-Augus. doi:10.1109/PESGM.2018.8586158.

[22] Freitas TRS De, Menegáz PJM, Simonetti DSL. Rectifier topologies for permanent magnet synchronous generator on wind energy conversion systems : A review. Renew Sustain Energy Rev 2016;54:1334–44. doi:10.1016/j.rser.2015.10.112.

[23] Blaabjerg F, Liserre M, Ma K. Power Electronics Converters for Wind Turbine Systems. IEEE Trans Ind Appl 2012;48:708–19. doi:10.1109/TIA.2011.2181290.

[24] Peng FZ. Z-source inverter. Conf. Rec. 2002 IEEE Ind. Appl. Conf. 37th IAS Annu. Meet. (Cat. No.02CH37344), vol. 2, IEEE; 2002, p. 775–81. doi:10.1109/IAS.2002.1042647.

[25] Peng FZ. Z-Source Inverter. IEEE Trans Ind Appl 2003;39:775–81.

[26] Ellabban O, Abu-Rub H. An overview for the Z-Source Converter in motor drive applications. Renew Sustain Energy Rev 2016;61:537–55.

doi:10.1016/j.rser.2016.04.004.

[27]   Zhang G, Li Z, Zhang B, Halang WA. Power electronics converters : Past , present and future. Renew Sustain Energy Rev 2018;81:2028–44. doi:10.1016/j.rser.2017.05.290.

[28]   Anderson J, Peng FZ. A Class of Quasi-Z-Source Inverters. 2008 IEEE Ind. Appl. Soc. Annu. Meet., Edmonton, AB: IEEE; 2008, p. 1–7. doi:10.1109/08IAS.2008.301.

[29]   Yushan Liu, Haitham Abu-Rub, Baoming Ge, Frede Blaabjerg, Omar Ellabban PCL. Impedance Source Power Eletronic Converters. 2016.

[30]   Li X, Hui D, Lai X. Battery energy storage station (BESS)-based smoothing control of photovoltaic (PV) and wind power generation fluctuations. IEEE Trans Sustain Energy 2013;4:464–73. doi:10.1109/TSTE.2013.2247428.

[31]   Althubaiti M, Bernard M, Musilek P. Fuzzy Logic Controller for Hybrid Renewable Energy System with Multiple Types of Storage. IEEE 30th Can Conf Electr Comput Eng 2017:699–704. doi:10.1109/CCECE.2017.7946738.

[32]   Toledo OM, Oliveira Filho D, Diniz ASAC. Distributed photovoltaic generation and energy storage systems: A review. Renew Sustain Energy Rev 2010;14:506–11. doi:10.1016/j.rser.2009.08.007.

[33]   Agency IE. Renewables 2021: Analysis and forecast to 2026 2021.

[34]   Swennen R. China's Energy Revolution in the Context of the Global Energy Transition. Cham: Springer International Publishing; 2020. doi:10.1007/978-3-030-40154-2.

[35]   Nelson VC. Introduction to Renewable Energy. CRC Press; 2011. doi:10.1201/9781439891209.

[36]   Ellabban O, Abu-Rub H, Blaabjerg F. Renewable energy resources: Current status, future prospects and their enabling technology. Renew Sustain Energy Rev 2014;39:748–64. doi:10.1016/j.rser.2014.07.113.

[37]   IEA. Net Zero by 2050: A Roadmap for the Global Energy Sector. Int Energy Agency 2021:224.

[38]   European Commission. 2030 Climate Target Plan n.d. https://ec.europa.eu/clima/eu-action/european-green-deal/2030-climate-target-plan_en (accessed December 9, 2021).

[39]   Barroco F, Cunha F, Cândida M, Miranda A De, Carvalho L, Fernandes F, et al. Renewable energy planning policy for the reduction of poverty in Brazil : lessons from Juazeiro. Environ Dev Sustain 2021;23:9792–810. doi:10.1007/s10668-020-00857-0.

[40]   Yang X, He L, Xia Y, Chen Y. Effect of government subsidies on renewable energy investments: The threshold effect. Energy Policy 2019;132:156–66. doi:10.1016/j.enpol.2019.05.039.

[41]   Burke MJ, Stephens JC. Political power and renewable energy futures: A

critical review. Energy Res Soc Sci 2018;35:78–93. doi:10.1016/j.erss.2017.10.018.

[42]   Newell RG, Pizer WA, Raimi D. U.S. federal government subsidies for clean energy: Design choices and implications. Energy Econ 2019;80:831–41. doi:10.1016/j.eneco.2019.02.018.

[43]   Safari A, Das N, Langhelle O, Roy J, Assadi M. Natural gas: A transition fuel for sustainable energy system transformation? Energy Sci Eng 2019;7:1075–94. doi:10.1002/ese3.380.

[44]   Mohammad N, Mohamad Ishak WW, Mustapa SI, Ayodele BV. Natural Gas as a Key Alternative Energy Source in Sustainable Renewable Energy Transition: A Mini Review. Front Energy Res 2021;9:1–6. doi:10.3389/fenrg.2021.625023.

[45]   (IAEA) I atomic energy agency. Nuclear Energy for a Net Zero World. 2021.

[46]   Abdulla A, Vaishnav P, Sergi B, Victor DG. Limits to deployment of nuclear power for decarbonization: Insights from public opinion. Energy Policy 2019;129:1339–46. doi:10.1016/j.enpol.2019.03.039.

[47]   Richard W. The Future of Nuclear Power. Environ Sci Technol 1992;26:1116–20. doi:10.1021/es50002a013.

[48]   Bilgili M, Yasar A, Simsek E. Offshore wind power development in Europe and its comparison with onshore counterpart. Renew Sustain Energy Rev 2011;15:905–15. doi:10.1016/j.rser.2010.11.006.

[49]   Perveen R, Kishor N, Mohanty SR. Off-shore wind farm development: Present status and challenges. Renew Sustain Energy Rev 2014;29:780–92. doi:10.1016/j.rser.2013.08.108.

[50]   Esteban MD, Diez JJ, López JS, Negro V. Why offshore wind energy? Renew Energy 2011;36:444–50.

[51]   Enevoldsen P, Valentine SV. Do onshore and offshore wind farm development patterns differ? Energy Sustain Dev 2016;35:41–51. doi:10.1016/j.esd.2016.10.002.

[52]   Sun X, Huang D, Wu G. The current state of offshore wind energy technology development. Energy 2012;41:298–312.

[53]   Rodrigues S, Restrepo C, Kontos E, Teixeira Pinto R, Bauer P. Trends of offshore wind projects. Renew Sustain Energy Rev 2015;49:1114–35. doi:10.1016/j.rser.2015.04.092.

[54]   deCastro M, Salvador S, Gómez-Gesteira M, Costoya X, Carvalho D, Sanz-Larruga FJ, et al. Europe, China and the United States: Three different approaches to the development of offshore wind energy. Renew Sustain Energy Rev 2019;109:55–70. doi:10.1016/j.rser.2019.04.025.

[55]   Higgins P, Foley AM. Review of offshore wind power development in the United Kingdom. 2013 12th Int. Conf. Environ. Electr. Eng., IEEE; 2013, p. 589–93. doi:10.1109/EEEIC.2013.6549584.

[56] Colmenar-Santos A, Perera-Perez J, Borge-Diez D, DePalacio-Rodríguez C. Offshore wind energy: A review of the current status, challenges and future development in Spain. Renew Sustain Energy Rev 2016;64:1–18. doi:10.1016/j.rser.2016.05.087.

[57] Behrendt Lars. Taxes and incentives for renewable energy. 2015.

[58] Wilkes J, Moccia J, Fichaux DN, Guillet J, Wilczek P. The European offshore wind industry - key trends and statistics 2009. 2010.

[59] Giorgio Corbetta. The European offshore wind industry - Key trends and statistics 2013. 2013.

[60] Pineda I, Tardieu P. The European offshore wind industry - Key trends and statistics 2016. 2016.

[61] Wilkes J, Moccia J. The European offshore wind industry key trends and statistics 2010. 2011.

[62] Wilkes J, Jacopo Moccia, Arapogianni A, Dragan M, Plytas N, Genachte A-B, et al. The European offshore wind industry key 2011 trends and statistics. European Wind Energy Association; 2012.

[63] Corbetta G, Mbistrova A, Ho A, Guillet J, Pineda I, Wilkes J. The European offshore wind industry - key trends and statistics 2014. 2015.

[64] Ho A, Mbistrova A, Corbetta G. The European offshore wind industry - key trends and statistics 2015. 2016.

[65] Tom Remy, Ariola Mbistrova. Offshore Wind in Europe - Key trends and statistics 2017. 2018.

[66] Intelligence WB, Komusanac I, Fraile D, Guy Brindley. Wind energy in Europe in 2018 - Trends and statistics. 2019.

[67] Intelligence WB, Komusanac I, Fraile D, Guy Brindley. Wind energy in Europe in 2019 - Trends and statistics. 2020.

[68] Giorgio C, Ho A, Pineda I. Wind energy scenarios for 2030. 2015.

[69] Nghiem A, Pineda I. Wind energy in Europe: Scenarios for 2030. Wind Eur 2017:32.

[70] Ho A, Mbistrova A. The European offshore wind industry– key trends and statistics 2016. 2017.

[71] McDonald A, Carroll J. Design of generators for offshore wind turbines. Offshore Wind Farms, Elsevier; 2016, p. 159–92. doi:10.1016/B978-0-08-100779-2.00008-8.

[72] BARD Holding. The Wind Power 2013. https://www.thewindpower.net/turbine_en_291_bard_vm.php (accessed May 2, 2019).

[73] Repower Systems. Wind Turbine 5M - Technical specifications 2004:1–57.

[74] Senvion GmbH. Wind Turbine 6.2M - 126 - Technical specifications 2018:2.

[75]   A/S VWS. Wind Turbine V90-2MW - Technical specifications 2011:20.

[76]   A/S VWS. Wind Turbine V90-3MW - Technical specifications 2011:20.

[77]   ADWEN. ADWEN 2013. http://www.adwenoffshore.com/products/5-mw-turbines/adwen-5-mw-platform/ (accessed May 2, 2019).

[78]   Areva. Wind Turbine M 5000-135 - Technical specifications 2011:1.

[79]   Energy GER. Wind Turbine Haliade 150 - 6MW Technical specifications. 2014.

[80]   A/S VWS. Wind Turbine Vestas V164-8.4MW - Technical specifications 2019:1–8.

[81]   Siemens. Wind Turbine SWT-3M-108 - Technical specifications 2007.

[82]   Siemens. Wind Turbine SWT-6.0-154 Technical specifications 2016:3.

[83]   Vestas Wind Systems A/S. Wind Turbine V112-3.0 MW - Technical specifications 2009:20.

[84]   Vestas Wind Systems A/S. Vestas V164-8.0MW - Technical specifications 2011:8.

[85]   Siemens. Wind Turbine SWT-7.0-154 - Technical specifications 2016.

[86]   Siemens. Wind Turbine SWT-3.6-107 - Technical specifications 2011.

[87]   Siemens. Wind Turbine SWT-3.6-120 - Technical specifications 2011:10.

[88]   Siemens. Wind Turbine SWT-4.0-120 - Technical specifications 2016:3.

[89]   Siemens. Wind Turbine SWT-2.3-93 - Technical specifications 2009:8.

[90]   A/S VWS. Wind Turbine V112 - 3.3/3.45 MW General Specification 2015:1–62.

[91]   A/S VWS. Vestas Wind Systems A/S 2019. https://www.vestas.com/ (accessed May 5, 2019).

[92]   Energy SGR. Siemens Gamesa Renewable Energy 2019. https://www.siemensgamesa.com/en-int/products-and-services (accessed May 5, 2019).

[93]   Nicolas Fichaux, Jos Beurskens, Peter Hjuler Jensen JW. Design limits and solutions for very large wind turbines A 20 MW turbine is feasible. UpWind / EWEA 2011:1–103.

[94]   Sartori L, Bellini F, Croce A, Bottasso C. Preliminary design and optimization of a 20MW reference wind turbine. J Phys Conf Ser 2018;1037:042003. doi:10.1088/1742-6596/1037/4/042003.

[95]   Hoang T-K, Queval L, Berriaud C, Vido L. Design of a 20-MW Fully Superconducting Wind Turbine Generator to Minimize the Levelized Cost of Energy. IEEE Trans Appl Supercond 2018;28:1–5. doi:10.1109/TASC.2018.2810309.

[96] Peeringa J, Brood R, Ceyhan O, Wouter E, de Winkel G. Upwind 20MW Wind Turbine Pre- Design. Ecn-E–11-017 2011.

[97] Eerens H, de Visser E. Wind-energy potential in Europe 2020-2030. 2008.

[98] Pickard WF. The limits of HVDC transmission. Energy Policy 2013;61:292–300. doi:10.1016/j.enpol.2013.03.030.

[99] Green J, Bowen A, Fingersh LJJ, Wan Y. Electrical collection and transmission systems for offshore wind power. 2007 Offshore Technol Conf 2007:10.

[100] Reed GF, Al Hassan HA, Korytowski MJ, Lewis PT, Grainger BM. Comparison of HVAC and HVDC solutions for offshore wind farms with a procedure for system economic evaluation. 2013 IEEE Energytech, IEEE; 2013, p. 1–7. doi:10.1109/EnergyTech.2013.6645302.

[101] Lazaridis LP. Economic Comparison of HVAC and HVDC Solutions for Large Offshore Wind Farms under Special Consideration of Reliability. Electr Eng 2005;12:203–8.

[102] Kalair A, Abas N, Khan N. Comparative study of HVAC and HVDC transmission systems. Renew Sustain Energy Rev 2016;59:1653–75. doi:10.1016/j.rser.2015.12.288.

[103] Lakshmanan P, Liang J, Jenkins N. Assessment of collection systems for HVDC connected offshore wind farms. Electr Power Syst Res 2015;129:75–82. doi:10.1016/j.epsr.2015.07.015.

[104] Zubiaga M, Abad G, Barrena J a., Aurtenetxea S, A. Cárcar. Energy Transmission and Grid Integration of AC Offshore Wind Farms. InTech; 2012.

[105] Davidson CC. The Use of High-Voltage Direct Current Transmission for Offshore Wind Projects. Eng Technol Ref 2014:1–12. doi:10.1049/etr.2014.0001.

[106] Carr J, Das D, Li J, Pan J, Ebner S, Apeldoorn O. Modular multilevel converter for direct MVDC connection of offshore wind farms. 2015 IEEE Energy Convers. Congr. Expo., IEEE; 2015, p. 976–82. doi:10.1109/ECCE.2015.7309794.

[107] Holtsmark N, Bahirat HJ, Molinas M, Mork BA, Hoidalen HK. An All-DC Offshore Wind Farm With Series-Connected Turbines: An Alternative to the Classical Parallel AC Model? IEEE Trans Ind Electron 2013;60:2420–8. doi:10.1109/TIE.2012.2232255.

[108] de Prada Gil M, Gomis-Bellmunt O, Sumper A. Technical and economic assessment of offshore wind power plants based on variable frequency operation of clusters with a single power converter. Appl Energy 2014;125:218–29. doi:10.1016/j.apenergy.2014.03.031.

[109] de Prada M, Igualada L, Corchero C, Gomis-Bellmunt O, Sumper A. Hybrid AC-DC Offshore Wind Power Plant Topology: Optimal Design. IEEE Trans Power Syst 2015;30:1868–76. doi:10.1109/TPWRS.2014.2354457.

[110] Mulroy MJ, Ebden C, Neumann AP. The Use of 66kV technology for Offshore Wind Demonstration sites. 3rd Renew. Power Gener. Conf. (RPG 2014), vol. 2014, Institution of Engineering and Technology; 2014, p. 2.1.4-2.1.4. doi:10.1049/cp.2014.0832.

[111] Ferguson A, De Villiers P, Fitzgerald B, Matthiesen J. Benefits in moving the inter-array voltage from 33 kV to 66 kV AC for large offshore wind farms. Eur Wind Energy Conf Exhib 2012, EWEC 2012 2012;2:902–9.

[112] Thyssen A. Wind power plants internal distribution system and grid connection A technical and economical comparison between a 33 kV and a 66 kV. 2015.

[113] Schlemmer T, Greedy L. 66 kV Systems for Offshore Wind Farms. 2015.

[114] Prässler T, Schaechtele J. Comparison of the Financial Attractiveness Among Prospective Offshore Wind Parks in Selected European Countries. SSRN Electron J 2011;45:86–101. doi:10.2139/ssrn.1940375.

[115] Hevia-Koch P, Klinge Jacobsen H. Comparing offshore and onshore wind development considering acceptance costs. Energy Policy 2019;125:9–19. doi:10.1016/j.enpol.2018.10.019.

[116] Barthelmie RJ, Pryor S. A Review of the Economics of Offshore Wind Farms. Wind Eng 2001;25:203–13. doi:10.1260/0309524011496024.

[117] Levitt AC, Kempton W, Smith AP, Musial W, Firestone J. Pricing offshore wind power. Energy Policy 2011;39:6408–21. doi:10.1016/j.enpol.2011.07.044.

[118] Green R, Vasilakos N. The economics of offshore wind. Energy Policy 2011;39:496–502. doi:10.1016/j.enpol.2010.10.011.

[119] Schwanitz VJ, Wierling A. Offshore wind investments – Realism about cost developments is necessary. Energy 2016;106:170–81. doi:10.1016/j.energy.2016.03.046.

[120] IRENA. Renewable Power Generation Costs in 2018. Abu Dhabi: International Renewable Energy Agency; 2019.

[121] Administration USEI. Levelized Cost and Levelized Avoided Cost of New Generation Resources in the Annual Energy Outlook 2019 Levelized Cost of Electricity. 2019.

[122] Musial W, Beiter P, Spitsen P, Nunemaker J, Gevorgian V. 2018 Offshore Wind Technologies Market Report. 2018.

[123] Global Wind Energy Council. Offshore wind. 2016.

[124] 4C Offshore 2018. https://www.4coffshore.com/ (accessed August 10, 2018).

[125] Musial W, Beiter P, Schwabe P, Tian T, Stehly T, Spitsen P. 2016 Offshore Wind Technologies Market Report. 2016.

[126] Agency EE. Europe's onshore and offshore wind energy potential: An assessment of environmental and economic constraints. vol. 6. 2009.

[127] Bergström L, Kautsky L, Malm T, Rosenberg R, Wahlberg M, Åstrand Capetillo N, et al. Effects of offshore wind farms on marine wildlife—a generalized impact assessment. Environ Res Lett 2014;9:034012. doi:10.1088/1748-9326/9/3/034012.

[128] Vaissière A, Levrel H, Pioch S, Carlier A. Biodiversity offsets for offshore wind farm projects: The current situation in Europe. Mar Policy 2014;48:172–83. doi:10.1016/j.marpol.2014.03.023.

[129] European Comission to the Environment. Natura 2000 2019. https://ec.europa.eu/environment/nature/natura2000/index_en.htm (accessed December 10, 2019).

[130] Bloomfield S, Roberts C, Cotterell M. Batteries and Solar Power: Guidance for domestic and small commercial consumers. Build Res Establ 2016.

[131] Mariaud A, Acha S, Ekins-Daukes N, Shah N, Markides CN. Integrated optimisation of photovoltaic and battery storage systems for UK commercial buildings. Appl Energy 2017;199:466–78. doi:10.1016/j.apenergy.2017.04.067.

[132] Grgi I, Basic M, Vukadinovic D. Optimization of electricity production in a grid-tied solar power system with a three-phase quasi-Z-source inverter. J Clean Prod 2019;221:656–66. doi:https://doi.org/10.1016/j.jclepro.2019.02.245.

[133] Ghaderi D, Padmanaban S, Maroti PK, Papari B, Holm-nielsen JB. Design and implementation of an improved sinusoidal controller for a two-phase enhanced impedance source boost. Comput Electr Eng 2020;83. doi:https://doi.org/10.1016/j.compeleceng.2020.106575.

[134] Liu Y, Ge B, Abu-Rub H, Peng FZ. Overview of Space Vector Modulations for Three-Phase Z-Source/Quasi-Z-Source Inverters. IEEE Trans Power Electron 2014;29:2098–108. doi:10.1109/TPEL.2013.2269539.

[135] Yilmaz AR, Erkmen B. FPGA-Based Space Vector PWM and Closed Loop Controllers Design for the Z Source Inverter. IEEE Access 2019;7:130865–73. doi:10.1109/ACCESS.2019.2940670.

[136] Mosa M, Balog RS, Abu-Rub H. High-performance predictive control of quasi-impedance source inverter. IEEE Trans Power Electron 2017;32:3251–62. doi:10.1109/TPEL.2016.2531989.

[137] Li Y, Peng FZ, Cintron-Rivera JG, Jiang S. Controller design for quasi-Z-source inverter in photovoltaic systems. 2010 IEEE Energy Convers. Congr. Expo. ECCE 2010 - Proc., IEEE; 2010, p. 3187–94. doi:10.1109/ECCE.2010.5618288.

[138] Sun D, Ge B, Bi D, Peng FZ. Analysis and control of quasi-Z source inverter with battery for grid-connected PV system. Int J Electr Power Energy Syst 2013;46:234–40. doi:10.1016/j.ijepes.2012.10.008.

[139] Ge B, Abu-Rub H, Peng FZ, Lei Q, De Almeida AT, Ferreira FJTE, et al. An energy-stored quasi-Z-source inverter for application to photovoltaic power

system. IEEE Trans Ind Electron 2013;60:4468–81. doi:10.1109/TIE.2012.2217711.

[140] Sun D, Ge B, Liang W, Abu-Rub H, Peng FZ. An energy stored Quasi-Z-Source cascade multilevel inverter-based photovoltaic power generation system. IEEE Trans Ind Electron 2015;62:5458–67. doi:10.1109/TIE.2015.2407853.

[141] Liu Y, Ge B, Abu-Rub H, Peng FZ. Modelling and controller design of quasi-Z-source inverter with battery-based photovoltaic power system. IET Power Electron 2014;7:1665–74. doi:10.1049/iet-pel.2013.0389.

[142] Guichi A, Talha A, Madjid E, Mekhilef S. Energy management and performance evaluation of grid connected PV- battery hybrid system with inherent control scheme. Sustain Cities Soc 2018;41:490–504. doi:10.1016/j.scs.2018.05.026.

[143] Sing C, Jia Y, Lei L, Xu Z, Mcculloch MD, Po K. A comprehensive review on large-scale photovoltaic system with applications of electrical energy storage. Renew Sustain Energy Rev 2017;78:439–51. doi:10.1016/j.rser.2017.04.078.

[144] Lai CS, Jia Y, Lai LL, Xu Z, McCulloch MD, Wong KP. A comprehensive review on large-scale photovoltaic system with applications of electrical energy storage. Renew Sustain Energy Rev 2017;78:439–51. doi:10.1016/j.rser.2017.04.078.

[145] Denholm P, Eichman J, Margolis R. Evaluating the Technical and Economic Performance of PV Plus Storage Power Plants : Report Summary 2017.

[146] Periyanayagam M, Suresh Kumar V, Chokkalingam B, Padmanaban S, Mihet-Popa L, Adedayo Y. A modified high voltage gain quasi-impedance source coupled inductor multilevel inverter for photovoltaic application. Energies 2020;13. doi:10.3390/en13040874.

[147] Yuan J, Yang Y, Blaabjerg F. A Switched Quasi-Z-Source Inverter with Continuous Input Currents. Energies 2020;13:1390. doi:10.3390/en13061390.

[148] Chung HSH, Wang H, Blaabjerg F, Pecht M. Reliability of power electronic converter systems. 2016. doi:10.1049/PBPO080E.

[149] Piasecki S, Zaleski J, Jasinski M, Bachman S, Turzyński M. Analysis of ac/dc/dc converter modules for direct current fast-charging applications. Energies 2021;14:1–24. doi:10.3390/en14196369.

[150] Canteli MM. Regulación, control y protección de Máquinas Eléctricas 2010:1–52.

[151] Cabrera-Tobar A, Bullich-Massagué E, Aragüés-Peñalba M, Gomis-Bellmunt O. Topologies for large scale photovoltaic power plants. Renew Sustain Energy Rev 2016;59:309–19. doi:10.1016/j.rser.2015.12.362.

[152] Sheik Mohammed S, Devaraj D, Imthias Ahamed TP. A novel hybrid Maximum Power Point Tracking Technique using Perturb & Observe algorithm and Learning Automata for solar PV system. Energy 2016;112:1096–106. doi:10.1016/j.energy.2016.07.024.

[153] Mao M, Zhang L, Duan P, Duan Q, Yang M. Grid-connected modular PV-Converter system with shuffled frog leaping algorithm based DMPPT controller. Energy 2018;143:181–90. doi:10.1016/j.energy.2017.10.099.

[154] Barelli L, Bidini G, Pelosi D, Ciupageanu DA, Cardelli E, Castellini S, et al. Comparative analysis of AC and DC bus configurations for flywheel-battery HESS integration in residential micro-grids. Energy 2020;204. doi:10.1016/j.energy.2020.117939.

[155] Shen M, Joseph A, Wang J, Peng FZ, Adams DJ. Comparison of traditional inverters and Z-source inverter for fuel cell vehicles. IEEE Trans Power Electron 2007;22:1453–63. doi:10.1109/TPEL.2007.900505.

[156] Fang Zheng Peng. Z-source inverter. IEEE Trans Ind Appl 2003;39:504–10. doi:10.1109/TIA.2003.808920.

[157] Vinnikov D, Roasto I, Strzelecki R, Adamowicz M. Step-Up DC/DC Converters With Cascaded Quasi-Z-Source Network. IEEE Trans Ind Electron 2012;59:3727–36. doi:10.1109/TIE.2011.2178211.

[158] Poorali B. Improved High Step-Up Z -Source DC – DC Converter. IEEE Trans Power Electron 2018;33:9647–55.

[159] Ortega M, Ortega MV, Jurado F, Carpio J, Vera D. Bidirectional DC–DC converter with high gain based on impedance source. IET Power Electron 2019;12:2069–78. doi:10.1049/iet-pel.2018.5385.

[160] Li Y, Jiang S, Cintron-Rivera JG, Peng FZ. Modeling and Control of Quasi-Z-Source Inverter for Distributed Generation Applications. IEEE Trans Ind Electron 2013;60:1532–41. doi:10.1109/TIE.2012.2213551.

[161] Mosa M, Abu-Rub H, Rodriguez J. High performance predictive control applied to three phase grid connected Quasi-Z-Source Inverter. IECON Proc. (Industrial Electron. Conf., vol. 1, 2013, p. 5812–7. doi:10.1109/IECON.2013.6700087.

[162] Zhang S, Tseng KJ, Vilathgamuwa DM, Nguyen TD, Wang XY. Design of a robust grid interface system for pmsg-based wind turbine generators. IEEE Trans Ind Electron 2011;58:316–28. doi:10.1109/TIE.2010.2044737.

[163] Dehghanzadeh AR, Behjat V, Banaei MR. Electrical Power and Energy Systems Double input Z-source inverter applicable in dual-star PMSG based wind turbine. Int J Electr Power Energy Syst 2016;82:49–57. doi:10.1016/j.ijepes.2016.02.017.

[164] Bajestan MM, Madadi H, Shamsinejad MA. Controller Design for a Wind Turbine-Based Variable Speed Permanent Magnet Synchronous Generator Using Quasi-Z-Source Inverter in Stand-Alone Operation. 2019 10th Int. Power Electron. Drive Syst. Technol. Conf., Iran: IEEE; 2019, p. 558–65. doi:10.1109/PEDSTC.2019.8697260.

[165] Bajestan MM, Madadi H, Shamsinejad MA. Control of a new stand-alone wind turbine-based variable speed permanent magnet synchronous generator using quasi-Z-source inverter. Electr Power Syst Res 2019;177:106010.

doi:10.1016/j.epsr.2019.106010.

[166] Rajesh R, Mabel MC. A comprehensive review of photovoltaic systems. Renew Sustain Energy Rev 2015;51:231–48. doi:10.1016/j.rser.2015.06.006.

[167] Akbari H, Browne MC, Ortega A, Huang MJ, Hewitt NJ, Norton B, et al. Efficient energy storage technologies for photovoltaic systems. Sol Energy 2018:1–25. doi:10.1016/j.solener.2018.03.052.

[168] Li X, Yao L, Hui D. Optimal control and management of a large-scale battery energy storage system to mitigate fluctuation and intermittence of renewable generations. J Mod Power Syst Clean Energy 2016;4:593–603. doi:10.1007/s40565-016-0247-y.

[169] Solomon AA, Faiman D, Meron G. Appropriate storage for high-penetration grid-connected photovoltaic plants. Energy Policy 2012;40:335–44. doi:10.1016/j.enpol.2011.10.019.

[170] Zini G, Dalla Rosa A. Hydrogen systems for large-scale photovoltaic plants: Simulation with forecast and real production data. Int J Hydrogen Energy 2014;39:107–18. doi:10.1016/j.ijhydene.2013.10.076.

[171] Tamalouzt S, Benyahia N, Rekioua T, Rekioua D, Abdessemed R. Performances analysis of WT-DFIG with PV and fuel cell hybrid power sources system associated with hydrogen storage hybrid energy system. Int J Hydrogen Energy 2016;41:21006–21. doi:10.1016/j.ijhydene.2016.06.163.

[172] Hadjipaschalis I, Poullikkas A, Efthimiou V. Overview of current and future energy storage technologies for electric power applications. Renew Sustain Energy Rev 2009;13:1513–22. doi:10.1016/j.rser.2008.09.028.

[173] European Commission. Energy storage – the role of electricity. Brussels: 2017.

[174] IBRAHIM H, ILINCA A, PERRON J. Energy storage systems—Characteristics and comparisons. Renew Sustain Energy Rev 2008;12:1221–50. doi:10.1016/j.rser.2007.01.023.

[175] Chen H, Cong TN, Yang W, Tan C, Li Y, Ding Y. Progress in electrical energy storage system: A critical review. Prog Nat Sci 2009;19:291–312. doi:10.1016/j.pnsc.2008.07.014.

[176] Karpinski AP, Makovetski B, Russell SJ, Serenyi JR, Williams DC. Silver – zinc : status of technology and applications 1999.

[177] Lopes PP, Stamenkovic VR. Past, present, and future of lead–acid batteries. Science (80-) 2020;369:923–4. doi:10.1126/science.abd3352.

[178] Omar N, Firouz Y, Monem MA, Samba A, Gualous H, Coosemans T, et al. Analysis of Nickel-Based Battery Technologies for Hybrid and Electric Vehicles. Elsevier Inc.; 2014. doi:10.1016/b978-0-12-409547-2.10740-1.

[179] Deng D. Li-ion batteries: Basics, progress, and challenges. Energy Sci Eng 2015;3:385–418. doi:10.1002/ese3.95.

[180] IEC. Electrical Energy Storage - White Paper. Int Electrotech Comm 2011:1–78. doi:10.1002/bse.3280020501.

[181] Liserre M, Blaabjerg F, Hansen S. Design and control of an LCL-filter-based three-phase active rectifier. IEEE Trans Ind Appl 2005;41:1281–91. doi:10.1109/TIA.2005.853373.

[182] SunPower Corporation. X-Series Residential Solar Panels s | X21-335-BLK | X21-345. Sunpower Coorporation 2016.

[183] De Soto W, Klein SA, Beckman WA. Improvement and validation of a model for photovoltaic array performance. Sol Energy 2006;80:78–88. doi:10.1016/j.solener.2005.06.010.

[184] Villalva MG, Gazoli JR, Filho ER. Comprehensive approach to modeling and simulation of photovoltaic arrays. IEEE Trans Power Electron 2009;24:1198–208. doi:10.1109/TPEL.2009.2013862.

[185] Lang Z, Zhang Y. Parameter identification and performance estimation for PV modules based on reduced forms model. J Renew Sustain Energy 2020;12. doi:10.1063/5.0019511.

[186] Yazdani A, Iravani R. Voltage-Sourced converters in power systems: Modeling, control and applications. 1st ed. Hoboken, New Jersey: John Wiley & Sons, INC.; 2010.

[187] Heier S. Grid integration of wind energy: Onshore and offshore conversion systems. Third edit. 2014.

[188] Rolan A, Luna A, Vazquez G, Aguilar D, Azevedo G. Modeling of a variable speed wind turbine with a Permanent Magnet Synchronous Generator. 2009 IEEE Int. Symp. Ind. Electron., vol. 7, IEEE; 2009, p. 734–9. doi:10.1109/ISIE.2009.5218120.

[189] De Oliveira-Assis L, Soares-Ramos EPP, Sarrias-Mena R, Garcia-Trivino P, Fernandez-Ramirez LM. Large-Scale Grid Connected Quasi-Z-Source Inverter-Based PV Power Plant. Proc. - 2020 IEEE Int. Conf. Environ. Electr. Eng. 2020 IEEE Ind. Commer. Power Syst. Eur. EEEIC / I CPS Eur. 2020, 2020, p. 1–6. doi:10.1109/EEEIC/ICPSEurope49358.2020.9160529.

[190] Ould Amrouche S, Rekioua D, Rekioua T, Bacha S. Overview of energy storage in renewable energy systems. Int J Hydrogen Energy 2016;41:20914–27. doi:10.1016/j.ijhydene.2016.06.243.

[191] Dufo-López R, Cortés-Arcos T, Artal-Sevil JS, Bernal-Agustín JL. Comparison of lead-acid and li-ion batteries lifetime prediction models in stand-alone photovoltaic systems. Appl Sci 2021;11:1–16. doi:10.3390/app11031099.

[192] SimPowerSystems TM. Reference, Hydro-Québec and the MathWorks. Inc, Natick, MA 2015.

[193] Krug D, Bernet S. Design and Comparison of Medium Voltage Multi-Level Converters for Industry Applications. Conf Rec 2004 IEEE Ind Appl Conf 2004 39th IAS Annu Meet 2004;2:781–90 vol.2.

doi:10.1109/IAS.2004.1348503.

[194] Kahn MTE. A pattern for LCL filter design for renewable power 2018:5–10.

[195] Peng FZ, Shen M, Qian Z. Maximum boost control of the Z-source inverter. IEEE Trans Power Electron 2005;20:833–8. doi:10.1109/TPEL.2005.850927.

[196] Shen M, Wang J, Joseph A, Peng FZ, Tolbert LM, Adams DJ. Maximum Constant Boost Control of the Z-Source Inverter. Conf Rec 2004 IEEE Ind Appl Conf 2004 39th IAS Annu Meet 2004;1:142–7. doi:10.1109/IAS.2004.1348400.

[197] Europe TI. Field Orientated Control of 3-Phase 1998.

[198] Yazdani A, Iravani R. Voltage-sourced converters in power systems: Modeling, Control, and Applications. 2010.

[199] Liu Y, Abu-Rub H, Ge B, Blaabjerg F, Ellabban O, Loh PC. Impedance Source Power Electronic Converters. 2016th ed. 2016.

[200] Liu Y, Ge B, Abu-Rub H, Peng FZ. Overview of Space Vector Modulations for Three-Phase Z-Source/Quasi-Z-Source Inverters. IEEE Trans Power Electron 2014;29:2098–108. doi:10.1109/TPEL.2013.2269539.

[201] Kazimierczuk MK. Pulse-width modulated DC-DC power converters. John Wiley & Sons; 2015.

[202] Li Y, Anderson J, Peng FZ, Dichen L. Quasi-z-source inverter for photovoltaic power generation systems. Conf Proc - IEEE Appl Power Electron Conf Expo - APEC 2009:918–24. doi:10.1109/APEC.2009.4802772.

[203] Singh N, Jain SK. A novel strategy for indirect control of peak dc-link voltage of grid-connected qZS inverter fed through renewable energy sources. Electr Eng 2020;102:611–25. doi:10.1007/s00202-019-00897-4.

[204] García P, Torreglosa JP, Fernández LM, Jurado F. Improving long-term operation of power sources in off-grid hybrid systems based on renewable energy, hydrogen and battery. J Power Sources 2014;265:149–59. doi:10.1016/j.jpowsour.2014.04.118.

List of publications

Publications in indexed journals in JCR-SCIE:

1. Soares-Ramos, E. P. P., de Oliveira-Assis, L., Sarrias-Mena, R., Garcia-Triviño, P., Garcia-Vazquez, C. A., Fernandez-Ramirez, Luis M. "Averaged Dynamic Modelling and Control of a Quasi-Z-Source Inverter for Wind Power Applications". *IEEEAccess. v.9, p.1 - 1, 2021.*
   DOI: 10.1109/ACCESS.2021.3104797
   JCR: 3.367 (Q1)

2. Soares-Ramos, E. P. P., de Oliveira-Assis, L., Sarrias-Mena, R., Fernandez-Ramirez, L. M. "Current status and future trends of offshore wind power in Europe*". Energy., v.202, p.117787- ,2020.*
   DOI: https://doi.org/10.1016/j.energy.2020.117787
   JCR: 7.147 (Q1)

3. de Oliveira-Assis, L., Garcia-Triviño, P., Soares-Ramos, E. P. P., Sarrias-Mena, R., Garcia-Vazquez, C. A., Ugalde-Loo, C. E., Fernandez-Ramirez, L. M. "Optimal energy management system using biogeography based optimization for grid-connected MVDC microgrid with photovoltaic, hydrogen system, electric vehicles and Z-source converters". *Energy Conversion and Management. v.248, p.114808, 2021.*
   DOI: https://doi.org/10.1016/j.enconman.2021.114808
   JCR: 9.709 (Q1)

4. de Oliveira-Assis, L., Soares-Ramos, E.P.P., Sarrias-Mena, R., García-Triviño, P., González-Rivera, E., Sánchez-Sainz, H., Llorens-Iborra, F., Fernández-Ramírez, L.M. *"*Simplified Model of Battery Energy-Stored Quasi-Z-Source Inverter-Based Photovoltaic Power Plant with Twofold Energy Management System*". Energy 2021.*
   DOI: https://doi.org/10.1016/j.energy.2021.122563
   JCR: 7.147 (Q1)

Publications in international congress proceedings with peer review:

1. Soares-Ramos, E. P. P., de Oliveira-Assis, L., Sarrias-Mena, R., García-Triviño, P., Garcia-Vazquez, C. A., Fernandez-Ramirez, L. M. "Large-Scale Wind Turbine with Quasi-Z-Source Inverter and Battery" *In: 2021 22nd IEEE International Conference on Industrial Technology (ICIT), 2021, Valencia.*
   DOI: 10.1109/ICIT46573.2021.9453537

2. Soares-Ramos, E. P. P., de Oliveira-Assis, L., Sarrias-Mena, R., García-Triviño, P., Garcia-Vazquez, C. A., Fernandez-Ramirez, L. M. "Control of a Grid-connected Wind Turbine with Quasi-Z-Source Inverter" *In: 2020 9th International Conference on Renewable Energy Research and Application (ICRERA), 2020, Glasgow. IEEE, 2020.*
   DOI: 10.1109/ICRERA49962.2020.9242843

3. de Oliveira-Assis, L., Soares-Ramos, E. P. P., Sarrias-Mena, R., García-Triviño, P., Fernandez-Ramirez, L. M. "Large-Scale Grid Connected Quasi-Z-Source Inverter-Based PV Power Plant" *In: 2020 IEEE International Conference on Environment and Electrical Engineering and 2020 IEEE Industrial and Commercial Power Systems Europe (EEEIC / I&CPS Europe), 2020, Madrid.*
   DOI: 10.1109/EEEIC/ICPSEurope49358.2020.9160529

4. de Oliveira-Assis, L., Soares-Ramos, E. P. P., García-Triviño, P., Sarrias-Mena, R., Garcia-Vazquez, C. A., Fernandez-Ramirez, L. M. "Fuzzy-based Energy Management System for a MVDC PV Power Plant with Battery Stored Quasi-Z-Source Inverter". *In: 2021 IEEE International Conference on Environment and Electrical Engineering and 2020 IEEE Industrial and Commercial Power Systems Europe (EEEIC / I&CPS Europe), 2021, Bari.*
    DOI: 10.1109/EEEIC/ICPSEurope51590.2021.9584829

5. Garcia-Triviño, P., de Oliveira-Assis, L., Soares-Ramos, E. P. P., Sarrias-Mena, R., Garcia-Vazquez, C. A., Fernandez-Ramirez, L. M. "Configuration and Control of a MVDC Hybrid Charging Station of Electric Vehicles with PV / Battery / Hydrogen System" *In: 2021 IEEE International Conference on Environment and Electrical Engineering and 2020 IEEE Industrial and Commercial Power Systems Europe (EEEIC / I&CPS Europe), 2021, Bari.*
    DOI: 10.1109/EEEIC/ICPSEurope51590.2021.9584795

Curriculum vitae

Emanuel Philipe Pereira Soares Ramos

PhD student in Energy and Sustainable Engineering at University of Cádiz (2021), Spain. Master in Electrical Engineering from Federal Center for Technological Education of Minas Gerais (2014) and graduation in Electrical Engineering from University Center of Belo Horizonte (2011).

Address to access this CV: http://lattes.cnpq.br/8094743298562984

Personal Information

Name	Emanuel Philipe Pereira Soares Ramos
Bibliographic Citation	SOARES-RAMOS, EMANUEL P.P.
Professional Address	Centro Federal de Educação Tecnológica de Minas Gerais. Rua Santa Rita Santa Rita 35790000 - Curvelo, MG - Brasil Phone: (38) 37293900 Website URL: www.cefetmg.br

Formal Education/Degree

2018   Ph.D. in progress in Ingeniería Energética y Sostenible .
Universidad de Cádiz, UCA, Espanha. *Advisor:* Dr. D. Luis Miguel Fernández Ramírez.

2012 - 2014   Master´s in Engenharia Elétrica .
Centro Federal de Educação Tecnológica de Minas Gerais, CEFET/MG, Brasil. *Year of degree:* 2014.
Advisor: Eduardo Gonzaga da Silveira.

2009 - 2011   Graduation in Engenharia Elétrica .
Centro Universitário de Belo Horizonte, UniBH, Brasil.
Advisor: Igor Amariz Pires, Arlete Vieira da Silva.

2006 incomplete   Graduation discontinued in 2009 in Engenharia Elétrica .
Pontifícia Universidade Católica de Minas Gerais, PUC Minas, Brasil.
Year of interruption: 2009

2004 - 2005   Professional/Technical Course in Telecomunications .
SENAI, CETEL, Brasil.

Professional Experience

Centro Federal de Educaçao Tecnológica de Minas Gerais (CEFET-MG)
Professor. (2014 – actual).
Serviço Nacional de Aprendizagem Industrial (SENAI – MG)
Professor (2009 - 2014).
Progen
Designer of electrical projects (2006 - 2009).
EPC
Designer of electrical projects (2009 - 2009).

Languages

Portuguese	Native.
English	Escuela Oficial de Idiomas, Algeciras, Espanha. B1 level (2019).
Spanish	Universidad de Cádiz, Spain. B1 level (2018).
French	Escuela Oficial de Idiomas, Algeciras, Espanha. B1 level (2019).

Articles in Scientific Journals

1. SOARES-RAMOS, EMANUEL P. P. ; DE OLIVEIRA-ASSIS, LAIS ; SARRIAS-MENA, RAUL ; GARCIA-TRIVINO, PABLO ; Garcia-Vazquez, Carlos Andres ; FERNANDEZ-RAMIREZ, LUIS M. . Averaged Dynamic Modelling and Control of a Quasi-Z-Source Inverter for Wind Power Applications. IEEE Access, v. 9, p. 1-1, 2021.

2. DE OLIVEIRA-ASSIS, LAIS ; GARCÍA-TRIVIÑO, PABLO ; SOARES-RAMOS, EMANUEL P.P. ; SARRIAS-MENA, RAÚL ; GARCÍA-VÁZQUEZ, CARLOS ANDRÉS ; UGALDE-LOO, CARLOS ERNESTO ; FERNÁNDEZ-RAMÍREZ, LUIS M. . Optimal energy management system using biogeography based optimization for grid-connected MVDC microgrid with photovoltaic, hydrogen system, electric vehicles and Z-source converters. ENERGY CONVERSION AND MANAGEMENT, v. 248, p. 114808, 2021.

3. DE OLIVEIRA-ASSIS, LAIS ; SOARES-RAMOS, EMANUEL P.P. ; SARRIAS-MENA, RAÚL ; GARCÍA-TRIVIÑO, PABLO ; González-Rivera, Enrique ; SÁNCHEZ-SAINZ, HIGINIO ; Llorens-Iborra, Francisco ; FERNÁNDEZ-RAMÍREZ, LUIS M. . Simplified model of battery energy-stored quasi-Z-source inverter-based photovoltaic power plant with Twofold energy management system. ENERGY, v. xxx, p. 122563, 2021.

4. SOARES-RAMOS, EMANUEL P.P. ; DE OLIVEIRA-ASSIS, LAIS ; SARRIAS-MENA, RAÚL ; FERNÁNDEZ-RAMÍREZ, LUIS M. . Current status and future trends of offshore wind power in Europe. ENERGY, v. 202, p. 117787, 2020.

5. RAMOS, E. P. P. S. ; SILVA, A. V. ; PIRES, I. A. ; ASSIS, L. O. . Comportamento do Gerador Eólico Duplamente Alimentado Submetido Distúrbios na rede Elétrica e à Variação da Velocidade do Vento. Revista Brasileira de Energia, v. 20, p. 129-157, 2014.

6. RAMOS, E. P. P. S. ; SILVA, A. V. . SIMULAÇÃO DO GERADOR EÓLICO DUPLAMENTE ALIMENTADO QUANDO SUBMETIDO À VARIAÇÃO DA VELOCIDADE DO VENTO. E-xacta (Belo Horizonte), v. v4, p. 1-11, 2011.

Complete works published in proceedings of conferences

1. DE OLIVEIRA-ASSIS, LAIS ; SOARES-RAMOS, EMANUEL P. P. ; GARCIA-TRIVINO, PABLO ; SARRIAS-MENA, RAUL ; Garcia-Vazquez, Carlos Andres ; FERNANDEZ-RAMIREZ, LUIS M. . Fuzzy-based Energy Management System for a MVDC PV Power Plant with Battery Stored Quasi-Z-Source Inverter, 2021, Bari. 2021 IEEE International Conference on Environment and Electrical Engineering and 2021 IEEE Industrial and Commercial Power Systems Europe (EEEIC / I&CPS Europe), 2021. p. 1.

2. GARCIA-TRIVINO, PABLO ; OLIVEIRA-ASSIS, LAIS DE ; SOARES-RAMOS, EMANUEL P. P. ; SARRIAS-MENA, RAUL ; Garcia-Vazquez, Carlos Andres ; FERNANDEZ-RAMIREZ, LUIS M. . Configuration and Control of a MVDC Hybrid Charging Station of Electric Vehicles with PV/Battery/Hydrogen System, 2021, Bari. 2021 IEEE International Conference on Environment and Electrical Engineering and 2021 IEEE Industrial and Commercial Power Systems Europe (EEEIC / I&CPS Europe), 2021. p. 1.

3. SOARES-RAMOS, EMANUEL P. P. ; DE OLIVEIRA-ASSIS, LAIS ; SARRIAS-MENA, RAUL ; GARCIA-TRIVINO, PABLO ; GARCIA-VAZQUEZ, CARLOS A. ; FERNANDEZ-RAMIREZ, LUIS M. . Large-Scale Wind Turbine With Quasi-Z-Source Inverter and Battery, 2021, Valencia. 2021 22nd IEEE International Conference on Industrial Technology (ICIT), 2021. p. 403.

4. DE OLIVEIRA-ASSIS, LAIS ; SOARES-RAMOS, EMANUEL P. P. ; SARRIAS-MENA, RAUL ; GARCIA-TRIVINO, PABLO ; FERNANDEZ-RAMIREZ, LUIS M. . Large-Scale Grid Connected Quasi-Z-Source Inverter-Based PV Power Plant, 2020, Madrid. 2020 IEEE International Conference on Environment and Electrical Engineering and 2020 IEEE Industrial and Commercial Power Systems Europe (EEEIC / I&CPS Europe), 2020. p. 1-6.

5. SOARES-RAMOS, EMANUEL P. P. ; DE OLIVEIRA-ASSIS, LAIS ; SARRIAS-MENA, RAUL ; GARCIA-TRIVINO, PABLO ; GARCIA-VAZQUEZ, CARLOS A. ; FERNANDEZ-RAMIREZ, LUIS M. . Control of a Grid-connected Wind Turbine with Quasi-Z-Source Inverter, 2020, Glasgow. 2020 9th International Conference on Renewable Energy Research and Application (ICRERA), 2020. p. 309.

6. FRANCA, J. V. G. ; COSTA, P. A. ; GONCALVES, B. M. ; SOARES-RAMOS, EMANUEL P. P. . Análise, Simulação E Implementação De Um Controlador Mppt Aplicado A Um Sistema Fotovoltaico, 2017, São Paulo. 15º FEBRACE - Feira Brasileira de Ciências e Engenharia, 2017.

7. CALDEIRA, A. G. ; ARAUJO, L. S. ; SOARES-RAMOS, EMANUEL P. P. . Automação de instalações elétricas residenciais por comando de voz, 2016, São Paulo - São Paulo. 14º FEBRACE - Feira Brasileira de Ciências e Engenharia, 2016.

8. MENEZES, T. N. O. ; RAMOS, E. P. P. S. ; ASSIS, L. O. ; MENEZES, J. J. P. . Estudo Comparativo de Viabilidade de Implantação de Energia Alternativa na Ilha de Arapiranga na Região Amazônica: Uma Solução Para o Problema da Falta de Energia Elétrica, 2016. CLADE - III Congreso de Las Américas de Distribución Eléctrica, 2016.

9. SOARES-RAMOS, EMANUEL P. P. ; SILVEIRA, Eduardo Gonzaga da ; ROCHA, S. A. . Avaliação da proteção de distância utilizando curvas Mho polarizadas em linhas de transmissão com compensação série, 2016, Córdoba - República Argentina. CLADE - III Congreso de Las Américas de Distribución Eléctrica, 2016.

10. ASSIS, L. O. ; RIBEIRO, C. L. O. S. ; RAMOS, E. P. P. S. . The Relevance of humanistic subjects in Energy Engineering, 2014, Santiago de Cuba, Cuba. CONVENCIÓN INTERNACIONAL DE CIENCIAS TÉCNICAS - I Conferencia sobre la Enseñanza de la Ingeniería, 2014.

11. SOARES-RAMOS, EMANUEL P. P. ; SILVEIRA, Eduardo Gonzaga da . Protección diferencial de líneas de transmisión con compensación serie, 2014, Buenos Aires - Argentina. CIDEL - International Conference on Electricity Distribution, 2014.